MAPPING BRAIN CIRCUITS IN HEALTH AND DISEASE

by

Qiuyu Wu

A Dissertation

Submitted to the Faculty of Purdue University

In Partial Fulfillment of the Requirements for the degree of

Doctor of Philosophy

Department of Biological Sciences

West Lafayette, Indiana

August 2019

THE PURDUE UNIVERSITY GRADUATE SCHOOL
STATEMENT OF COMMITTEE APPROVAL

Dr. Alexander A. Chubykin, Chair
Department of Biological Sciences

Dr. Donna Fekete
Department of Biological Sciences

Dr. Richard van Rijn
Department of Medicinal Chemistry and Molecular Pharmacology

Dr. Edward Bartlett
Department of Biological Sciences

Approved by:

Dr. Janice Evans
Head of the Graduate Program

This work is dedicated to my parents, Ruilin Wu and Xiaobai Lv. They are my biggest inspiration in science and in life.

ACKNOWLEDGMENTS

It has been five very fulfilling years since I moved from China to West Lafayette, Indiana. During these years, I grew as a scientist and as a person, a leader, and a team player. This dissertation could not have come to completion without the help from so many people, my supportive family, loving husband, dear friends, respected mentors, helpful colleagues, and trusting collaborators.

I thank my parents, Ruilin Wu and Xiaobai Lv, who raised me to be independent, to embrace life's new challenges, and to be graceful no matter what I am facing.

I thank my husband, Dr. Mark Sayles, who I met at Purdue through our common love in neuroscience and found out that what we share reaches far beyond science. I am so lucky to have a person who I love to also understand my work, my thoughts, and my struggles.

I thank my PhD supervisor Dr. Alexander A. Chubykin, who took me into his lab and gave me tremendous opportunities to explore new directions, to take on responsibilities, and to grow from a naive college graduate into a confident scientist.

I thank my committee members, Dr. Donna M. Fekete, Dr. Richard M. van Rijn, and Dr. Edward L. Bartlett. They were the most supportive committee and gave me so much more than guiding my research project.

I thank my colleagues, Samuel T. Kissinger, Mang Gao, Alexandr Pak, Yu Tang, and others working on the second floor of Lilly Hall. We bounce ideas, we help each other out on experiments, and we occasionally have fun together. I could not have finished my PhD work without them.

I'd like to thank my collaborators, Dr. Gong Chen and his team from Pennsylvania State University, for trusting me to work with them, sharing ideas, and helping with experiments. I'd also like to thank other collaborators, Dr. Shriram Ramanathan, Dr. Chen Yang, Dr. Jixin Chen, Dr. Edward Fox, Dr. Saeed Mohammadi, Dr. Alexey Shashurin, and Dr. Guangjun Zhang. Each collaboration was a different exciting challenge.

Lastly, I'd like to thank the Purdue University Interdisciplinary Life Science Program (PULSe), Purdue University Department of Biological Sciences, the National Institutes of Health (NIH), and Whitehall Foundation for funding and supporting my graduate studies.

TABLE OF CONTENTS

LIST OF TABLES

LIST OF FIGURES

LIST OF ABBREVIATIONS

AAV: adeno-associated virus

ACRs: anion-selective channelrhodopsins

ACSF: artificial cerebrospinal fluid

AMPA(R): α-amino-3-hydroxy-5-methyl-4-isoxazolepropionic acid (receptor)

AP(s): action potential(s)

Arch: Archaerhodopsin

ASD: Autism spectrum disorder

BHK: baby hamster kidney (cell line)

BNC: Bayonet Neill–Concelman (connector)

CCD: charge-coupled device

CDC: Centers for Disease and Prevention

CD-ROM: compact disc read-only memory

COM port: communication port

ChR2: Channelrhodopsin 2

CRACM: Channelrhodopsin Assisted Circuit Mapping

DAG: diacylglycerol

DAQ: data acquisition

DIC: differential interference contrast

EEG: electro-encephalogram

EPSC(s): excitatory post synaptic current(s)

ESC(s): embryonic stem cell(s)

ET-1: endothelin-1

EYFP: enhanced yellow fluorescent protein

FMRP: fragile X mental retardation protein

FS: fast-spiking

FXS: Fragile X syndrome

GFAP: Glial fibrillary acidic protein

GFP: green fluorescent protein

GPCR(s): G-protein coupled receptor(s)

G-protein: guanine nucleotide-binding proteins

GUI: graphical user interface

HCN: Hyperpolarization-Activated Cyclic Nucleotide-Gated

HEK 293: human embryonic kidney293 (cell line)

HEPES: 4-(2-hydroxyethyl)-1-piperazineethanesulfonic acid

HFS: high frequency stimulation

HRP: horseradish peroxidase

HSDB: high-sucrose dissection buffer

HSV: herpes simplex virus

IB: intrinsically bursting

IC: current clamp

IP: intra-peritoneal

iPSCs: induced pluripotent cells

IP_3: inositol trisphosphate

IP_3R: IP_3 receptors

LED: Light-emitting diode

LFS: low frequency stimulation

LGN: dorsal lateral geniculate nucleus

LTD: long term depression

LTP: long-term potentiation

L2/3: layer 2/3

L4: layer 4

L5: layer 5

mACR: metabotropic acetylcholine receptor

mCMV: murine cytomegalovirus

MOSFETs: metal-oxide semiconductor field-effect transistors

NIH: National Institutes of Health

NMDA(R): N-methyl-D-aspartate (receptor)

NMDG: N-methyl-D-glucamine

NpHR: halorhodopsin from natronomonas

PACUC: Purdue University animal care and use committee

PBS: Phosphate-buffered saline

PC: personal computer

PCB: printed circuit board

PFA: paraformaldehyde

PIP_2: phosphatidylinositol bisphosphate

RS: regular-spiking

PLC-β: β isoform of phospholipase C

PV: parvalbumin

RO4: rat rhodopsin 4

SC(s): Schaffer Collateral(s)

STDP: spike timing-dependent plasticity

S1: somatosensory cortex

TTL: transistor-transistor logic

TTX: tetrodotoxin

VC: voltage clamp

VEP(s): visually evoked potential(s)

V1: primary visual cortex

WT: wild-type

YFP: yellow fluorescent protein

2D: two dimensions

4-AP: 4-Aminopyridine

5-HT_2: 5-hydroxytryptamine receptor 2

ABSTRACT

Author: Wu, Qiuyu PhD
Institution: Purdue University
Degree Received: August 2019
Title: Mapping Brain Circuits in Health and Disease
Committee Chair: Alexander A. Chubykin

Intricate neural circuits underlie all brain functions. However, these neural circuits are highly dynamic. The ability to change, or the plasticity, of the brain has long been demonstrated at the level of isolated single synapses under artificial conditions. Circuit organization and brain function has been extensively studied by correlating neuronal activity with information input. The primary visual cortex has become an important model brain region for the study of sensory processing, in large part due to the ease of manipulating visual stimuli. Much has been learned from studies of visual cortex focused on understanding the signal-processing of visual inputs within neural circuits. Many of these findings are generalizable to other sensory systems and other regions of cortex. However, few studies have directly demonstrated the orchestrated neural-circuit plasticity occurring during behavioral experience.

It is vital to measure the precise circuit connectivity and to quantitatively characterize experience-dependent circuit plasticity to understand the processes of learning and memory formation. Moreover, it is important to study how circuit connectivity and plasticity in neurological and psychiatric disease states deviates from that in healthy brains. By understanding the impact of disease on circuit plasticity, it may be possible to develop therapeutic interventions to alleviate significant neurological and psychiatric morbidity. In the case of neural trauma or ischemic injury, where neurons and their connections are lost, functional recovery relies on neural-circuit repair. Evaluating whether neurons are reconnected into the local circuitry to re-establish the lost connectivity is crucial for guiding therapeutic development.

There are several major technical hurdles for studies aiming to quantify circuit connectivity. First, the lack of high-specificity circuit stimulation methods and second, the low throughput of the gold-standard patch-clamp technique for measuring synaptic events have limited progress in this area. To address these problems, we first engineered the patch-clamp experimental system to automate the patching process, increasing the throughput and consistency of patch-clamp

electrophysiology while retaining compatibility of the system for experiments in *ex vivo* brain slices. We also took advantage of optogenetics, the technology that enables control of neural activity with light through ectopic expression of genetically encoded photo-sensitive channels in targeted neuronal populations. Combining optogenetic stimulation of pre-synaptic axonal terminals and whole-cell patch-clamp recording of post-synaptic currents, we mapped the distribution and strength of synaptic connections from a specific group of neurons onto a single cell. With the improved patch-clamp efficiency using our automated system, we efficiently mapped a significant number of neurons in different experimental conditions/treatments. This approach yielded large datasets, with sufficient power to make meaningful comparisons between groups.

Using this method, we first studied visual experience-dependent circuit plasticity in the primary visual cortex. We measured the connectivity of local feedback and recurrent neural projections in a Fragile X syndrome mouse model and their healthy counterparts, with or without a specific visual experience. We found that repeated visual experience led to increased excitatory drive onto inhibitory interneurons and intrinsically bursting neurons in healthy animals. Potentiation at these synapses was absent or abnormal in Fragile X animals. Furthermore, recurrent excitatory input onto regular spiking neurons within the same layer remained stable in healthy animals but was depressed in Fragile X animals following repeated visual experience. These results support the hypothesis that visual experience leads to selective circuit plasticity which may underlie the mechanism of visual learning. This circuit plasticity process is impaired in a mouse model of Fragile X syndrome.

In a separate study, in collaboration with the laboratory of Dr. Gong Chen, we applied the circuit-mapping method to measure the effect of a novel brain-repair therapy on functional circuit recovery following ischemic injury, which locally kills neurons and creates a glial scar. By directly reprogramming astrocytes into neurons within the region of the glial scar, this gene-therapy technology aims to restore the local circuit and thereby dramatically improve behavioral function after devastating neurological injury. We found that direct reprogramming converted astrocytes into neurons, and importantly, we found that these newly reprogrammed neurons integrated appropriately into the local circuit. The reprogramming also improved connections between surviving endogenous neurons at the injury site toward normal healthy levels of connectivity. Connections formed onto the newly reprogrammed neurons spontaneously

remodeled, the process of which resembled neural development. By directly demonstrating functional connectivity of newly reprogrammed neurons, our results suggest that this direct reprogramming gene-therapy technology holds significant promise for future clinical application to restore circuit connectivity and neurological function following brain injury.

INTRODUCTION

The circuitry of the primary visual cortex

Vision is an important sensory modality, with a critical role in guiding behavior for most animals. Emitted and reflected light from the environment enters the eyes and stimulates photoreceptors in the retina; that is, the sensory organ that converts light energy into electrical signals in neurons. From here, visual neural signals travel from the eyes through the optic nerve, across the optic chiasm, and enter the dorsal lateral geniculate nucleus (LGN). After some processing in LGN circuits, visual information enters the primary visual cortex (V1), where more complex visual processing takes place (Remington, 2012). Numerous studies on the visual cortex have revealed fundamental neurophysiological properties of this area, its response patterns to visual inputs, the information that the neuronal activity carries, and the implied signal-processing functions that explain the principals of how vision works(Werner & Chalupa, 2014). Compared to some of the higher-level cortical areas responsible for making executive decisions based on complex multi-sensory input as well as the brain's internal state, the primary visual cortex receives (primarily) simple information input which is also easy to manipulate. Because of this advantage, the primary visual cortex has also become one of the "model areas" for studying the general organization of the neocortex, the so-called "canonical circuitry." A similar situation applies to the somatosensory cortex (S1), in that it receives a relatively simple input and has become a model system for the study of somatosensory processing. For this reason, V1 and S1 are the most extensively studied cortical areas. Similarities between the two shed light on the fundamental processing principles of the common circuit structure of the cortex, while differences between them help inform circuit specializations to accommodate different functions.

Searching for canonical circuitry

Now classical studies describing neuronal response properties in the visual cortex in response to different forms of visual stimulation came from the work of Hubel and Wiesel (Hubel & Wiesel, 1959, 1962, 1963). Their seminal work in cat primary visual cortex laid the foundation for later studies about cortical circuitry and function. They discovered that some neurons in V1 have a simple preference for stimuli within an area of visual space (receptive field) that either

elicits excitation or inhibition, divided by an axis in the middle of the area ("simple cells"). Other cells have preferences based on more complex characteristics of the visual stimuli, such as the location (receptive field), orientation (static), direction (moving), size and shape, and boundary between bright and dark (edge detection) ("complex cells"). The preferences, or tuning, of the cells also corelate with the physical location of the cells in a way that cells with similar tuning tend to group together in a "column" perpendicular to the surface of the brain. Hubel and Wiesel proposed a hierarchical cortical circuitry that could explain the tuning properties of different groups of cells. Simple tuning cells receive multiple inputs from cells in the LGN, each of which have concentric receptive fields and align along an axis. Complex tuning cells receive multiple inputs from simple tuning cortical cells, of which the receptive fields have the same axis and are organized in ways that their summed response could explain the activity of the complex cell. Hubel and Wiesel's raw data, presented in their papers, showed that simple cells are mostly located in cortical layer 4 (L4) while complex cell are in superficial layers and deeper layers. If their proposed circuit model is true, this suggests that L4 receives direct input projections from the LGN and then sends output projections to other cortical layers. This model largely agrees with current understanding. Soon after their initial discovery, it was shown that although the majority of inputs from LGN enter V1 at L4, all the other cortical layers receive LGN input to some extent, except for layer 1 (Martin & Whitteridge, 1984). A simplified circuit can be summarized as starting from LGN to L4 to L2/3 to L5 to L6 in a feed-forward direction. Even today, this model still generally holds true in a number of cortical areas (Barbour & Callaway, 2008; Koralek, Jensen, & Killackey, 1988; Shepherd & Svoboda, 2005; Sun, Tan, Mensh, & Ji, 2016; Weiler, Wood, Yu, Solla, & Shepherd, 2008). From here, the most fundamental feed-forward circuitry of V1 and the cortical column processing unit theory was born. Under this assumption, the neocortex consists of repeating processing units with similar circuitry. Each of these processing units possesses a basic level of computing power (Mountcastle, 1997). Depending on the input and output, groups of similar units make up different brain areas that carry out different functions (R. J. Douglas & Martin, 2004).

It is not surprising that many updates have been made to the original V1 circuit model which Hubel and Wiesel proposed decades ago. Details of contralateral vs. ipsilateral thalamic input to V1 were discovered along with subtypes of neurons in the LGN that project to specific layers in V1, which carry certain functional implications (Gilbert, 1993). With better understanding of the

cell-type diversity in V1 (Tasic et al., 2016) and the corresponding functional specialization, more consideration was given to not only the hierarchy but also the types of projections (Niell, 2015). One class of neuron, the inhibitory interneurons, was seldom mentioned in the early studies. This was primarily due to the small percentage of these cells in the total number, and a lack of specificity in stimulation methods used. With recent advances in optogenetics and genetic targeting, characterization of inhibitory neuron projections was added to the picture. The inhibitory network was found to have an intra-cortical structure distinct from the feed-forward excitatory pathway. Unlike the relatively clear organization of trans-laminar excitatory projections, the majority of inhibition comes from intra-laminar (within the same layer) input, although some trans-laminar inhibition also exists (Kätzel, Zemelman, Buetfering, Wölfel, & Miesenböck, 2010). In V1, one group of inhibitory neurons expressing parvalbumin (PV+) has high firing rates and narrow action potential widths ("fast-spiking" cells). These neurons have large receptive fields and are broadly tuned to visual stimulation (Hofer et al., 2011). It is believed that their inhibitory output to neighboring excitatory neurons controls the overall "gain" of the local functional unit rather than affecting stimulus selectivity of individual excitatory neuron. Depending on the situation, this gain control during visual experience may sharpen the tuning of the microcircuit (Atallah, Bruns, Carandini, & Scanziani, 2012). Remarkably, the patterns of inhibitory input to excitatory cells in different cortical areas (V1, somatosensory, and motor cortices) share little resemblance, so that the precise pattern of inhibition could theoretically serve as an identifier to assign which cortical area an excitatory cell belongs to (Kätzel et al., 2010). This could be interpreted as a challenge to the "canonical circuit" theory because when taking into account the inhibitory circuit, different cortical areas are not close replicas of each other. Alternatively, the inhibitory modulation of excitatory circuitry can be interpreted as the specialization and adaptation to the different functions each cortical area undertakes.

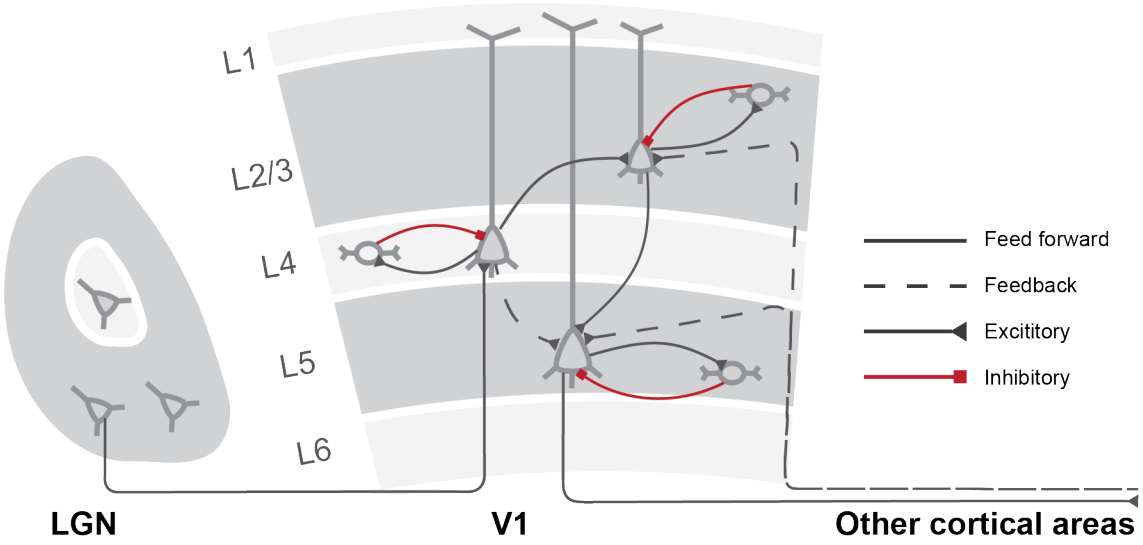

Figure 1. Simplified primary visual cortex circuitry

Predictive coding theory of the primary cortex

Classical studies of V1, including those by Hubel and Wiesel, assumed that V1 extracts visual features, such as orientation, direction, edges, etc., based on input from the LGN. Therefore, in this classical view, the function of the V1 circuit is to compute these features mainly through summation of smaller visual information units in the LGN. However, more recent studies postulate that V1 computes the differences between expectation and actual received input, so-called "predictive coding" (Adams, Friston, & Bastos, 2015). In theory, predictive coding is more energy efficient than descriptive coding in the sense that it only computes the difference or "predictive error" rather than all the information of a stimulus. It is now generally accepted that the brain is actively inferring a general model of the environment constructed from sensory inputs it receives. When "real" input is compared with the model, the most meaningful information is the difference. With the addition of an intrinsic feedback microcircuit from L5 to L4 and L2/3 to the canonical feedforward circuit (Usrey & Fitzpatrick, 1996), the basic circuit infrastructure for predictive coding already exists in V1 (and also other cortical areas). The majority of L2/3 and L5 neurons do not send projections to other cortical areas in the feedforward direction, which implies that they participate in local feedback and recurrent (intralaminar) circuitry (Briggs & Callaway, 2005). While layers 2/3 and 4 receive the external input, inter-laminal projections from excitatory to inhibitory neurons, especially from

deep layers to superficial layers, carry the "prediction." Whether the predictive coding theory of V1 is true or not is still under debate, but it is clear that the intrinsic feedforward and recurrent projections, which consist the majority of projections in V1, must carry out significant computational functions.

There is no doubt that some fundamental common theme exists throughout the neocortex in mammals, but variations for functional adaptation in different cortical areas within and across species are also ubiquitous (Harris & Shepherd, 2015). Indeed, as more and more exceptions of cortical micro-circuitry in different species and different functional areas are detailed, it is hard to determine whether the term "canonical circuit" is an over-simplification or is indeed the fundamental rule from which diversity evolves. Progress in our detailed understanding of V1 circuitry was largely driven by advances in technology. The increasing specificity and resolution in stimulation methods along with cell type classification based on gene expression profiles permitted us to dissect projections that were formerly grouped together or masked by a single dominant output. Some of the key technical advances will be discussed in the following sections. While it seems to be a daunting task, some institutions, like the Allen Brain Institute (https://alleninstitute.org), are conducting ambitious projects to systematically map all projections in V1 (as opposed to anecdotal studies). The resulting comprehensive map of V1 circuitry might enable a renewed and better functional understanding of cortical circuits.

Dynamics of circuitry: synaptic plasticity

The complex circuitry of the brain is not static. In fact, the idea that the "connections" between cells in the brain change with experience was proposed as early as in the late 18th century by the Scottish philosopher Bain (Bain, 1875), even before the discovery of synapses and before Cajal's beautiful work on neuron morphology and circuitry (see Edward G Johns's history on Cajal, 1990 (Jones, 1999)). We could only speculate how Bain had this idea so far ahead of physical evidence. Perhaps it was because of the intuitive inference from observations such as skills being learned by repetition, and our ability to mentally associate events occurring in temporal sequence. With the development of electrophysiology, scientists began searching for the rules for such change in synaptic connections as an underlying physiological basis for circuit plasticity.

Hebbian plasticity

The neuropsychologist Donald Hebb first pin-pointed that activity and timing are the key to synaptic plasticity. In his seminal book "The Organization of Behavior", he famously proposed the rule "neurons that fire together, wire together", which is known today as the "Hebbian postulate" (Hebb, 1949). Hebb thought that if one neuron consistently contributes to the activation of another neuron, biochemical process happens in either or both cells to make the synapse grow stronger so that the first cell's input contributes more for the firing of the second in subsequent events. He also proposed that synaptic plasticity is the neuronal basis of learning and memory. Assemblies of neurons, what we would now call a neural circuit, that group together because of stimulus induced synaptic plasticity is how a memory or learned concept is represented in the brain.

To test the Hebbian postulate, scientists tried to artificially stimulate the pre-synaptic cells and post-synaptic cells in various ways. Most of these studies were done in acute brain slice preparations. That is, the brain tissue was sectioned while cells in it were maintained alive so that projections are exposed in 2D. This gives easy access for stimulation and recording. Some experimental evidence from such studies supported the Hebbian postulate in a quite literal way. For example, when stimulating two distinct pathways projecting to the same post synaptic cell, simultaneous weak activation could induce long-term potentiation (LTP), or strengthening of the synapse, in both pathways. In contrast, weak activation of either pathway alone would not result in LTP. Furthermore, strong activation of one pathway leads to LTP specifically in the stimulated pathway and long term depression (LTD), or weakening of the synapse, in the unstimulated pathway (Lynch, Dunwiddie, & Gribkoff, 1977). More generally, people found that high-frequency stimulation to pre-synaptic cells induces LTP (R. M. Douglas & Goddard, 1975), while low-frequency stimulations induced LTD (Dunwiddie & Lynch, 1978). This was collectively known as the "BCM learning rule" after the three people who discovered it, Elie Bienenstock, Leon Cooper, and Paul Munro (Bienenstock, Cooper, & Munro, 1982). The discovery that LTD can be induced by stimulation below a certain threshold (generally at 1Hz) as opposed to complete absence of stimulation was very significant for the theory of homeostatic plasticity. This means that neurons adjust the overall synaptic strength based on their own firing rate (most likely corelated to the overall network activity level), also referred to as "synaptic scaling" (Turrigiano, 2008). Homeostatic plasticity is the perfect rescue for the theoretical flaw if

Hebbian plasticity is the only rule – strong synapses will overpower the network and weak synapses will be completely silenced. Homeostatic plasticity sets the limit for the overall connectivity of the network so that Hebbian-style plasticity can only change relative weights of the synaptic connections but doesn't push the network to either extreme.

Timing is important in plasticity

The rules for synaptic plasticity discussed above largely ignored the temporal relationship between pre- and post-synaptic activity. Around the time the Hebbian postulate was proposed, patch-clamp had not been invented and there was no good method to precisely control the post-synaptic activity. Some studies indirectly addressed this issue by activating two distinct pathways leading to the same post-synaptic cell sequentially with different stimulation intensity. The strong input most likely induced above-threshold depolarization leading to firing while the weak input could only induce below threshold depolarization. They found that when the strong input came before the weak input, the weak input was depressed; when the strong input came after the weak input, the weak input was potentiated (Levy & Steward, 1983).

At the same time, the discovery of the N-methyl-D-aspartate (NMDA) receptor as a coincidence detector provided a molecular substrate for associative plasticity. The NMDA receptor is an ionotropic glutamate receptor that is commonly expressed at the post-synaptic terminal. The NMDA receptor ion channel is blocked by a magnesium ion at resting membrane potential. In this condition, glutamate binding to the receptor will not lead to the influx of cations. Post-synaptic depolarization releases the blockade by Mg^{2+} and, if glutamate is bound to the receptor at the same time, the ion channel will open and cations will flow into the cell (F. Li & Tsien, 2009). This property of the NMDA receptor dictates that it is only activated when pre-synaptically released glutamate binds to it in the presence of post-synaptic cell membrane depolarization (Collingridge, Kehl, & McLennan, 1983). This post-synaptic depolarization is usually is the result of a back-propagating action potential (Gasparini & Migliore, 2013). Gating of the NMDAR allows influx of Na+, leading to further membrane depolarization. In addition, Ca^{2+} ions pass through the NMDAR channel. The resulting increase of intracellular Ca^{2+} levels leads to a subsequent signaling cascade, resulting in insertion, phosphorylation, endocytosis, and dephosphorylation of α-amino-3-hydroxy-5-methyl-4-isoxazolepropionic acid (AMPA) receptors at the post-synaptic terminal (VanDongen, 2008). Post-synaptic depolarization that activates

NMDA receptors can be achieved via AMPA receptor currents as a result of high frequency pre-synaptic release at the same synapse (homosynaptic), or via back propagating action potentials (APs) from the cell body to the dendrites as a result of activity at other synapses of the same neuron (heterosynaptic).

With increasing use of patch clamp electrophysiology, a previously unrecognized form of synaptic plasticity strictly dependent on the timing of activation was discovered (Dan & Poo, 2004). This has since become a favorite for theoretical and computational models of associative learning. Not only do cells have to be activated relatively close in time, as Donald Hebb proposed, but additionally they must be activated in the correct sequence. When the pre-synaptic cell fires consistently before the post-synaptic cell (causal sequence) within a short time range (10s of milli seconds), LTP is induced; when the pre-synaptic cell fires consistently after the post-synaptic cell (acausal sequence) also within a short time range, LTD is induced (Markram, Lubke, Frotscher, & Sakmann, 1997). This new set of rules for synaptic plasticity was later coined as "Spike Timing-Dependent Plasticity (STDP)" (Song, Miller, & Abbott, 2000). STDP partially supported Hebb's postulate that two neurons need to be repeatedly activated in close temporal association to induce strengthening of the connection that is stable in the long term. However, it further revealed that the temporal sequence is as important as mere temporal proximity. It also provided a perfect synaptic mechanism for associative learning: the presumed causal relationship between two information stream will be connected.

Neuromodulation in plasticity

Recent compelling evidence showed that neuromodulators may play a role as the "supervisor" to regulate some forms of activity-dependent plasticity (Gu & Yakel, 2011; K. He et al., 2015). New computational models have been created to explain these findings (Gavornik & Shouval, 2011; Gavornik, Shuler, Loewenstein, Bear, & Shouval, 2009). These models combine some features of both the unsupervised Hebbian and of the supervised synaptic modification rules. According to these computational models, Hebbian plasticity "tags" synapses with "synaptic tags/eligibility traces," which make the synapses eligible to be modified but does not directly change the synaptic strength. Next, these tagged synapses may express different plasticity (direction, amplitude, etc.) in the presence of different neuromodulators. For example, some forms of experience-dependent plasticity, such as monocular deprivation, are reported to

demonstrate features similar to Hebbian plasticity in the thalamocortical synapse (Cooke & Bear, 2014). However, other forms of reward-dependent learning in visual cortex may depend both on Hebbian and supervised forms of plasticity. For example, pairing visual stimuli with reward delivered at a delay leads to changes in neuronal responses, the process of which depends on the cholinergic system (Chubykin, Roach, Bear, & Shuler, 2013).

Recent findings that acetylcholine is released by the basal forebrain at the time of reward or punishment supports the model that acetylcholine may serve as a reinforcement agent in the visual cortex (S. C. Lin, Brown, Hussain Shuler, Petersen, & Kepecs, 2015). One interesting aspect of this question is that many neuromodulator receptors, such as metabotropic acetylcholine receptor (mAChR) 1, 3, and 5 for acetylcholine, 5-hydroxytryptamine receptor 2 ($5\text{-}HT_2$) for serotonin, and α1 adrenergic receptors for norepinephrine, share the same Gq protein coupled secondary messenger pathway, but are involved in different brain functions. However, how neuromodulators precisely determine the expression and regulate the direction of synaptic plasticity is not entirely clear. This is partially limited by the methods that we could use to manipulate neuromodulation. Pharmacological application of neuromodulator, their analogues, or agonists and antagonists of their receptors are all useful ways to study neuromodulation, but the time scale of drug application is often too slow to resolve the real-time neuronal activity and synaptic plasticity. Electrically activating known neuromodulatory axonal inputs to a brain area has the desired temporal resolution but is rarely feasible because these axons are usually diffusely located. On the other hand, it is possible to stimulate deep brain nuclei where neuromodulatory cell bodies reside, but this will result in systemic activation of the neuromodulation, which leads to complex effects in many brain areas. Recent developments in optogenetics have provided many exciting new options, which will be discussed in later sections.

Experience dependent plasticity and learning

While synaptic plasticity rules have been tested in single isolated synapses, learning at the whole-animal level is much more complex and involves simultaneous changes in multiple synapses. Because most animals constantly receive numerous sensory inputs that activate the brain, the basic structure of circuitry that provides fundamental information processing needs to be relatively stable to maintain a stable world view. However, under some extreme circumstances, drastic synaptic changes can be induced that are easy to observe. The classical

experience-dependent plasticity example was monocular deprivation in kittens. This was discovered also by Hubel and Wiesel, the same people who first described the circuit organization of cat primary visual cortex. In the early 1960s, soon after they first discovered receptive fields and selective tuning properties of V1 neurons, they found that if all visual input was abolished from one eye for an extended period (by suturing the eye lids closed), V1 neurons change their preferred eye (ocular dominance) dramatically to favor the open eye. However, this was only true in kittens, and not in adult cats. When the same monocular deprivation procedure was applied to adult cats, the V1 cell ocular dominance remained largely unchanged (Wiesel & Hubel, 1963). Additionally, the ocular dominance from monocular deprivation in kittens can be reversed by closing the opposite eye while re-opening the previously deprived eye if this procedure was done at young age (Blakemore & Van Sluyters, 1974). These findings led to the proposed "critical period," during which the brain is highly susceptible to plasticity and after which period the brain loses its ability to change its circuitry. Change of overall activity, for example through dark rearing, can prolong the critical period (Cynader & Mitchell, 1980). Studies even showed that dark exposure can re-open the critical period, or re-sensitize to plasticity, and aid the reversal of monocular deprivation in adults (H.-Y. He, Ray, Dennis, & Quinlan, 2007; Montey & Quinlan, 2011).

Experience-dependent plasticity is not confined to the visual cortex. For example, a somatosensory equivalent to monocular deprivation is the trimming of whiskers in rodents. This procedure results in large changes to whisker mapping in the somatosensory cortex (Feldman & Brecht, 2005). However, both blinding of one eye and losing whiskers/appendages are extreme conditions where a major branch sensory input to the brain is completely abolished. Moreover, many of the circuit changes during this form of experience-dependent plasticity were observed indirectly. That is, circuit changes are inferred through measures of cell response preference or mapping of the input signal. This limitation is partially because only drastic changes in connectivity can be easily observed at the neuronal population scale. Since information passes through multiple synapses from the sensory organ to the cortex, it is hard to pin point which synapse underwent what kind of change.

Recent technological advances have provided potential solutions. High density silicon-based electrode arrays allow us to record from hundreds to thousands of neurons simultaneously with the approximate physical location of the cell relative to the channels on the probe. Through

spike-train analysis, we can infer the information flow between neurons based on the relative timing and pattern of firing (Brown, Kass, & Mitra, 2004). However, this is still an indirect way to measure connections between neurons. As is common in neuroscience, technological advances have driven new discoveries. In the field of synaptic plasticity, patch-clamp (which will be discussed in some detail in later sections) permitted the discovery of back propagating action potentials and STDP. Studying complex plasticity during natural experience and learning requires new technology that can directly measure circuit connectivity, and changes in circuit connectivity, in real time.

Morphological and functional circuit mapping

There are two aspects of circuit connectivity: morphological and functional. The former emphasizes the physical structure of the neural processes and the physical presence of synapses, while the later emphasizes the ability to conduct signals from one cell to another. Undoubtedly, these two aspects are intertwined because to conduct signals from one cell to the other, there has to be a physical synapse. The size and type of synapse correlates (to a certain extent) with its ability to conduct signals. Larger synapses exert a greater influence on the post-synaptic cell than do smaller synapses. Also, as it was discussed in the previous section, activity in the pre and post synaptic neurons is important to maintain and modify the presence of synapses through synaptic plasticity (Yuste & Bonhoeffer, 2001). However, largely due to the presence of silent synapses that do not respond to neurotransmitters (Kerchner & Nicoll, 2008), morphological connectivity does not completely match functional connectivity. Pure morphological assessments may therefore over-estimate the degree to which neurons are functionally connected.

Morphological circuit mapping

At the brain region-scale, morphological connectivity mapping can be done very effectively by injecting tracer to the source region and then locating the projection destination through histology and imaging (Sawchenko & Swanson, 1981). The tracer can range from horseradish peroxidase (HRP) and its conjugates (Benson & Voigt, 1995), to biotin derivatives including biocytin (Mishra, Dhingra, Schuz, Logothetis, & Canals, 2010) and neurobiotin (Huang, Zhou, & DiFiglia, 1992), to chemical fluorescent dye (Stewart, 1981), to genetically encoded fluorescent

protein. The tracing direction can be either anterograde, meaning along the direction of information flow, or retrograde, meaning opposite to the direction of information flow. For example, for anterograde tracing, the tracer is injected to the source of the projection of interest so that the cell bodies take up the tracer which defuses along the processes and eventually reach the axonal terminals.

There is growing popularity to use genetically encoded fluorescent proteins to trace projections. This technique allows the gene expression to be targeted through both focal injection and cell-type specific promotors, sometimes in combination with transgenic animals, to achieve better specificity in tracing than is achievable by other methods. Adeno-associated virus (AAV) is the most commonly used viral vector to deliver tracer protein because of the low cytotoxicity, robust expression, and no pathogenic risk (Muzyczka, 1992). The Allen Brain Institute has generated a large comprehensive connectivity data set across brain regions using AAV and, in some cases, cell type specific cre-recombinase transgenic mouse lines (Oh et al., 2014). While most studies use viral vectors to deliver the fluorescent protein-encoding gene *in vivo* to a population of neurons (Chamberlin, Du, de Lacalle, & Saper, 1998), some studies directly deliver the DNA to a single cell through a pipette to achieve mapping at the astonishing single-cell resolution (Pala & Petersen, 2015). Consequently, this method is extremely difficult and laborious, and therefore only reported in a few studies. The Allen Brain Institute has attempted to generate a large database containing primary visual cortical single cell projection maps along with electrophysiological characterizations and gene-expression profiling. With its large-scale financial resources and consolidated expertise, Allen Brain Institute is enabling data generation at a scale not feasible for single-investigator led studies.

Although anterograde tracing can give us a lot of useful information, one disadvantage is that the post-synaptic target is unclear, only the brain region can be located unless used in combination with cell-type specific reporter transgenic lines and super-resolution imaging. Retrograde tracing, however, is used to trace back the neurons that project onto a specific region. Although chemical retrograde tracing dyes have been used for decades, engineered rabies virus that can pass from the post-synaptic neuron to the pre-synaptic neuron is extremely useful for precise tracing for up-stream projection sources (Wickersham, Finke, Conzelmann, & Callaway, 2006). By combining AAV carrying cell-type specific promoter driven cre-recombinase genes injected at the source with retrograde tracing rabies virus carrying cre-dependent fluorescent

protein genes injected at the projection target, this method can effectively trace medium to long range projections with cell-type specificity.

Functional circuit mapping

Ultimately, it is the functional conductance that dictates information processing. To measure synaptic strength, one has to stimulate the pre-synaptic neuron and measure the synaptic event triggered in the post-synaptic neuron. The most precise way to measure and manipulate single cells in high temporal resolution is whole-cell patch-clamp (details about the development of patch-clamp will be discussed in later sections). Two cells (usually within a few hundreds of micrometers distance) are patched. Stimulation and recording can be done for both cells, to measure bidirectional synaptic strength (Qi, Radnikow, & Feldmeyer, 2015; Russo & Taverna, 2014). A tracer dye can be included in the patch pipette. This diffuses into the patched neuron during the recording, allowing morphological reconstruction in post-hoc histology and imaging. One study attempted to measure thousands of such pairs in the neocortex and reconstructed cell morphology, based on which they categorized cortical neurons into cell types and sub-types and derived a general connectivity model (Jiang et al., 2015). This study was by far the most systematic circuit mapping using the paired patch method and generated incredibly detailed and substantial data that is very laborious to obtain. Despite the huge dataset, this study still received criticism over the clam that they found the "principle" for neocortical micro-circuitry because they most likely did not cover the complete circuitry (Barth et al., 2016). Indeed, it is arguably impossible to draw the complete picture of cortical circuitry using currently available technology. However, the strength of the paired patch technique is clear: high precision and high temporal resolution with bidirectional synaptic strength measurement and potential for morphological reconstruction. On the other hand, the disadvantages are also obvious: high technical barrier and very low throughput.

While patch-clamp remains the gold standard for measuring sub-threshold synaptic events, other strategies have been employed to stimulate pre-synaptic neurons. Most existing studies on cortical functional connectivity focused on excitatory synapses, which utilize glutamate as the main neurotransmitter. When the effect of pre-synaptic changes affecting synaptic conductance is not in consideration, instead of triggering pre-synaptic release of glutamate, the post-synaptic cell can be directly stimulated by application of exogenous glutamate that diffuses into the

synaptic cleft. To apply glutamate with high spatial precision and for ease of control, chemically "caged" glutamate molecules were synthesized by adding a blocking group linked to glutamate with a photosensitive covalent bond. The caged glutamate molecule cannot activate glutamate receptors, but certain wavelengths of light can break the chemical bond and "uncage" glutamate, which then activates the receptors. This process is called glutamate uncaging. It is combined with focal light stimulation, often in a grid pattern, to map the distribution and strength of glutamatergic synapses on a single cell under whole-cell patch clamp (Callaway & Katz, 1993). There are three significant draw backs of this method: first, as mentioned before, pre-synaptic influences are not accounted for; second, synapses close to the cell body cannot be accurately measured due to the presence of extra-synaptic glutamate receptors on the cell body (Petralia et al., 2010); and third, glutamate uncaging is only effective in acute brain slices in which caged glutamate can adequately penetrate the thin tissue slice. It is not feasible in most *in vivo* preparations.

While the need for direct measurement of circuit connectivity is high, the significant technical challenge limits the number of studies that are conducted and the questions that can be answered. For functional mapping, the two major hurdles are the specificity and resolution of presynaptic stimulation and the low throughput nature of the whole-cell patch-clamp technique. As is always the case, the needs of scientific research drive technology development, and new revolutionary technological leaps permit waves of new discovery.

Optogenetics: controlling neurons with light

Optogenetics is one of the most recent influential technical breakthroughs in the field of neuroscience. It is a simple idea that by expressing exogenous photosensitive ion channels in neurons, the cell will be photo-sensitive and thus controllable by light. The question is, where do you find suitable photosensitive ion channels that are compatible with neuronal physiology? The answer came a little bit by surprise: single-cell green algae *Chlamydomonas reinhardtii.* Chlamydomonas needs a mechanism to detect light so that it can swim towards light to conduct photosynthesis and obtain energy. Being a single-celled phytoplankton, it doesn't have complex systems dedicated to light detection (it has only 1 cell after all) but relies simply on cation gradients created by a photosensitive cation channel which, upon light stimulation, changes its conformation and allows cations to flow through (Ridge, 2002). Another class of opsins from

bacteria, halorhodopsin which opens a chloride channel upon light exposure, is also used as an optogenetic tool to manipulate, in this case inhibit, neuronal activity (Okuno, Asaumi, & Muneyuki, 1999). However, due to the long evolutionary distance between microbes and vertebrate animals, microbial opsins were not the first choice when people first explored ways to engineer neurons to introduce light sensitivity. Because of the drastic difference between prokaryotic and eukaryotic cells, there were doubts whether microbial proteins could even be expressed in animal cells, let alone carry out their original function. Ironically, microbial opsins are far more broadly used today as optogenetic tools than animal opsins.

The invention of optogenetics

Before the early 2000s, studies about bacterial and algal opsins were primarily limited to the ecological and biophysical aspects. In parallel, some attempts to stimulate neurons with light were made using the phototransduction cascade from *Drosophila* (Zemelman, Lee, Ng, & Miesenbock, 2002). Comparing to algae and bacterial opsins which are directly coupled with ion channels (Zhang et al., 2011), animal opsins are generally coupled with guanine nucleotide-binding proteins (G-protein) and activate the specific G-protein subunit signaling pathway which eventually leads to the opening of ion channels (Terakita, 2005). A distinct difference between vertebrate and invertebrate animal phototransduction is that vertebrate photoreceptor cells remain depolarized in the dark, while light exposure results in closure of cation channels and re-polarization of the cell. In contrast, for invertebrate opsins, light opens cation channels and depolarizes cells (Rayer, Naynert, & Stieve, 1990). Because the majority of neurons in the central nervous system signal through above-threshold depolarization and action potentials, the invertebrate photo cascade seemed preferable because of the depolarizing nature of activation and the ease of expression in vertebrate systems. However, the initial success of adopting the fly photo cascade to activate hippocampal neurons did not result in an avalanche of studies using this technology for the simple reason of very low temporal resolution: it took several seconds of light application to trigger action potentials. G-protein signaling is inherently slow because it relies on protein binding kinetics. It is also subjected to complicated modulations in the cell involving many signaling pathways, which can lead to inconsistency of stimulation effect and long-term change in cell excitability and synaptic plasticity. Ion channels, on the other hand, are

much faster (conformation change) and is subject to much less internal modulation. However, there were no known light sensitive ion channels in the animal kingdom.

The development of modern molecular biology and techniques to express exogenous proteins in eukaryotic cells, for example in *Xenopus* oocytes, greatly advanced ion channel research (Hsuei-Chin, Beer, Sassano, Blume, & Ziai, 1991). Membrane bound ion channels are notoriously difficult to purify and many channels of interest have very low endogenous expression levels, thus adding an additional layer of complication to study the physiological behavior of a single type of channel (S. H. Lin & Guidotti, 2009). In 2003, Georg Nagel from the Max-Plank institute for biophysics first expressed Channelrhodopsin 2 (ChR2) from *C. reinhardtii* in *Xenopus* oocytes and two mammalian cell lines (HEK293 and BHK cells). They demonstrated that ChR2 is a light-gated cation channel with fast channel kinetics (Georg Nagel et al., 2003). Soon after this study, biophysicist Nagel started collaborating with Karl Deisseroth at Stanford University to explore the feasibility to use ChR2 as a tool to control neurons with light. At the same time, several groups around the world were also working on applying the ideal property of ChR2 in neuroscience, which includes re-sensitizing the retina to light in photoreceptor degenerated mouse retinal ganglion cells (Bi et al., 2006) and observing light-induced behavioral changes after ChR2 expression in the *C. elegans* nervous system (G. Nagel et al., 2005). Two other groups attempted to demonstrate the use of ChR2 as a tool to control neuronal activity: Herlize's group used the combination of rat rhodopsin 4 (RO4) and ChR2 to stimulate and inhibit neurons for precise control (X. Li et al., 2005), and Yawo's group demonstrated that ChR2 is compatible with controlling neuronal firing for its time scale (Ishizuka, Kakuda, Araki, & Yawo, 2006). However, Deisseroth's group was the first to claim ChR2 as a powerful and highly robust tool to control neuronal activity at the millisecond time scale, in both excitatory and inhibitory circuits (Boyden, Zhang, Bamberg, Nagel, & Deisseroth, 2005). Soon after the first report of ChR2 as an optogenetic tool, inhibitory optogenetic tools were reported. One of the first to be used was the bacterial light-activated chloride-pump Halorhodopsin from *Natronomonas* (NpHR) (Zhang et al., 2007). Even today, there are still disputes over who first invented "optogenetics" in the scientific community, but what is crystal clear is that optogenetics revolutionized the field of neuroscience (Hegemann & Nagel, 2013).

Optogenetic toolkit

Since the initial application of ChR2 in neuroscience, new light-sensitive proteins have been discovered and added to the optogenetic toolkit. For fast channel kinetics and robustness, microbial channelrhodopsins is a major category of optogenetic proteins. Continuous efforts have been made to develop new tools. Members from the family of anion-selective (mainly Cl^-) channelrhodopsins (ACRs) from an algal species, *Guillardia theta,* have the potential to be used as inhibitory optogenetic proteins (Govorunova et al., 2017). However, ACRs seem to exhibit unintended effects when expressed in axon terminals and are therefore not widely used so far. Another class of inhibitory optogenetic protein is Archaerhodopsin (Arch) from Archaea, which are light sensitive proton pumps which hyperpolarize the cell upon light exposure (Chow et al., 2010). Arch and its variant ArchT are probably the most routinely used inhibitory optogenetic proteins currently in active research, having lower cytotoxicity and other negative effects compared to halorhodopsin (El-Gaby et al., 2016). Efforts were also made to optimize the natural form of light-sensitive channels through protein engineering to tailor their properties to specific applications. There are over a dozen variants of the original ChR2 with different channel kinetics (open and close speed), conductance, light sensitivity, and optimum wavelength (e.g., Red-shifted) (J. Y. Lin, 2011).

On the other hand, light-sensitive non-channel proteins, mainly animal opsins, gained interest not primarily for controlling membrane potential but for directly manipulating G-protein signaling pathways. G-protein coupled receptors (GPCRs) are one of the most important group of receptors, especially in the central nervous system. GPCRs are a group of seven-transmembrane domain receptors that, upon ligand binding, initiate signal transduction pathways via G proteins. Heterotrimeric guanine nucleotide-binding proteins (G proteins) consist α, β, and γ subunits, of which G_α binds to GTP and $G_{\beta\gamma}$ dissociate from the heterotrimeric complex when the receptor is activated. The G_α unit has four major subtypes, G_s, G_i, $G_{q/11}$, and $G_{12/13}$, each of which has different secondary signaling pathways (Katritch, Cherezov, & Stevens, 2013). GTP-bound G_q protein activates the β isoform of phospholipase C (PLC-β) to catalyze the hydrolysis of phosphatidylinositol bisphosphate (PIP_2) into inositol trisphosphate (IP_3) and diacylglycerol (DAG) (Mizuno & Itoh, 2009). IP_3 then diffuses into the cytoplasm and binds to IP_3 receptors (IP_3R) to release Ca^{2+} from the intracellular calcium pool (Patterson, Boehning, & Snyder, 2004). On the other hand, G_q-coupled GPCRs can regulate gene translation/protein synthesis

independently from calcium signaling. One such calcium-independent pathway is tyrosine phosphorylation (Moult, Correa, Collingridge, Fitzjohn, & Bashir, 2008) and another is the β-arrestin pathway (Gerber, Gee, & Benquet, 2007). One example of an optogenetic protein for the control of GPCRs is melanopsin. Melanopsin is an evolutionally conserved G_q protein-coupled opsin that is expressed in intrinsically photosensitive retinal ganglion cells, and is involved in regulation of the circadian cycle (Freedman et al., 1999). Ectopically expressed melanopsin provides a temporally precise way to control G_q activation, mimicking the activity of neuromodulatory systems (Bailes & Lucas, 2013). Bypassing different neuromodulator receptors will eliminate receptor kinetics and downstream signaling differences from different G-protein isoforms as a factor, as well as alleviate the difficulties caused by pharmacodynamics of chemical compounds. In contrast, using optogenetics to directly manipulate G_q signaling, and precisely control temporal duration and latency in relation to synaptic activation will allow one to test the precise temporal range of G_q activation that leads to modulation of synaptic plasticity. Similarly, optogenetic control of G_s (Bailes, Zhuang, & Lucas, 2012) and $G_{i/o}$ (Gutierrez et al., 2011) pathways was achieved using vertebrate rhodopsin.

Application of optogenetics

With the ever-growing optogenetic toolkit came the explosive growth in applications. Instantaneous control of animal behavior was achieved by stimulating/inhibiting certain brain area in behaving animals. The striking experimental outcomes were eye-catching by themselves but also directly demonstrated functional specializations of brain areas (especially motor areas) (Bernstein & Boyden, 2011). Stemming from this, researchers are able to study functional long-range projections *in vivo* when combining optogenetics with extracellular recording techniques (usually with high-density silicon-based electrodes) (Carter & de Lecea, 2011). Furthermore, to study brain circuitry at the synaptic level, optogenetics is extremely useful because of the flexibility and precision to target a genetically defined population of cells. Mapping micro-circuitry is most commonly conducted in acute brain slices with spatial scanning laser or LED light stimulation. This method is sometimes referred to as “Channelrhodopsin Assisted Circuit Mapping” or “CRACM.” With the presence of the sodium channel blocker tetrodotoxin (TTX) and potassium channel blocker 4-Aminopyridine (4-AP), synaptic release can be triggered by depolarizing the axonal terminal without initiating somatic action potentials. This helps to

correlate the physical location of the synapse with functional synaptic strength. On the other hand, without blocking Na^+ and K^+ currents, light stimulation can be tuned down so that axonal depolarization is not sufficient to trigger a response and above-threshold action potentials can only be triggered by optogenetic stimulation at the cell body. In this case one could use the technique to map the location of the cell bodies of the projection source.

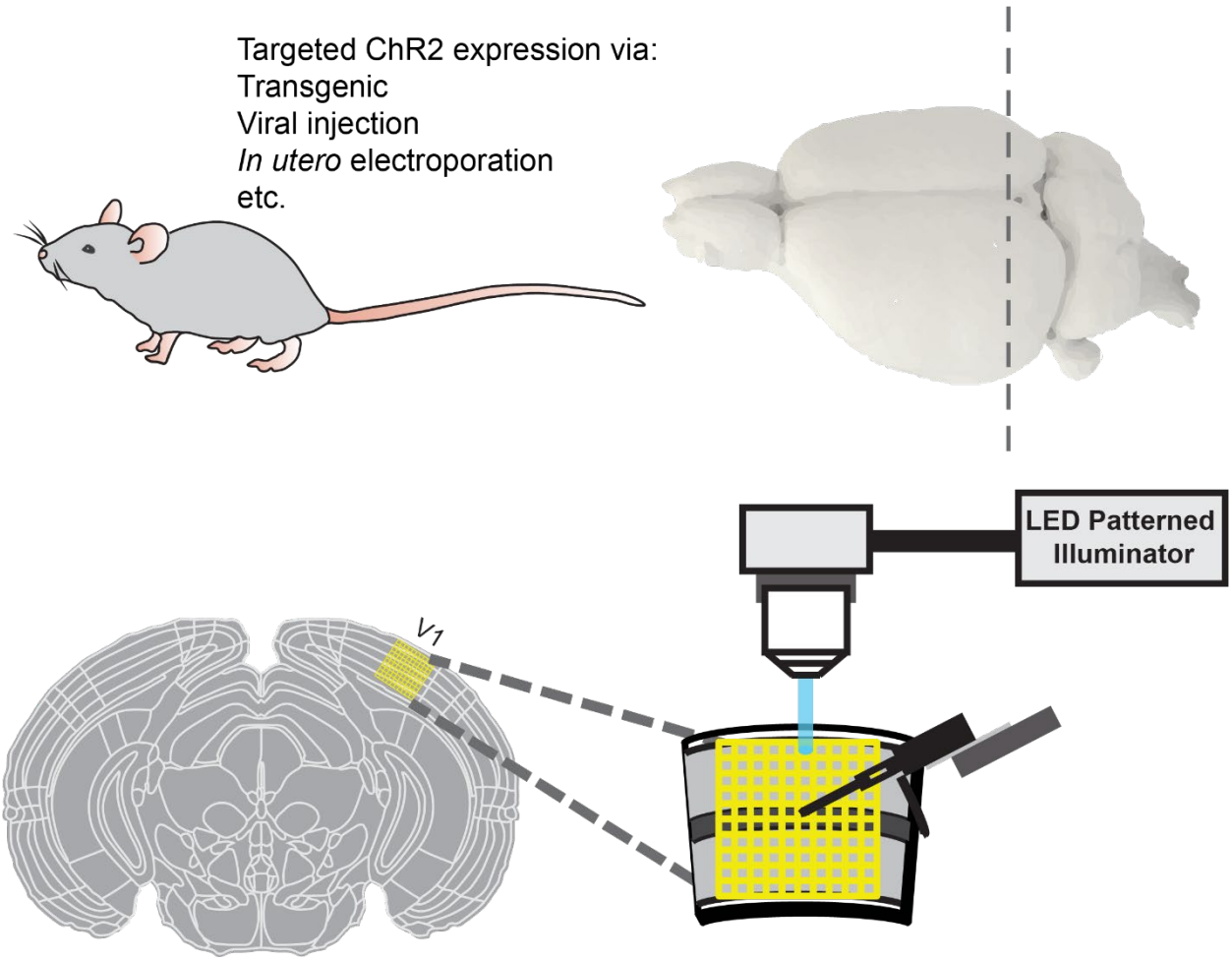

Figure 2. Channelrhodopsin-Assisted Circuit Mapping (CRACM) illustration

Almost 15 years since the invention of optogenetics, this technology has integrated with many other technologies as a powerful tool for multifaceted research. Specific targeting can be achieved through genetics and combinations of anterograde/retrograde labeling; gene delivery and expression through viral vectors, liposome, or nano-particles. Meanwhile, neuroengineering research strives to improve electrodes and optics for stimulation and recording. The simplicity of

the idea, “opto-” and “genetics,” means we take advantage of light, one of the easiest forms of stimulus to control with spatial and temporal precision and resolution, and harness advances in molecular biology and genetics. This is particularly valuable in the field of functional circuit mapping for there were no prior methods that could allow this level of resolution and specificity. The application of optogenetics specifically in functional microcircuit mapping will be discussed in detail in later chapters.

Patch-clamp electrophysiology and current development

Patch-clamp recording has been the gold-standard technique for measuring the electrophysiological properties of excitable cells, as well as single ion channels, since its invention by Neher and Sakmann in the late 1970s to early 1980s (Neher & Sakmann, 1976). Patch-clamp evolved from two early electrophysiology techniques: sharp recordings and two-electrode voltage clamp (not to be confused with the patch clamp mode “voltage clamp” under whole-cell configuration). Sharp recordings were first done by Ling and Gerard on frog sciatic nerve preparation (Ling & Gerard, 1949) but was soon expanded to recording various types of excitable cells from both the soma and axons. This technique utilizes glass pipettes with a very fine tip and usually a relatively long taper that can impale cell membranes while causing minimal disruption to the integrity of the cell function for as long as several hours. The glass pipette is filled with a salt solution and acts as an electrode placed at the inside of the cell membrane while the reference electrode is placed in the extracellular environment. Before sharp recording was invented, only anatomical exceptions like the giant squid axon or mollusk neurons could be recorded from because of their large size. In fact, sharp recording is still commonly used in *in vivo* preparations to record single cells/axons in deep brain nuclei that are difficult to access with any other method. However, due to the high input resistance, it is not possible to record small current signals from individual channels, or to control the membrane potential with a single intracellular sharp electrode (W. C. Li, Soffe, & Roberts, 2004). We now know that the conductance of most ion channels depends on the potential difference across the membrane, making the ability to study channel conductivity at different controlled potentials vital to the characterization of the complete electrophysiological property of a channel. The “two-electrode” voltage clamp partially solved this problem by employing two relatively low impedance electrodes, one for current injection and the other for comparing potentials (Polder & Swandulla,

2001). Because the current injected must equal to the current crossing the membrane through open channels, one can measure current passing through all the channels on the cell membrane. The biggest advantage of the method is that it can inject very large currents, which is useful when the channel density is very high. At the same time, the biggest limitation to this method is that it requires relatively large cells/axons for the insertion of two electrodes, making it impractical in most scenarios.

The invention of patch-clamp

The patch-clamp method was first developed for the "gigaseal" configuration, in which case the electrode and the cell membrane are tightly connected with over 1 giga Ohm resistance. This is usually achieved by applying a small negative pressure to the inside of the pipette. The rational was that during some early experiments, Neher and his colleagues found that when using large diameter (~100 μm) glass pipettes, the noise or instability in the signal was too big to record individual channel currents due to leak current. To reduce this noise, they had to use much smaller pipettes and form a much tighter connection. In 1976, Neher and Sakmann recorded current from nicotinic acetylcholine receptors. They later won the Nobel Prize in Physiology or Medicine in 1991 for their discoveries concerning the function of single ion channels in cells. This study also marks the invention of the patch-clamp technique. Apart from the high signal-to-noise ratio and the ability to "clamp" membrane potential, patch-clamp has an additional advantage in the ease of controlling the intracellular environment (e.g., ion concentration). That is, by manipulating the internal solution composition in the pipette, the ionic composition of the intra-cellular environment can be altered in a controlled way. This technique has proven extremely powerful for studying channel and receptor pharmacology.

From the initial "gigaseal" configuration used by Neher and Sakmann, several additional configurations were derived for different purposes: 1) inside-out configuration, which is when the piece of membrane within the pipette tip during gigaseal is ripped off from the cell and the cytosolic side of the membrane exposed to the recording bath while the extracellular side of the membrane faces the inside of the pipette; 2) whole-cell configuration, which gains direct access to the inside of the cell by creating a hole on the patched membrane while maintaining a tight seal around the hole; and 3) outside-out configuration, which is formed after achieving whole-cell configuration by pulling away the pipette from the cell to rip a piece of the membrane off, at

which point the open lipid bilayer ends fuse together in the aqueous environment, thereby making a patch with the cytosolic side of the membrane facing the inside of the pipette and the extracellular side of the membrane in contact with the bath solution (Molleman, 2003). While gigaseal, inside-out, and outside-out configurations were mostly used to study single channels, the whole-cell configuration is by far the most commonly used patch-clamp configuration to study synaptic plasticity and circuit connectivity in intact neurons. Whole-cell patch-clamp enables direct electrical recording from the inside of a cell through the formation of a direct connection between the glass pipette and the cytoplasm with very low leak current (tight seal). With this direct tight connection, we not only can measure membrane potential (current clamp) or current (voltage clamp) with high precision, but also precisely control the membrane potential or current flow through a feedback circuit without the need of a second electrode (comparing to two-electrode voltage clamp). It is the only method that enables measurement of sub-threshold synaptic events in the scale of milli volts (mV) and pico amperes (pA) and at kilohertz (kHz) acquisition rates. Compared to sharp recordings and two-electrode voltage clamp, patch-clamp can easily manipulate ion concentration on both sides of the cell membrane and is compatible with most cell sizes, even dendrites (Davie et al., 2006) and axonal blebs (self-annealed axon openings) (Hu & Shu, 2012). Apart from neurons, patch-clamp is used in all types of excitable cells from various species and preparations, including but not restricted to glial cells, cardiomyocytes (Richardson & Xiao, 2010), skeletal muscle cells (Wen & Brehm, 2010), smooth muscle cells (Quinn & Beech, 1998), stem-cell derived excitable cells (Verkerk et al., 2017), and cell lines expressing ion channels. With additional steps to remove cell walls, one can even patch plant cells (Elzenga, 2012).

Improving patch-clamp

As the applications for patch-clamp electrophysiology continue to expand, there have been few widely adopted improvements to this challenging and laborious technique (Farre et al., 2009). The intrinsic low throughput and heavy reliance on empirical experience in the traditional manual patch-clamp process does not allow this technique to meet the demands of high throughput testing such as drug screens and large-scale characterization/mapping studies. One of the attempts for high-throughput patch-clamp is planar patch clamp, which substitutes glass pipettes with two-layer glass chips, on which there are micro-fabricated openings that connect

the external and internal fluid chambers, corresponding to the bath solution and pipette internal solution. A single chip can have multiple holes (up to 96) for simultaneous recordings. Instead of using an individual pipette to approach the cell, commercial planner patch-clamp employs microfluidics to carry cells in suspension through the chip, and negative pressure to the internal chamber "draws" cells to the opening to form a seal (Fertig, Blick, & Behrends, 2002; Klemic, Klemic, & Sigworth, 2005; Py et al., 2011). Subsequently, the system can achieve the whole-cell configuration and conduct current-clamp and voltage-clamp recordings. Interestingly, the idea to position a cell in between two chambers and disrupting one side of the membrane to manipulate ion concentration was not a 21st century idea. In 1977, only one year after the first gigaseal experiment, a Russian team measured calcium conductance using a two-chamber system very similar to the design of a single unit planner-patch (Kryshtal & Pidoplichko, 1977). They placed the cell between two chambers separated with a film, on which there was a small hole that the cell could sit on top of. Negative pressure was also applied to the "internal" side of the chamber to help the cell lodge firmly on the hole, after which they disrupted one side of the cell membrane to record specific ionic current flowing through the membrane. However, they most likely did not achieve a giga-Ohm seal because the film they used was made with plastic. This idea was seldomly re-visited until more recently, probably limited by the micro-fabrication processes critical for making glass chips capable of forming the required gigaseals. Even with the most advanced commercial planar patch systems, it cannot always achieve high-quality giga-ohm resistance seals. This is considered an acceptable compromise when throughput is more important (e.g., drug screening) but less appealing when precision is required (e.g., studying detailed single-channel properties). Moreover, planar patch clamp only applies to high density cells in suspension. This does not represent the physiological condition for most excitable cells, and it cannot be used to investigate cell to cell communications such as synapses and neuro-muscular junctions. Therefore, planar patch-clamp systems are adopted by large pharmaceutical companies but not commonly seen in primary academic research institutions.

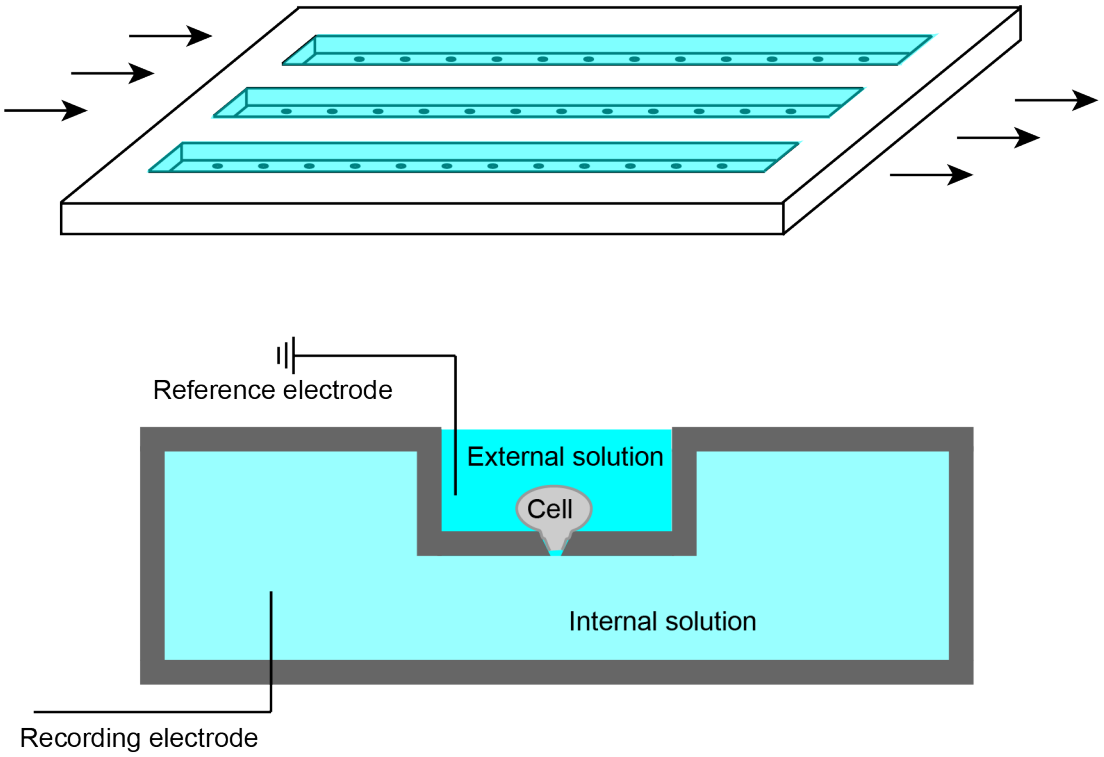

Figure 3. Planner patch illustration

Another engineering approach to the problem is to mimic manual patch-clamp procedures (a moving pipette approaching a static cell target) with machines. Modern patch-clamp pipette manipulators can be digitally controlled, as are the amplifiers and other components of the patch equipment "rig." In 2012, an automated system for *in vivo* whole-cell patch-clamp was developed by controlling one dimensional movement (up and down) of the pipette to target cells, and applying pressure with a digitally controlled air pump (Kodandaramaiah, Franzesi, Chow, Boyden, & Forest, 2012). The procedure very closely resembles manual *in vivo* whole-cell patch without imaging guidance (so called "blind" patch), an extremely difficult and low yield experimental technique. Using pipette resistance measurements through voltage steps (the substances surrounding the pipette act as a resister), it is possible to determine whether the pipette has reached the cell membrane while the manipulator is slowly lowering in the vertical direction. Similarly, the system can determine whether a gigaseal has been formed after applying negative pressure and decide whether to break-in and obtain a whole-cell configuration based on the resistance measurement. Although, judging from the software and hardware components, the system was by no means advanced or sophisticated, it was the first to achieve true automatic

patch-clamp using conventional glass pipettes. The application of this system, however, was limited to *in vivo* preparations, which is not where the biggest need for improved patch-clamp methodology lies.

To date, patch-clamp is still an indispensable method to accurately measure small synaptic events with high temporal resolution. While fluorescent voltage sensors are developing fast, the temporal resolution and measurement sensitivity/accuracy are not comparable with patch-clamp (St-Pierre, Chavarha, & Lin, 2015). In addition, it requires ectopic protein expression (as opposed to label-free imaging methods). In the field of cortical micro circuit and synaptic strength mapping, optogenetics perfectly solved the stimulation problem and the limiting factor is the path-clamp methodology. In the next chapter, I will discuss our work to improve patch-clamp for *ex vivo* acute brain slice preparations and *in vitro* culture preparations, aiming to improve throughput and robustness for optogenetics aided micro-circuit mapping.

References

Adams, R. A., Friston, K. J., & Bastos, A. M. (2015). Active Inference, Predictive Coding and Cortical Architecture. In M. F. Casanova & I. Opris (Eds.), *Recent Advances on the Modular Organization of the Cortex* (pp. 97-121). Dordrecht: Springer Netherlands.

Atallah, B. V., Bruns, W., Carandini, M., & Scanziani, M. (2012). Parvalbumin-expressing interneurons linearly transform cortical responses to visual stimuli. *Neuron, 73*(1), 159-170. doi: 10.1016/j.neuron.2011.12.013

Bailes, H. J., & Lucas, R. J. (2013). Human melanopsin forms a pigment maximally sensitive to blue light (lambdamax approximately 479 nm) supporting activation of G(q/11) and G(i/o) signalling cascades. *Proc Biol Sci, 280*(1759), 20122987. doi: 10.1098/rspb.2012.2987

Bailes, H. J., Zhuang, L. Y., & Lucas, R. J. (2012). Reproducible and sustained regulation of Galphas signalling using a metazoan opsin as an optogenetic tool. *PLoS One, 7*(1), e30774. doi: 10.1371/journal.pone.0030774

Bain, A. (1875). *Mind and Body: The Theories of Their Relation*: D. Appleton.

Barbour, D. L., & Callaway, E. M. (2008). Excitatory local connections of superficial neurons in rat auditory cortex. *J Neurosci, 28*(44), 11174-11185. doi: 10.1523/jneurosci.2093-08.2008

Barth, L., Burkhalter, A., Callaway, E. M., Connors, B. W., Cauli, B., DeFelipe, J., . . . Yuste, R. (2016). Comment on "Principles of connectivity among morphologically defined cell types in adult neocortex". *Science, 353*(6304), 1108. doi: 10.1126/science.aaf5663

Benson, T. E., & Voigt, H. F. (1995). Neuron labeling by extracellular delivery of horseradish peroxidase in vivo: a method for studying the local circuitry of projection and interneurons at physiologically characterized sites. *J Neurosci Methods, 57*(1), 81-91.

Bernstein, J. G., & Boyden, E. S. (2011). Optogenetic tools for analyzing the neural circuits of behavior. *Trends in Cognitive Sciences, 15*(12), 592-600. doi: https://doi.org/10.1016/j.tics.2011.10.003

Bi, A., Cui, J., Ma, Y. P., Olshevskaya, E., Pu, M., Dizhoor, A. M., & Pan, Z. H. (2006). Ectopic expression of a microbial-type rhodopsin restores visual responses in mice with photoreceptor degeneration. *Neuron, 50*(1), 23-33. doi: 10.1016/j.neuron.2006.02.026

Bienenstock, E. L., Cooper, L. N., & Munro, P. W. (1982). Theory for the development of neuron selectivity: orientation specificity and binocular interaction in visual cortex. *J Neurosci, 2*(1), 32-48.

Blakemore, C., & Van Sluyters, R. C. (1974). Reversal of the physiological effects of monocular deprivation in kittens: further evidence for a sensitive period. *The Journal of physiology, 237*(1), 195-216. doi: doi:10.1113/jphysiol.1974.sp010478

Boyden, E. S., Zhang, F., Bamberg, E., Nagel, G., & Deisseroth, K. (2005). Millisecond-timescale, genetically targeted optical control of neural activity. *Nat Neurosci, 8*(9), 1263-1268. doi: 10.1038/nn1525

Briggs, F., & Callaway, E. M. (2005). Laminar patterns of local excitatory input to layer 5 neurons in macaque primary visual cortex. *Cereb Cortex, 15*(5), 479-488. doi: 10.1093/cercor/bhh154

Brown, E. N., Kass, R. E., & Mitra, P. P. (2004). Multiple neural spike train data analysis: state-of-the-art and future challenges. *Nature neuroscience, 7*, 456. doi: 10.1038/nn1228

Callaway, E. M., & Katz, L. C. (1993). Photostimulation using caged glutamate reveals functional circuitry in living brain slices. *Proceedings of the National Academy of Sciences, 90*(16), 7661. doi: 10.1073/pnas.90.16.7661

Carter, M. E., & de Lecea, L. (2011). Optogenetic investigation of neural circuits in vivo. *Trends in Molecular Medicine, 17*(4), 197-206. doi: https://doi.org/10.1016/j.molmed.2010.12.005

Chamberlin, N. L., Du, B., de Lacalle, S., & Saper, C. B. (1998). Recombinant adeno-associated virus vector: use for transgene expression and anterograde tract tracing in the CNS. *Brain Res, 793*(1), 169-175. doi: https://doi.org/10.1016/S0006-8993(98)00169-3

Chow, B. Y., Han, X., Dobry, A. S., Qian, X., Chuong, A. S., Li, M., . . . Boyden, E. S. (2010). High-performance genetically targetable optical neural silencing by light-driven proton pumps. *Nature, 463*(7277), 98-102. doi: 10.1038/nature08652

Chubykin, A. A., Roach, E. B., Bear, M. F., & Shuler, M. G. (2013). A cholinergic mechanism for reward timing within primary visual cortex. *Neuron, 77*(4), 723-735. doi: 10.1016/j.neuron.2012.12.039

Collingridge, G. L., Kehl, S. J., & McLennan, H. (1983). Excitatory amino acids in synaptic transmission in the Schaffer collateral-commissural pathway of the rat hippocampus. *J Physiol, 334*, 33-46.

Cooke, S. F., & Bear, M. F. (2014). How the mechanisms of long-term synaptic potentiation and depression serve experience-dependent plasticity in primary visual cortex. *Philos Trans R Soc Lond B Biol Sci, 369*(1633), 20130284. doi: 10.1098/rstb.2013.0284

Cynader, M., & Mitchell, D. E. (1980). Prolonged sensitivity to monocular deprivation in dark-reared cats. *J Neurophysiol, 43*(4), 1026-1040. doi: 10.1152/jn.1980.43.4.1026

Dan, Y., & Poo, M.-m. (2004). Spike Timing-Dependent Plasticity of Neural Circuits. *Neuron, 44*(1), 23-30. doi: https://doi.org/10.1016/j.neuron.2004.09.007

Davie, J. T., Kole, M. H., Letzkus, J. J., Rancz, E. A., Spruston, N., Stuart, G. J., & Hausser, M. (2006). Dendritic patch-clamp recording. *Nat Protoc, 1*(3), 1235-1247. doi: 10.1038/nprot.2006.164

Douglas, R. J., & Martin, K. A. (2004). Neuronal circuits of the neocortex. *Annu Rev Neurosci, 27*, 419-451. doi: 10.1146/annurev.neuro.27.070203.144152

Douglas, R. M., & Goddard, G. V. (1975). Long-term potentiation of the perforant path-granule cell synapse in the rat hippocampus. *Brain Res, 86*(2), 205-215.

Dunwiddie, T., & Lynch, G. (1978). Long-term potentiation and depression of synaptic responses in the rat hippocampus: localization and frequency dependency. *J Physiol, 276*, 353-367.

El-Gaby, M., Zhang, Y., Wolf, K., Schwiening, C. J., Paulsen, O., & Shipton, O. A. (2016). Archaerhodopsin Selectively and Reversibly Silences Synaptic Transmission through Altered pH. *Cell reports, 16*(8), 2259-2268. doi: 10.1016/j.celrep.2016.07.057

Elzenga, J. T. M. (2012). Patch Clamp Techniques for Plant Cells. In A. G. Volkov (Ed.), *Plant Electrophysiology: Methods and Cell Electrophysiology* (pp. 225-243). Berlin, Heidelberg: Springer Berlin Heidelberg.

Farre, C., Haythornthwaite, A., Haarmann, C., Stoelzle, S., Kreir, M., George, M., . . . Fertig, N. (2009). Port-a-patch and patchliner: high fidelity electrophysiology for secondary screening and safety pharmacology. *Comb Chem High Throughput Screen, 12*(1), 24-37.

Feldman, D. E., & Brecht, M. (2005). Map Plasticity in Somatosensory Cortex. *Science, 310*(5749), 810. doi: 10.1126/science.1115807

Fertig, N., Blick, R. H., & Behrends, J. C. (2002). Whole cell patch clamp recording performed on a planar glass chip. *Biophys J, 82*(6), 3056-3062. doi: 10.1016/S0006-3495(02)75646-4

Freedman, M. S., Lucas, R. J., Soni, B., von Schantz, M., Munoz, M., David-Gray, Z., & Foster, R. (1999). Regulation of mammalian circadian behavior by non-rod, non-cone, ocular photoreceptors. *Science, 284*(5413), 502-504.

Gasparini, S., & Migliore, M. (2013). Action Potential Backpropagation. In D. Jaeger & R. Jung (Eds.), *Encyclopedia of Computational Neuroscience* (pp. 1-6). New York, NY: Springer New York.

Gavornik, J. P., & Shouval, H. Z. (2011). A network of spiking neurons that can represent interval timing: mean field analysis. *J Comput Neurosci, 30*(2), 501-513. doi: 10.1007/s10827-010-0275-y

Gavornik, J. P., Shuler, M. G., Loewenstein, Y., Bear, M. F., & Shouval, H. Z. (2009). Learning reward timing in cortex through reward dependent expression of synaptic plasticity. *Proc Natl Acad Sci U S A, 106*(16), 6826-6831. doi: 10.1073/pnas.0901835106

Gerber, U., Gee, C. E., & Benquet, P. (2007). Metabotropic glutamate receptors: intracellular signaling pathways. *Curr Opin Pharmacol, 7*(1), 56-61. doi: 10.1016/j.coph.2006.08.008

Gilbert, C. D. (1993). Circuitry, architecture, and functional dynamics of visual cortex. *Cereb Cortex, 3*(5), 373-386.

Govorunova, E. G., Sineshchekov, O. A., Rodarte, E. M., Janz, R., Morelle, O., Melkonian, M., . . . Spudich, J. L. (2017). The Expanding Family of Natural Anion Channelrhodopsins Reveals Large Variations in Kinetics, Conductance, and Spectral Sensitivity. *Scientific Reports, 7*, 43358. doi: 10.1038/srep43358 https://www.nature.com/articles/srep43358#supplementary-information

Gu, Z., & Yakel, J. L. (2011). Timing-dependent septal cholinergic induction of dynamic hippocampal synaptic plasticity. *Neuron, 71*(1), 155-165. doi: 10.1016/j.neuron.2011.04.026

Gutierrez, D. V., Mark, M. D., Masseck, O., Maejima, T., Kuckelsberg, D., Hyde, R. A., . . . Herlitze, S. (2011). Optogenetic control of motor coordination by Gi/o protein-coupled vertebrate rhodopsin in cerebellar Purkinje cells. *The Journal of biological chemistry, 286*(29), 25848-25858. doi: 10.1074/jbc.M111.253674

Harris, K. D., & Shepherd, G. M. G. (2015). The neocortical circuit: themes and variations. *Nature neuroscience, 18*, 170. doi: 10.1038/nn.3917

He, H.-Y., Ray, B., Dennis, K., & Quinlan, E. M. (2007). Experience-dependent recovery of vision following chronic deprivation amblyopia. *Nature neuroscience, 10*, 1134. doi: 10.1038/nn1965 https://www.nature.com/articles/nn1965#supplementary-information

He, K., Huertas, M., Hong, Su Z., Tie, X., Hell, Johannes W., Shouval, H., & Kirkwood, A. (2015). Distinct Eligibility Traces for LTP and LTD in Cortical Synapses. *Neuron, 88*(3), 528-538. doi: 10.1016/j.neuron.2015.09.037

Hebb, D. O. (1949). *The Organization of Behavior: A Neuropsychological Theory*: Wiley.

Hegemann, P., & Nagel, G. (2013). From channelrhodopsins to optogenetics. *EMBO molecular medicine, 5*(2), 173-176. doi: 10.1002/emmm.201202387

Hofer, S. B., Ko, H., Pichler, B., Vogelstein, J., Ros, H., Zeng, H., . . . Mrsic-Flogel, T. D. (2011). Differential connectivity and response dynamics of excitatory and inhibitory neurons in visual cortex. *Nature neuroscience, 14*, 1045. doi: 10.1038/nn.2876 https://www.nature.com/articles/nn.2876#supplementary-information

Hsuei-Chin, W., Beer, B., Sassano, D., Blume, A. J., & Ziai, M. R. (1991). Gene expression in Xenopus oocytes. *International Journal of Biochemistry, 23*(3), 271-276. doi: https://doi.org/10.1016/0020-711X(91)90106-W

Hu, W., & Shu, Y. (2012). Axonal bleb recording. *Neurosci Bull, 28*(4), 342-350. doi: 10.1007/s12264-012-1247-1

Huang, Q., Zhou, D., & DiFiglia, M. (1992). Neurobiotin, a useful neuroanatomical tracer for in vivo anterograde, retrograde and transneuronal tract-tracing and for in vitro labeling of neurons. *J Neurosci Methods, 41*(1), 31-43.

Hubel, D. H., & Wiesel, T. N. (1959). Receptive fields of single neurones in the cat's striate cortex. *The Journal of physiology, 148*(3), 574-591.

Hubel, D. H., & Wiesel, T. N. (1962). Receptive fields, binocular interaction and functional architecture in the cat's visual cortex. *The Journal of physiology, 160*(1), 106-154.

Hubel, D. H., & Wiesel, T. N. (1963). Shape and arrangement of columns in cat's striate cortex. *The Journal of physiology, 165*(3), 559-568.

Ishizuka, T., Kakuda, M., Araki, R., & Yawo, H. (2006). Kinetic evaluation of photosensitivity in genetically engineered neurons expressing green algae light-gated channels. *Neurosci Res, 54*(2), 85-94. doi: 10.1016/j.neures.2005.10.009

Jiang, X., Shen, S., Cadwell, C. R., Berens, P., Sinz, F., Ecker, A. S., . . . Tolias, A. S. (2015). Principles of connectivity among morphologically defined cell types in adult neocortex. *Science, 350*(6264), aac9462. doi: 10.1126/science.aac9462

Jones, E. G. (1999). Golgi, Cajal and the Neuron Doctrine. *Journal of the History of the Neurosciences, 8*(2), 170-178. doi: 10.1076/jhin.8.2.170.1838

Katritch, V., Cherezov, V., & Stevens, R. C. (2013). Structure-function of the G protein-coupled receptor superfamily. *Annu Rev Pharmacol Toxicol, 53*, 531-556. doi: 10.1146/annurev-pharmtox-032112-135923

Kätzel, D., Zemelman, B. V., Buetfering, C., Wölfel, M., & Miesenböck, G. (2010). The columnar and laminar organization of inhibitory connections to neocortical excitatory cells. *Nature neuroscience, 14*, 100. doi: 10.1038/nn.2687 https://www.nature.com/articles/nn.2687#supplementary-information

Kerchner, G. A., & Nicoll, R. A. (2008). Silent synapses and the emergence of a postsynaptic mechanism for LTP. *Nature Reviews Neuroscience, 9*, 813. doi: 10.1038/nrn2501

Klemic, K. G., Klemic, J. F., & Sigworth, F. J. (2005). An air-molding technique for fabricating PDMS planar patch-clamp electrodes. *Pflugers Arch, 449*(6), 564-572. doi: 10.1007/s00424-004-1360-8

Kodandaramaiah, S. B., Franzesi, G. T., Chow, B. Y., Boyden, E. S., & Forest, C. R. (2012). Automated whole-cell patch-clamp electrophysiology of neurons in vivo. *Nat Methods, 9*(6), 585-587. doi: 10.1038/nmeth.1993

Koralek, K. A., Jensen, K. F., & Killackey, H. P. (1988). Evidence for two complementary patterns of thalamic input to the rat somatosensory cortex. *Brain Res, 463*(2), 346-351.

Kryshtal, O. A., & Pidoplichko, V. I. (1977). [Analysis of current fluctuations shunted from small portions of the membrane of a nerve cell soma]. *Neirofiziologiia, 9*(6), 644-646.

Levy, W. B., & Steward, O. (1983). Temporal contiguity requirements for long-term associative potentiation/depression in the hippocampus. *Neuroscience, 8*(4), 791-797.

Li, F., & Tsien, J. Z. (2009). Memory and the NMDA receptors. *N Engl J Med, 361*(3), 302-303. doi: 10.1056/NEJMcibr0902052

Li, W. C., Soffe, S. R., & Roberts, A. (2004). A direct comparison of whole cell patch and sharp electrodes by simultaneous recording from single spinal neurons in frog tadpoles. *J Neurophysiol, 92*(1), 380-386. doi: 10.1152/jn.01238.2003

Li, X., Gutierrez, D. V., Hanson, M. G., Han, J., Mark, M. D., Chiel, H., . . . Herlitze, S. (2005). Fast noninvasive activation and inhibition of neural and network activity by vertebrate rhodopsin and green algae channelrhodopsin. *Proc Natl Acad Sci U S A, 102*(49), 17816-17821. doi: 10.1073/pnas.0509030102

Lin, J. Y. (2011). A user's guide to channelrhodopsin variants: features, limitations and future developments. *Experimental physiology, 96*(1), 19-25. doi: 10.1113/expphysiol.2009.051961

Lin, S. C., Brown, R. E., Hussain Shuler, M. G., Petersen, C. C., & Kepecs, A. (2015). Optogenetic Dissection of the Basal Forebrain Neuromodulatory Control of Cortical Activation, Plasticity, and Cognition. *J Neurosci, 35*(41), 13896-13903. doi: 10.1523/JNEUROSCI.2590-15.2015

Lin, S. H., & Guidotti, G. (2009). Purification of membrane proteins. *Methods Enzymol, 463*, 619-629. doi: 10.1016/s0076-6879(09)63035-4

Ling, G., & Gerard, R. W. (1949). The normal membrane potential of frog sartorius fibers. *Journal of Cellular and Comparative Physiology, 34*(3), 383-396. doi: 10.1002/jcp.1030340304

Lynch, G. S., Dunwiddie, T., & Gribkoff, V. (1977). Heterosynaptic depression: a postsynaptic correlate of long-term potentiation. *Nature, 266*(5604), 737-739. doi: 10.1038/266737a0

Markram, H., Lubke, J., Frotscher, M., & Sakmann, B. (1997). Regulation of synaptic efficacy by coincidence of postsynaptic APs and EPSPs. *Science, 275*(5297), 213-215.

Martin, K. A., & Whitteridge, D. (1984). Form, function and intracortical projections of spiny neurones in the striate visual cortex of the cat. *The Journal of physiology, 353*, 463-504.

Mishra, A., Dhingra, K., Schuz, A., Logothetis, N. K., & Canals, S. (2010). Improved neuronal tract tracing with stable biocytin-derived neuroimaging agents. *ACS Chem Neurosci, 1*(2), 129-138. doi: 10.1021/cn900010d

Mizuno, N., & Itoh, H. (2009). Functions and regulatory mechanisms of Gq-signaling pathways. *Neurosignals, 17*(1), 42-54. doi: 10.1159/000186689

Molleman, A. (2003). *Patch Clamping: An Introductory Guide to Patch Clamp Electrophysiology*: Wiley.

Montey, K. L., & Quinlan, E. M. (2011). Recovery from chronic monocular deprivation following reactivation of thalamocortical plasticity by dark exposure. *Nature Communications, 2*, 317. doi: 10.1038/ncomms1312

Moult, P. R., Correa, S. A., Collingridge, G. L., Fitzjohn, S. M., & Bashir, Z. I. (2008). Co-activation of p38 mitogen-activated protein kinase and protein tyrosine phosphatase underlies metabotropic glutamate receptor-dependent long-term depression. *J Physiol, 586*(10), 2499-2510. doi: 10.1113/jphysiol.2008.153122

Mountcastle, V. B. (1997). The columnar organization of the neocortex. *Brain, 120 (Pt 4)*, 701-722.

Muzyczka, N. (1992). Use of Adeno-Associated Virus as a General Transduction Vector for Mammalian Cells. In N. Muzyczka (Ed.), *Viral Expression Vectors* (pp. 97-129). Berlin, Heidelberg: Springer Berlin Heidelberg.

Nagel, G., Brauner, M., Liewald, J. F., Adeishvili, N., Bamberg, E., & Gottschalk, A. (2005). Light activation of channelrhodopsin-2 in excitable cells of Caenorhabditis elegans triggers rapid behavioral responses. *Curr Biol, 15*(24), 2279-2284. doi: 10.1016/j.cub.2005.11.032

Nagel, G., Szellas, T., Huhn, W., Kateriya, S., Adeishvili, N., Berthold, P., . . . Bamberg, E. (2003). Channelrhodopsin-2, a directly light-gated cation-selective membrane channel. *Proc Natl Acad Sci U S A, 100*(24), 13940-13945. doi: 10.1073/pnas.1936192100

Neher, E., & Sakmann, B. (1976). Single-channel currents recorded from membrane of denervated frog muscle fibres. *Nature, 260*(5554), 799-802.

Niell, C. M. (2015). Cell types, circuits, and receptive fields in the mouse visual cortex. *Annu Rev Neurosci, 38*, 413-431. doi: 10.1146/annurev-neuro-071714-033807

Oh, S. W., Harris, J. A., Ng, L., Winslow, B., Cain, N., Mihalas, S., . . . Zeng, H. (2014). A mesoscale connectome of the mouse brain. *Nature, 508*, 207. doi: 10.1038/nature13186 https://www.nature.com/articles/nature13186#supplementary-information

Okuno, D., Asaumi, M., & Muneyuki, E. (1999). Chloride Concentration Dependency of the Electrogenic Activity of Halorhodopsin. *Biochemistry, 38*(17), 5422-5429. doi: 10.1021/bi9826456

Pala, A., & Petersen, Carl C. H. (2015). In Vivo Measurement of Cell-Type-Specific Synaptic Connectivity and Synaptic Transmission in Layer 2/3 Mouse Barrel Cortex. *Neuron, 85*(1), 68-75. doi: https://doi.org/10.1016/j.neuron.2014.11.025

Patterson, R. L., Boehning, D., & Snyder, S. H. (2004). Inositol 1,4,5-trisphosphate receptors as signal integrators. *Annu Rev Biochem, 73*, 437-465. doi: 10.1146/annurev.biochem.73.071403.161303

Petralia, R. S., Wang, Y. X., Hua, F., Yi, Z., Zhou, A., Ge, L., . . . Wenthold, R. J. (2010). Organization of NMDA receptors at extrasynaptic locations. *Neuroscience, 167*(1), 68-87. doi: 10.1016/j.neuroscience.2010.01.022

Polder, H.-R., & Swandulla, D. (2001). The use of control theory for the design of voltage clamp systems: a simple and standardized procedure for evaluating system parameters. *J Neurosci Methods, 109*(2), 97-109. doi: https://doi.org/10.1016/S0165-0270(01)00385-5

Py, C., Martina, M., Diaz-Quijada, G. A., Luk, C. C., Martinez, D., Denhoff, M. W., . . . Mealing, G. A. (2011). From understanding cellular function to novel drug discovery: the role of planar patch-clamp array chip technology. *Front Pharmacol, 2*, 51. doi: 10.3389/fphar.2011.00051

Qi, G., Radnikow, G., & Feldmeyer, D. (2015). Electrophysiological and morphological characterization of neuronal microcircuits in acute brain slices using paired patch-clamp recordings. *Journal of visualized experiments : JoVE*(95), 52358-52358. doi: 10.3791/52358

Quinn, K., & Beech, D. J. (1998). A method for direct patch-clamp recording from smooth muscle cells embedded in functional brain microvessels. *Pflugers Arch, 435*(4), 564-569. doi: 10.1007/s004240050553

Rayer, B., Naynert, M., & Stieve, H. (1990). Phototransduction: different mechanisms in vertebrates and invertebrates. *J Photochem Photobiol B, 7*(2-4), 107-148.

Remington, L. A. (2012). Chapter 1 - Visual System. In L. A. Remington (Ed.), *Clinical Anatomy and Physiology of the Visual System (Third Edition)* (pp. 1-9). Saint Louis: Butterworth-Heinemann.

Richardson, E. S., & Xiao, Y.-F. (2010). Electrophysiology of Single Cardiomyocytes: Patch Clamp and Other Recording Methods. In D. C. Sigg, P. A. Iaizzo, Y.-F. Xiao & B. He (Eds.), *Cardiac Electrophysiology Methods and Models* (pp. 329-348). Boston, MA: Springer US.

Ridge, K. D. (2002). Algal rhodopsins: phototaxis receptors found at last. *Curr Biol, 12*(17), R588-590.

Russo, G., & Taverna, S. (2014). Investigation of synaptic microcircuits using patch-clamp paired recordings in acute brain slices. *Methods Mol Biol, 1183*, 183-193. doi: 10.1007/978-1-4939-1096-0_11

Sawchenko, P. E., & Swanson, L. W. (1981). A method for tracing biochemically defined pathways in the central nervous system using combined fluorescence retrograde transport and immunohistochemical techniques. *Brain Res, 210*(1), 31-51. doi: https://doi.org/10.1016/0006-8993(81)90882-9

Shepherd, G. M., & Svoboda, K. (2005). Laminar and columnar organization of ascending excitatory projections to layer 2/3 pyramidal neurons in rat barrel cortex. *J Neurosci, 25*(24), 5670-5679. doi: 10.1523/jneurosci.1173-05.2005

Song, S., Miller, K. D., & Abbott, L. F. (2000). Competitive Hebbian learning through spike-timing-dependent synaptic plasticity. *Nature neuroscience, 3*, 919. doi: 10.1038/78829

St-Pierre, F., Chavarha, M., & Lin, M. Z. (2015). Designs and sensing mechanisms of genetically encoded fluorescent voltage indicators. *Current Opinion in Chemical Biology, 27*, 31-38. doi: https://doi.org/10.1016/j.cbpa.2015.05.003

Stewart, W. W. (1981). Lucifer dyes—highly fluorescent dyes for biological tracing. *Nature, 292*(5818), 17-21. doi: 10.1038/292017a0

Sun, W., Tan, Z., Mensh, B. D., & Ji, N. (2016). Thalamus provides layer 4 of primary visual cortex with orientation- and direction-tuned inputs. *Nature neuroscience, 19*(2), 308-315. doi: 10.1038/nn.4196

Tasic, B., Menon, V., Nguyen, T. N., Kim, T. K., Jarsky, T., Yao, Z., . . . Zeng, H. (2016). Adult mouse cortical cell taxonomy revealed by single cell transcriptomics. *Nature neuroscience, 19*(2), 335-346. doi: 10.1038/nn.4216

Terakita, A. (2005). The opsins. *Genome biology, 6*(3), 213-213. doi: 10.1186/gb-2005-6-3-213

Turrigiano, G. G. (2008). The self-tuning neuron: synaptic scaling of excitatory synapses. *Cell, 135*(3), 422-435. doi: 10.1016/j.cell.2008.10.008

Usrey, W. M., & Fitzpatrick, D. (1996). Specificity in the axonal connections of layer VI neurons in tree shrew striate cortex: evidence for distinct granular and supragranular systems. *The Journal of Neuroscience, 16*(3), 1203. doi: 10.1523/JNEUROSCI.16-03-01203.1996

VanDongen, A. M. (2008). *Biology of the NMDA Receptor*: CRC Press.

Verkerk, A. O., Veerman, C. C., Zegers, J. G., Mengarelli, I., Bezzina, C. R., & Wilders, R. (2017). Patch-Clamp Recording from Human Induced Pluripotent Stem Cell-Derived Cardiomyocytes: Improving Action Potential Characteristics through Dynamic Clamp. *International journal of molecular sciences, 18*(9), 1873. doi: 10.3390/ijms18091873

Weiler, N., Wood, L., Yu, J., Solla, S. A., & Shepherd, G. M. G. (2008). Top-down laminar organization of the excitatory network in motor cortex. *Nature neuroscience, 11*, 360. doi: 10.1038/nn2049 https://www.nature.com/articles/nn2049#supplementary-information

Wen, H., & Brehm, P. (2010). Paired patch clamp recordings from motor-neuron and target skeletal muscle in zebrafish. *J Vis Exp*(45). doi: 10.3791/2351

Werner, J. S., & Chalupa, L. M. (2014). *The New Visual Neurosciences*: MIT Press.

Wickersham, I. R., Finke, S., Conzelmann, K.-K., & Callaway, E. M. (2006). Retrograde neuronal tracing with a deletion-mutant rabies virus. *Nature Methods, 4*, 47. doi: 10.1038/nmeth999 https://www.nature.com/articles/nmeth999#supplementary-information

Wiesel, T. N., & Hubel, D. H. (1963). SINGLE-CELL RESPONSES IN STRIATE CORTEX OF KITTENS DEPRIVED OF VISION IN ONE EYE. *J Neurophysiol, 26*, 1003-1017. doi: 10.1152/jn.1963.26.6.1003

Yuste, R., & Bonhoeffer, T. (2001). Morphological changes in dendritic spines associated with long-term synaptic plasticity. *Annu Rev Neurosci, 24*, 1071-1089. doi: 10.1146/annurev.neuro.24.1.1071

Zemelman, B. V., Lee, G. A., Ng, M., & Miesenbock, G. (2002). Selective photostimulation of genetically chARGed neurons. *Neuron, 33*(1), 15-22.

Zhang, F., Vierock, J., Yizhar, O., Fenno, L. E., Tsunoda, S., Kianianmomeni, A., . . . Deisseroth, K. (2011). The Microbial Opsin Family of Optogenetic Tools. *Cell, 147*(7), 1446-1457. doi: 10.1016/j.cell.2011.12.004

Zhang, F., Wang, L.-P., Brauner, M., Liewald, J. F., Kay, K., Watzke, N., . . . Deisseroth, K. (2007). Multimodal fast optical interrogation of neural circuitry. *Nature, 446*, 633. doi: 10.1038/nature05744 https://www.nature.com/articles/nature05744#supplementary-information

PART I. AUTOMATED IMAGE-GUIDED PATCH-CLAMP SYSTEM FOR *IN VITRO* APPLICATIONS

This part was adapted from two published articles in Journal of Neurophysiology and Journal of Visualized Experiments. Minor alterations were made to accommodate for unified formatting and better comprehension.

Patch-clamp is an old yet indispensable electrophysiology technique especially in measuring sub-threshold synaptic activities and single channel currents. The inherent low throughput and high dependence on experimenter expertise presented a challenge to the high demand for this gold-standard method. Yet, challenges mean opportunity for innovation. In this chapter, I will discuss an attempt to improve traditional patch-clamp electrophysiology through automated instrumentation. The first article describes the components and organization of the system, the work flow, and comprehensive testing of the efficiency and effectiveness of the system against traditional patch-clamp method. The second article details the installation, calibration, and working protocol, as well as examples of experimental applications.

CHAPTER 1. INTEGRATION OF AUTOPATCHING WITH AUTOMATED PIPETTE AND CELL DETECTION IN VITRO

Reproduced from:
Wu Q, Kolb I, Callahan BM, Su Z, Stoy W, Kodandaramaiah SB, Neve R, Zeng H, Boyden ES, Forest CR, Chubykin AA. Integration of autopatching with automated pipette and cell detection in vitro. J Neurophysiol 116: 1564 –1578, 2016.

Abstract

Patch clamp is the main technique for measuring electrical properties of individual cells. Since its discovery in 1976 by Neher and Sakmann, patch clamp has been instrumental in broadening our understanding of the fundamental properties of ion channels and synapses in neurons. The conventional patch-clamp method requires manual, precise positioning of a glass micropipette against the cell membrane of a visually identified target neuron. Subsequently, a tight "gigaseal" connection between the pipette and the cell membrane is established, and suction is applied to establish the whole cell patch configuration to perform electrophysiological recordings. This procedure is repeated manually for each individual cell, making it labor intensive and time consuming. In this article we describe the development of a new automatic patch-clamp system for brain slices, which integrates all steps of the patch-clamp process: image acquisition through a microscope, computer vision-based identification of a patch pipette and fluorescently labeled neurons, micromanipulator control, and automated patching. We validated our system in brain slices from wild-type and transgenic mice expressing Channelrhodopsin 2 under the Thy1 promoter (line 18) or injected with a herpes simplex virus-expressing archaerhodopsin, ArchT. Our computer vision-based algorithm makes the fluorescent cell detection and targeting user independent. Compared with manual patching, our system is superior in both success rate and average trial duration. It provides more reliable trial-to-trial control of the patching process and improves reproducibility of experiments.

Key Words

patch-clamp; computer vision; fluorescent cell detection; in vitro slice electrophysiology

New and Noteworthy

This work presents a new automated, image-guided patch-clamp system for brain slices. We have developed novel computer vision-based algorithms of user-independent identification of patch pipettes and fluorescently labeled neurons. Our system integrates all steps of the patch-clamp.

Introduction

Patch-clamp recording is a gold-standard technique for accurate measurement of membrane voltage fluctuations, synaptic currents, and ionic channel activity in neurons(Neher & Sakmann, 1976). It has allowed neuroscientists to study properties of individual ion channels (Hoshi, Zagotta, & Aldrich, 1990) and synapses (Edwards, Konnerth, & Sakmann, 1990) and to characterize synaptic plasticity (Jaffe & Johnston, 1990; Zalutsky & Nicoll, 1990) and dendritic integration (Larkum, Zhu, & Sakmann, 1999). Patch-clamp recording also has been essential for dissecting the pathophysiology of neurological disorders caused by mutations in channels and synaptic proteins (Ackerman & Clapham, 1997). In combination with morphological characterization, this method has been used for classifying cell types in the brain (Kawaguchi & Kubota, 1993) and elucidating connectivity among nearby neurons (Markram, Lubke, Frotscher, Roth, & Sakmann, 1997). It also has been successfully coupled with optogenetics (Boyden, Zhang, Bamberg, Nagel, & Deisseroth, 2005) and applied to map long-range neuronal circuits (Petreanu, Huber, Sobczyk, & Svoboda, 2007).

There is a growing demand for large data sets of patch-clamp recordings and morphological reconstructions. For ex-ample, large-scale cell-type classification of neurons based on electrophysiology and morphology as well as the study of their synaptic connections are some of the highest-priority goals in modern neuroscience (Alivisatos, 2012, 2013; Insel, Landis, & Collins, 2013; Jiang et al., 2015; Kandel, Markram, Matthews, Yuste, & Koch, 2013). However, patch-clamp recording of a large number of neurons has limitations: it is a challenging, laborious technique, akin to an art form, requiring a skilled and highly trained investigator. It is also low through-put: even the most skilled and experienced patch-clamp investigators can only record from a few neurons per day.

A typical patch-clamp experiment is highly repetitive, making it strenuous and error prone for the investigator. For example, when the micropipette is being advanced toward the target cell,

errors such as advancing the pipette too far into the tissue, breaking the pipette tip, and improperly setting the pipette pressure are common among novices and occasional among experienced researchers. Furthermore, these errors usually accumulate toward the end of the day when researchers get fatigued. Some steps of the patch-clamp process are difficult to control manually. For example, the delicate pneumatic pressure changes applied to the pipette are necessary to form a whole cell configuration. This pressure control is typically performed by mouth or with a syringe (Boulton, Baker, & Walz, 1995; Walz, 2007), making it difficult to replicate among laboratories, among different investigators in the same laboratory, and even by the same researcher. Consequently, wide variability in manual patch-clamp methodology creates challenges when large data sets collected by various laboratories for a single study must be directly comparable (Tripathy, Burton, Geramita, Gerkin, & Urban, 2015). Furthermore, when multiple cells must be patched simultaneously or when patch clamping must be integrated with other techniques such as optogenetics, the compounded complexity of the procedure could prohibit new investigators from initiating such projects. Thus, there is a need to automate the patch-clamp process and minimize human involvement in its technical aspects.

Some of the currently available open-source and commercial software packages attempt to make some parts of the process more convenient (Campagnola, Kratz, & Manis, 2014; Edelstein, Amodaj, Hoover, Vale, & Stuurman, 2010; Long, Li, Knoblich, Zeng, & Peng, 2015; Perin & Markram, 2013; Suter et al., 2010). However, there is no comprehensive free and open-source solution that automates the patch-clamp procedure in vitro. We previously developed and tested the "Autopatcher," a robot for automated "blind" patch-clamp recording in vivo (Kodandaramaiah, Franzesi, Chow, Boyden, & Forest, 2012). The Autopatcher was designed to use only electrical resistance, not visual information, as an indicator of cell proximity. However, in brain slice preparations, targeting cells on the basis of visual cues such as the shape or fluorescence of a cell is often required (Komai, Denk, Osten, Brecht, & Margrie, 2006; Lefort, Tomm, Floyd Sarria, & Petersen, 2009). Currently, no automation software exists to assist in the performance of such visually guided patch-clamp experiments in tissue.

We have developed the Autopatcher IG ("Image Guided"), a system that enables a conventional electrophysiology rig to automatically perform patch-clamp electrophysiology in vitro. The system reduces the need for manual intervention by automating highly skilled but repetitive tasks in the patch-clamp process (**Fig. 1*A***). This is accomplished by automation of

pipette calibration (**Fig. 1*B***), fluorescent cell detection (**Fig. 1*C***), manipulator trajectory planning and execution, pneumatic pressure control, electrophysiological measurements, and data logging (**Fig. 1**). We have validated the performance of the Autopatcher IG by performing patch-clamp recordings of over 200 cells in mouse brain slices from wild-type, transgenic, and virally injected mice. The Autopatcher IG demonstrated robust performance, reproducibility, and twofold improvement in speed and likelihood of obtaining a successful recording com-pared with manual patching.

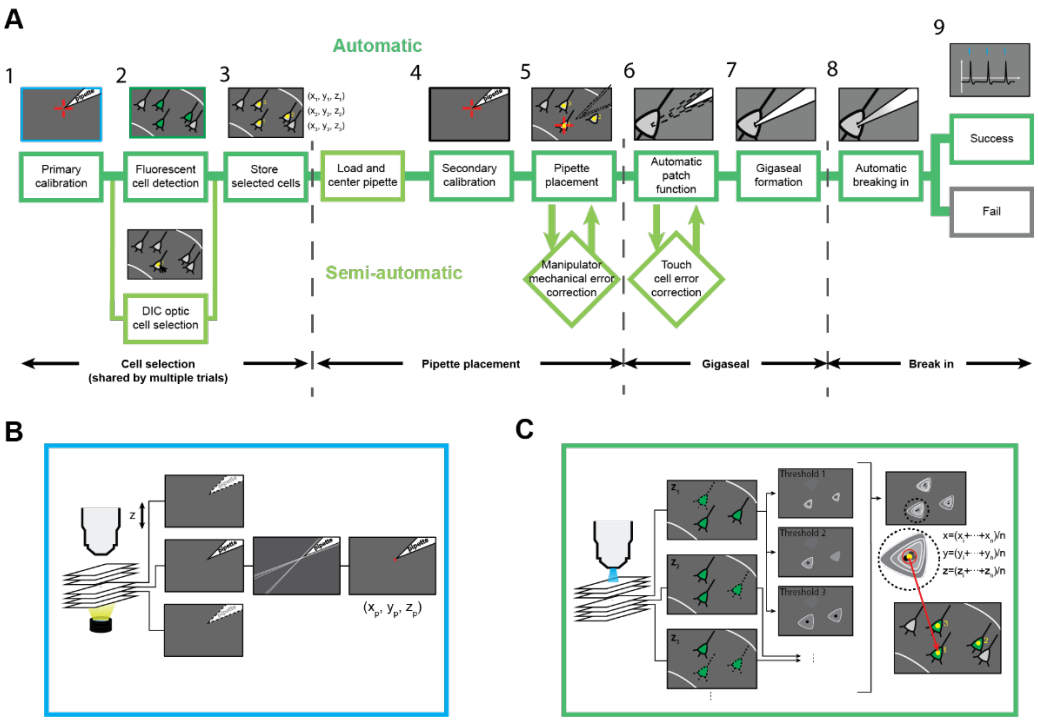

Figure 4. Automated image-guided in vitro patch-clamp workflow.

A) Steps in an automated in vitro patch-clamp experiment. 1, Primary calibration is done automatically through computer vision (also see B). 2, Target cell selection is then done using either mouse clicks (bottom) or automatic fluorescent cell detection (top; algorithm explained in detail in C). 3, Selected cell coordinates are stored for further patching (subscripts indicate the cell identification no.). 4, This is followed by a pipette calibration step that determines the coordinates of the patch pipette with micrometer-scale accuracy and resolution (indicated by red crosshairs). 5, With the coordinates of the pipette tip and target neuron determined, a pipette guidance algorithm determines the trajectory to be taken by the pipette and automatically guides the pipette to the targeted cells. 6 – 8, The patch algorithm (also see Fig. 6 for detailed algorithm flowchart) is then initiated, which uses pipette impedance measurements to detect contact with the neuron (6), form a gigaseal (7), and break in (8). 9, After successful break-in, a whole cell recording is performed. A fully automatic patching process is defined as the successful automatic execution of all steps from loading a new pipette to obtaining a whole cell patch (marked by dark green lines). If adjustments are to be made at any point to this automatic process, it is defined as a semiautomatic patching trial (marked by light green lines). Such adjustments are mainly manipulator mechanical error correction, caused by mechanical errors in manipulator positioning, and touch cell error correction, caused by incorrect cell contact detection. Dark green borders indicate fully automatic procedure; light green borders indicate a semiautomatic trial, involving at least some human interference. DIC, differential interference contrast. **B)** Computer vision algorithm is used to determine the coordinates of the pipette tip during automatic calibration. A series of images along the optical z-axis are acquired under bright-field illumination to determine if the pipette tip is in focus using local contrast detection. Gaussian blur, Canny edge detection, and Hough transform are then applied to identify the pipette tip (indicated by red dot), and the tip coordinates are identified (xp, yp, zp; also see Fig. 4A). **C)** computer vision algorithm used to detect and log coordinates of fluorescent cells. A series of images are acquired under epifluorescence illumination along the optical z-axis of the microscope (left), with the step size and the depth defined by an experimenter. Each acquired image at depth zn is analyzed using a series of thresholds to detect cell contours. The centroids of the identified cell contours for each threshold are superimposed and clustered along the x and y dimensions. Final cell coordinates are computed as the average of the corresponding x, y, z cluster coordinates.

Materials and Methods

Animals

All animal procedures were approved by the Committee on Animal Care at the Allen Institute for Brain Science, the Massachusetts Institute of Technology, and the Purdue Animal Care and Use Committee. Both male and female animals were used in acute brain slice preparation. C57BL/6 (wild type) mice were used in all experiments except for testing fluorescent cell detection and patching algorithm. A stable mouse line expressing Channelrhodopsin 2 (ChR2) fused with enhanced yellow fluorescent protein (EYFP) under Thy1 promotor, B6.Cg-Tg(Thy1-COP4/EYFP)18Gfng/J (Thy1-ChR2-EYFP line 18), was purchased from Jackson Laboratory (Arenkiel et al., 2007).

Acute mouse cortical slice preparation

Visual cortical slices from young (postnatal day 21 – 50; P21 – P50) mice were prepared as de-scribed previously (Philpot, Sekhar, Shouval, & Bear, 2001). Mice were anesthetized with isoflurane and decapitated after confirmation of deep anesthesia using tests of corneal reflex and toe pinch. The brain was removed and sliced with the use of a vibrating-blade microtome (Leica Microsystems, Buffalo Grove, IL) in an ice-cold, oxygenated, high-sucrose dissection buffer containing (in mM) 75 sucrose, 10 glucose, 87 NaCl, 2.5 KCl, 1.25 NaH_2PO_4, 25 $NaHCO_3$, 0.5 $CaCl_2$, 7 $MgCl_2$, and 1.3 ascorbic acid. Coronal slices (350 μm) containing primary visual cortex were incubated at 32°C for 15 min in a holding chamber with oxygenated artificial cerebrospinal fluid (ACSF) containing (in mM) 124 NaCl, 3.5 KCl, 1 $CaCl_2$, 0.8 $MgCl_2$, 1.23 NaH_2PO_4, 26 $NaHCO_3$, and 10 glucose, and were subsequently incubated at 30°C for the remainder of the day.

Acute brain slices were prepared from adult (P50 – P180) mice using the protective recovery method described in detail elsewhere (Ting, Daigle, Chen, & Feng, 2014). Briefly, animals were heavily anesthetized with isoflurane and perfused transcardially with *N*-methyl-D-glucamine (NMDG) solution containing (in mM) 93 NMDG, 2.5 KCl, 1.2 NaH_2PO_4, 30 $NaHCO_3$, 20 HEPES, 25 glucose, 5 Na-ascorbate, 3 Na-pyruvate, 10 $MgSO_4 \cdot 7H_2O$, and 0.5 $CaCl_2 \cdot 2H_2O$ (pH titrated to 7.3 – 7.4, osmolarity 300 – 310 mOsm). Mice were quickly decapitated, and the brain was extracted, embedded in 2% agarose, and cut into 300 μm coronal slices in the cutting solution using a VF200 compresstome (Precisionary Instruments). The slices were incubated at

34°C in the cutting solution for 10 –12 min. They were then transferred to a recovery solution containing (in mM) 92 NaCl, 2.5 KCl, 1.2 NaH_2PO_4, 30 $NaHCO_3$, 20 HEPES, 25 glucose, 5 Na-ascorbate, 2 thiourea, 3 Na-pyruvate, 2 $MgSO_4 \cdot 7H_2O$, and 2 $CaCl_2 \cdot 2H_2O$ (pH 7.3–7.4, osmolarity 300 –310 mOsm) for at least 60 min before recording began. Recordings were performed at room temperature (25°C) in an open bath chamber (RC-29; Warner Instruments) with standard recording solution containing (in mM) 124 NaCl, 2.5 KCl, 1.2 NaH_2PO_4, 24 $NaHCO_3$, 5 HEPES, 12.5 glucose, 2 $MgSO_4 \cdot 7H_2O$, and 2 $CaCl_2 \cdot 2H_2O$. The liquid junction potential was not corrected.

Electrophysiology recordings

In both preparations, patch-clamp electrodes were pulled from filamented borosilicate glass tubes (BF150-86-10; Sutter Instruments) with the use of a P-97 micropipette puller (Sutter Instruments) to a resistance of 3.5–7.9 MOhm. Internal solution contained (in mM) 20 KCl, 100 K-gluconate, 10 HEPES, 4 MgATP, 0.3 Na_2GTP, 7 phosphocreatine, and 0.2% biocytin (pH adjusted to 7.4, osmolarity adjusted to 300 mOsm). In some experiments, 4% (wt/vol) Alexa Fluor 594 (A-10438; Life Technologies) or Lucifer yellow (L-453; Life Technologies) was added to the intracellular solution to visualize patch-clamped cells under fluorescent optics. Cell characteristics were obtained 5 min after a successful break-in using Clampex. The algorithm is considered to yield a successful whole cell recording if access resistance is less than 80 MOhm and holding current at 70 mV is larger than 200 pA.

All data are reported as means standard error (SE). A two-tailed Student's *t*-test was used to compare between groups, and $P < 0.05$ is considered significant.

Cell labeling with fluorescent dye

A glass pipette (with filament) was back-filled with 5 mM Alexa Fluor 568 in 5 mM KCl by contacting the back of the glass pipette (opposite side of the tip) with the dye solution such that a small volume of the dye solution filled the tip of the pipette by capillary force. The pipette was then back-filled with internal solution. The patch-clamp experiment was performed as described, and the cell was held for at least 30 min after whole cell configuration was formed to allow the dye to diffuse into the projections.

Immunohistochemistry and imaging

Acute brain slices were fixed in 4% paraformaldehyde solution for 30 min at room temperature, washed with PBS three times over 1 h, and subjected to antibody labeling or directly mounted for imaging. We used chicken anti-green fluorescent protein (anti-GFP; ab13970; Abcam) diluted 1:1,000 in PBS with 5% bovine serum albumin and 0.1% Triton X-100 overnight at 4°C to label Channelrhodopsin-EYFP. Slices were washed in PBS three times over 1 h and incubated with goat anti-chicken Alexa 488 (A-11039: Thermal Fisher) overnight at 4°C in the same buffer used for primary antibody labeling. Slices were then washed and mounted for imaging with confocal scanning microscopy (Zeiss LSM710).

Viral injection surgery

ArchT-EYFP was cloned into the herpes simplex virus (HSV) amplicon vector p1006, under the control of the murine cytomegalovirus (mCMV) promoter. It was packaged using the standard amplicon packaging protocol. The titer was $3x10^8$ infectious units (i.u.)/ml. C57BL/6 (wild type) mice ages P16 –P25 were used to inject HSV-ArchT-EYFP in the primary visual cortex. Animals were initially anesthetized with 5% isoflurane and 1.5% during the surgery. The surgical site was shaved and disinfected with 75% ethanol. The skin above the visual cortex was surgically removed, and connective tissue was removed with 3% hydrogen peroxide. Four craniotomies (2 per hemisphere) at the primary visual cortex (coordinates determined by mouse brain atlas) were carefully drilled by a robotic rodent stereotactic surgery system (Neurostar). Virus (500nl) was injected to each site at a 0.6-mm depth over a period spanning 10 min. The surgical site was sealed locally with Kwik-Cast sealant (WPI), and then the skull was sealed with dental cement (Ortho-Jet; Lang Dental). Animals recovered for 2–3 days before preparation of acute cortical slices reparation to allow optimum protein expression. The same procedure was then performed to prepare acute brain slices as described above.

Pressure control unit parts

Parts used to construct the pressure control unit are as follows: a secondary data acquisition board (USB-1208FS; Measurement Computing, Norton, MA), solenoid valves

(LHDA0531115H; The Lee Company), an air pump (VMP1625MX-12-90-CH mini-pump; Virtual Industries), and an air pressure sensor (MPXV7025G; Freescale Semiconductor).

Results

Hardware

The Autopatcher IG utilizes off-the-shelf patch-clamp in vitro electrophysiology hardware. The setup is based on an upright microscope outfitted with differential interference contrast (DIC) optics. Brain slices are visualized using low-magnification (4x/10x) and high-magnification (40x/60x) water-immersion objectives that can be exchanged manually using a swinging nosepiece or automatically using a motorized carriage. Image guidance is accomplished by interfacing with a charge-coupled device (CCD) camera (QImaging). The Autopatcher IG relies on motorized three-axis control of the microscope stage and the patch-clamp pipette micromanipulator (Scientifica SliceScope Pro 1,000; Scientifica). A pipette holder is connected to the headstage of a patch-clamp amplifier (Multiclamp 700B). The headstage is mounted on the pipette manipulator (**Fig. 2*A***). A data acquisition system (Digi-data 1550A; Molecular Devices) relays the electrical signal from the amplifier to the computer for processing and storage (**Fig. 2**). Autopatcher IG also can be implemented to hardware systems different from that described above with driver programming.

The only additional hardware component that is necessary for the Autopatcher IG is a custom-built pipette pneumatic pressure control unit (**Fig. 2, *B*** and ***C***). Pneumatic pressure in the pipette is sensed and algorithmically controlled by interfacing with a secondary data acquisition board (USB-1208FS; Measurement Computing) that controls a series of valves, an air pump, and an air pressure sensor. Alternatively, we also have adopted the Autopatcher IG to utilize a commercially available patch-clamp pressure control system (Autopatcher pressure control box; Neuromatic Devices, Atlanta, GA).

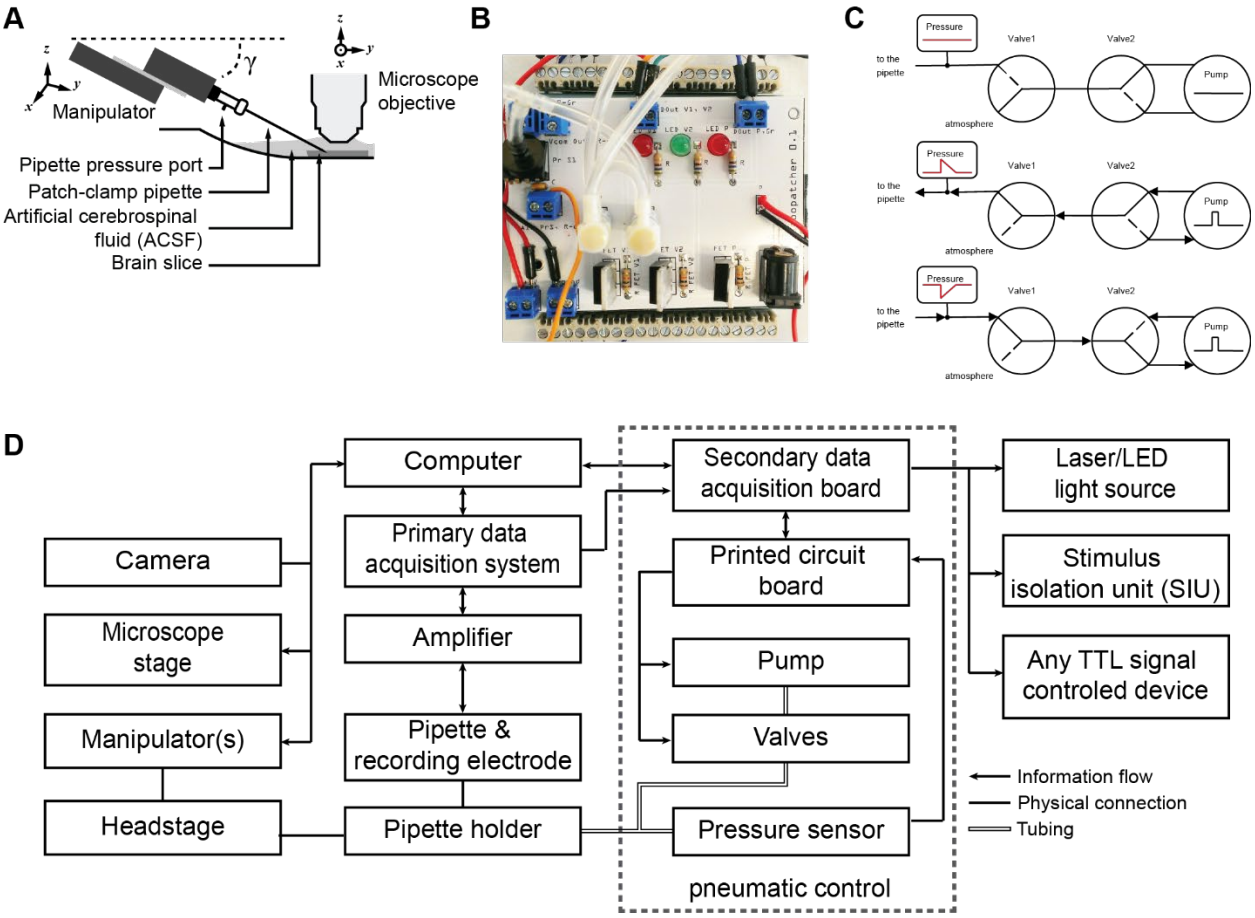

Figure 5. Experimental setup.

A) Standard patch-clamp electrophysiology equipment is used in conjunction with a pneumatic pressure control unit (also see Fig.3) and our custom-written software. **B)** Image of the pipette pneumatic pressure control unit prototype. Two solenoid valves (white circles, center) and an air pressure sensor (black square, top left) are connected to control the pipette internal pressure. The air pump is not shown. **C)** 3 different valve configurations resulting in no pressure (top) or brief pulses of positive (middle) or negative pressure (bottom) applied to the back end of the pipette when the pump is activated by a transistor-transistor logic (TTL) signal. The pressure sensor provides feedback information to control the minimum and maximum pressure during patching. **D)** Block diagram of the hardware setup. A central computer controls all components of the Autopatcher IG. The primary data acquisition system provides an interface to the patch-clamp amplifier and allows the user to perform a standard electrophysiology experiment. The secondary data acquisition board provides an interface to the pressure control unit and to the external electronics hardware, which can communicate via TTL signals. On the sensor side are signals from the patch pipette, microscope camera, and internal pipette pressure sensor. The custom graphical user interface (GUI; see Fig. 3) allows the user to control the manipulator, camera setting, microscope stage, pressure control unit, and patch-clamp amplifier [via software development kits (SDK) for digital amplifiers (Axon MultiClamp 700B)].

Software architecture and graphical user interface

Autopatcher IG is organized modularly with the capability of easy functional expansion. Different modules communicate with each other through the main module and can run independently. The software is written in Python, a free and open-source programming language, using free and open-source libraries, such as the graphical user interface (GUI) PyQt (Riverbank Computing), which provides a Python interface to a popular open-source cross-platform GUI library, Qt (https:// www.qt.io/), and OpenCV, an open-source computer vision library (Bradski 2000) (**Fig. 3**). Autopatcher IG software, user manual, tutorials, and an alternative implementation in LabVIEW are available online (www.autopatcher.org or https://github.com/chubykin/AutoPatcher_IG).

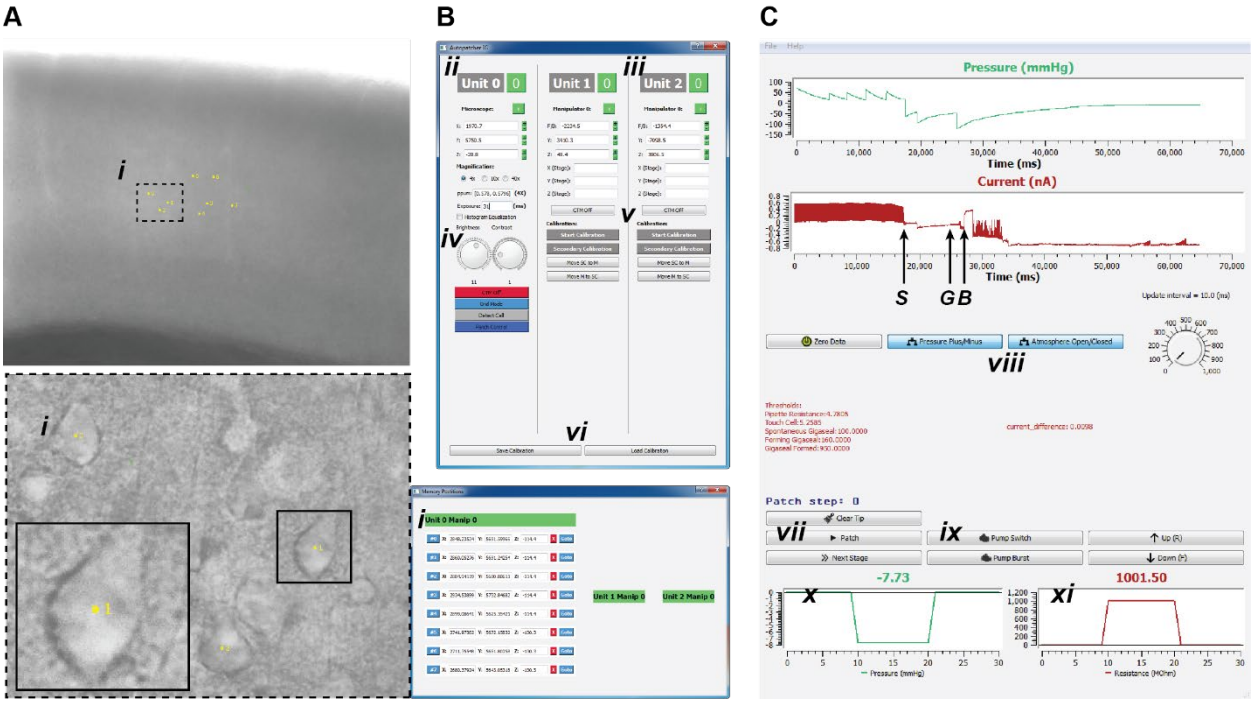

Figure 6. GUIs of the Python-based software featuring image acquisition, manipulator, and patch control.

A) Camera view of a brain slice with target cells (i) selected at a low magnification of 4 (top) and at a high magnification of 40 (bottom left). Yellow labels indicate the cell no.; coordinates of the cells are stored as the corresponding sequence of memory positions and indicated in the GUI (bottom right) **B)** Main GUI providing settings for image acquisition, microscope stage, and micromanipulator control. ii, Microscope stage: controls include settings for stage coordinates, magnification, pixel-mm calibration; iii, micromanipulators: user can initiate automatic calibration and control individual micromanipulators; additional micromanipulator units are automatically recognized and added; iv, controls for camera exposure (in ms), image brightness, and contrast; v, automatic pipette calibration; vi, calibration save and load. **C)** Patch control GUI during an ongoing patching experiment. Top trace indicates pressure (in mmHg); bottom trace indicates current measurements from the patch amplifier (letters denote key events in the patch-clamping process: S denotes the touch cell surface event, G denotes the time point at which a gigaseal is obtained, and B denotes when break-in is achieved). vii, Automatic patch algorithm; viii, independent valve configuration control: allows user to override the patch algorithm and manually apply user-required positive or suction pressure; ix, independent pump control: allows user to override the patch algorithm and control the pump; x, real-time pressure; xi, real-time resistance.

Computer vision-aided pipette tip calibration

A preliminary step to using the Autopatcher IG is manipulator primary calibration, which allows the software to manipulate the stage and pipette from the same reference coordinate system. It is performed once during initial setup and at any time the hardware configuration is changed. In the calibration process, the manipulator will move predefined distances along the *x*-, *y*-, and *z*-axes, and the position of the pipette tip will be identified using a computer vision algorithm after each movement as described in **Fig. 4**. A secondary calibration realigns the two coordinate systems by detecting the pipette tip and then applying transformation coefficients that were obtained from the primary calibration. Secondary calibration is performed every time a new pipette is installed.

In the automatic patching experiments we performed, each image after manipulator movement along the specific axis was subjected to Gaussian blur to decrease noise, the result of which was then used to extract pipette contour through Canny edge detection. Hough transform was subsequently applied to derive perfect lines fitting the pipette contour, which were then color inverted. The brightest point indicated where most of the pipette outlines intersected. The coordinates of this intersection point were assigned as the tip of the pipette (as shown in **Fig. 4*A***). Such image processing was carried out twice on each image; the first iteration narrowed the detection range to a small cropped image near the tentative pipette tip, and the second iteration determined the final pipette tip coordinate. The reason for dual processing was to take into account changes in the angle of the pipette wall at different distances from the tip caused by the varying shapes of the pipettes prepared with the use of different pulling programs. For calibration along the *z*-axis, a focus detection algorithm was applied to derive the third pipette tip coordinate. The primary calibration process was performed only when the angles of the manipulator setup were changed. The secondary calibration process was performed each time a new pipette was installed and positioned within the visual field.

Automatic pipette tip calibration together with manual new pipette installation and positioning within the visual field took on average about 68 ± 6 s (mean ± SE; $n = 10$ trials), the average positioning error was 1.6 ± 0.215 μm when the pipette traveling distance was within a 200 μm radius after calibration (**Fig. 4*B***). In addition, all of the automatic patching experiments described used the same primary calibration coefficients, which were saved and reloaded each day. There was no observable deterioration in performance, given that our hard-ware setup was

stable (the angle and magnitude of manipulator movement relative to the microscope view did not change).

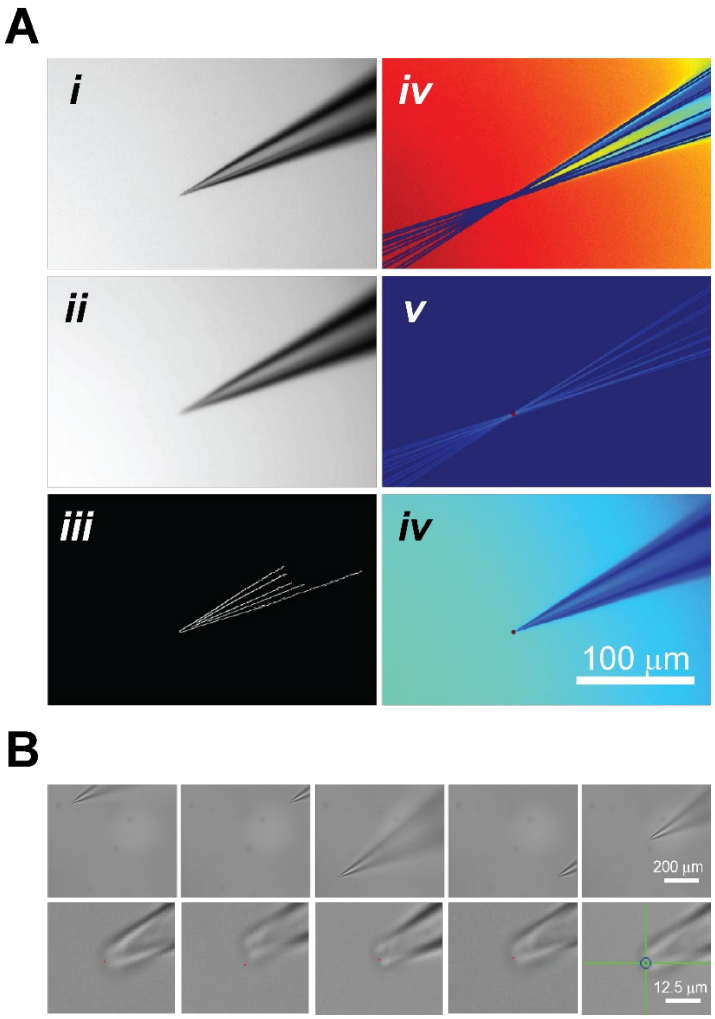

Figure 7. Computer vision-aided identification of the pipette tip coordinates.

A) Image acquisition and pipette tip detection. i, Original pipette image acquired by the microscope; ii, image after application of Gaussian blur; iii, Canny edge detection algorithm applied to the image in ii defines the contours of the pipette tip; iv, Hough transform performs feature extraction to fit the pipette contours with lines; v, color inversion and intensity calculation are used to detect the lines' point of intersection; vi, pipette tip detected by the algorithm as indicated by red dot. **B)** Automatic pipette calibration achieves high precision. To test the precision of automatic pipette calibration, a predefined calibration grid was used and the pipette tip was then targeted to the centroids of four quadrants and the screen center. Top row shows the relative location of the pipette on the screen at 4x magnification; bottom row shows the precision of the pipette placement at 40x magnification. Red dots are 1 pixel in size and are the target locations.

After the manipulator/pipette calibration was performed, the trajectory of the pipette could be controlled by using memory positions stored as target coordinates or by using a keyboard or a mouse to direct positioning. The automatic patching experiments described in this article used memorized target cell coordinates to direct both microscope and pipette to the target cell. After calibration, the pipette did not need to be located within the microscope view for targeting and positioning.

Automatic patching algorithm

Gigaseal formation and break-in are automated by Autopatcher IG through the "Patch Control" module. After a cell is selected and a patch trial initiated, the pipette moves to the target coordinates offset by a user-defined "final approach" distance (10 μm, but can be changed by the user). The user can choose to approach the cell either along the shortest trajectory or vertically along the *z*-axis; all results shown were acquired using a vertical approach. Upon reaching the final approach distance, the manipulator starts descending in predefined step size (1 μm, but can be changed by the user) while the system is monitoring the resistance change calculated from membrane test current injection. Nine distinct stages are defined in the patching process, and the transitions between these stages are determined by a series of pipette resistance and pressure threshold configurations that can be changed and updated at any time point (**Fig. 5**, **Table 1**). A small positive pressure (35– 60 mmHg by default) in the glass pipette is maintained through a pump-pressure sensor feedback loop. When the resistance has increased over the threshold (15% increase from initial pipette resistance by default), manipulator descent is stopped and the valve configuration is switched to apply negative pressure to the pipette to facilitate formation of a gigaseal. The Patch Control applies negative pressure pulses (starting at 60 mmHg and peaking at 100 mmHg by default) through the pressure control loop. When the next resistance threshold (90 MOhm) is reached, the holding voltage potential is decreased to 70 mV to match the cell resting membrane potential. The algorithm then stops applying negative pressure and waits for gigaseal formation, as defined by pipette resistance being 1 GOhm (**Figs. 5** and **6*A***). After the gigaseal is formed, the program will halt and give an experimenter an option to apply "zap" as an alternative method to break in. By default, it will apply pulses of negative pressure to break in and establish a whole cell configuration (**Fig. 6*B***). If the cell membrane resistance falls to 300

MOhm (default) and the holding current is within the range 200 to 100 pA (same as our definition for a successful patch), the break-in is considered to be successful and the whole cell configuration is established. Otherwise, if the success criteria or any intermediate thresholds are not met, the program will stay in the current stage and keep executing the respective action until the time limit (4 min by default) is exceeded. Successful patches were validated by measuring resting potential (less than 55 mV) and step current injection-induced action potentials (**Fig. 6*C***). All pressure and resistance parameters are recorded and saved as patch logs to be used in post hoc analysis for experiment quality control and configuration optimization (**Fig. 6*A***). The Autopatcher IG system is scalable and allows automated patching and recording from two or more cells simultaneously (**Fig. 6, *D*–*G***).

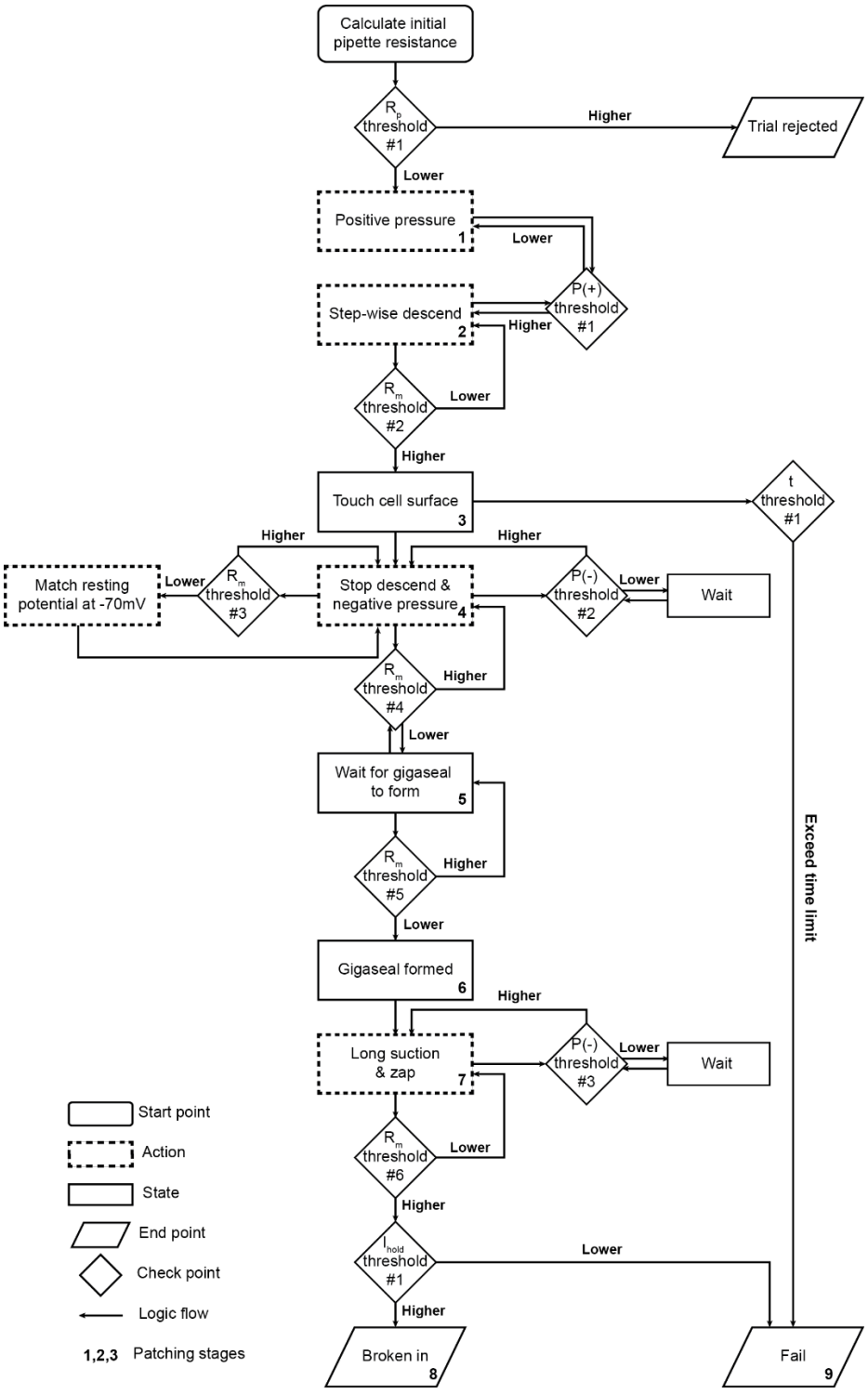

Figure 8. Automatic patch function algorithm logic.

Nine distinct stages are defined by a series of resistance (Rp, pipette resistance; Rm, membrane resistance; Ra, access resistance), positive and negative pressure [P(+/-)], and time (t) thresholds. Thresholds used in actual experiments are shown in Table 1.

Table 1 Default threshold values in the gigasealing algorithm

Parameter	*Value*	*Factor Contributing to Variation*
R_p threshold 1: initial pipette resistance	10 MOhm	Pipette tip diameter, clogging
P(+) threshold 1: minimum positive pressure	30 mmHg	Extracellular matrix composition, target cell depth (higher pressure may be necessary for deeper cells)
R_m threshold 2: touch cell resistance coefficient	115% of initial R_p	Cell size/type
P(-) threshold 1: negative pressure for sealing	Less than 60 mmHg	Cell size/type
R_m threshold 3: for 70-mV adjustment	100 MOhm	Based on experience; may be optimized by data mining
R_m threshold 4: wait for gigasealing resistance	200 MOhm	Based on experience; may be optimized by data mining
R_m threshold 5: gigaseal resistance	1,000 MOhm	Patch quality requirement; a higher value will result in the tighter seal
P(-) threshold 2: minimum negative pressure for break-in	Less than 85 mmHg	Cell size/type, zapping
R_m threshold 6: broken-in resistance	300 MOhm	Cell size/type
I_{hold} threshold 1: broken-in holding current	Greater than 200 pA and 100 pA	Seal quality
t threshold 1: time to fail	4 min	Based on experience

Listed values are those used in the experiments described in this article. All listed thresholds are related to the representative patch in Fig. 4, and all can be changed by the user and saved in the Autopatcher IG configuration file.

Figure 9. Automatic image-guided patch clamp yields high-quality whole cell recordings comparable with manual patching.

A) Example patch log of a successful patching trial with a history of current (I), resistance (R), and internal pipette pressure (P) parameters. Top, raw voltage input from the data acquisition board (light green) and the membrane test current (dark green). Middle, membrane resistance. Bottom, internal pipette pressure (letters denote key events in the patch-clamping process: S denotes the touch cell surface event, G denotes the time point at which a gigaseal is obtained, and B denotes when break-in is achieved). The "saw tooth" pressure pattern is caused by the on-off feedback pressure controller switching between pump-on and pump-off states. **B)** Representative images show an automatically patched cell at 4 magnification (left) and 40 magnification DIC optics (middle) in a mouse visual cortex brain slice. Right, the same neuron filled with Lucifer yellow, post-fixed, and visualized with 40 magnification epifluorescence optics. **C)** Electrophysiological responses of an automatically patch-clamped neuron to hyperpolarizing and depolarizing current injections. **D)** Representative image of 2 simultaneously patched cells in a slice. **E)** Confocal image of the 2 cells in D filled with Alexa 568 hydrazide and fixed after patching. **F)** Electrophysiological responses of these 2 patched cells to hyperpolarizing and depolarizing current injections. Top, cell on the left (L); bottom, cell on the right (R). **G)** Simultaneous recordings of excitatory postsynaptic potentials (EPSPs) from these neurons evoked by white matter stimulation. **H)** Automatic patching (top; n = 30 from 3 mice) generates high-quality patches that are comparable to those obtained using conventional manual patching (bottom; n = 30 from 6 mice). There was no significant difference between the 2 groups in the distribution of membrane capacitance ($P = 0.06$), holding potential ($P = 0.70$), access resistance ($P = 0.70$), membrane resistance ($P = 0.97$), and seal resistance ($P = 0.33$, 2-tailed Student's t-test).

Figure 6

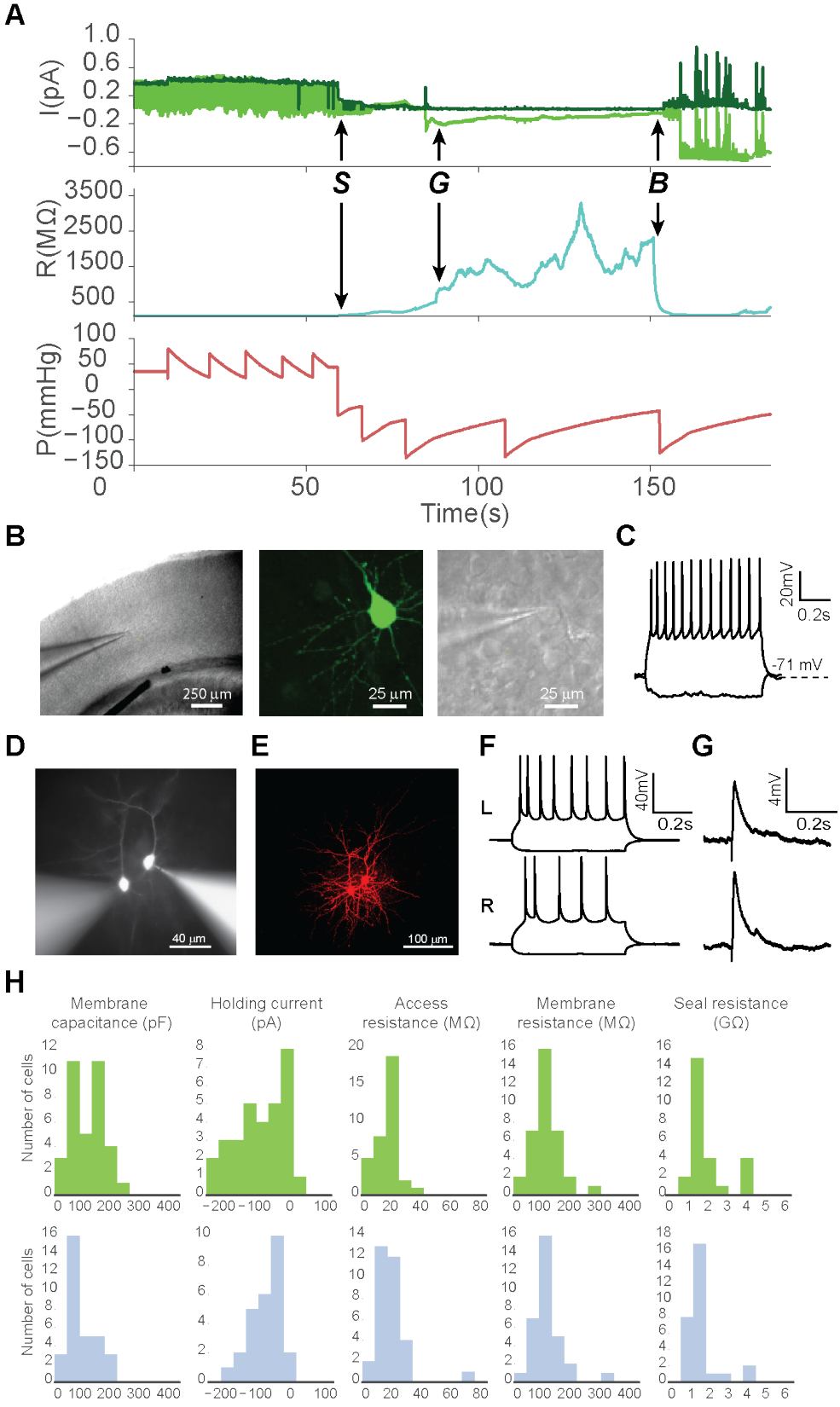
A
I(pA)
1.0
0.6
0.2
−0.2
−0.6
S
G
B
R(MΩ)
3500
2500
1500
500
P(mmHg)
100
50
0
−50
−100
−150
0
50
100
150
Time(s)
B
250 μm
25 μm
25 μm
C
20mV
0.2s
-71 mV
D
40 μm
E
100 μm
F
L
R
40mV
0.2s
G
4mV
0.2s
H
Membrane capacitance (pF)
Holding current (pA)
Access resistance (MΩ)
Membrane resistance (MΩ)
Seal resistance (GΩ)
Number of cells
Number of cells

We conducted automatic and manual patch-clamp experiments to evaluate the efficiency and effectiveness of Autopatcher IG. We defined a trial as fully automatic if the system successfully completed a full whole cell patch-clamp trial from the beginning to the end without any interruption or user interference. We defined a semiautomatic trial as a trial that required any user interruption (**Fig. 1*A***). Most of the interruptions were caused by either manipulator inaccuracies in pipette positioning or failures of the algorithm to establish a gigaseal. A total of 30 successful whole cell configurations were achieved in 44 automatic/semiautomatic patching trials, with a total success rate of 68.2%, whereas the success rate of manual patching was only 35.3% (30 of 85 trials). Among all 44 trials performed using Autopatcher IG, 23 trials (52.3%) were fully automatic, 19 of which were successful, which accounts for 82.6% in the fully automatic subcategory or 43.2% in total. The other 21 trials of the total 44 (47.7%) were semiautomatic, and 11 trials were successful, which accounts for 52.4% in the semiautomatic subcategory and 25.0% in total (**Fig. 7, *B*** and ***D***). There was no significant difference (Student's *t*-test) in the quality of patches obtained using the two methods, based on the seal resistance ($P = 0.33$), the membrane capacitance ($P = 0.06$) and resistance ($P = 0.97$), the access resistance ($P = 0.70$), and the holding current ($P = 0.70$) (**Fig. 7*H***). Both fully automatic and semiautomatic patching yielded a higher success rate compared with manual patching.

The average times for positioning a pipette tip next to a target cell, forming a gigaseal, and breaking in were significantly shorter when performed using automatic patching compared with manual patching (**Fig. 7, *A*** and ***D***). Moving a pipette tip to a saved target cell location, with secondary calibration of the pipette offset, took on average 103.2 ± 2.7 s ($n = 44$) for both fully automatic and semiautomatic trials (no difference at this stage). This was significantly faster than manual pipette tip placement, which took 183.0 ± 4.4 s ($n = 85$, $P = 0.0001$, Student's *t*-test). Furthermore, the use of automatic manipulator control and memory positions enabled pipette tip placement outside of the microscope's visual field, which is impossible with manual patching. Automatic patch-clamp algorithm resulted in faster gigaseal formation, 119.5 ± 18.3 s ($n = 23$) for fully automatic and 122.6 ± 10.1 s ($n = 19$) for semiautomatic patching (no significant difference between the two, $P = 0.88$) compared with 233.6 ± 30.3 s ($n = 85$) for manual patching ($P = 0.001$). Precise, fast pressure control in response to resistance changes significantly decreased the break-in time from 49.1 ± 8.1 s for manual trials to 15.3 ± 4.3 s for semiautomatic trials ($P = 0.036$ compared with manual) and further decreased to 5.2 ± 1.0 s for fully automatic

trials ($P = 0.0002$ compared with manual; $P = 0.025$ compared with semiautomatic; **Fig. 7*A***). There was no significant difference between the duration of failed trials for either automatic or manual algorithms. However, because the duration of a successful trial was two times shorter, and the success rate was two times higher, the overall time spent to achieve comparable productivity was much shorter for the automatic algorithm.

Furthermore, the time limit for automatic trial attempt may be further decreased, leading to less time spent during failed trials. Use of the Autopatcher IG also proved to be more consistent because the time spent during each automatic trial was less variable compared with manual patching (**Fig. 7*C***).

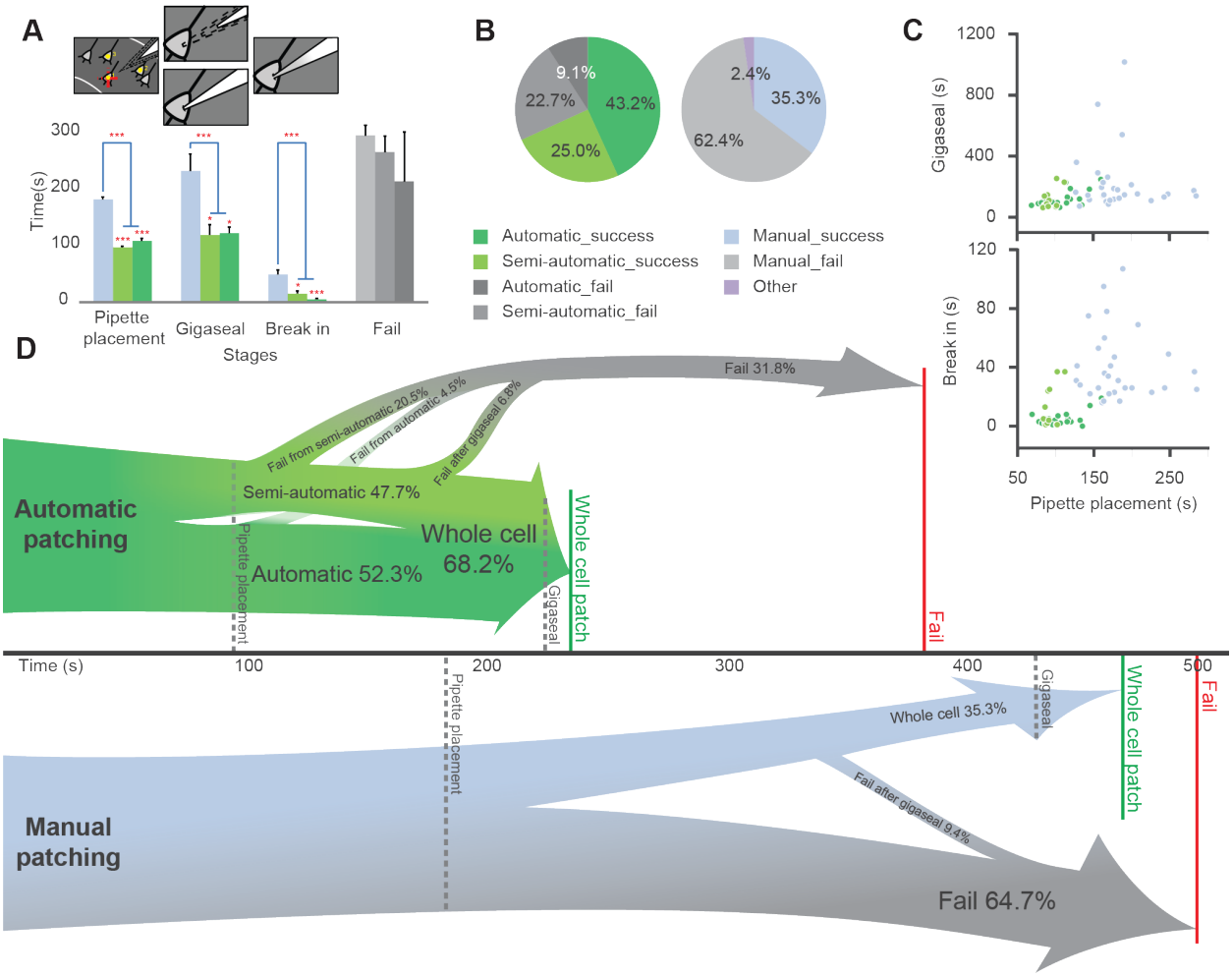

Figure 10. Automatic patching algorithm significantly improves patch clamp efficiency.

A) Average time spent during pipette placement, gigaseal formation, and establishment of whole cell configuration (break in) in both automatic patching (dark green) and semiautomatic patching (light green) is significantly shorter than in manual patching (light blue) in successful trials. The time from the end of pipette placement to termination of a failed trial (gray) is not significantly different between the 2 methods (*P < 0.05; ***P < 0.001; 2-tailed Student's t-test). Error bars represent SE. **B)** Success rate for automatic (n = 44 from 3 animals) and manual patching (n = 85 from 6 animals). **C)** Distribution of times spent during the 3 patching steps. The automatic patching steps are faster and more reproducible compared with the manual patching steps. Data points are the times for pipette placement in all successful trials vs. gigaseal time (top) and break-in time (bottom). **D)** Schematic illustration showing the average time and success/failure rates of automatic and manual patching.

Computer vision-aided fluorescent cell detection and patch clamp

The Autopatcher IG can be used to automatically detect a fluorescent cell, determine the coordinates of this cell, and store the coordinates for subsequent patch-clamp experiments. This automation of cell detection is achieved using computer vision processing of fluorescent images acquired at different slice depths. The program takes a *z* stack (20 images, 2-μm *z*-step size, default settings), and each acquired image is transformed into a series of black-and-white images using different thresholds (0.5 to 5 times mean pixel intensity). The use of multiple thresholds instead of one single threshold ensures that the detection algorithm can accommodate a wide range of fluorescence intensities. After initial Canny edge detection, cell contours within the range of 75–250 μm^2 in size and 60% circularity are considered to be tentative cells (**Figs. 1*C*** and **8*Aiii***). The centroids of these tentative cell contours from different thresholds are then clustered into groups on the basis of their distance from each other (Fig. 8*Aiv*). A threshold of a minimal number of detected centroids in a cluster is used to detect and exclude false positives. The final coordinates of each detected cell are the mean of all centroid coordinates along the *x*- and *y*- axes and the median along the *z*-axis (**Fig. 8*A***). Automatic cell detection yields cell coordinates that are stored and can be saved in a file. These coordinates are shown in the memory positions GUI (**Fig. 3**) that is used to direct a patch pipette and also can be used for directing a puff pipette for local drug application, single-cell laser-scanning photostimulation, or chemical compound uncaging.

We tested our computer vision algorithm for detecting fluorescent cells in both cortical slices from a Thy1-channelrhodopsin 2-EYFP line 18 (Thy1-ChR2-EYFP) transgenic mouse (**Fig. 8**) and from a wild-type (WT) mouse injected with HSV-ArchT-EYFP virus (**Fig. 9**). The average time required to locate the cell centroids was 84.2 ± 0.9 s for ArchT-EYFP (n = 10 trials) and 89.3 ± 1.3 s for Thy1-ChR2-EYFP (n = 10 trials). The average false-positive rate, or computed coordinates not visibly centered over a cell, was low for both preparations at 4.9 ± 2.25% for HSV-ArchT-EYFP and 3.43 ± 1.75% for Thy1-ChR2-EYFP. Detection sensitivity (the percentage of fluorescent cells that can be detected within the field of view) was 76.4 ± 4.6% for HSV-ArchT-EYFP and 79.7 ± 8.8% for Thy1-ChR2-EYFP. There was no significant difference in false-positive rate or detection sensitivity between the two experimental preparations (P = 0.6 for both, Student's t-test). The detection threshold range and computing power could affect the total detection time, but they were sufficient for a standard desktop personal computer used in

our experiments. The low variation demonstrates that our detection system reliably detects the majority of fluorescent cells in the field of view.

We then demonstrated the feasibility of a complete automatic patching algorithm from cell detection to whole cell configuration using Autopatcher IG. A total of 20 whole cell patches were formed from fluorescence-positive layer 5 neurons in Thy1-ChR2-EYFP cortical slices (**Fig. 8, *B*** and ***C***). The average times were 98.5 ± 2.8 s for pipette positioning, 136.5 ± 20.1 s for gigaseal formation, and 9.8 ± 2.8 s for break-in, all of which were not significantly different from times in automatic and semiautomatic patching trials in WT mice ($P = 0.4$ for all). Patched cells were subjected to light activation to confirm ChR2-EYFP expression (**Fig. 8*D***). Patch qualities were consistent with those for WT patches (**Figs. 6*H*** and **8*E***). No differences in seal resistance ($P = 0.71$, Student's t-test), membrane resistance ($P = 0.05$), access resistance ($P = 0.95$), and holding current ($P = 0.96$) were observed compared with the same measurements in manually patched cells. The success rate for automatic detection and patching of fluorescent cells was comparable to that for manual patching at 31.0% ($n = 65$ from 3 animals), the majority of which required adjustment at the touch cell surface step. The membrane capacitance of automatically patched fluorescent cells was significantly larger than that of nonfluorescent cells ($P = 0.001$), which could be potentially explained by changes in conductivity caused by expression of ChR2. Furthermore, expression of ChR2 was specific to larger layer 5 pyramidal cells, which may require different thresholds in the patching algorithm that can be determined after the corresponding patch logs are analyzed. The lower success rate and the need for threshold adjustments may also be explained by neuronal cell firing during fluorescence visualization. Alternatively, previous reports suggest that long-term high levels of expression of ChR2 may influence the health of a cell (Feldbauer et al., 2009; Lin, 2011; Miyashita, Shao, Chung, Pourzia, & Feldman, 2013).

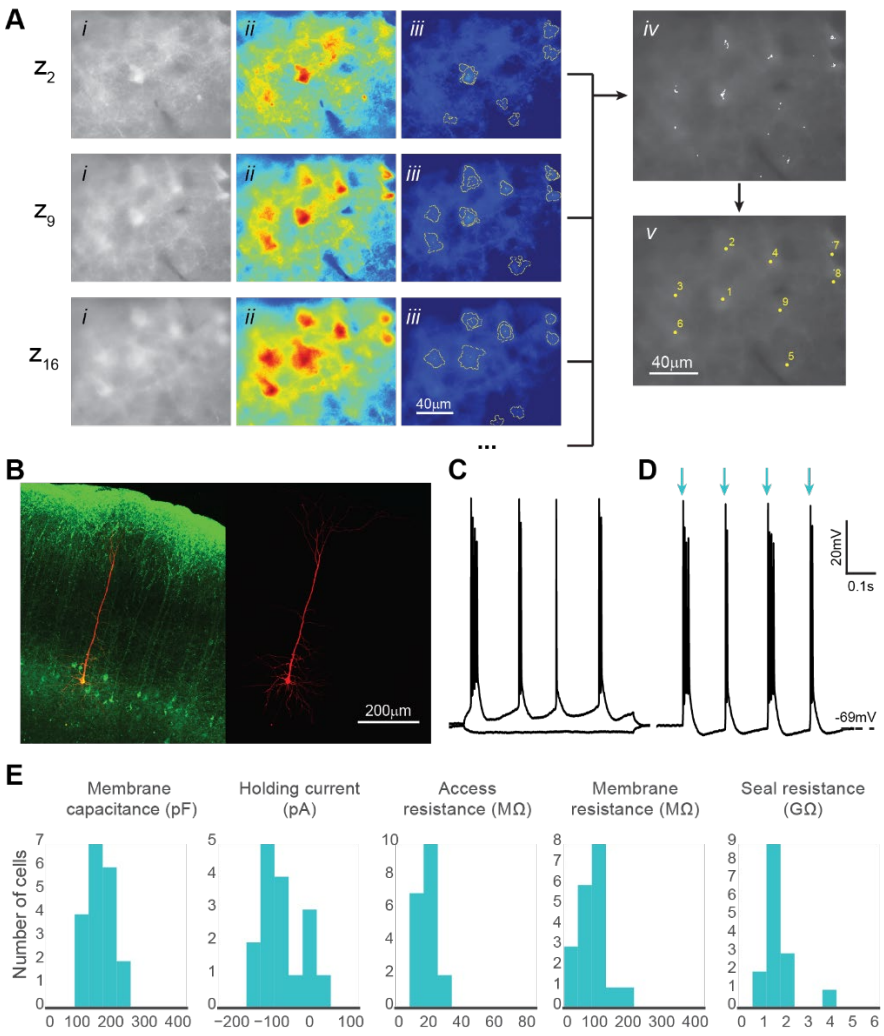

Figure 11. Automatic identification and patch clamp of fluorescent neurons in brain slices.

A) Computer vision processing of images acquired with epifluorescence optics detects fluorescent neurons and identifies their x, y, z coordinates. Three representative z sections are shown from a complete experiment (20 total z sections) using brain slices prepared from a mouse expressing channelrhodopsin-2-EYFP in layer 5 pyramidal cells (Thy1-ChR2-EYFP mouse line 18). i, Original image after histogram equalization; ii, pseudo-colored image after thresholding; iii, superimposed cell-like contours detected after a series of varying thresholds; iv, centroids of detected contours are accumulated from z sections; v, centroids from the complete z scan (20 z sections) are clustered and the final coordinates calculated. **B)** Representative patched fluorescent neuron (green) filled with Alexa Fluor 568 dye (red) in layer 5 mouse neocortex. An acute brain slice was post fixed and immunolabeled with the anti-GFP antibody. Image acquisition was performed using confocal microscopy. **C)** Current-clamp recordings of a patched cell responding to hyperpolarizing and depolarizing current injection. Firing pattern shows intrinsic bursting, which is characteristic of a layer 5 intrinsically bursting pyramidal neuron. **D)** The same neuron as in C reacts to light (480 nm) activation with bursts of action potentials. Blue arrows show the light on epochs that are 2 ms each and 150 ms apart. **E)** Patched cell properties measured from each successful trial (n 20 from 3 animals). No significant differences in holding current, access resistance, membrane resistance, and seal resistance were observed compared with those for nonfluorescent cells, shown in Fig. 6. Membrane capacitance distribution was significantly different from that in nonfluorescent cells, which can be explained by the larger size of the layer 5 pyramidal cells (P 0.05, 2-tailed Student's t-test).

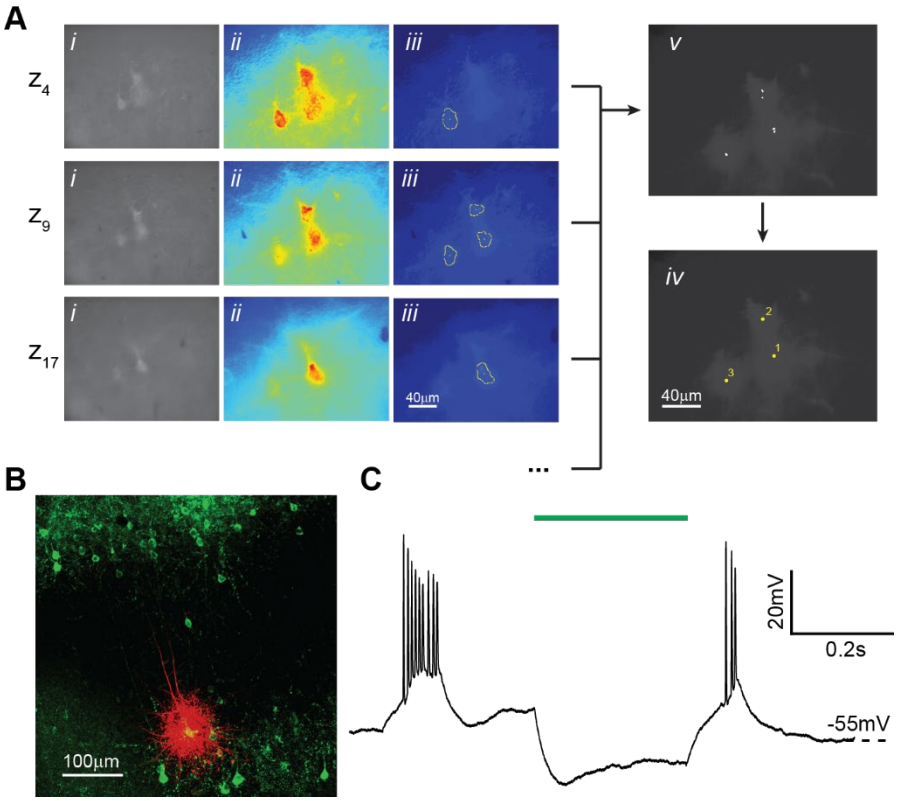

Figure 12. Computer vision-aided automatic cell detection of ArchT-EYFP-positive cells.

A) Computer vision processing of images acquired with epifluorescence optics detects fluorescent neurons and identifies their x, y, z coordinates. Three representative z sections are shown from a complete experiment (20 total z sections) using brain slices prepared from a mouse injected with HSV-ArchT-EYFP virus. i, Original image after histogram equalization; ii, pseudo-colored image after thresholding; iii, superimposed cell-like contours detected after a series of varying thresholds; iv, centroids of detected contours are accumulated from z sections; v, centroids from the complete z scan (20 z sections) are clustered and the final coordinates calculated. **B)** Representative ArchT-EYFP-positive cell (green) filled with Alexa Fluor 568, post fixed, and immunolabeled with the anti-GFP antibody. Images are acquired using confocal microscopy. **C)** Representative current-clamp recording trace of a layer 5 bursting cell hyperpolarized in response to light (550 nm) activation (green bar).

Discussion

We have developed an image-guided patch-clamp electro-physiology software package, the Autopatcher IG, which achieves high-level automation for whole cell patch-clamp experiment in vitro. Some existing systems have attempted to automate separate steps in the whole process, such as cell detection (Long et al., 2015), pressure control (Desai, Siegel, Taylor, Chitwood, & Johnston, 2015), and pipette positioning (Long et al., 2015; Perin & Markram, 2013); however, there has not been an integrated system that automates the entire patching process from targeting cells to forming whole cell patch clamp in vitro. We have tested Autopatcher IG performance in patch-clamp experiments conducted by a newly trained experimenter and have shown a twofold improvement of success rate and decrease in average time spent on each trial compared with the traditional manual patching procedure. Both factors contributed to an overall increase in throughput, which will improve the utilization of each tissue sample and decrease the time required to obtain large patch-clamp data sets. This is especially advantageous when experiments are conducted on valuable transgenic animals or require viral injection, or when long and complex training protocols must be implemented prior to the slice electrophysiology experiment. Furthermore, Autopatcher IG enables control of experimental parameters that is hard to achieve even for a trained user (for example, uniform descent speed and pressure application), which helps to minimize trial variability and promote reproducibility. The system is widely adaptable because the software is suitable for a broad range of hardware configurations augmented only by a pneumatic pressure control unit.

Some limitations of Autopatcher IG led to human interference during the automatic patch process, which was then followed by the fully automatic continuation of the algorithm (**Figs. 1*A*** and **8**). In these "semiautomatic" trials there were errors in mechanical manipulator positioning at distances longer than 200 μm. There are two potential solutions to this problem: more accurate micromanipulators or a close-loop computer vision algorithm for pipette tip detection and real-time coordinate tracking. Another limitation that led to human interruption was caused by variability in automatic patching threshold parameters, which could be explained by cell heterogeneity. Optimization of these thresholds for specific cell types may solve this problem. Nonetheless, the system still achieved a 43.2% success rate when only fully automatic patching was counted. It is noteworthy that the rest of the trials were not failures and that the whole cell configurations could be reached with only minor adjustment in semiautomatic trials.

By integrating and automating all steps of the patching process, Autopatcher IG improves the speed and reproducibility of patching, leading to an increase in throughput. The age of the animal, duration of the experiment, area of the brain, and many more experimental details can have dramatic effects on the "health" of neurons and thus their ability to form stable gigaseals and whole cell configurations (Boulton et al., 1995; Walz, 2007). Autopatcher IG is intended to serve as a frame-work for quantifying and standardizing in vitro patch-clamp recording. The ability to algorithmically control all relevant peripheral devices from a single interface makes it possible to document and standardize existing "best practices" in obtaining whole cell recordings (Boulton et al., 1995; Walz, 2007). Integrated algorithmic control also makes it possible to explore and quantify new ways of obtaining whole cell recordings. For instance, a millisecond-timescale closed-loop pipette pressure control system could potentially outperform even an expert in quickly establishing a gigaseal and breaking into a cell delicately. In the future, these algorithms can then be refined and optimized in a systematic fashion.

The difficulty of patch-clamp recording in brain slices is compounded when multiple cells must be patched simultaneously, for example, to profile interneuronal connectivity in a region of the brain (Le Be & Markram, 2006; Perin, Berger, & Markram, 2011). Because of its modular nature, the Autopatcher IG software is readily scalable for multiple manipulators, limited only by the hardware (manipulators, data acquisition board, amplifiers). Multipatch experiments are still impractical for many electrophysiology laboratories, despite notable system engineering efforts (Perin & Markram, 2013; Wang et al., 2015). The improvements in whole cell yield and automation provided by Autopatcher IG may increase the likelihood of obtaining multiple stable simultaneous recordings. This could lower the barrier to entry for laboratories wishing to perform multipatch experiments.

A major innovation of Autopatcher IG is the incorporation of computer vision into image processing to robustly and reliably extract cell and pipette coordinate information. It is especially beneficial for detecting and storing the *z* coordinate of multiple fluorescent cells, which is complicated and time consuming in manual patching. However, the selection of a suitable target cell without fluorescent signal is still a difficult user-dependent task that is manually performed in the current system. Another rate-limiting step is the filling and changing of glass pipettes before each trial. In future versions of the software, we intend to develop computer vision algorithms to reliably identify and track healthy cell bodies under DIC optics (Alexopoulos,

Erickson, & Guilak, 2002), along with robotic devices for automatically swapping patch electrodes to perform patch-clamp experiments completely autonomously. The software presented in this article and the accompanying user manuals are freely available online for the neuroscience community (www.autopatcher.org or https://github.com/chubykin/Auto-Patcher_IG). Software updates and bug fixes will be announced on those websites.

Acknowledgements

We thank the Allen Institute founders, Paul G. Allen and Jody Allen, for their vision, encouragement, and support.

Grants

We are grateful for financial support from National Institutes of Health (NIH) Computational Neuroscience Training Grant DA032466-02 and NIH BRAIN Initiative Grant 1-U01-MH106027-01, the Simons Center for the Social Brain, and the Whitehall Foundation.

Disclosures

No conflicts of interest, financial or otherwise, are declared by the authors.

Author contributions

Q.W., I.K., B.M.C., Z.S., W.S., S.B.K., R.N., and A.A.C. performed experiments; Q.W., I.K., and A.A.C. analyzed data; Q.W., I.K., H.Z., C.R.F., and A.A.C. interpreted results of experiments; Q.W., I.K., and A.A.C. prepared figures; Q.W., I.K., C.R.F., and A.A.C. drafted manuscript; Q.W., I.K., S.B.K., E.S.B., C.R.F., and A.A.C. edited and revised manuscript; C.R.F. and A.A.C. conception and design of research; C.R.F. and A.A.C. approved final version of manuscript.

References

Ackerman, M. J., & Clapham, D. E. (1997). Ion channels--basic science and clinical disease. *N Engl J Med, 336*(22), 1575-1586. doi: 10.1056/NEJM199705293362207

Alexopoulos, L. G., Erickson, G. R., & Guilak, F. (2002). A method for quantifying cell size from differential interference contrast images: validation and application to osmotically stressed chondrocytes. *J Microsc, 205*(Pt 2), 125-135.

Alivisatos, A. P. (2012). The brain activity map project and the challenge of functional connectomics. *Neuron, 74*, 970-974.

Alivisatos, A. P. (2013). The Brain Activity Map. *Science, 339*, 1284-1285.

Arenkiel, B. R., Peca, J., Davison, I. G., Feliciano, C., Deisseroth, K., Augustine, G. J., . . . Feng, G. (2007). In vivo light-induced activation of neural circuitry in transgenic mice expressing channelrhodopsin-2. *Neuron, 54*(2), 205-218. doi: 10.1016/j.neuron.2007.03.005

Boulton, A. A., Baker, G. B., & Walz, W. (1995). *Patch-clamp applications and protocols*. Totowa, N.J.: Humana Press.

Boyden, E. S., Zhang, F., Bamberg, E., Nagel, G., & Deisseroth, K. (2005). Millisecond-timescale, genetically targeted optical control of neural activity. *Nat Neurosci, 8*(9), 1263-1268. doi: 10.1038/nn1525

Campagnola, L., Kratz, M. B., & Manis, P. B. (2014). ACQ4: an open-source software platform for data acquisition and analysis in neurophysiology research. *Front Neuroinform, 8*, 3. doi: 10.3389/fninf.2014.00003

Desai, N. S., Siegel, J. J., Taylor, W., Chitwood, R. A., & Johnston, D. (2015). MATLAB-based automated patch-clamp system for awake behaving mice. *J Neurophysiol, 114*(2), 1331-1345. doi: 10.1152/jn.00025.2015

Edelstein, A., Amodaj, N., Hoover, K., Vale, R., & Stuurman, N. (2010). Computer control of microscopes using microManager. *Curr Protoc Mol Biol, Chapter 14*, Unit14 20. doi: 10.1002/0471142727.mb1420s92

Edwards, F. A., Konnerth, A., & Sakmann, B. (1990). Quantal analysis of inhibitory synaptic transmission in the dentate gyrus of rat hippocampal slices: a patch-clamp study. *J Physiol, 430*, 213-249.

Feldbauer, K., Zimmermann, D., Pintschovius, V., Spitz, J., Bamann, C., & Bamberg, E. (2009). Channelrhodopsin-2 is a leaky proton pump. *Proc Natl Acad Sci U S A, 106*(30), 12317-12322. doi: 10.1073/pnas.0905852106

Hoshi, T., Zagotta, W. N., & Aldrich, R. W. (1990). Biophysical and molecular mechanisms of Shaker potassium channel inactivation. *Science, 250*(4980), 533-538.

Insel, T. R., Landis, S. C., & Collins, F. S. (2013). Research priorities. The NIH BRAIN Initiative. *Science, 340*(6133), 687-688. doi: 10.1126/science.1239276

Jaffe, D., & Johnston, D. (1990). Induction of long-term potentiation at hippocampal mossy-fiber synapses follows a Hebbian rule. *J Neurophysiol, 64*(3), 948-960.

Jiang, X., Shen, S., Cadwell, C. R., Berens, P., Sinz, F., Ecker, A. S., . . . Tolias, A. S. (2015). Principles of connectivity among morphologically defined cell types in adult neocortex. *Science, 350*(6264), aac9462. doi: 10.1126/science.aac9462

Kandel, E. R., Markram, H., Matthews, P. M., Yuste, R., & Koch, C. (2013). Neuroscience thinks big (and collaboratively). *Nat Rev Neurosci, 14*(9), 659-664. doi: 10.1038/nrn3578

Kawaguchi, Y., & Kubota, Y. (1993). Correlation of physiological subgroupings of nonpyramidal cells with parvalbumin- and calbindinD28k-immunoreactive neurons in layer V of rat frontal cortex. *J Neurophysiol, 70*(1), 387-396.

Kodandaramaiah, S. B., Franzesi, G. T., Chow, B. Y., Boyden, E. S., & Forest, C. R. (2012). Automated whole-cell patch-clamp electrophysiology of neurons in vivo. *Nat Methods, 9*(6), 585-587. doi: 10.1038/nmeth.1993

Komai, S., Denk, W., Osten, P., Brecht, M., & Margrie, T. W. (2006). Two-photon targeted patching (TPTP) in vivo. *Nat Protoc, 1*(2), 647-652. doi: 10.1038/nprot.2006.100

Larkum, M. E., Zhu, J. J., & Sakmann, B. (1999). A new cellular mechanism for coupling inputs arriving at different cortical layers. *Nature, 398*(6725), 338-341. doi: 10.1038/18686

Le Be, J. V., & Markram, H. (2006). Spontaneous and evoked synaptic rewiring in the neonatal neocortex. *Proc Natl Acad Sci U S A, 103*(35), 13214-13219. doi: 10.1073/pnas.0604691103

Lefort, S., Tomm, C., Floyd Sarria, J. C., & Petersen, C. C. (2009). The excitatory neuronal network of the C2 barrel column in mouse primary somatosensory cortex. *Neuron, 61*(2), 301-316. doi: 10.1016/j.neuron.2008.12.020

Lin, J. Y. (2011). A user's guide to channelrhodopsin variants: features, limitations and future developments. *Exp Physiol, 96*(1), 19-25. doi: 10.1113/expphysiol.2009.051961

Long, B., Li, L., Knoblich, U., Zeng, H., & Peng, H. (2015). 3D Image-Guided Automatic Pipette Positioning for Single Cell Experiments in vivo. *Sci Rep, 5*, 18426. doi: 10.1038/srep18426

Markram, H., Lubke, J., Frotscher, M., Roth, A., & Sakmann, B. (1997). Physiology and anatomy of synaptic connections between thick tufted pyramidal neurones in the developing rat neocortex. *J Physiol, 500 (Pt 2)*, 409-440.

Miyashita, T., Shao, Y. R., Chung, J., Pourzia, O., & Feldman, D. E. (2013). Long-term channelrhodopsin-2 (ChR2) expression can induce abnormal axonal morphology and targeting in cerebral cortex. *Front Neural Circuits, 7*, 8. doi: 10.3389/fncir.2013.00008

Neher, E., & Sakmann, B. (1976). Single-channel currents recorded from membrane of denervated frog muscle fibres. *Nature, 260*(5554), 799-802.

Perin, R., Berger, T. K., & Markram, H. (2011). A synaptic organizing principle for cortical neuronal groups. *Proc Natl Acad Sci U S A, 108*(13), 5419-5424. doi: 10.1073/pnas.1016051108

Perin, R., & Markram, H. (2013). A computer-assisted multi-electrode patch-clamp system. *J Vis Exp*(80), e50630. doi: 10.3791/50630

Petreanu, L., Huber, D., Sobczyk, A., & Svoboda, K. (2007). Channelrhodopsin-2-assisted circuit mapping of long-range callosal projections. *Nat Neurosci, 10*(5), 663-668. doi: 10.1038/nn1891

Philpot, B. D., Sekhar, A. K., Shouval, H. Z., & Bear, M. F. (2001). Visual experience and deprivation bidirectionally modify the composition and function of NMDA receptors in visual cortex. *Neuron, 29*(1), 157-169.

Suter, B. A., O'Connor, T., Iyer, V., Petreanu, L. T., Hooks, B. M., Kiritani, T., . . . Shepherd, G. M. (2010). Ephus: multipurpose data acquisition software for neuroscience experiments. *Front Neural Circuits, 4*, 100. doi: 10.3389/fncir.2010.00100

Ting, J. T., Daigle, T. L., Chen, Q., & Feng, G. (2014). Acute brain slice methods for adult and aging animals: application of targeted patch clamp analysis and optogenetics. *Methods Mol Biol, 1183*, 221-242. doi: 10.1007/978-1-4939-1096-0_14

Tripathy, S. J., Burton, S. D., Geramita, M., Gerkin, R. C., & Urban, N. N. (2015). Brain-wide analysis of electrophysiological diversity yields novel categorization of mammalian neuron types. *J Neurophysiol*, jn 00237 02015. doi: 10.1152/jn.00237.2015

Walz, W. (2007). *Patch-clamp analysis : advanced techniques* (2nd ed.). Totowa, N.J.: Humana Press.

Wang, G., Wyskiel, D. R., Yang, W., Wang, Y., Milbern, L. C., Lalanne, T., . . . Zhu, J. J. (2015). An optogenetics- and imaging-assisted simultaneous multiple patch-clamp recording system for decoding complex neural circuits. *Nat Protoc, 10*(3), 397-412. doi: 10.1038/nprot.2015.019

Zalutsky, R. A., & Nicoll, R. A. (1990). Comparison of two forms of long-term potentiation in single hippocampal neurons. *Science, 248*(4963), 1619-1624.

CHAPTER 2. APPLICATION OF AUTOMATED IMAGE-GUIDED PATCH CLAMP FOR THE STUDY OF NEURONS IN BRAIN SLICES

Adopted from:
Wu, Q., Chubykin, A.A. Application of Automated Image-guided Patch Clamp for the Study of Neurons in Brain Slices. J. Vis. Exp. (125), e56010, doi:10.3791/56010 (2017).

Abstract

Whole-cell patch clamp is the gold-standard method to measure the electrical properties of single cells. However, the *in vitro* patch clamp remains a challenging and low-throughput technique due to its complexity and high reliance on user operation and control. This manuscript demonstrates an image-guided automatic patch clamp system for *in vitro* whole-cell patch clamp experiments in acute brain slices. Our system implements a computer vision-based algorithm to detect fluorescently labeled cells and to target them for fully automatic patching using a micromanipulator and internal pipette pressure control. The entire process is highly automated, with minimal requirements for human intervention. Real-time experimental information, including electrical resistance and internal pipette pressure, are documented electronically for future analysis and for optimization to different cell types. Although our system is described in the context of acute brain slice recordings, it can also be applied to the automated image-guided patch clamp of dissociated neurons, organotypic slice cultures, and other non-neuronal cell types.

Key Words

Neuroscience, Issue 125, Automatic patching, patch clamp, in vitro electrophysiology, computer vision, fluorescent cell detection, Python

Video Link

The video component of this article can be found at https://www.jove.com/video/56010/

Introduction

The patch clamp technique was first developed by Neher and Sakmann in the 1970s to study the ionic channels of excitable membranes (Sakmann & Neher, 1984). Since then, patch clamping has been applied to the study of many different subjects at the cellular, synaptic, and circuit level—both *in vitro* and *in vivo*—in many different cell types, including neurons, cardiomyocytes, Xenopus oocytes, and artificial liposomes (Collins & Gordon, 2013). This process involves the correct identification and targeting of a cell of interest, intricate micromanipulator control to move the patch pipette in close proximity to the cell, the application of positive and negative pressure to the pipette at the proper time to establish a tight gigaseal patch, and a break-in to establish a whole-cell patch configuration. Patch clamping is typically conducted manually and requires extensive training to master. Even for a researcher experienced with the patch clamp, the success rate is relatively low. More recently, several attempts have been made to automate patch-clamp experiments. Two main strategies have evolved to accomplish automation: augmenting standard patch clamp equipment to provide automatic control of the patching process and the design of new equipment and techniques from the ground up. The former strategy is adaptable to existing hardware and can be used in a variety of patch clamp applications, including *in vivo* blind patch clamp (Desai, Siegel, Taylor, Chitwood, & Johnston, 2015; S. B. Kodandaramaiah, Franzesi, Chow, Boyden, & Forest, 2012; Suhasa B. Kodandaramaiah et al., 2016), *in vitro* patch clamp of acute brain slices, organotypic slice cultures, and cultured dissociated neurons (Wu et al., 2016). It enables the interrogation of complex local circuits by using multiple micromanipulators simultaneously (Perin & Markram, 2013). The planar patch method is an example of the new development strategy, which can achieve the high-throughput simultaneous patch clamp of cells in suspension for drug screening purposes (Fertig, Blick, & Behrends, 2002). However, the planar patch method is not applicable to all cell types, particularly neurons with long processes or intact circuits containing extensive connections. This limits its application to mapping the intricate circuitry of the nervous system, which is a key advantage of traditional patch clamp technology.

We have developed a system that automates the manual patch clamp process *in vitro* by augmenting standard patch clamp hardware. Our system, Autopatcher IG, provides automatic pipette calibration, fluorescent cell target identification, automatic control of pipette movement, automatic whole-cell patching, and data logging. The system can automatically acquire multiple

images of brain slices at different depths; analyze them using computer vision; and extract information, including the coordinates of fluorescently labeled cells. This information can then be used to target and automatically patch cells of interest. The software is written in Python—a free, open-source programming language—using several open-source libraries. This ensures its accessibility to other researchers and improves the reproducibility and rigor of electrophysiology experiments. The system has a modular design, such that additional hardware can easily be interfaced with the current system demonstrated here.

Protocol

1. System Setup

1. Construct the pressure control unit.
    1. Assemble the pressure control unit according to the circuit map (**Fig. 10**). Solder the necessary parts onto the Printed Circuit Board (PCB) manufactured according to the electrical circuit schematics (**Fig. 10*B***). Use standard resistors, LEDs, Metal-Oxide Semiconductor Field-effect Transistors (MOSFETs), capacitors, and connectors (see the **Table 2**). Solder solenoid valves onto the PCB. Connect the air pump and air pressure sensor to the PCB with electrical wire.
    NOTE: It should take about 2 h to construct the pressure control unit with all necessary parts made available.

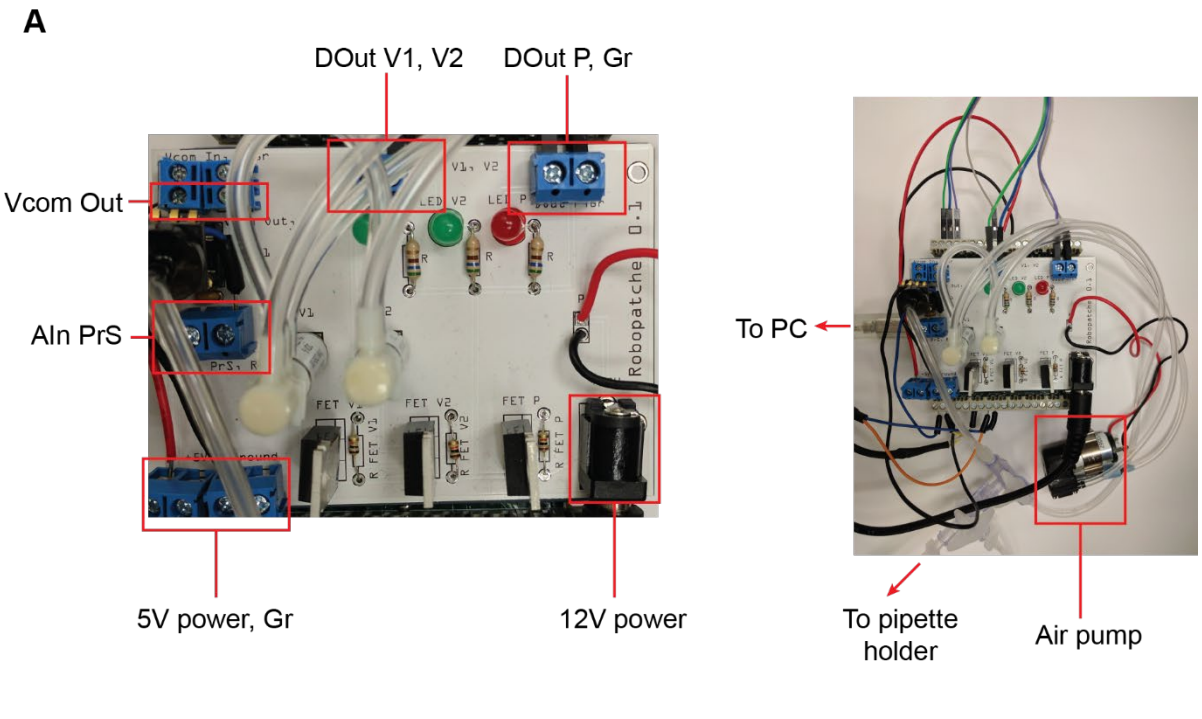

Figure 13. Pressure Control Unit.

A) Printed Circuit Board (PCB) for connecting the valves, pressure sensor, and air pump. The left shows details on the PCB, labeling locations of outputs that are mentioned in the protocol. The right shows the connection between the PCB and the air pump, USB port, and tubing. **B)** Circuit map for the PCB.

Table 2. Materials list

Name	***Company***	***Catalog Number***	***Comments***
CCD Camera	QImaging	Rolera Bolt	
Electrophysiology rig	Scientifica	SliceScope Pro 2000	Include microscope and manipulators. The manufacturer provided manipulator control software demonstrated in this manuscript is "Linlab2".
Amplifier	Molecular Devices	MultiClamp 700B	computer-controlled microelectrode amplifier
Digitizer	Molecular Devices	Axon Digidata 1550	
LED light source	Cool LED	pE-100	488 nm wavelength
Data acquisition board	Measurement Computing	USB1208-FS	Secondary DAQ. See manual at : http://www.mccdaq.com/pdfs/manuals/USB-1208FS.pdf
Solenoid valves	The Lee Co.	LHDA0531115H	
Air pump	Virtual industry	VMP1625MX-12-90-CH	
Air pressure sensor	Freescale semiconductor	MPXV7025G	
Slice hold-down	Warner instruments	64-1415 (SHD-40/2)	Slice Anchor Kit, Flat for RC-40 Chamber, 2.0 mm, 19.7 mm
Python	Anaconda	version 2.7 (32-bit for windows)	https://www.continuum.io/downloads
Screw Terminals	Sparkfun	PRT - 08084	Screw Terminals 3.5 mm Pitch (2-Pin)
(2-Pin)			
N-Channel MOSFET 60 V 30 A	Sparkfun	COM - 10213	
DIP Sockets Solder Tail - 8-Pin	Sparkfun	PRT-07937	
LED - Basic Red 5 mm	Sparkfun	COM-09590	
LED - Basic Green 5mm	Sparkfun	COM-09592	

Table 2. Continued

Name	**Company**	**Catalog Number**	**Comments**
DC Barrel Power Jack/Connector (SMD)	Sparkfun	PRT-12748	
Wall Adapter Power Supply - 12 V DC 600 mA	Sparkfun	TOL-09442	
Hook-Up Wire - Assortment (Solid Core, 22 AWG)	Sparkfun	PRT-11367	
Locking Male x Female x Female Stopcock	ARK-PLAS	RCX10-GP0	
Fisherbrand Tygon S3 E-3603 Flexible Tubing	Fisher scientific	14-171-129	Outer Diameter: 1/8 in. Inner Diameter: 1/16 in.
BNC male to BNC male coaxial cable	Belkin Components	F3K101-06-E	
560 Ohm Resistor (5% tolerance)	Radioshack	2711116	
Picospritzer	General Valve	Picospritzer II	

2. Connect the secondary data acquisition (DAQ) board.
    1. Connect data outputs from the printed circuit board to the DAQ board, following **Table 3**.

       NOTE: The DAQ board will be running in "Single-ended mode." The port map can be found in the user manual (see the **Table 2**).
    2. Connect "AIn Pr S" to one of the analog input (AI) channels and "R-Gr" to one of the analog grounds on the secondary DAQ board.
    3. Connect the primary output from the amplifier to one of the AI channels and the ground to the analog ground of the secondary DAQ board.

       NOTE: A standard BNC cable can be used to connect the primary output from the amplifier.
    4. Strip the other end and connect the positive signal (*i.e.* copper core) to the AI channel and the ground (*i.e.* the thin wire around the core) to the analog ground. Repeat this step for a second channel if more than one patch channel is used.

       NOTE: The analog input to the DAQ board will be configured in later steps.
    5. Connect power to the power output of the secondary DAQ board. Use a separate 12 V power source for the pump.
3. Connect the tubing.
    1. Connect the air pump and the two valves according to **Table 4**. Use a 3-way connector to connect the soft tubing from the valve 2 top port, the pressure sensor, and the pipette holder in the last step.
    2. Add another 3-way connector to the tubing connected to the pipette holder if two pipettes are used. Manually switch between the valves and the pipettes in use when patching.

Table 3. Printed Circuit Board (PCB) to secondary data acquisition (DAQ) board connection configuration.

Use this table to connect PCB outputs (first column from left) to ports on the DAQ board (second column from left). The port name and number on the secondary DAQ refer to single-ended mode.

Outlet on the PCB	***Port name on the DAQ board***	***Port # on DAQ board***	***Remark***
DOUT V1	Port A channel 1	22	Control valve 1
DOUT V2	Port A channel 2	23	Control valve 2
DOUT P	Port A channel 3	24	Control air pump
Gr	Ground	29	Ground

Table 4. Tubing Connections from the Pressure Control Unit to the Pipette Holder(s).

	Connection 1	Connection 2	Connection 3	Connection 4
Port name				
Pump air intake				
Pump air output				
Valve 1 top port				
Valve 1 middle port				
Valve 1 bottom port				
Valve 2 top port				
Valve 2 middle port				
Valve 2 bottom port				
Pressure sensor				
Pipette holder				

For each connection, connect the corresponding ports, highlighted with a grey box, using soft tubing (see the **Table 2**).

4. Install Autopatcher IG.

   NOTE: System requirement: Autopatcher IG was only tested on a PC running Windows 7. It has not been validated for other operating systems. The described procedure applies specifically to the hardware listed in the Table of Materials.

   1. Download Autopatcher-IG from GitHub (https://github.com/chubykin/AutoPatcher_IG).
   2. Install Python (see the **Table 2** for the version and download address).
   3. Uninstall the PyQt4 library by typing "pip uninstall PyQt4" in a command line terminal.

      NOTE: The system uses an older version of the PyQt4 library to achieve compatibility with the Qwt and Opencv libraries.
   4. Install Python libraries from historic wheel files (http://www.lfd.uci.edu/~gohlke/pythonlibs/). Find the following files: Numpy (pymc-2.3.6-cp27-cp27m-win32.whl), Opencv (opencv_python-2.4.13.2-cp27-cp27m-win32.whl), Pyqt (PyQt4-4.11.4-cp27-none-win32.whl), and Qwt (PyQwt-5.2.1-cp27-none-win32.whl).
      1. To install the wheel files, go to the directory where the files are saved and type "pip install ***wheelfilename***.whl." Substitute "***wheelfilename***" with the actual name of the file.

         NOTE: "cp27" in the wheel file name indicates Python 2.7 and "win32" indicated Windows 32-bit. If "win32" does not work, try "win64."
   5. To control the CCD camera, download and install the installer for 64-bit (https://www.qimaging.com/support/software/). Then download MicroManager for 64-bit (https://micro-manager.org/wiki/Download_Micro-Manager_Latest_Release) to control the camera in Python.
   6. To control the manipulators and the microscope stage, install control software provided by the manufacturer.

      NOTE: By doing this, the driver necessary to control the manipulators is also installed. The installation package is commonly provided in a CD-ROM.
   7. To control the secondary DAQ board, install the Universal Library from CD-ROM, provided with the purchase of the DAQ board.
5. Configure the hardware for Autopatcher IG.

1. Connect the microscope stage and manipulator controllers to the computer via USB ports.
2. Assign COM port numbers to unit 0: microscope stage, unit 1: left manipulator, and unit 2: right manipulator, in this order, in the "ports.csv" configuration file in the "configuration" folder. Leave the other parameters in the ports.csv file (*i.e.* "SCI" and "1") unchanged. NOTE: The COM port number information can be found by running the manipulator configuration software provided by the manufacturer. Go to the "settings" tab, select "settings" and the "Motion" page, and read the labels for each tab at the top. Alternatively, this information can be found in the PC Device Manager.
3. Assign analog input channel numbers on the DAQ board for a pressure sensor and patch channel 1 and 2 (corresponding to unit 1 and 2). Enter the channel number in the "DAQchannels.csv" file in the "configuration" folder.
   NOTE: It is recommended to open the .csv files with the Notepad application instead of a spreadsheet, as it may alter the information when saving changes.

6. Run Autopatcher IG.
   1. Turn on the amplifier, microscope controller, and manipulator controller. Ensure that the amplifier software is running.
   2. Run Autopatcher IG with Python from a command line terminal as follows: first, change the directory (command "cd" for most common terminals) where Autopatcher IG is installed, type "python Autopatcher_IG.pyw" in the command line terminal, and hit the "Enter" key.
      NOTE: Do not run the manipulator control software before running Autopatcher IG because it will occupy the microscope stage and manipulator, causing Autopatcher IG to be unable to find the hardware. Manipulator control software can be run after Autopatcher IG is fully initiated if there are additional modules to be controlled (*e.g.,* the inline heater).
7. Calibrate the primary pipette.
   1. Pull patch pipettes as described previously (Brown, Johnson, & Goodman, 2008). Fill a pulled glass pipette with internal solution and load it onto the head stage. NOTE: Empty glass pipettes have different contrasts under the microscope and may lead to inaccurate calibration.

2. Move the pipette tip to the microscope visual field and bring it into focus. If the dial pad is used to move the manipulators and/or microscope stage, update the coordinates by pressing "z" on the keyboard.
   NOTE: This action is not necessary if the keyboard (microscope stage: A/D - x-axis, W/S - y-axis, R/F - z-axis; manipulators: H/K - x-axis, U/J - y-axis, O/L - z-axis, 1/2 - unit number) is used to control movement because the coordinates will be updated in real time.
3. Click the "Start calibration" button on the main Graphic User Interface (GUI) for the corresponding unit on which the pipette is loaded (**Fig. 11**).
   NOTE: A pop-up window will appear when the calibration is finished.
   NOTE: Calibration will be carried out automatically, which will take about 3.5 min. Clicking on the same button (switched now to "cancel calibration" after initiating calibration) will abort the calibration attempt.
4. Save the calibration by clicking "save calibration" at the bottom of the main GUI (it saves the current calibration for both manipulators and can be loaded in the future).
   NOTE: The field of view under low (4 or 10X) and high (40X) magnification must be aligned for secondary calibration to function properly. Please refer to the user manual of the optical system in use for the alignment procedures.

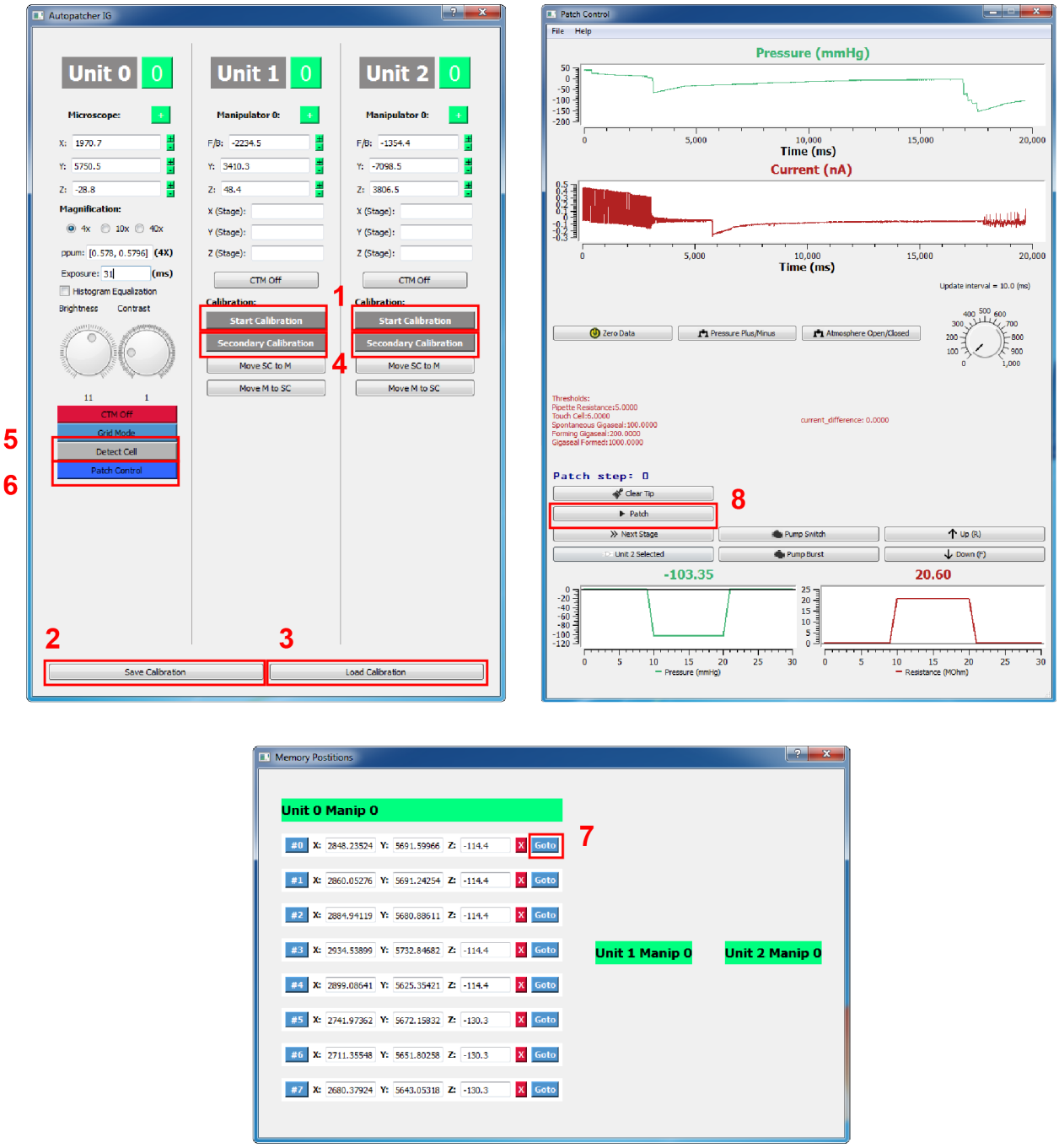

Figure 14. Autopatcher GUI.

The buttons mentioned in the protocol are shown in red squares and are numbered. 1: Start Calibration, 2: Save Calibration, 3: Load Calibration, 4: Secondary Calibration, 5: Detect Cell, 6: Patch Control, 7: Go to (target cell coordinate), and 8: Patch.

2. Automatic Patch Clamp Procedure

1. Prepare acute brain slices, as described previously (Segev, Garcia-Oscos, & Kourrich, 2016).
2. Prepare glass pipettes for the patch clamp.
3. Place one brain slice in the center of the recording chamber. Stabilize the slice with a slice hold-down, or "harp."
4. Detect the fluorescent cell.
    1. Find the area of interest under the 4X lens. Move the microscope stage by turning on click-to-move ("CTM") mode and click the center of the area of interest. Alternatively, use the keypad to move the microscope stage (A/D - x-axis, W/S - y-axis, R/F - z-axis).
    2. Switch to the high-magnification lens and adjust the focus by moving the microscope in the z-axis, using R/F on the keypad. NOTE: It is recommended to adjust the water bath level so that the focal plane under the low- and high-magnification lenses are the same or similar in the z-axis.
    3. Click the "Detect Cell" button on the main GUI column, "Unit 0." If the LED or laser light source of the setup cannot be controlled by the TTL signal, manually turn on the LED/laser; a pop-up window will appear when the cell detection is finished.
        1. Turn off the LED/laser if necessary; a list of cell coordinates will appear in the "Memory positions" GUI. Remove undesired cells from the list by clicking the "X" button next to the coordinates.
        2. Alternatively, if target cells are not fluorescently labeled, click "Mouse mode" on the main GUI. Click on the cell of interest; a yellow dot with a number will appear on the cell, and the coordinates of the cell will appear in the "Memory positions" GUI.
5. Calibrate the secondary pipette.
    1. Fill 1/3 of a glass pipette with internal solution. Load the pipette onto the pipette holder attached to the head stage.
    2. Use the low-magnification lens. Bring the pipette into the visual field and adjust the focus using the keypad (H/K - x-axis, U/J - y-axis, O/L - z-axis). Use "1" and "2" to switch between unit 1 and unit 2.

3. Load the primary calibration by clicking on "Load calibration." Click the "Secondary calibration" button on the main GUI under the unit that is in use. For example, if unit 2 is in use, click the "Secondary calibration" button in the "Unit 2" column. Follow the pop-up window instructions to switch to the high-magnification lens.

6. Patch a target cell.
    1. Make sure that the "MultiClamp" (*i.e.* amplifier) software is running. Click on the "Patch control" button to open the "Patch control" GUI; it may take up to a few min to open this GUI.
    2. Use the 40X magnification lens by checking "40X" on the main GUI "Unit 0" column. Click the "go to" button next to the cell of interest on the coordinate list in the "Memory position" GUI; the microscope will move to the cell.
    3. Click on the CTM button of the unit in use in the main GUI to enable movement following a mouse click. Click on the cell of interest; the pipette tip will move to the cell.
    4. Click on the "Patch" button on the "Patch control" GUI.
       NOTE: Automatic patching will begin, and the pressure and resistance can be monitored on the "Patch control" GUI.
        1. Use the "Unit 1 selected" button to switch the input signal between the two units.
           NOTE: The system will approach the target cell, apply negative pressure, match the cell membrane potential, and detect gigaseal formation based on a series of pressure and resistance thresholds and logic.
        2. Manipulate the automatic process at any point by clicking on the respective buttons on the "Patch control" GUI. For example, click on the "Patch" button again to cancel the patch trial and click on "Next stage" to advance the patching process to the next step, regardless of the threshold.
           NOTE: A pop-up window will notify the user when a gigaseal has formed, and the option to apply zap along with large negative pressure will be presented.
    5. Select "Yes" to break in with combined zap and suction. Alternatively, select "No" to break in with suction only.
       NOTE: When a successful whole-cell patch is completed, a pop-up window will remind the user to save the experiment patch log.

6. Save the experiment patch log.

   NOTE: If a patching trial is unsuccessful, a pop-up window will notify the user, and the patch process will reset.

7. Go back to step 2.4 and repeat the steps with a different cell.

7. Refine the patching thresholds (optional).

   NOTE: Thresholds for the initial pipette resistance range, positive and negative pressure, gigaseal resistance, *etc*. can be modified from a configuration file.

   1. Open the "PatchControlConfiguration.csv" file in the "Configuration" folder at the destination where the system is installed. Change the numbers corresponding to each threshold value. Do not change the names of the values; this will result in unrecognizable entries in the system.
   2. Implement the new threshold values immediately by pressing "Ctrl+L" without restarting the program; restarting the program will implement the newest threshold value from the file.

3. Performing Recordings

NOTE: The mode in the computer-controlled microelectrode amplifier will be set automatically to Current Clamp ("IC") by the autopatcher software once a successful patch has been achieved. Whole-cell patch clamp recordings can be done using the recording software of choice (this system does not include a recording function). If multiple target cells were identified, after finishing a recording, go back to step 2.4 and try another cell.

1. Perform automatic local drug application experiments using a picospritzer (optional).

   NOTE: Here, a local drug application experiment is used as an example to describe how to use the additional "Command Sequence" function to control external hardware through TTL signals.

   1. Connect port A channel 0 and the ground on the secondary DAQ board to the start trigger input on the digitizer using a stripped BNC cable (as described in step 1.2.3). Connect one digital output channel on the digitizer to the external trigger on the picospritzer.
   2. Prepare the picospritzer according to the user manual. Connect the picospritzer air output to the drug-puff pipette holder attached to a micromanipulator.

3. Load a pipette filled with a drug of choice. Attach it to the pipette holder. Calibrate the pipette, as described in step 1.7.
4. After patching a cell as described in step 2.6, select a desired location for drug delivery by mouse-clicking in the camera view GUI under "mouse mode" (switched from the main GUI). Alternatively, use the "Grid" GUI to design a grid, with each pixel in the grid as one of the target locations.
   NOTE: The grid can be manipulated in the camera view GUI by dragging with the mouse.
5. In the "Command Sequence" GUI, select the manipulator unit that the drug pipette is mounted on. Click "load mouse points" or "load grid points" to import all coordinates for drug delivery.
   1. Click on each coordinate entry to edit the specific command TTL signal in the right column. In the first command entry, click on the right-most digit to turn it from "0" to "1," sending a +5-V TTL signal. Set the time (T) to the desired TTL signal duration, in ms.
   2. In the second command entry, set all digits to "0" and set T to the duration of the recording length of the trial. Edit commands for all coordinate entries. Add command entries by clicking "+" if multiple TTL signals are necessary.
      NOTE: The 8-digit bits represent port A channels 0-7 on the secondary DAQ (ports 1 - 3 are occupied by the pump and two valves) can be switched, if necessary.
6. Create a recording protocol in the data acquisition module so that the start of a sweep is triggered by the external start trigger. Edit the protocol to deliver the drug at the desired time.
7. In the "Command Sequence" GUI, click "Run" on the left to run all coordinates. Alternatively, click "Run" on the right to run only the selected sequence.
   NOTE: The pipette will move to each coordinate and execute the TTL signal as defined to start the recording sweep.

Representative results

Our system has been tested on its ability to patch cells in acute brain slices, mouse induced Pluripotent Stem Cells (iPSCs) differentiated into neurons, and HEK 293 cells artificially expressing channels of interest. **Fig. 12** shows an experiment using Thy1-ChR2-YFP transgenic mice (B6.Cg-Tg(Thy1-COP4/EYFP)18Gfng/J) targeting fluorescently labeled layer 5 pyramidal neurons in the visual cortex. The target cell was one of the automatically identified green fluorescent-positive cells (**Fig. 12*B***). **Fig. 12*A*** is the Differential Interference Contrast (DIC) image of the patched neuron. The whole-cell configuration was achieved by the automatic patching protocol in steps 2.5 - 2.6 and was validated by step current injection-induced action potentials (**Fig. 12*C***)

To demonstrate the additional "Command Sequence" function, we delivered 500 mM KCl for 200 ms to three locations on a brain slice while patching a cell (**Fig. 13**). First, we selected 3 locations on the brain slice: one close to the patched cell body and two far away from the patched cell. The coordinates were stored in the "Memory Positions" GUI. The coordinates were loaded to the "Command Sequence" GUI under "Unit1," which was the manipulator that the KCl-containing pipette was mounted on. We set the commands in the left column to send a +5-V TTL signal for 500 ms, followed by 0 V for 10 s (**Fig. 13*A***), from port A channel 0 on the secondary DAQ board, which was connected to the digitizer "start trigger" input. **Fig. 13*C*** shows that the patched cell was a regular spiking neuron. The drug application pipette (Unit 1) traversed the three selected locations automatically (**Fig. 13*B***), and we recorded 10 s for each application under voltage-clamp (**Fig. 13*D***). The color of the traces in **Fig. 13*D*** corresponds to the border color in **Fig. 13*B***. When KCl was puffed at the cell, a large inward current was observed, which slowly diminished as KCl diffused. Red fluorescent dye was added to the KCl solution to indicate the spatial distribution of drug delivery and was imaged using combined DIC and epifluorescent imaging. This experiment illustrated the ease and flexibility of our system to control manipulator/ microscope movement and external hardware through TTL signals.

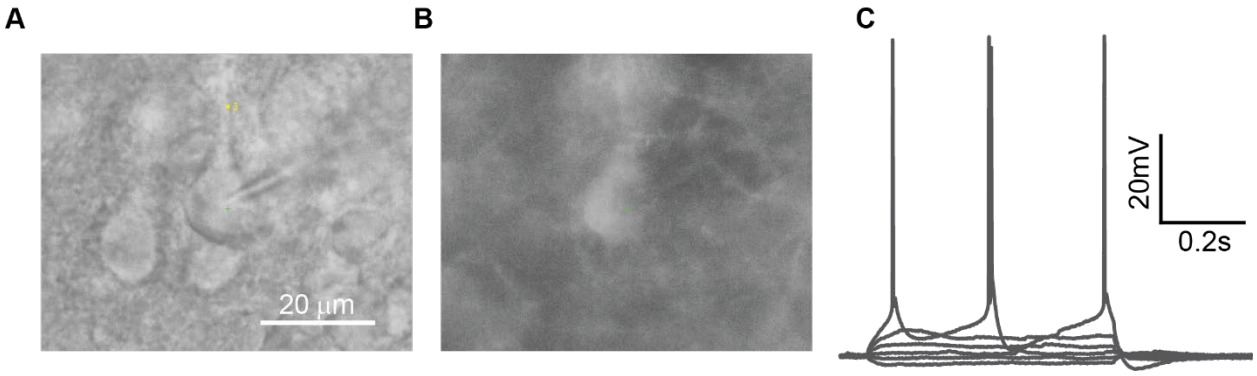

Figure 15. An Example of the Patched ChR2-YFP-positive Cell.

A) 40X magnification under DIC optics. **B)** Epifluorescence image of the same cell in panel A (LED illumination at 488 nm). **C)** Current-clamp recordings from the patched cell during a series of hyperpolarizing and depolarizing step current injections.

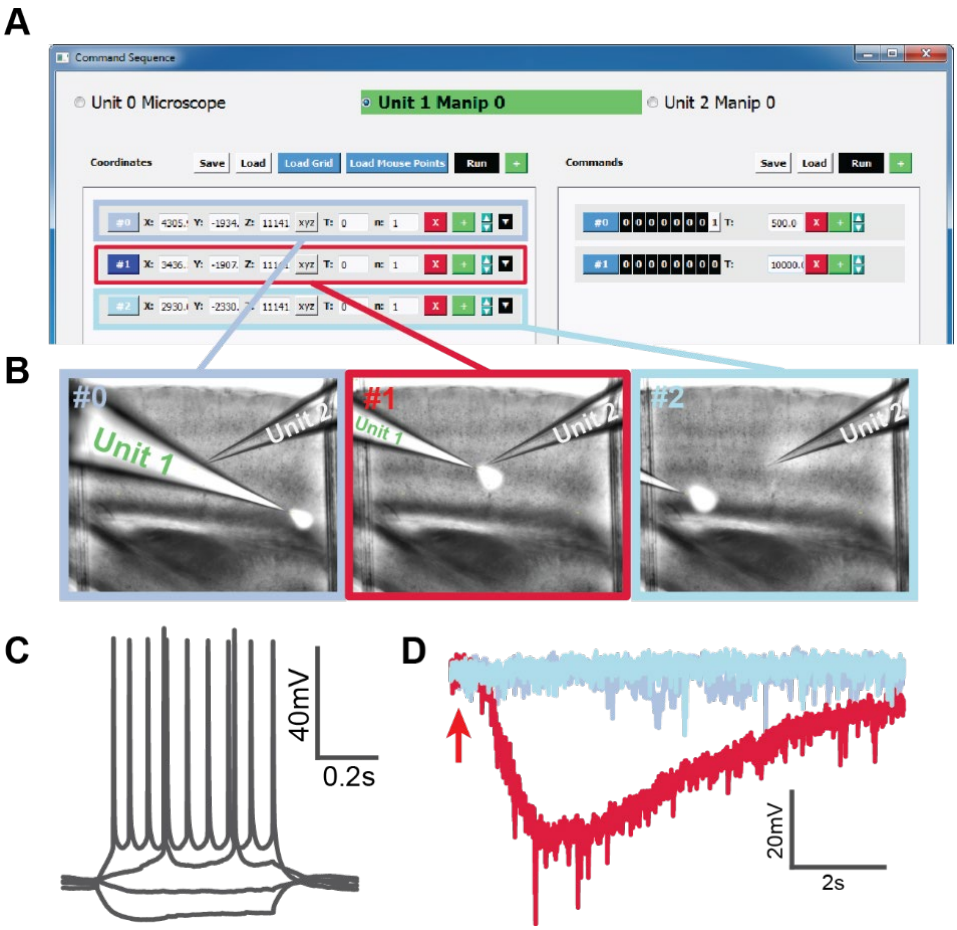

Figure 16. Conducting an Automated Drug Delivery Experiment.

A) Selected locations loaded to the "Command Sequence" GUI. The left column shows the list of coordinates, and the right column shows the list of commands in the form of TTL signals for each location. **B)** Screenshots during the drug application experiment corresponding to the three selected locations. Unit 1 was the KCl-containing pipette and Unit 2 was the patching pipette. KCl solution was mixed with red fluorescent dye for the purpose of visualization. Images were obtained by combining DIC and fluorescence imaging. **C)** Step current injections showing a regular spiking neuron. D: Voltage-clamp recording traces from the local application of 500 mM KCl solution at three locations. The red trace with inward current was recorded from the trial when KCl application was close to the patched cell. The red arrow indicates the timing of KCl application.

Discussion

Here, we describe a method for automatic image-guided patch clamp recordings *in vitro*. The key steps in this process are summarized as follows. First, computer vision is used to automatically recognize the pipette tip using a series of images acquired via a microscope. This information is then used to calculate the coordinate transformation function between the microscope and the manipulator coordinate systems. Computer vision is used to automatically detect fluorescently labeled cells and to identify their coordinates. These steps are integrated with pipette targeting and the automatic patching algorithm using the open-source Python programming language, PyQT, and OpenCV libraries.

Compared to existing *in vitro* patch clamp methods, this system makes significant improvements in the several areas. It minimizes human intervention. This system automates most of the steps in the patch clamp experiment, minimizing the requirement for human intervention. Some of the remaining manual steps, including switching between the low-/high-magnification microscope lenses, can be automated using additional motorized hardware.

The patch-clamp method improves throughput. Patch-clamp experiments using this system achieved higher success rates and shorter times for each trial, contributing to a significant increase in overall throughput. The computer vision algorithm for fluorescent cell detection and pipette tip detection is very robust, and the error rate was very low. The average error for pipette tip detection was 1.6 μm, and the false-positive rate for fluorescent cell detection was 4.9% ±2.25%. A detailed comparison between traditional manual patching and automatic patching has been made (Wu et al., 2016).

Detailed documentation of experiments is possible. Patch logs of each trial can be saved and analyzed *post hoc*. Such detailed documentation was not previously available for manual patching. This allows for the systematic analysis of patching experiments in unique experimental conditions, cell types, species, and slice preparations.

This method shows compatibility with standard *in vitro* patch clamp equipment. Our system, as demonstrated in this manuscript, is designed to augment existing *in vitro* patch clamp rigs, giving them the capacity to conduct automatic patching. Unlike the planar patch approach, this system is suitable for laboratories already conducting manual patch clamping to convert their equipment at minimal cost. At the same time, there is still the option to patch manually or semi-automatically using the same system.

Because of the adaptability of the system mentioned above, connecting the hardware and configuring the software is required by the experimenter when the system is set up for the first time. Problems may result from incorrect port assignment and inadequate driver libraries for the control of certain hardware. Please refer to steps 1.2 - 1.4 when troubleshooting.

Compared to the partial automation of existing systems, this system achieves the maximum level of automation in the conventional *in vitro* patch clamping of acute brain slices (and other *in vitro* preparations). This is true for all steps, from cell detection to pipette calibration to patching (Campagnola, Kratz, & Manis, 2014; Perin & Markram, 2013). The only bottleneck is the manual process of filling and changing the patch pipettes between trails. Recent developments in the reuse of patch pipettes can potentially solve this problem (Kolb et al., 2016). Besides the quality of slice preparation, the most common reason for unsuccessful trials originates from manipulator mechanical errors and the movement of the slice in the chamber. These limitations are beyond our control in the current system. Efforts are being made to implement close-loop, real-time detection and control of pipette movement to account for this problem.

For future development, we are interested in expanding the current fluorescent cell detection capabilities to general cell detection under DIC optics.

Disclosure

A non-provisional patent application "SYSTEMS AND METHODS FOR AUTOMATED IMAGE-GUIDED PATCH-CLAMP ELECTROPHYSIOLOGY IN VITRO," U.S. Serial No.: 15/353,719, was filed on November 16, 2016, Ref. No.: PRF 67270-02.

Acknowledgements

We are grateful for the financial support from the Whitehall Foundation. We would like to thank Samuel T. Kissinger for the valuable comments.

References

Brown, A. L., Johnson, B. E., & Goodman, M. B. (2008). Making patch-pipettes and sharp electrodes with a programmable puller. *J Vis Exp*(20). doi: 10.3791/939

Campagnola, L., Kratz, M. B., & Manis, P. B. (2014). ACQ4: an open-source software platform for data acquisition and analysis in neurophysiology research. *Front Neuroinform, 8*, 3. doi: 10.3389/fninf.2014.00003

Collins, M. D., & Gordon, S. E. (2013). Giant liposome preparation for imaging and patch-clamp electrophysiology. *J Vis Exp*(76). doi: 10.3791/50227

Desai, N. S., Siegel, J. J., Taylor, W., Chitwood, R. A., & Johnston, D. (2015). MATLAB-based automated patch-clamp system for awake behaving mice. *J Neurophysiol, 114*(2), 1331-1345. doi: 10.1152/jn.00025.2015

Fertig, N., Blick, R. H., & Behrends, J. C. (2002). Whole cell patch clamp recording performed on a planar glass chip. *Biophysical journal, 82*(6), 3056-3062.

Kodandaramaiah, S. B., Franzesi, G. T., Chow, B. Y., Boyden, E. S., & Forest, C. R. (2012). Automated whole-cell patch-clamp electrophysiology of neurons in vivo. *Nat Methods, 9*(6), 585-587. doi: 10.1038/nmeth.1993

Kodandaramaiah, S. B., Holst, G. L., Wickersham, I. R., Singer, A. C., Franzesi, G. T., McKinnon, M. L., . . . Boyden, E. S. (2016). Assembly and operation of the autopatcher for automated intracellular neural recording in vivo. *Nat. Protocols, 11*(4), 634-654. doi: 10.1038/nprot.2016.007 http://www.nature.com/nprot/journal/v11/n4/abs/nprot.2016.007.html#supplementary-information

Kolb, I., Stoy, W., Rousseau, E., Moody, O., Jenkins, A., & Forest, C. (2016). Cleaning patch-clamp pipettes for immediate reuse. *Scientific reports, 6*.

Perin, R., & Markram, H. (2013). A computer-assisted multi-electrode patch-clamp system. *J Vis Exp*(80), e50630. doi: 10.3791/50630

Sakmann, B., & Neher, E. (1984). Patch clamp techniques for studying ionic channels in excitable membranes. *Annu Rev Physiol, 46*, 455-472. doi: 10.1146/annurev.ph.46.030184.002323

Segev, A., Garcia-Oscos, F., & Kourrich, S. (2016). Whole-cell Patch-clamp Recordings in Brain Slices. *J Vis Exp*(112). doi: 10.3791/54024

Wu, Q., Kolb, I., Callahan, B. M., Su, Z., Stoy, W., Kodandaramaiah, S. B., . . . Chubykin, A. A. (2016). Integration of autopatching with automated pipette and cell detection in vitro. *J Neurophysiol, 116*(4), 1564-1578. doi: 10.1152/jn.00386.2016

PART II. APPLICATION OF CHANNELRHODOPSIN-ASSISTED CIRCUIT MAPPING (CRACM)

Functional local circuit mapping is useful in a variety of research areas. Change in circuit connectivity underlies learning and encoding memory. Understanding how the circuit undergo plasticity in healthy conditions and in intellectual disability will shed light upon the mechanism of learning impairment in these conditions. On the other hand, brain injury disrupts circuits which leads to functional impairment. Circuit repair is the basis of functional recovery and should be an important test in developing new brain repair therapy. In this part, I will discuss the application of an optogenetics-enabled functional circuit mapping method in the above-mentioned research questions.

CHAPTER 3: CIRCUIT PLASTICITY DURING VISUAL EXPERIENCE AND THE IMPAIRMENT IN FRAGILE X SYNDROM

Abstract

Fragile X Syndrome (FXS) is the leading genetic cause of learning disability and has a high co-morbidity with Autism Spectrum Disorder (ASD). It has been reported that FXS patients have visual perceptual abnormalities, but no study has been conducted to specifically test visual learning in FXS. Given that abnormal intrinsic cell excitability, synaptic plasticity, and circuit connectivity were observed in FXS mouse models, we hypothesize that visual experience-induced circuit plasticity in FXS differ from their neurotypical counterparts. To test this hypothesis, we have established a visual training paradigm followed by *ex vivo* Channelrhodopsin Assisted Circuit Mapping (CRACM), which combines whole-cell patch-clamp and optogenetic stimulation to measure synaptic strength. Littermate-controlled wild-type (WT) and FXS mice with a Thy1-ChR2 background were either subjected to 200 trials of sinusoidal-grating visual stimuli for 4 days or remained naïve to this visual stimulus. We measured the circuit connectivity strength specifically in L5 to L4, and in L5 recurrent connections. There was a prominent increase in circuit connectivity from L5 to L4 fast-spiking neurons in WT, but not in FXS mice. On the contrary, connections from L5 to L5 regular spiking neurons were significantly weakened in FXS mice, but remained stable in WT. This result is a direct demonstration of the circuit plasticity mechanisms underlying visual learning. As hypothesized, these connectivity changes were altered in FXS mice. These alterations in circuit plasticity may explain the finding of impaired visual learning in FXS.

Introduction

There are an estimated 1.5 million children diagnosed with Autism Spectrum Disorders (ASDs) in the US (1 in every 40 US children), according to a survey by the Centers for Disease and Prevention (CDC) in 2018 (Kogan et al., 2018). ASDs are related to both genetics and environmental factors, but for most cases the exact cause and detailed pathological mechanisms are unclear (Robinson et al., 2016). It is most likely that multiple genetic variations along with some high-risk environmental factors contribute to convergent manifestations of similar

symptoms, including social disability, learning impairment, atypical language development, etc. Since the cause of ASD is extremely complex, it may be more feasible to find the common functional neural pathophysiological changes in ASDs to help guide the development of effective ASDs therapy. Diseases with known genetic causes and high co-morbidity with ASDs, namely fragile X syndrome and tuberous sclerosis, may shed light on the link between ASD common pathology and genetics.

Fragile X syndrome (FXS) is one of the most actively researched targets in the ASD field, due to its known genetic cause. FXS is the most common inherited form of intellectual disability. In healthy individuals, the *FMR1* gene on the X chromosome has a section of CGG repeats in the 5' untranslated region, which can be of varying length but not exceeding 55 repeats. Abnormal extension of this CGG cluster promotes gene methylation (Verkerk et al., 1991) and subsequently disrupts fragile X mental retardation protein (FMRP) expression (Penagarikano, Mulle, & Warren, 2007). Patients are clinically diagnosed with FXS if the length of this trinucleotide motif extends to over 200 repeats. Their FMRP expression is nearly completely abolished by gene methylation (Mila, Alvarez-Mora, Madrigal, & Rodriguez-Revenga, 2018).

FXS animal models have been generated in multiple animal species, including drosophila (McBride, Bell, & Jongens, 2012), zebra fish (Tucker, Richards, & Lardelli, 2004), rat (Hamilton et al., 2014), and mouse. The most commonly studied mouse model of FXS is the *FMR1* gene knockout (*Fmr1-KO*) mouse ("Fmr1 knockout mice: a model to study fragile X mental retardation. The Dutch-Belgian Fragile X Consortium," 1994). *Fmr1-KO* mice recapitulate the pathology of FXS, which is the lack of FMRP expression, as well as many aspects of human FXS symptoms. This mouse strain has been carefully characterized on a variety of physiological and psychological traits including macroorchidism, audiogenic seizure vulnerability, stimuli hypersensitivity, attention, hyperactivity, repetitive behaviors, anxiety, sociability, social communication, and cognitive deficits (Kazdoba, Leach, Silverman, & Crawley, 2014). Although some high-level cognitive functions and social behaviors cannot be directly assessed in this mouse model, it is generally accepted that *Fmr1-KO* mice are useful tools for studying the basic neurophysiology of FXS.

FMRP is an RNA binding protein and translational repressor. Apart from its functions in other parts of the body, FMRP has been known to be a master regulator of synaptic plasticity-related protein expression in the central nervous system (Darnell & Klann, 2013). Lack of FMRP

is hypothesized to release the suppression of LTD-related protein synthesis, leading to an excessive amount of such proteins at the synapses. Metabotropic glutamate receptor (mGluR) signaling is abnormal in this FXS mouse model (Waung & Huber, 2009) and is thought to be a major downstream effect of FMRP signaling that can serve as a drug target to treat FXS. In fact, mGluR targeted therapy showed promising preclinical efficacy in animals (Hagerman, Lauterborn, Au, & Berry-Kravis, 2012). However, numerous attempts to alleviate FXS symptoms in human patients using mGluR-targeted drug treatment failed in clinical trials (Erickson et al., 2017), implying that abnormal mGluR signaling may not be the only clinically significant problem.

Besides intellectual deficits, impairment in visual perception and learning have also been found in FXS. Studies using visual tasks to assess infant and adult human individuals with FXS suggest that the presence of neural dysfunction in the visual system is associated with the loss of FMRP expression (Farzin, Rivera, & Whitney, 2011; Farzin, Whitney, Hagerman, & Rivera, 2008; Freund & Reiss, 1991; Gallego, Burris, & Rivera, 2014). Recent two-photon calcium imaging studies have also revealed decreased activity of PV+ interneurons in V1 of adult FXS mice, as well as over-synchronized neural activity in the developing somatosensory cortex of young FXS mice (Goel et al., 2018; Goncalves, Anstey, Golshani, & Portera-Cailliau, 2013).

It is generally believed that abnormal neurophysiological changes are the direct cause of the major symptoms of FXS that are related to brain function. Mounting evidence shows that there is altered long-term plasticity in FXS mouse models, including exaggerated LTD and protein-synthesis independent LTD (Nosyreva & Huber, 2006), reduced level of LTP (Shang et al., 2009; Yun & Trommer, 2011), and an elevated threshold for spike-timing-dependent potentiation (STDP) (Huber, Gallagher, Warren, & Bear, 2002; Yun & Trommer, 2011). Altered regulation of LTD-related proteins, due to the lack of FMRP in FXS, may be the reason for the impairment of long-term plasticity (Darnell & Klann, 2013). It has also been shown that there is an abnormal expression level and regulation of ion channels in FXS (Darnell & Klann, 2013), leading to increased intrinsic neuronal excitability (Myrick et al., 2015). Additionally, studies in postmortem patient samples and in mouse models have revealed abnormal dendritic spine morphology and a higher density of dendritic spines, most of which are immature, in cortical neurons (Patel, Loerwald, Huber, & Gibson, 2014). This leads to a prediction that there may be

hyper-connectivity within the sensory cortices of FXS. At the same time, the circuit may undergo abnormal plasticity during experience, which could explain the learning impairment in FXS.

Circuit connectivity and plasticity are intertwined. Similar to FXS, impaired circuit connectivity and plasticity have been observed in Rett syndrome (Dani et al., 2005; Dani & Nelson, 2009). At the systems level, it is known that circuit hypersensitivity is common in FXS, matching the clinical symptoms of increased seizure tendency and sensory startle reflex (Chuang et al., 2005; Gibson, Bartley, Hays, & Huber, 2008). An electroencephalogram EEG study in human patients suggested that connectivity between brain areas is disrupted, which may be a consequence of excitation/inhibition imbalance (van der Molen, Stam, & van der Molen, 2014; Van der Molen & Van der Molen, 2013). We hypothesize that prolonged persistent activity (a result of aberrant circuitry) interfering with sensory input, along with changes in synaptic plasticity, may contribute to the learning deficits in FXS patients. To test this theory, we need to understand the functional local circuit connectivity and plasticity induced by sensory experience in FXS.

However, it is not understood how perceptual learning impacts changes in synaptic plasticity among excitatory and inhibitory cell types across different cortical layers. As illustrated in **Fig. 14**, most studies regarding the neurophysiology of FXS have concentrated at the synaptic or systems level, leaving out the intermediate local circuitry. Indeed, there is little knowledge about functional circuit alterations, not only in FXS, but also in other neuropsychiatric diseases. This is partially due to the technical difficulty in obtaining high-quality measurements of a cohort of neurons within a local circuit. The recent development of two-photon calcium imaging has provided valuable neuronal ensemble activation data with relative high throughput (Mank et al., 2008). However, two-photon imaging cannot provide information about the strength of synaptic connections and the intrinsic properties of individual neurons in a circuit. To map local circuit connectivity as well as the synaptic changes, we still rely on simultaneous multi-cell patch-clamp electrophysiology. This method is very time consuming, low throughput, highly technical, and has a limit to the number of cells (number of potential connections) that can be patched at the same time (Wang et al., 2015).

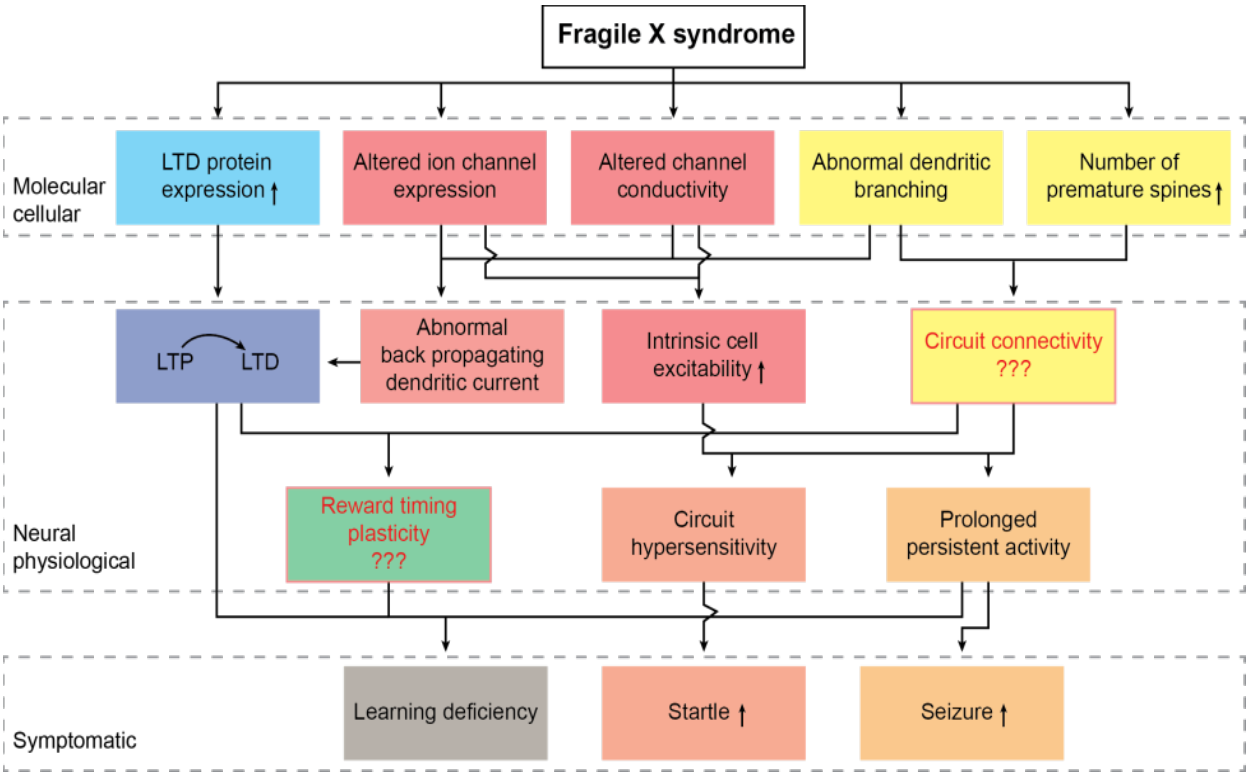

Figure 17. Current knowledge about Fragile X syndrome from basic science to clinical symptoms.

Advances in optogenetics have offered new ways to directly and systematically measure local-circuit connectivity from specific synapses. To conduct Channelrhodopsin Assisted Circuit Mapping, or CRACM (Petreanu, Huber, Sobczyk, & Svoboda, 2007), we stimulated presynaptic axonal terminals expressing ChR2 with scanning LEDs and recorded synaptic currents from individual post-synaptic cells through whole-cell patch clamp electrophysiology (for details see methods section in this chapter). With this technology, we measured the strength of local feedback projections originating from L5 pyramidal neurons and compared between wild-type and *Fmr1-KO* mice, and between naïve and visually trained animals. From analyses of these data, we tested our hypothesis that experience-dependent circuit plasticity is impaired in FXS.

Materials and methods

Animals

All animal procedures in this study were approved by Purdue Animal Care and Use Committee (PACUC, protocol number 1408001112), and followed guidance issues by the National Institutes of Health. We used mice for visual experience-dependent circuit plasticity studies because mouse visual acuity is well studied (Prusky & Douglas, 2003; Wong & Brown, 2006), and there are well established visual experience training paradigms in our laboratory (Samuel T. Kissinger, Alexandr Pak, Yu Tang, Sotiris C. Masmanidis, & Alexander A. Chubykin, 2018) and from other studies (Cooke & Bear, 2010).

Adult B6.129P2-*Fmr1*tm1Cgr/J (*Fmr1-KO*, JAX Stock No. 003025), B6.Cg-Tg (Thy1-COP4/EYFP)18Gfng/J (Thy1-ChR2-YFP, JAX Stock No. 007612), and wild type (WT) C57/BL6 mice (all strains obtained from JAX) were used as breeders. 40 male mice aged between P35 to P39 were used in the main study. Among which, there were 20 vs. 20 littermate-controlled WT and *Fmr1-KO* respectively, in the background of heterozygous Thy1-ChR2-YFP were used. An additional 7 mice were used in measurement control. These mice were generated from breeding homozygous Thy1-ChR2-YFP female with *Fmr1-KO* male. Mice were group housed (up to 5 mice per cage) on 12h/12h light/dark cycle with water and standard rodent chow *ad libitum*.

Head-fixation

To ensure consistent viewing of the visual stimuli, a custom head-post was fixed to each mouse for head-fixation during visual training. Dead-posts were installed through a short stereotaxic surgery. All non-disposable tools were heat-sterilized.

Deep anesthesia was induced by isoflurane inhalation, initially at 5% (carried by room air) then reduced to 1.5 to 2% when the mouse stops responding to toe pinch. Flow rate was adjusted to mouse weight and responses to anesthesia. The mouse was then fixed into the stereotaxic frame. Moisturizing eye ointment (Puralube® Vet Ointment) was applied to both eyes to protect them during the surgery. Skin above the skull was disinfected and removed with a pair of scissors. The exposed skull was further disinfected with 3% H_2O_2, cleaned and dried. Then, the skull surface was lightly scored with crossing scratches to increase surface area. To prepare a

head-post, the pointy end of a flat bottom nail was cut off. The head-post was glued to the skull about 1-2mm posterior to bregma with acrylic glue (generic super glue). After the glue settles, a strong protective skull was built with dental cement (C&B Matabond) to cover all the exposed skull. Mouse was released from the stereotaxic frame and allowed to recover from anesthesia. An additional day was allowed for recovery before training.

During habituation and training, mice were head-fixed by fixing the head-post that is attached to their skull. Their body rested in a tube large enough for body movement to some degree. If the head-post detaches during any stage of the experiment, the animal would be excluded from the study and humanely euthanized.

Visual stimulation

Visual stimulus was presented on a monitor in front of the head-fixed mouse. Open source python-based psychology software (PsychoPy) was used to generate and present visual stimuli. Control gray screen was created using the color space "gray". The mean luminance of the monitor was 73 cd/m^2. After a day of recovery, mice began habituation to the head-fixation apparatus. During habituation, mice viewed a control gray screen for 90mins per day. The visual stimuli used in visual training are 0.2s long sinusoidal drifting gratings at spatial frequency (SF) of 0.03 cycles per degree of visual angle and temporal frequency (Katzel, Zemelman, Buetfering, Wolfel, & Miesenbock) of 3 Hz, drifting at speed of 100 deg/s, oriented at an angle of 150 degrees. Gray screen was presented for 0.5 s before stimulus onset and the inter-trial interval was 8 s. Mice were head-fixed and presented the same stimulus 200 times in 30 mins each day for 4 days.

***Ex vivo* acute cortical slice preparation**

Animals were euthanized the next day after the last visual training (or age match date for control group), at which point they were between P35 and P39. A cocktail of ketamine (100mg/kg body weight) and xylazine (16mg/kg body weight) was intraperitoneally (IP) injected to anesthetize the animal. Then, the animal was trans-cardially perfused with chilled high-sucrose dissection buffer (HSDB) containing (in mM) 75 sucrose, 10 glucose, 87 NaCl, 2.5 KCl, 1.25 NaH2PO4, 25 NaHCO3, 0.5 CaCl2, 7 MgCl2, and 1.3 ascorbic acid. The brain was quickly

removed from the skull, the cortices were cut into blocks and super-glued onto the vibratome (Leica VT1000) stage. Coronal brain slices were cut at 300μm thickness in ice-cold HSDB and then transferred into a holding chamber in 32°C artificial cerebral-spinal fluid (ACSF) containing (in mM): 124 NaCl, 3.5 KCl, 1 CaCl2, 0.8 MgCl2, 1.23 NaH2PO4, 26 NaHCO3, and 10 glucose. Brain slices were initially incubated at 32°C for 30min then at room temperature (about 25°C) for 1h or until used for recording. Brain slices were kept for up to 7h after slicing. All HSDB and ACSF used in the above described procedures were aerated with a gas mixture containing 95% oxygen and 5% carbon dioxide to maintain the pH at around 7.4 and oxygen saturation.

Whole-cell patch clamp recording

Whole-cell patch-clamp recording electrodes were pulled from filamented borosilicate glass capillaries (BF150-86-10, Sutter Instruments) using a micropipette puller (P-97, Sutter Instruments) to a resistance of 3.5-7.9 MΩ. The glass electrodes were filled with an internal solution containing (in mM): 20 KCl, 100 K-gluconate, 10 HEPES, 4 MgATP, 0.3 Na2GTP, 7 phosphocreatine, and 0.2% biocytin with pH adjusted to 7.4 and osmolarity adjusted to 300 mOsm. In some experiments, a small amount of 4% w/v Alexa Fluor 594 (A-10438, ThermoFisher Scientific) dissolved in internal solution was back-loaded into the glass electrode to label the patched cell. The dye loading method was described in previous literature (Wu et al., 2016). The whole-cell patching procedure was conducted using the image-guided automatic *in vitro* patching system (Autopatcher IG) described in the first chapter (Wu & Chubykin, 2017; Wu et al., 2016). The patch clamp recording signal was amplified (Multiclamp 700B) and digitized at 20 kHz sampling rate (Digidata 1550A, Molecular Devices) before being saved to the computer. All raw traces were low-pass filtered at 10 kHz before further analysis.

Channelrhodopsin-assisted Circuit Mapping (CRACM)

CRACM is a technology combining optogenetics and patch-clamp electrophysiology to measure functional connectivity. In this study, we used CRACM in *ex vivo* acute brain slices from transgenic mice that has targeted Channelrhodopsin expression in layer 5 cortical neurons to measure local micro-circuitry originated from layer 5. CRACM was conducted in acute *ex vivo* visual cortical slices on a patch-clamp electrophysiology rig. Light stimulation was

generated by a high-power LED (470 nm, 50 W, Mightex). The stimulation pattern was generated by an LED patterned illuminator (Polygon 400, Mightex) and projected onto the brain slice via a 10x objective lens. The total area scanned for each map is 0.67 mm by 0.67 mm, which is divided into 10x10 grid. Each stimulus (one pixel) is 10 ms in length, with a 2 s inter-stimulus interval. The stimulation sequence was a pre-defined pseudo-random sequence, which avoids surrounding inhibition from scanning in sequence. All CRACM recordings were conducted under voltage-clamp mode with a -70 mV holding potential. LED stimulation patterns were designed and controlled with the manufacture's software. Stimulation and recording were synchronized by the patch-clamp digitizer.

Histology and Imaging

In some experiments, the recorded cells were traced with fluorescent dye to reveal the neuronal processes. After these experiments, the acute brain slices from *ex vivo* patch clamp recordings were fixed in 4% paraformaldehyde (PFA) for 30min to 1h, washed with phosphate buffered saline (PBS), then mounted onto microscopic slides. Images were obtained with confocal microscopy (Zeiss 710). Structural reconstruction were made using FIJI (ImageJ) extensions.

Results

To directly measure the V1 microcircuit and changes in its plasticity resulting from perceptual training, we conducted Channelrhodopsin-Assisted Circuit Mapping (CRACM) on brain slice preparations (Hooks et al., 2013; Petreanu et al., 2007). We measured the feedback and recurrently connectivity of V1 L4 and L5 neurons receiving projections from L5 excitatory neurons in naïve and visually trained animals. Any differences between the naïve and trained groups are presumed to reflect the circuit plasticity resulting from visual experience. We tested this in littermate matched *Fmr1-KO* and WT male mice. *Fmr1-KO* mice are referred to as FX mice from here on. First, we validated that the ChR2 expression levels are not affected by the FX genotype. There was no significant difference in evoked action potential frequency at a series of light intensity steps between WT and FX age-matched litter-mates (**Fig. 15**).

To study the effect of the FX genotype on visual experience-induced circuit plasticity, WT and FX littermates with Thy1-ChR2-YFP background were pseudo-randomly assigned to either naïve or trained groups and the experimenter was blinded to the genotype during data collection. The trained group was subjected to habituation and visual training as described in the methods. Acute brain slices were made for CRACM on the day after the end of visual training.

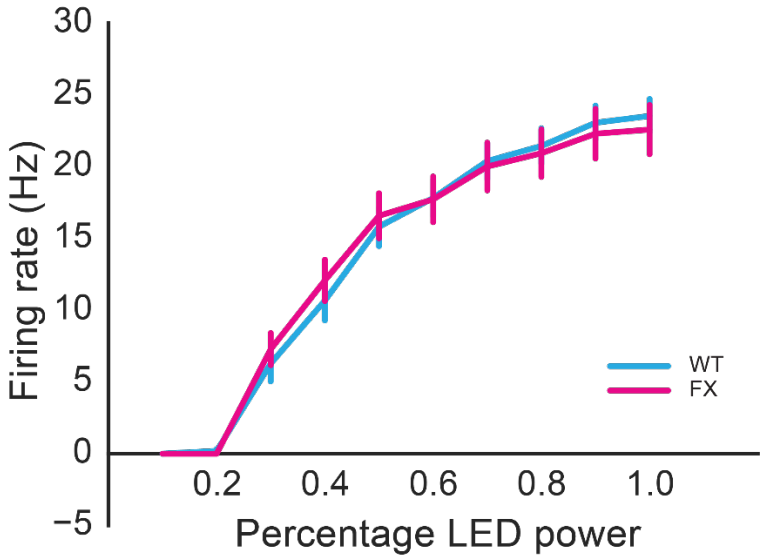

Figure 18. Optogenetic input-output curve for ex vivo circuit mapping.

ChR2-YFP positive L5 neurons in V1 were held under current clamp while full-field LED illumination was applied to measure the action potential frequency. N = 3 animals/21 neurons for WT and 4 animals/28 neurons for FX. Data reported in the curve are mean ± standard error of mean.

Decreased synaptic plasticity of connections from L5 to L4 FS interneurons following visual experience in FX mice

We performed whole-cell patch clamp recordings of L4 neurons in V1 on acute brain slices from 4 groups of animals: WT naïve, FX naïve, WT trained, and FX trained (**Fig 16*A***). To measure local L5 to L4 synaptic strength, we optically stimulated individual cells in a 10 by 10 grid (0.67mm by 0.67mm) covering a square area from L2/3 to L5 of V1 using an LED patterned illuminator (Polygon 400, Mightex) (**Fig 16*B***). For each 10ms light pulse at each pixel, excitatory post-synaptic currents (EPSCs) were recorded under voltage clamp at -70mV. All CRACM recordings were conducted with the presence of 10μM tetrodotoxin (TTX) and 50μM

4-Aminopyridine (4-AP) to block action potentials and thus block multi-synaptic responses to the stimulation. Based on the current-voltage curve measured from step-current injections, there is a bimodal distribution of low and high cell impedance, corresponding to regular-spiking (RS) excitatory neurons and fast-spiking (FS) interneurons, respectively (Van der Molen et al.) (**Fig 17**). For a subpopulation of recorded cells, evoked action potentials were recorded before applying TTX/4-AP. In some recordings, fluorescent dye (Alexa Fluor 568 Hydrazide) was added to the pipette internal solution to allow for the subsequent reconstruction of cell morphology. There were consistent and expected correlations between impedance and action potential waveform, cell body morphology under DIC optics, and whole cell morphology following reconstruction that corresponds to cell types (**Fig 18 *A-E, I-M***). We found that there was no significant difference in impedance among RS cells (**Fig 17*C***) and among FS cells (**Fig 17*E***) between the WT and FX groups. Training had no effect on cell impedance, as expected (**Fig 17*F***).

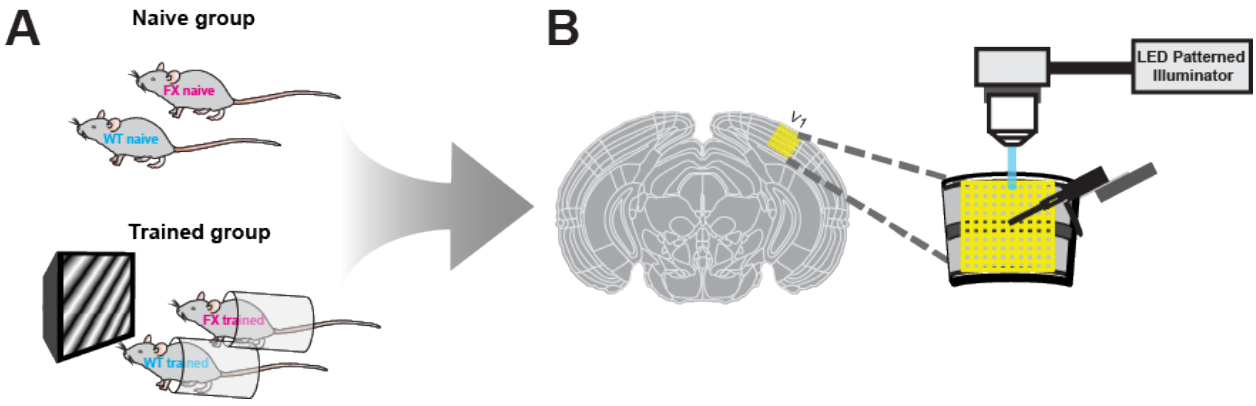

Figure 19. Visual training and CRACM experimental setups.

A) Experimental groups. **B)** Acute visual cortical slices CRACM setup.

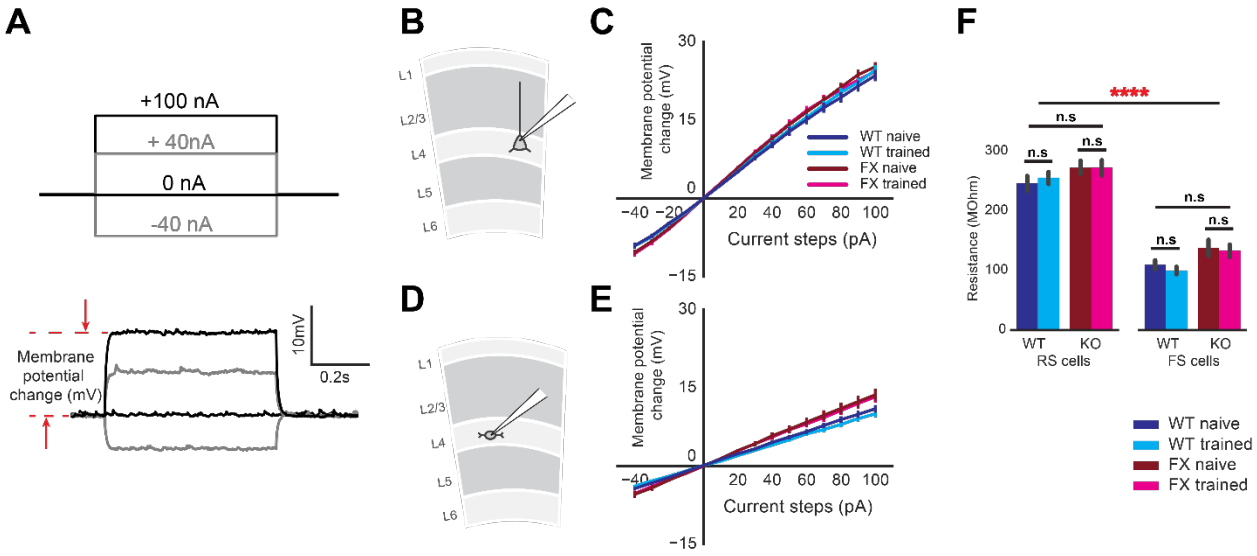

Figure 20. Characterizing layer 4 patched cell types

A) Step current injection illustration and representative current-clamp traces from a layer 4 fast-spiking (FS) interneuron. **B)** Layer 4 (L4) regular spiking (RS) neuron illustration. **C)** Averaged current-voltage curve from L4 RS neurons showing the membrane potential change (demonstrated in A) at each current injection step. **D)** L4 FS interneuron illustration. **E)** Averaged current-voltage curve from L4 FS interneurons showing the membrane potential change (demonstrated in A) at each current injection step. **F)** Mean input resistance for each group. Data reported in bar graphs are mean ± standard error of mean. Statistical significance on means were reported from three-way ANOVA followed by Tukey's HSD tests.

We then compared the distributions of excitatory post synaptic current (EPSC) amplitudes in the naïve and trained groups, separated by cell types. There was no significant difference in EPSCs of RS neurons between the WT and FX groups without visual training (**Fig 18*F***) or with visual training (**Fig 18*G***, Kolmogorov-Smirnov test: WT naïve vs. FX naïve D = 0.0381 p=0.0117; WT trained vs. FX trained D = 0.0365 p=0.01593. Significance threshold p<0.005). For RS neurons, there was also no significant difference between the naïve and trained groups in both WT and FX mice (**Fig 19** (top row), Kolmogorov-Smirnov test, WT naïve vs. WT trained D = 0.0404 p=0.0096; FX naïve vs. FX trained D = 0.0753 p= 0.0287). In other words, the projection strength from L5 to L4 RS cells was stable following visual training of both WT and FX mice. The distribution of synaptic weights is known to follow a logarithmic normal distribution (Buzsaki & Mizuseki, 2014; Song, Sjöström, Reigl, Nelson, & Chklovskii, 2005). Therefore, we conducted a natural-log transformation of the absolute value of all EPSC amplitudes and tested that they were normally distributed (see methods for details). Training had no significant effect on the mean of the log value of the EPSCs among the 4 groups while genotype had a significant effect (**Fig 18*H***, 2-way ANOVA, p=0.037 for genotype, p=0.0788 for training, and p=0.00197 for the cross interaction. Tukey's post hoc: WT naïve vs. FX naïve: p=0.0103; WT trained vs. FX trained: p=0.9981; WT naïve vs. WT trained: p=0.9801; FX naïve vs. FX trained: p=0.0127). The post-hoc Tukey test showed a significant difference in naïve animals between WT and FX, but not in trained groups. Training had a significant impact only in the FX group but not in the WT group. Despite the finding of statistical significance, the magnitude of the difference between these groups was very small.

Contrary to the marginal connectivity change in L4 RS cells receiving L5 input, L4 FS cells receiving L5 input exhibited significant potentiation after visual training in both genotypes (**Fig 19**, WT naïve vs. WT trained D = 0.2213 p=1.280e-34; FX naïve vs. FX trained D = 0.1309 p=2.807e-6. Significance threshold p<0.005). Although the direction of plasticity after visual training was the same in both genotypes, the magnitude of circuit potentiation was much smaller in FX comparing to in WT. This resulted in the larger difference between WT and FX in trained animals than in naïve animals (**Fig 18*N&O***, Kolmogorov-Smirnov test: WT naïve vs. FX naïve D = 0.0788 p=0.0005; WT trained vs. FX trained D = 0.1886 p=7.7582e-14. Significance threshold p<0.005). The mean of $\log_e$ transformed EPSC amplitudes in L4 FS cells receiving L5 projections was significantly different across genotype and training conditions: there was a large increase of EPSC amplitudes in WT with training (**Fig 18*P***, 2-way ANOVA, p=6.344e-12 for

genotype, p=1.256e-26 for training, and p=4.801e-8 for cross interaction. Tukey's post hoc: WT naïve vs. FX naïve: p=0.2376; WT trained vs. FX trained: p<0.0001; WT naïve vs. WT trained: p<0.0001; FX naïve vs. FX trained: p=0.0207). Although this increase was much less prominent in FX, both genotypes reached significance.

Figure 21. Visual experience induced cell-type specific circuit connectivity changes from L5 to L4 in V1 of WT and FX mice.

A) Illustration of L5 to L4 regular spiking neurons projections. **B & J)** Example confocal image of mapped neurons (magenta) filled with fluorescent dye (scale bar = 100μm). The green color indicates ChR2-YFP positive neurons and processes. **C & K)** Traced neuron from D & L showing the morphology of specific neuronal types. **D & L)** Step current injection traces showing action potentials corresponding to the neurons shown in D & L. **E & M)** Step current injection traces with application of TTX/4AP mix corresponding to the neurons shown in D & L. **F & G)** Cumulative density curves showing the distribution of light-induced EPSC amplitudes from L4 regular spiking neurons receiving L5 projections in naïve and trained WT and FX animals. The insert shows the average CRACM maps for each corresponding group. **H)** Bar graphs showing the mean of log-transformed EPSC amplitudes for each group ± standard error of mean. Significance is reported from two-way ANOVA followed by Tukey's HSD test for comparing mean log transformed EPSCs. **I)** L5 to L4 fast spiking neurons projection illustration. **N & O)** Cumulative density curves showing the distribution of light-induced EPSC amplitudes from L4 fast spiking neurons receiving L5 projections in naïve and trained WT and FX animals. Inserts show the average CRACM maps for each corresponding group**.**
(**P**) Bar graphs showing the mean of natural log-transformed EPSC amplitudes for each group ± standard error of the mean. Significance is reported from Kolmogorov–Smirnov tests for EPSC distributions and two-way ANOVA followed by Tukey's HSD tests to compare mean log transformed EPSCs.

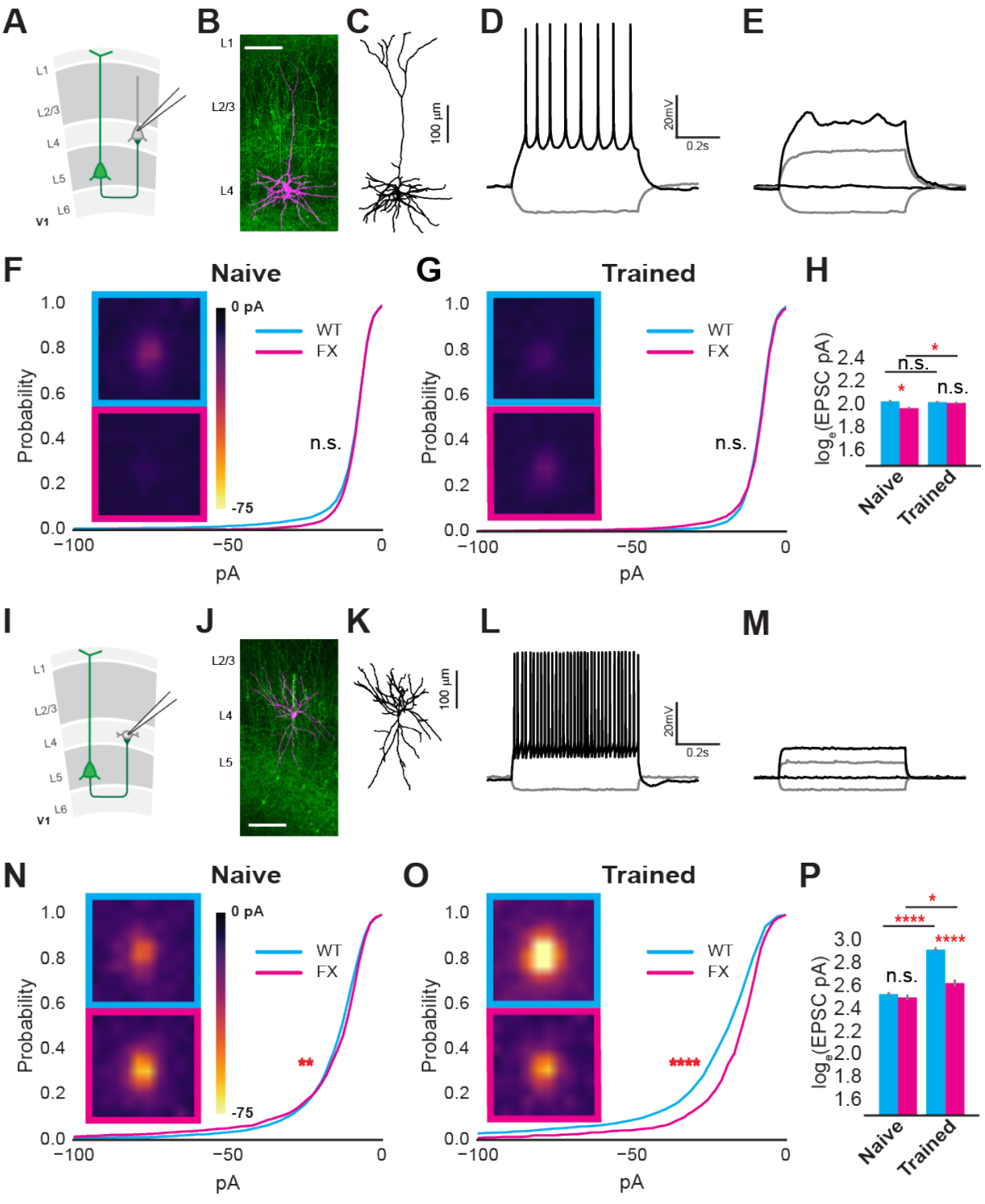
A
B
C
D
E
L1
L2/3
L4
L5
L6
V1
100 µm
20mV
0.2s
F
Naive
G
Trained
H
0 pA
-75
WT
FX
n.s.
Probability
pA
log$_e$(EPSC pA)
Naive
Trained
I
J
K
L
M
N
Naive
O
Trained
P
**
****

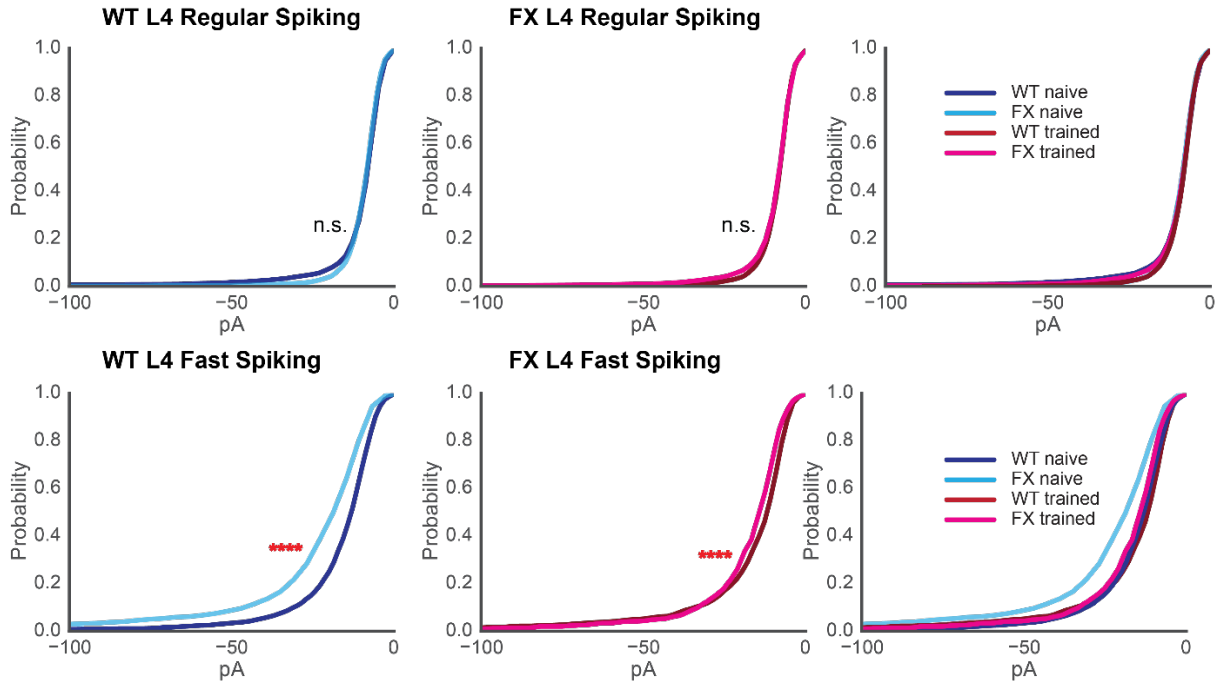

Figure 22. Cumulative density curves from EPSCs amplitude of L4 cells

Synaptic connectivity in L5-L5 regular spiking and intrinsically bursting cells

We next conducted CRACM measurements on L5 to L5 local connectivity in WT and FX mice, either with or without visual training. Putative FS interneurons (identified as described above) were discarded from the analysis due to low cell counts (0 to 2 cells per group). The remaining putative L5 excitatory neurons were divided into intrinsically bursting (IB) and regular-spiking (RS) neurons (**Fig 20*A-E*, *I-M***) based on input resistance, sag ratio, and the presence/absence of a compensatory current after a depolarizing current step (**Fig 21**). Consistent with the literature, L5 IB cells had lower input resistance and higher sag ratio, as well as a prominent compensatory current after depolarization compared to RS cells (Kasper, Larkman, Lubke, & Blakemore, 1994). Cell types determined by these three parameters were consistent in each of the patched cells and confirmed by cell morphology when available. Because IB cells and RS cells have distinctive projection targets (Kasper et al., 1994) and may contribute to familiarity-related oscillations in different ways, we analyzed the connectivity plasticity of these two groups of cells separately.

The projection from L5 to L5 RS cells was significantly larger in WT compared to FX naïve mice, but this relationship was inverted after visual training (**Fig 20*F&G*,** Kolmogorov-Smirnov test: WT naïve vs. FX naïve D = 0.1193 p=2.0902e-20; WT trained vs. FX trained D = 0.2192 p=2.2563e-70. Significance threshold p<0.005). This finding was caused by the small but significant depression in RS cells receiving L5 recurrent projections in the WT trained group compared to the naïve group, but this depression was greatly exaggerated in the FX group (**Fig 22**, Kolmogorov-Smirnov test, WT naïve vs. WT trained D= 0.0823 p=1.911e-9; FX naïve vs. FX trained D= 0.2192 p=2.256e-70). The same trend is true for the mean of the natural log EPSC amplitudes (**Fig 20*H***, 2-way ANOVA, p=0.7979 for genotype, p<0.0001 for training, and p<0.0001 for cross interaction; Tukey test p<0.0001 for all compares). Conversely, L5 IB cells receiving L5 recurrent projections in both WT and FX had similar connection strengths (**Fig 20*N***, Kolmogorov-Smirnov test, WT naïve vs. FX naïve D = 0.0397 p=0.1151) and exhibited potentiation following visual training in both genotypes (**Fig 22**, WT naïve vs. WT trained D = 0.15 p=3.989e-17, 71; FX naïve vs. FX trained D= 0.1883 p=2.735e-22. Significance threshold p<0.005). Although the increase in the mean $\log_e$ EPSC values was similar in WT and FX when comparing trained to naïve animals (**Figure 6*P***, 2-way ANOVA, p=0.651 for genotype, p<0.0001 for training, and p=0.230 for cross interaction; Tukey's post hoc: WT naïve vs. FX naïve: p=0.5693; WT trained vs. FX trained: p=0.9619; WT naïve vs. WT trained: p<0.0001; FX naïve vs. FX trained: p<0.0001), the distribution of the EPSCs in trained WT and FX mice was different (**Fig 21*O***, WT trained vs. FX trained D = 0.1571 p=3.9888e-17. Significance threshold p<0.005). In WT, there was an increase in EPSC number across all amplitudes in a relatively uniform fashion; this increase was dominated by the small EPSC amplitudes in FX animals. Overall, under the same visual training conditions, the L5 circuit shifted away from potentiation and toward depression in FX compared to WT mice. This observation is consistent with the previous reports of enhanced LTD and impaired LTP in FX mice (Huber et al., 2002; Lauterborn et al., 2007).

Figure 23. Visual experience induced cell-type specific local L5 circuit connectivity changes

A) Illustration of L5 to L5 regular spiking pyramidal neuron projections. **B & J)** Example confocal images of mapped neurons (magenta) filled with fluorescent dye (scale bar = 100µm). The green color indicates ChR2-YFP positive neurons and processes. **C & K)** Traced neuron from B & J showing the morphology of specific neuronal types corresponding to B & J. **D & I)** Step current injection traces showing action potentials corresponding to the neurons shown in B & J. **E & M)** Step current injection traces in the presence of TTX/4AP corresponding to the neurons shown in B & J. Arrow points to the absence/presence of compensatory potential after depolarizing current injection. **F & G)** Cumulative density curves showing the distribution of light-induced EPSC amplitudes from L5 regular spiking neurons receiving L5 local projections in naïve (semi-transparent) and trained (solid color) WT (cyan) and FX (magenta) animals. Inserts show the average CRACM maps for each corresponding group. **H)** Bar graphs showing the mean of log-transformed EPSC amplitude for each group ± standard error of the mean. Significance is reported from two-way ANOVA followed by Tukey's HSD test for comparing mean log transformed EPSCs. **N & O)** Cumulative density curve showing the distribution of light-induced EPSC amplitude from L5 intrinsically bursting neurons receiving L5 local projections in naïve (semi-transparent) and trained (solid color) WT (green) and fmr1 KO (orange) animals. Insert is the average CRACM map. **P)** Bar graph showing the mean of natural log-transformed EPSC amplitude for each group± standard error of mean. Significance reported from Kolmogorov–Smirnov test for EPSC distribution and two-way ANOVA followed by Tukey's HSD test for comparing mean log transformed EPSCs.

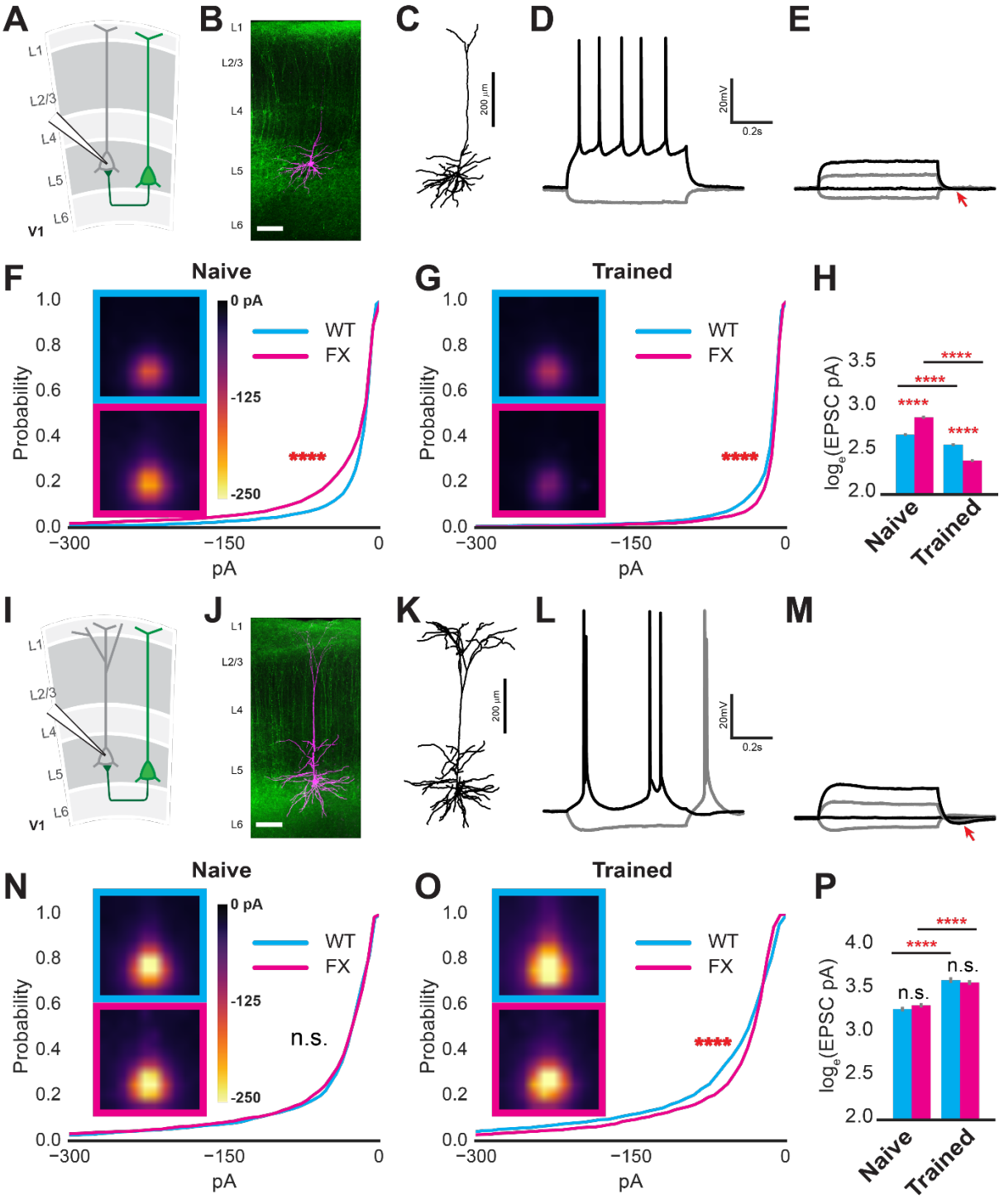
A
B
C
D
E
L1
L2/3
L4
L5
L6
V1
200 µm
20mV
0.2s
F
Naive
G
Trained
H
0 pA
-125
-250
WT
FX
Probability
pA
****
log$_e$(EPSC pA)
Naive
Trained
I
J
K
L
M
N
Naive
O
Trained
P
n.s.

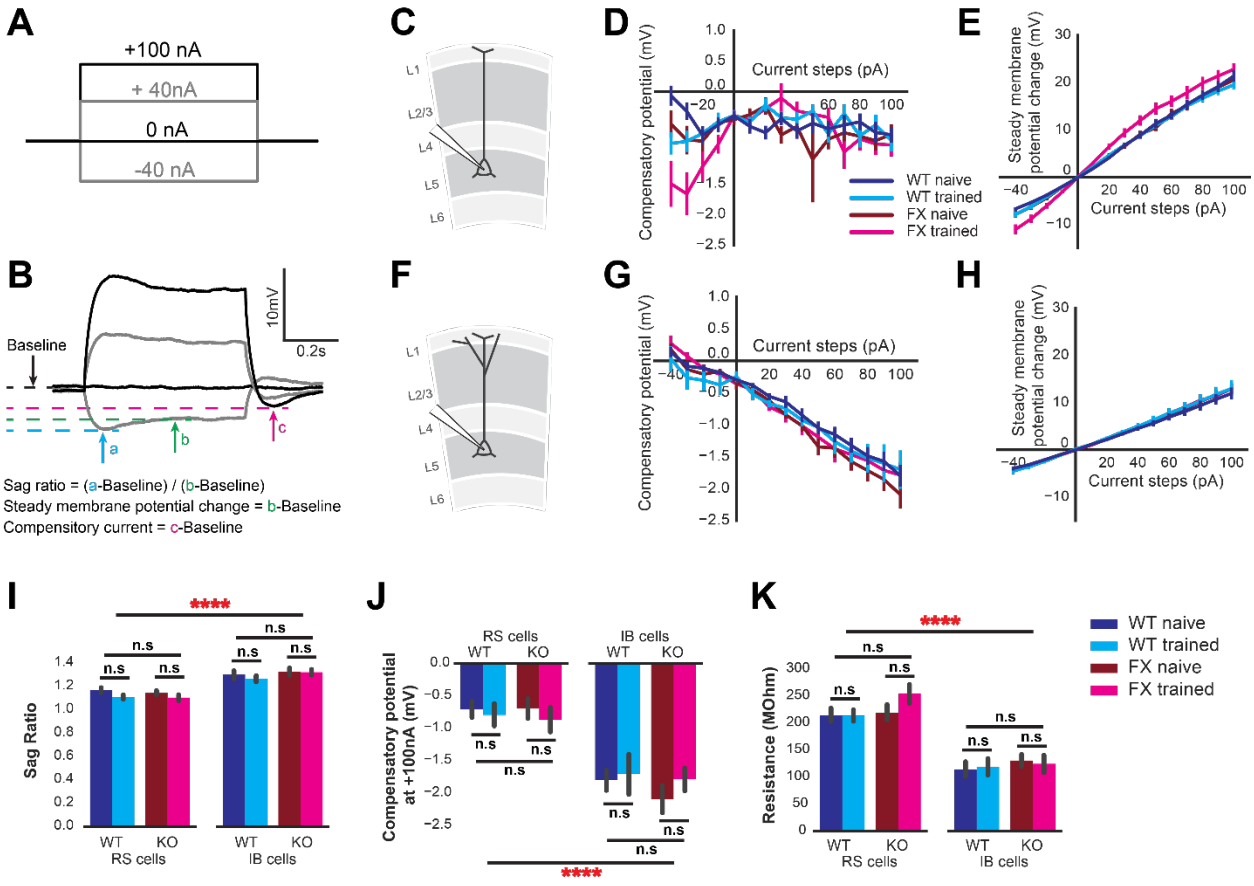

Figure 24. Characterizing layer 5 (L5) patched cell types.

A) Illustration of step current injections. **B)** Representative current-clamp traces from a layer 5 intrinsically-bursting (IB) neuron. **C)** Illustration of a L5 regular spiking (RS) neuron. **D)** Averaged compensatory current-voltage curve from L5 RS neurons showing the absence of rebound potential at the offset of step current injection. **E)** Averaged steady phase current-voltage curve from L5 RS neurons. The slop of the curves represents input resistance. **F)** Illustration of a L5 intrinsically bursting (IB) neuron. **G)** Averaged compensatory current-voltage curve from L5 IB neurons showing the presence of rebound potential at the offset of step current injection (demonstrated in B). **H)** Averaged steady phase current-voltage curve from L5 IB neurons. The slop of the curves represents input resistance. **I)** Mean sag ratio (defined in b) for each group. **J)** Mean hyperpolarizing compensatory potential at the offset of +100nA current injection for each group. **K)** Mean input resistance for each group. Data reported in bar graph are mean ± standard error of mean. Statistical test on means were three-way ANOVA followed by multiple comparison test using Tukey's honestly significant difference criterion.

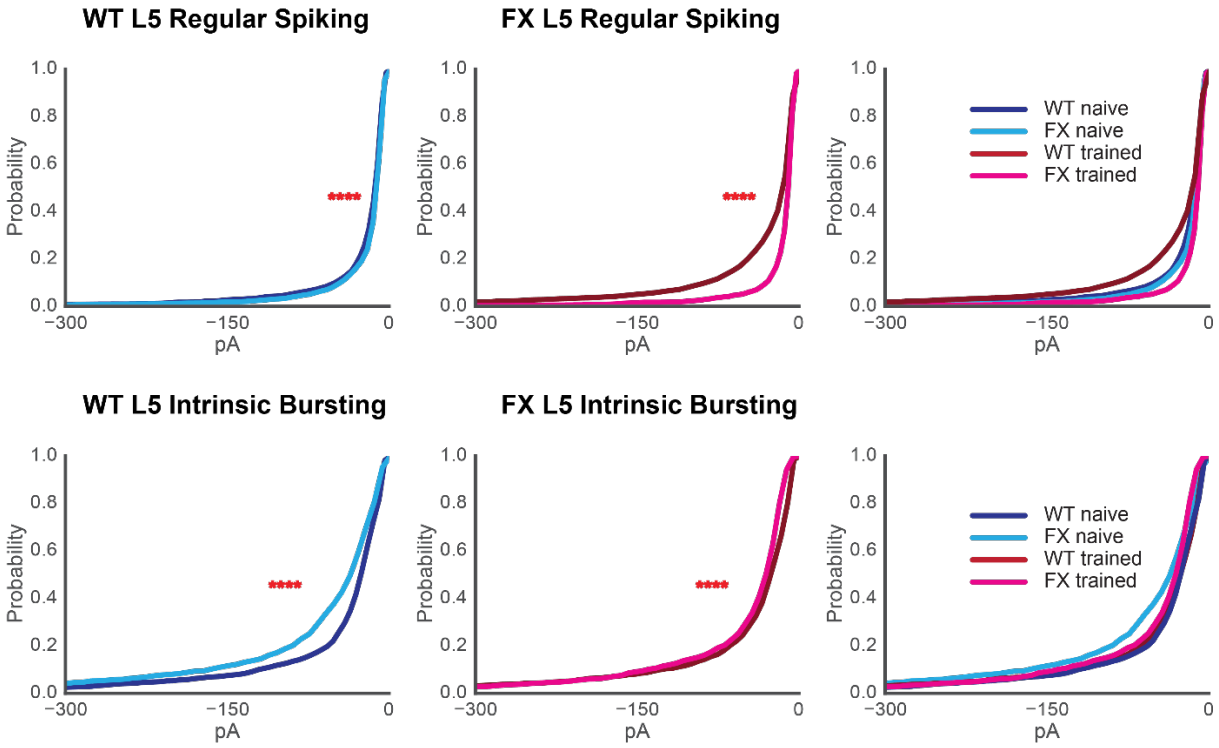

Figure 25. Cumulative density curves from EPSCs amplitude of L5 cells

Discussion

Here, we systematically measured multiple synaptic connections within the V1 microcircuit with and without perceptual training in WT and FXS mice. We observed a general shift towards depression (smaller magnitude of potentiation and/or larger magnitude of depression) in FXS compared to WT mice after perceptual training. This finding is consistent with previous observations of enhanced LTD and decreased LTP induced in FXS mice in brain slices (Lauterborn et al., 2007; Robic et al., 2015). This study is one of the first to directly show the effect of experience on specific synaptic strength in *ex vivo* acute brain slices. Studies using CRACM or laser-scanning glutamate uncaging to map local microcircuits have mainly focused on the spatial/laminal distribution of inputs (Hooks et al., 2011), as well as the synaptic-strength differences between different cell types (Yang, Carrasquillo, Hooks, Nerbonne, & Burkhalter, 2013). Moreover, the stable ChR2 expression level (**Fig 15**) under the Thy1-ChR2 transgenic background (as opposed to viral infection which is prone to variability) and strict age limit enabled us to compare synaptic strength between genotypes. With the help of Autopatcher IG to improve patching efficiency, we generated a respectable amount of data, from which we could categorize neurons based on their basic electrophysiological characteristics and gain insights on which specific projection was pertinent to visual experience.

We have identified a strengthening of the intra-cortical feedback connections from pyramidal cells in L5 onto FS inhibitory interneurons in L4 after perceptual training. FS inhibitory neurons in the visual cortex generally have broad tuning to visual stimuli, which means they are activated less selectively than RS excitatory neurons (Kerlin, Andermann, Berezovskii, & Reid, 2010). They send their inhibition to a cohort of neurons in the vicinity to control the "gain" of the circuit (Isaacson & Scanziani, 2011). Moreover, the FS inhibitory network is thought to contribute to intrinsic oscillatory activities of V1, particularly in the gamma frequency band (Chen et al., 2017). Human and primate electro-encephalogram (EEG) studies support the notion that gamma oscillations in cortical areas are generally related to learning (Miltner, Braun, Arnold, Witte, & Taub, 1999; Popescu, Popa, & Paré, 2009), and may indicate the acuity of change detection in the visual cortex (Womelsdorf, Fries, Mitra, & Desimone, 2006). The increase of feedback excitatory drive to L4 FS interneurons in WT mice may be associated with changes in visual processing because of visual training. We did not observe the same potentiation of L5 to L4 FS

projections in FXS mice, indicating that the visual experience did not have the same effect in FXS.

Another prominent difference in circuit plasticity between WT and FXS mice was at the L5 to L5 recurrent projection. Intrinsic L5 to L5 RS neurons' hyperconnectivity was observed in FXS mice compared to WT, which is in agreement with previous morphological studies (Comery et al., 1997). More interestingly, this hyperconnectivity was over-corrected after visual experience in FXS, exhibiting drastic depression while little change happened in WT mice at this synapse, which also agrees with the exaggerated LTD observed in brain slices of FX mice (Waung & Huber, 2009). On the other hand, L5 to L5 IB neurons' projections were potentiated in both genotypes, but in a different fashion. In WT mice, there was an overall increase of EPSC amplitude, while in FXS mice the change was mostly a larger number of weak synapses. Since most immature synapses primarily express NMDAR and are also electrophysiologically weak connections (Zhang, Peterson, & Liu, 2013), we speculate that these weak synapses in the FXS mice after visual experience were either newly formed immature synapses or activated pre-existing silent synapses. This hypothesis can also be supported by morphological observations of higher density of immature dendritic spines in FXS.

To differentiate between expected and novel stimuli, the brain needs to be able to recognize familiar, expected stimuli or their prominent physical features. However, there has been a poor understanding of how this process occurs at the mechanistic level. We have recently discovered a new mechanism encoding visual familiarity via persistent low-frequency oscillations in the mouse primary visual cortex (S. T. Kissinger, A. Pak, Y. Tang, S. C. Masmanidis, & A. A. Chubykin, 2018). This mechanism is dependent on the muscarinic cholinergic receptors and is specific to the spatial frequency of the familiar visual stimuli. Persistent (lasting beyond the initial stimulus) theta (4-8Hz) oscillations have been previously reported in primary visual cortex (V1) after the presentation of a familiar visual cue to report the time of a reward delivery (Zold & Hussain Shuler, 2015) and during the delayed part of visual cue-reward working memory tasks (Lee, Simpson, Logothetis, & Rainer, 2005). Our recent findings demonstrate persistent familiarity-induced theta oscillations presented as both visually evoked potentials (VEPs) and single unit responses (Samuel T. Kissinger et al., 2018).

Computational modeling suggests that the strengthening of excitatory drive to inhibition may be critical for the generation of the low-frequency oscillations in the cortical superficial layer

neurons (Visser & Van Gils, 2014). The electrophysiological properties of IB cells, including bursting and rebound-spiking, are due to the expression of Hyperpolarization-Activated Cyclic Nucleotide-Gated (HCN) channels (Kase & Imoto, 2012). These bursting cells have the potential to drive oscillatory activity in the network. Interestingly, following visual experience, synaptic strengths in V1 are not uniformly strengthened to the same magnitude. Some remained stable whilst others slightly weakened. The differential plasticity at different synapses of the circuit may be important for the emergence of oscillations.

In summary, we have demonstrated visual experience-induced plasticity at L5 to L4 and L5 to L5 local projections in an FXS mouse model and healthy control. Potentiation at L5 to L4 FS cells as well as L5 to L5 IB cells could potentially explain the circuit mechanism of familiarity encoding. The impairment of such plasticity in FXS mice correlates with evidence of disrupted visual perception and learning in FXS.

References

Buzsaki, G., & Mizuseki, K. (2014). The log-dynamic brain: how skewed distributions affect network operations. *Nat Rev Neurosci, 15*(4), 264-278. doi: 10.1038/nrn3687

Chen, G., Zhang, Y., Li, X., Zhao, X., Ye, Q., Lin, Y., . . . Zhang, X. (2017). Distinct Inhibitory Circuits Orchestrate Cortical beta and gamma Band Oscillations. *Neuron, 96*(6), 1403-1418.e1406. doi: 10.1016/j.neuron.2017.11.033

Chuang, S. C., Zhao, W., Bauchwitz, R., Yan, Q., Bianchi, R., & Wong, R. K. (2005). Prolonged epileptiform discharges induced by altered group I metabotropic glutamate receptor-mediated synaptic responses in hippocampal slices of a fragile X mouse model. *J Neurosci, 25*(35), 8048-8055. doi: 10.1523/jneurosci.1777-05.2005

Comery, T. A., Harris, J. B., Willems, P. J., Oostra, B. A., Irwin, S. A., Weiler, I. J., & Greenough, W. T. (1997). Abnormal dendritic spines in fragile X knockout mice: Maturation and pruning deficits. *Proceedings of the National Academy of Sciences, 94*(10), 5401-5404. doi: 10.1073/pnas.94.10.5401

Cooke, S. F., & Bear, M. F. (2010). Visual Experience Induces Long-Term Potentiation in the Primary Visual Cortex. *The Journal of Neuroscience, 30*(48), 16304. doi: 10.1523/JNEUROSCI.4333-10.2010

Dani, V. S., Chang, Q., Maffei, A., Turrigiano, G. G., Jaenisch, R., & Nelson, S. B. (2005). Reduced cortical activity due to a shift in the balance between excitation and inhibition in a mouse model of Rett syndrome. *Proc Natl Acad Sci U S A, 102*(35), 12560-12565. doi: 10.1073/pnas.0506071102

Dani, V. S., & Nelson, S. B. (2009). Intact long-term potentiation but reduced connectivity between neocortical layer 5 pyramidal neurons in a mouse model of Rett syndrome. *J Neurosci, 29*(36), 11263-11270. doi: 10.1523/jneurosci.1019-09.2009

Darnell, J. C., & Klann, E. (2013). The translation of translational control by FMRP: therapeutic targets for FXS. *Nat Neurosci, 16*(11), 1530-1536. doi: 10.1038/nn.3379

Erickson, C. A., Davenport, M. H., Schaefer, T. L., Wink, L. K., Pedapati, E. V., Sweeney, J. A., . . . Berry-Kravis, E. (2017). Fragile X targeted pharmacotherapy: lessons learned and future directions. *Journal of Neurodevelopmental Disorders, 9*(1), 7. doi: 10.1186/s11689-017-9186-9

Farzin, F., Rivera, S. M., & Whitney, D. (2011). Resolution of spatial and temporal visual attention in infants with fragile X syndrome. *Brain, 134*(Pt 11), 3355-3368. doi: 10.1093/brain/awr249

Farzin, F., Whitney, D., Hagerman, R. J., & Rivera, S. M. (2008). Contrast detection in infants with fragile X syndrome. *Vision Res, 48*(13), 1471-1478. doi: 10.1016/j.visres.2008.03.019

Fmr1 knockout mice: a model to study fragile X mental retardation. The Dutch-Belgian Fragile X Consortium. (1994). *Cell, 78*(1), 23-33.

Freund, L. S., & Reiss, A. L. (1991). Cognitive profiles associated with the fra(X) syndrome in males and females. *Am J Med Genet, 38*(4), 542-547. doi: 10.1002/ajmg.1320380409

Gallego, P. K., Burris, J. L., & Rivera, S. M. (2014). Visual motion processing deficits in infants with the fragile X premutation. *Journal of neurodevelopmental disorders, 6*(1), 29-29. doi: 10.1186/1866-1955-6-29

Gibson, J. R., Bartley, A. F., Hays, S. A., & Huber, K. M. (2008). Imbalance of neocortical excitation and inhibition and altered UP states reflect network hyperexcitability in the mouse model of fragile X syndrome. *J Neurophysiol, 100*(5), 2615-2626. doi: 10.1152/jn.90752.2008

Goel, A., Cantu, D. A., Guilfoyle, J., Chaudhari, G. R., Newadkar, A., Todisco, B., . . . Portera-Cailliau, C. (2018). Impaired perceptual learning in a mouse model of Fragile X syndrome is mediated by parvalbumin neuron dysfunction and is reversible. *Nature Neuroscience, 21*(10), 1404-1411. doi: 10.1038/s41593-018-0231-0

Goncalves, J. T., Anstey, J. E., Golshani, P., & Portera-Cailliau, C. (2013). Circuit level defects in the developing neocortex of Fragile X mice. *Nat Neurosci, 16*(7), 903-909. doi: 10.1038/nn.3415

Hagerman, R., Lauterborn, J., Au, J., & Berry-Kravis, E. (2012). Fragile X Syndrome and Targeted Treatment Trials. In R. B. Denman (Ed.), *Modeling Fragile X Syndrome* (pp. 297-335). Berlin, Heidelberg: Springer Berlin Heidelberg.

Hamilton, S. M., Green, J. R., Veeraragavan, S., Yuva, L., McCoy, A., Wu, Y., . . . Paylor, R. (2014). Fmr1 and Nlgn3 knockout rats: novel tools for investigating autism spectrum disorders. *Behav Neurosci, 128*(2), 103-109. doi: 10.1037/a0035988

Hooks, B. M., Hires, S. A., Zhang, Y. X., Huber, D., Petreanu, L., Svoboda, K., & Shepherd, G. M. (2011). Laminar analysis of excitatory local circuits in vibrissal motor and sensory cortical areas. *PLoS Biol, 9*(1), e1000572. doi: 10.1371/journal.pbio.1000572

Hooks, B. M., Mao, T., Gutnisky, D. A., Yamawaki, N., Svoboda, K., & Shepherd, G. M. (2013). Organization of cortical and thalamic input to pyramidal neurons in mouse motor cortex. *J Neurosci, 33*(2), 748-760. doi: 10.1523/JNEUROSCI.4338-12.2013

Huber, K. M., Gallagher, S. M., Warren, S. T., & Bear, M. F. (2002). Altered synaptic plasticity in a mouse model of fragile X mental retardation. *Proc Natl Acad Sci U S A, 99*(11), 7746-7750. doi: 10.1073/pnas.122205699

Isaacson, J. S., & Scanziani, M. (2011). How inhibition shapes cortical activity. *Neuron, 72*(2), 231-243. doi: 10.1016/j.neuron.2011.09.027

Kase, D., & Imoto, K. (2012). The Role of HCN Channels on Membrane Excitability in the Nervous System. *Journal of Signal Transduction, 2012*, 11. doi: 10.1155/2012/619747

Kasper, E. M., Larkman, A. U., Lubke, J., & Blakemore, C. (1994). Pyramidal neurons in layer 5 of the rat visual cortex. I. Correlation among cell morphology, intrinsic electrophysiological properties, and axon targets. *J Comp Neurol, 339*(4), 459-474. doi: 10.1002/cne.903390402

Katzel, D., Zemelman, B. V., Buetfering, C., Wolfel, M., & Miesenbock, G. (2011). The columnar and laminar organization of inhibitory connections to neocortical excitatory cells. *Nat Neurosci, 14*(1), 100-107. doi: 10.1038/nn.2687

Kazdoba, T. M., Leach, P. T., Silverman, J. L., & Crawley, J. N. (2014). Modeling fragile X syndrome in the Fmr1 knockout mouse. *Intractable & rare diseases research, 3*(4), 118-133. doi: 10.5582/irdr.2014.01024

Kerlin, A. M., Andermann, M. L., Berezovskii, V. K., & Reid, R. C. (2010). Broadly tuned response properties of diverse inhibitory neuron subtypes in mouse visual cortex. *Neuron, 67*(5), 858-871. doi: 10.1016/j.neuron.2010.08.002

Kissinger, S. T., Pak, A., Tang, Y., Masmanidis, S. C., & Chubykin, A. A. (2018). Oscillatory Encoding of Visual Stimulus Familiarity. *The Journal of Neuroscience, 38*(27), 6223. doi: 10.1523/JNEUROSCI.3646-17.2018

Kissinger, S. T., Pak, A., Tang, Y., Masmanidis, S. C., & Chubykin, A. A. (2018). Oscillatory Encoding of Visual Stimulus Familiarity. *J Neurosci, 38*(27), 6223-6240. doi: 10.1523/JNEUROSCI.3646-17.2018

Kogan, M. D., Vladutiu, C. J., Schieve, L. A., Ghandour, R. M., Blumberg, S. J., Zablotsky, B., . . . Lu, M. C. (2018). The Prevalence of Parent-Reported Autism Spectrum Disorder Among US Children. *Pediatrics, 142*(6). doi: 10.1542/peds.2017-4161

Lauterborn, J. C., Rex, C. S., Kramar, E., Chen, L. Y., Pandyarajan, V., Lynch, G., & Gall, C. M. (2007). Brain-derived neurotrophic factor rescues synaptic plasticity in a mouse model of fragile X syndrome. *J Neurosci, 27*(40), 10685-10694. doi: 10.1523/JNEUROSCI.2624-07.2007

Lee, H., Simpson, G. V., Logothetis, N. K., & Rainer, G. (2005). Phase locking of single neuron activity to theta oscillations during working memory in monkey extrastriate visual cortex. *Neuron, 45*(1), 147-156. doi: 10.1016/j.neuron.2004.12.025

Mank, M., Santos, A. F., Direnberger, S., Mrsic-Flogel, T. D., Hofer, S. B., Stein, V., . . . Griesbeck, O. (2008). A genetically encoded calcium indicator for chronic in vivo two-photon imaging. *Nature Methods, 5*, 805. doi: 10.1038/nmeth.1243 https://www.nature.com/articles/nmeth.1243#supplementary-information

McBride, S. M., Bell, A. J., & Jongens, T. A. (2012). Behavior in a Drosophila model of fragile X. *Results Probl Cell Differ, 54*, 83-117. doi: 10.1007/978-3-642-21649-7_6

Mila, M., Alvarez-Mora, M. I., Madrigal, I., & Rodriguez-Revenga, L. (2018). Fragile X syndrome: An overview and update of the FMR1 gene. *Clin Genet, 93*(2), 197-205. doi: 10.1111/cge.13075

Miltner, W. H. R., Braun, C., Arnold, M., Witte, H., & Taub, E. (1999). Coherence of gamma-band EEG activity as a basis for associative learning. *Nature, 397*(6718), 434-436. doi: 10.1038/17126

Myrick, L. K., Deng, P. Y., Hashimoto, H., Oh, Y. M., Cho, Y., Poidevin, M. J., . . . Klyachko, V. A. (2015). Independent role for presynaptic FMRP revealed by an FMR1 missense mutation associated with intellectual disability and seizures. *Proc Natl Acad Sci U S A, 112*(4), 949-956. doi: 10.1073/pnas.1423094112

Nosyreva, E. D., & Huber, K. M. (2006). Metabotropic receptor-dependent long-term depression persists in the absence of protein synthesis in the mouse model of fragile X syndrome. *J Neurophysiol, 95*(5), 3291-3295. doi: 10.1152/jn.01316.2005

Patel, A. B., Loerwald, K. W., Huber, K. M., & Gibson, J. R. (2014). Postsynaptic FMRP promotes the pruning of cell-to-cell connections among pyramidal neurons in the L5A neocortical network. *J Neurosci, 34*(9), 3413-3418. doi: 10.1523/JNEUROSCI.2921-13.2014

Penagarikano, O., Mulle, J. G., & Warren, S. T. (2007). The pathophysiology of fragile x syndrome. *Annu Rev Genomics Hum Genet, 8*, 109-129. doi: 10.1146/annurev.genom.8.080706.092249

Petreanu, L., Huber, D., Sobczyk, A., & Svoboda, K. (2007). Channelrhodopsin-2-assisted circuit mapping of long-range callosal projections. *Nat Neurosci, 10*(5), 663-668. doi: 10.1038/nn1891

Popescu, A. T., Popa, D., & Paré, D. (2009). Coherent gamma oscillations couple the amygdala and striatum during learning. *Nature neuroscience, 12*, 801. doi: 10.1038/nn.2305 https://www.nature.com/articles/nn.2305#supplementary-information

Prusky, G. T., & Douglas, R. M. (2003). Developmental plasticity of mouse visual acuity. *European Journal of Neuroscience, 17*(1), 167-173. doi: 10.1046/j.1460-9568.2003.02420.x

Robic, S., Sonie, S., Fonlupt, P., Henaff, M. A., Touil, N., Coricelli, G., . . . Schmitz, C. (2015). Decision-making in a changing world: a study in autism spectrum disorders. *J Autism Dev Disord, 45*(6), 1603-1613. doi: 10.1007/s10803-014-2311-7

Robinson, E. B., St Pourcain, B., Anttila, V., Kosmicki, J. A., Bulik-Sullivan, B., Grove, J., . . . Daly, M. J. (2016). Genetic risk for autism spectrum disorders and neuropsychiatric variation in the general population. *Nat Genet*. doi: 10.1038/ng.3529

Shang, Y., Wang, H., Mercaldo, V., Li, X., Chen, T., & Zhuo, M. (2009). Fragile X mental retardation protein is required for chemically-induced long-term potentiation of the hippocampus in adult mice. *J Neurochem, 111*(3), 635-646. doi: 10.1111/j.1471-4159.2009.06314.x

Song, S., Sjöström, P. J., Reigl, M., Nelson, S., & Chklovskii, D. B. (2005). Highly Nonrandom Features of Synaptic Connectivity in Local Cortical Circuits. *PLOS Biology, 3*(3), e68. doi: 10.1371/journal.pbio.0030068

Tucker, B., Richards, R., & Lardelli, M. (2004). Expression of three zebrafish orthologs of human FMR1-related genes and their phylogenetic relationships. *Dev Genes Evol, 214*(11), 567-574. doi: 10.1007/s00427-004-0438-9

van der Molen, M. J., Stam, C. J., & van der Molen, M. W. (2014). Resting-state EEG oscillatory dynamics in fragile X syndrome: abnormal functional connectivity and brain network organization. *PLoS One, 9*(2), e88451. doi: 10.1371/journal.pone.0088451

Van der Molen, M. J., & Van der Molen, M. W. (2013). Reduced alpha and exaggerated theta power during the resting-state EEG in fragile X syndrome. *Biol Psychol, 92*(2), 216-219. doi: 10.1016/j.biopsycho.2012.11.013

Van der Molen, M. J., Van der Molen, M. W., Ridderinkhof, K. R., Hamel, B. C., Curfs, L. M., & Ramakers, G. J. (2012). Auditory and visual cortical activity during selective attention in fragile X syndrome: a cascade of processing deficiencies. *Clin Neurophysiol, 123*(4), 720-729. doi: 10.1016/j.clinph.2011.08.023

Verkerk, A. J., Pieretti, M., Sutcliffe, J. S., Fu, Y. H., Kuhl, D. P., Pizzuti, A., . . . et al. (1991). Identification of a gene (FMR-1) containing a CGG repeat coincident with a breakpoint cluster region exhibiting length variation in fragile X syndrome. *Cell, 65*(5), 905-914.

Visser, S., & Van Gils, S. A. (2014). Lumping Izhikevich neurons. *EPJ Nonlinear Biomedical Physics, 2*(1), 6. doi: 10.1140/epjnbp19

Wang, G., Wyskiel, D. R., Yang, W., Wang, Y., Milbern, L. C., Lalanne, T., . . . Zhu, J. J. (2015). An optogenetics- and imaging-assisted simultaneous multiple patch-clamp recording system for decoding complex neural circuits. *Nat Protoc, 10*(3), 397-412. doi: 10.1038/nprot.2015.019

Waung, M. W., & Huber, K. M. (2009). Protein translation in synaptic plasticity: mGluR-LTD, Fragile X. *Current Opinion in Neurobiology, 19*(3), 319-326. doi: https://doi.org/10.1016/j.conb.2009.03.011

Womelsdorf, T., Fries, P., Mitra, P. P., & Desimone, R. (2006). Gamma-band synchronization in visual cortex predicts speed of change detection. *Nature, 439*(7077), 733-736. doi: 10.1038/nature04258

Wong, A. A., & Brown, R. E. (2006). Visual detection, pattern discrimination and visual acuity in 14 strains of mice. *Genes, Brain and Behavior, 5*(5), 389-403. doi: 10.1111/j.1601-183X.2005.00173.x

Wu, Q., & Chubykin, A. A. (2017). Application of Automated Image-guided Patch Clamp for the Study of Neurons in Brain Slices. *J Vis Exp*(125). doi: 10.3791/56010

Wu, Q., Kolb, I., Callahan, B. M., Su, Z., Stoy, W., Kodandaramaiah, S. B., . . . Chubykin, A. A. (2016). Integration of autopatching with automated pipette and cell detection in vitro. *J Neurophysiol, 116*(4), 1564-1578. doi: 10.1152/jn.00386.2016

Yang, W., Carrasquillo, Y., Hooks, B. M., Nerbonne, J. M., & Burkhalter, A. (2013). Distinct balance of excitation and inhibition in an interareal feedforward and feedback circuit of mouse visual cortex. *J Neurosci, 33*(44), 17373-17384. doi: 10.1523/jneurosci.2515-13.2013

Yun, S. H., & Trommer, B. L. (2011). Fragile X mice: reduced long-term potentiation and N-Methyl-D-Aspartate receptor-mediated neurotransmission in dentate gyrus. *J Neurosci Res, 89*(2), 176-182. doi: 10.1002/jnr.22546

Zhang, Z.-w., Peterson, M., & Liu, H. (2013). Essential role of postsynaptic NMDA receptors in developmental refinement of excitatory synapses. *Proc Natl Acad Sci U S A, 110*(3), 1095-1100. doi: 10.1073/pnas.1212971110

Zold, C. L., & Hussain Shuler, M. G. (2015). Theta Oscillations in Visual Cortex Emerge with Experience to Convey Expected Reward Time and Experienced Reward Rate. *J Neurosci, 35*(26), 9603-9614. doi: 10.1523/JNEUROSCI.0296-15.2015

CHAPTER 4: CIRCUIT RESTORATION THROUGH *IN VIVO* DIRECT REPROGRAMMING AFTER ISCHEMIC INJURY

Abstract

Specialized neural circuits underlie critical brain function. However, these circuits are vulnerable to damage from a variety of insults, including ischemic injury. Common sequelae of many brain injuries include neuronal loss, gliosis, and inhibition of re-innervation at the injury site. This combination impacts the integrity of local circuitry, leading to long-term functional impairment and disability. Recent technology development achieved the direct conversion of endogenous astrocytes to neurons *in situ* at the brain injury site; this promises to repair brain damage by simultaneously replenishing the neuronal population and reversing the adverse environment of the glial scar. While the robust reprogramming process and long-term transformed neuron survival are promising, it is unclear whether and how these neurons mature and integrate into local circuits to carry out appropriate functions. We investigated the effect of NeuroD1 gene-mediated *in vivo* direct reprogramming on circuit integration in a mouse model of focal ischemic injury in the primary visual cortex. We found that individual newly transformed neurons received abundant functional projections from endogenous neurons, as assessed by circuit mapping. Surviving neurons at the injury site also regain functional connections with local circuits after the reprogramming treatment. Our evidence from *ex vivo* circuit mapping suggests spontaneous maturation of newly transformed neurons, with local-circuit integration, and functional restoration following NeuroD1-mediated *in vivo* direct reprogramming.

Introduction

Stroke is a leading cause of mortality and long-term morbidity. In the United States, 2.7% of adults have had one or more strokes. This problem could worsen because the percentage may increase as population life expectancy increases. Ischemic stroke, the most common type, accounts for 87% of all stroke cases (Benjamin et al., 2018). Ischemic stroke typically results from acute cerebral arterial obstruction, leading to localized hypoxia and permanent brain damage. The aftermath of such an event includes excitotoxicity triggering oxidative stress, which leads to neuronal death, and eventually reactive gliosis (Endres, Dirnagl, & Moskowitz, 2008).

The only effective acute treatment for ischemic stroke is vessel recanalization via thrombolysis or thrombectomy. These therapies each have a narrow effective time window of only 3 hours from the onset of stroke symptoms, therefore limiting their application for many patients who do not receive prompt medical attention (Pena, Borlongan, Shen, & Davis, 2017). This leaves a large unmet need for new treatments in ischemic stroke patients with permanent brain damage. No existing treatments have been proven effective (Patel & McMullen, 2017; Powers et al., 2018). Although most patients partially regain functions over time, a significant portion of this is attributed to compensation rather than brain recovery per se (Levin, Kleim, & Wolf, 2008; Nakayma, Jørgensen, Raaschou, & Olsen, 1994; Roby-Brami et al., 2003). Complete functional recovery is rare.

Therefore, there is much interest in using regenerative medicine to treat permeant brain damage following an ischemic stroke. However, challenges in stem cell therapies, such as low cell transformation efficiency, low *in vivo* survival rate, as well as inadequate neuronal maturation and circuit integration, have hindered the clinical application of this approach (Bernstock et al., 2017; J. Y. Li, Christophersen, Hall, Soulet, & Brundin, 2008; Steinbeck & Studer, 2015). Moreover, the stem-cell source and differentiation protocol have major influences on the induced neurons, resulting in poorly understood biases in neuronal subtype and gene expression profile. (Tsunemoto et al., 2018; Wu et al., 2007). Meanwhile, progress was made in reprogramming non-neuronal cells, such as hepatocytes and fibroblasts, into neurons directly (Blanchard et al., 2014; Marro et al., 2011; Yang, Ng, Pang, Südhof, & Wernig, 2011). However, because the neurons were differentiated *in vitro*, this technology suffers from the same shortcomings as the classical stem cell transformation. Regenerating neurons *in situ* from resident cells in the brain may be able to solve these limitations and provide a more feasible strategy for brain repair.

After a stroke, the local environment drastically changes. A number of studies showed that in the penumbra, or peri-infarct zone adjacent to the injury core, synaptic plasticity happens over time to re-map the local circuit (review see Carmicheal (Carmichael, 2003)). Researchers propose that the ischemic insult could “re-open” the critical period, allowing neural plasticity to occur (T. H. Murphy & D. Corbett, 2009). Subsequently, methods promoting plasticity were applied in clinical practice in hope for improved functional recovery (Hermann & Chopp, 2012). Unfortunately, these methods are not cures and only have varying degrees of success to partially

improve stroke outcome. However, the potential to re-map circuitry after injury as a natural property of our brain provides the basis to restore circuit through a semi-spontaneous process. Perhaps with some help, the damaged brain tissue, especially the injury core where glial scar forms, could be restored and re-innervated.

NeuroD1 transcription factor overexpression alone has been demonstrated to convert human embryonic stem cells (ESCs) and induced pluripotent cells (iPSCs) into neurons (Y. Zhang et al., 2013). NeuroD1-mediated *in vivo* direct reprogramming technology converts reactive astrocytes directly into neurons *in situ*, bypassing the pluripotent and proliferating stem cell stage (G. Chen et al., 2015; H. Li & Chen, 2016). Many insults to the brain, including ischemic injury, trigger re-activation and proliferation of astrocytes around the injury site. Although the initial stage of gliosis may be beneficial to confining the injury through re-uptake of excessive extracellular glutamate and restoring homeostasis, glial scaring in the later stage is detrimental to axonal regeneration and functional recovery (Fitch & Silver, 2008; Kawano et al., 2012). Direct reprogramming *in vivo* has been demonstrated to efficiently transform astrocytes into physiologically active neurons in the mouse models of open wound traumatic brain injury, Alzheimer's disease(Guo et al., 2014), and ischemic injury(Y. Chen et al., 2018).

Whether the newly transformed neurons integrate into the local circuits and perform appropriate functions is vital for evaluating the potential of this technology as a clinically viable brain repair therapy. To examine circuit rewiring, we directly mapped the connectivity of the individual newly reprogrammed neurons in *ex vivo* brain slices. Furthermore, circuit connectivity strength was characterized longitudinally following reprogramming, revealing spontaneous local circuitry remodeling. These findings indicate that NeuroD1-mediated *in vivo* direct reprogramming functionally restored local circuitry in brains damaged by ischemia.

Materials and Methods

Animals

Wild type male and female C57BL/6 mice (Jackson Laboratory and Purdue University Transgenic Mouse Core Facility, postnatal day 34-90) were used for *in vivo* extracellular recording experiments. Thy1-ChR2-YFP line 18 (B6.Cg-Tg(Thy1-COP4/EYFP)18Gfng/J, JAX stock #007612) were used for *ex vivo* cortical slices preparation and whole cell patch clamp

experiments. All animals were housed in 12-hr light/dark cycle with *ad libitum* access to rodent chow food and water. All animal experimental use was approved by the Purdue University animal care and use committee (PACUC), and followed guidance issued by the National Institutes of Health.

Surgery, ischemic injury induction, and viral injections

Mice were anesthetized during all surgical procedures with inhaled isoflurane (5% for initial induction and 1.5% for maintaining anesthesia, carrier gas was air, SomnoSuite system). Deep anesthesia was confirmed by no response to toe/tail pinch. Skin over the skull was removed, and the skull over the cortices were exposed. The craniotomy was made first by thinning a small area of the skull about 0.5mm diameter at the injection site with a drill. Then, a tiny gap at the center of the whole for inserting the micro-injection pipette was opened using a sterile needle. To induce focal ischemia, a total volume of 1µl of 4µg/µl endothelin-1 (ET-1, Sigma) was injected into each hemisphere. ET-1 was dissolved in filter-sterilized pure water to make stock solution (10µg/µl) which was stored at -80°C and diluted to the final concentration (4µg/µl) with filter-sterilized artificial cerebral spinal fluid (ACSF) before each injection. ET-1 solution was injected at two depths, 700µm and 300µm below the brain surface, 500nl per depth at 100nl/min rate using a micro-injector (NanoJect II or NanoJect III, Drummond Scientific). For sham injections, 1µl of ACSF was injected at the same speed and depths. For mice used in extracellular recording experiments, a headpost was adhered to the skull at 4mm anterior to bregma using super-glue, and a gold-plated grounding pin (Parkell) was installed 1mm anterior to bregma by inserting the sharp end through the skull into the midline space (but not in the brain tissue). These steps were omitted in animals intended for *ex vivo* brain slice preparation. Following the procedures, acrylic dental cement (Metabond, C&B) was applied on the exposed skull to create a protective hard cap. 8 to 10 days after ET-1 injections, two adeno associated viruses (AAV), one carrying FLEX-NeuroD1-mCherry and the second carrying GFAP::Cre were injected together (10:1 ratio, 1ul total volume, injected at the same depths and speed as ET-1 injection) through the same craniotomy. For optogenetics experiment, ET-1 was injected in both hemispheres as described earlier. 8-10 days post ET-1 injection, AAV-GFAP::Cre, AAV-FLEX-NeuroD1-mCherry, and AAV-DIO-ChR2-eYFP were injected together (2:10:10 ratio) into both hemisphere at 700um and 300um below the brain surface (500nl per depth, speed 1nl/s). Coordinates used for primary

visual cortices injections were (relative to lambda): 0.8 mm anterior, ±3.0 mm lateral for animals used in extracellular recordings; or 0.8mm anterior, ±2.8 mm lateral for animals used in *ex vivo* slice recordings.

Acute brain slices preparation:

Mice were anesthetized with an intra-peritoneal (IP) injection of a cocktail of ketamine (100mg/kg body weight) and xylazine (16mg/kg body weight) diluted in sterile saline. Deep anesthesia was confirmed with no reflex to toe/tail pinch. For animals that were 55 days or younger, trans-cardiac perfusion was conducted using ice-cold High Sucrose Dissection Buffer (HSDB) containing (in mM) 75 sucrose, 10 glucose, 87 NaCl, 2.5 KCl, 1.25 NaH_2PO_4, 25 $NaHCO_3$, 0.5 $CaCl_2$, 7 $MgCl_2$, and 1.3 ascorbic acid. Following perfusion, the brain was quickly dissected out of the skull and the visual cortex was cut on a vibratome (VT1000, Leica) into slices at 300µm thickness in ice-cold HSDB. Brain slices were then carefully transferred into normal ACSF containing (in mM) 124 NaCl, 3.5 KCl, 1 CaCl2, 0.8 MgCl2, 1.23 NaH2PO4, 26 NaHCO3, and 10 glucose. The slices were first incubated at 32°C in ACSF for 30min then at room temperature (around 25°C) for 1 to 6 hours before recording. For animals that were older than 55 days, trans-cardiac perfusion was conducted using ice-cold N-methyl-D-glucamine (NMDG) ACSF containing (in mM) 92 mM NMDG, 2.5 mM KCl, 1.25 mM NaH_2PO_4, 30 mM $NaHCO_3$, 20 mM HEPES, 25 mM glucose, 2 mM thiourea, 5 mM Na-ascorbate, 3 mM Na-pyruvate, 0.5 mM $CaCl_2$ and 10 mM $MgCl_2$. Dissection and slicing were conducted in the same manner as for young animals but in ice-cold NMDG ACSF. Brain slices were then recovered in NMDG ACSF at 32°C for 4 to 7 min depending on the animal age, then in HEPES ACSF containing (in mM) 92 mM NaCl, 2.5 mM KCl, 1.25 mM NaH_2PO_4, 30 mM $NaHCO_3$, 20 mM HEPES, 25 mM glucose, 2 mM thiourea, 5 mM Na-ascorbate, 3 mM Na-pyruvate, 2 mM $CaCl_2$ and 2 mM $MgCl_2$ at room temperature for at least 2h before recording. All physiological solutions were continuously aerated with carbogen gas (95% O_2 5% CO_2) to maintain pH (7.3-7.4) and oxygen saturation. Brain slices were kept alive for up to 7h after cutting and each recorded slice was used for up to 1.5h.

Whole-cell patch clamp recordings

Patch-clamp recordings were conducted using a commercial slice physiology rig (SliceScope Pro 1000, Scientifica). Patch pipettes were pulled using a standard Flaming-Brown type puller (Sutter Instruments P97) from filamented borosilicate glass capillaries (BF150-86-10, Sutter Instruments). The recording internal solution contained (in mM) 20 KCl, 100 K-gluconate, 10 HEPES, 4 MgATP, 0.3 Na2GTP, and 7 phosphocreatine, with pH adjusted to 7.4 and osmolarity adjusted to 300 mOsm. In some experiments, a small amount of 4% w/v Alexa Fluor^{TM} 647 Hydrazide (A20502, ThermoFisher Scientific) dissolved in internal solution was back-loaded to the glass pipette through capillary force before loading the regular internal solution to label the patched cell. Pipette impedance was in the range of 3.5 to 7.9MΩ when filled with internal solution and submerged in ACSF. Brain slices were placed in a recording chamber continuously perfused with oxygenated ACSF and heated to 30-32°C. Cells were visualized with infrared illumination through differential interface contrast (DIC) optics and recorded with a charge-coupled device (CCD) camera. Signals were amplified using a Multiclamp 700B amplifier (Molecular Devices) and digitized using Digidata 1550A (Molecular Devices) at 20kHz and low-pass filtered at 10kHz. Recorded data were analyzed using custom-written Python scripts (detailed statistical tests see "Experimental design and statistical analysis"). For experiments during which cells were filled with fluorescent dye, the slices were fixed with 4% paraformaldehyde (PFA) for 30min-1h and mounted onto glass slides for imaging.

Channelrhodopsin-assisted circuit mapping (CRACM)

We used Thy1-ChR2-YFP line 18 (B6.Cg-Tg(Thy1-COP4/EYFP)18Gfng/J, JAX stoke #007612) which expressed ChR2 sparsely in layer 5 pyramidal cells in the cortex. To control for intrinsic synaptic strength difference in different projections, only layer 4 neurons were patched, therefore only L5 to L4 projection was compared. L4 cells were identified by the morphology and relative location in the brain slice (mid-point from pia to white matter). Light stimulation was generated with an LED light source (High-Power LED Collimator Source, 470nm, 50W, Mightex) and delivered through a patterned illuminator (Polygon 400, Mightex). A 10 by 10 grid covering a 670μm by 670μm square area was superimposed on the primary visual cortical slice, which spans the top border of L2/3 to lower border of L5 under 10x objective. Each pixel was

stimulated for 10ms, following a pseudo-random sequence with 2s inter-stimulus interval. Cells were held at -70mV in voltage-clamp mode during CRACM recordings. The LED and patterned illuminator were controlled by the manufacturer's software and stimulation and recording were synchronized by the digitizer. CRACM heat maps were plotted from light-induced EPSC amplitudes at each pixel.

Histology and immunohistochemistry (IHC)

Mice were anesthetized with 100mg/kg ketamine and 16mg/kg xylazine through IP injection before trans-cardiac perfusion. Deep anesthesia was confirmed with no reflex to toe/tail pinch. The thorax and abdomen were opened. A needle was inserted into the left ventricle of the heart, and a small incision was made in the right atrium. Mice were first perfused with 1x phosphate-buffered saline (PBS, 15 to 20ml) until the liver cleared, then with 4% paraformaldehyde (PFA, 10 to 15ml) for fixation. Mouse brains were post-fixed in 4% PFA for an additional 12-36hr before histology. Fixed brain tissue was sliced using a vibrating microtome (1000 Plus, TIP Vibratome) at 100μm thickness. When IHC staining was unnecessary, slides were made directly by mounting the slices with anti-fade mounting medium containing 0.2% n-propyl gallate. When IHC is necessary, the slices were stained free-floating in 24-well tissue-culture plates. They were first blocked and membrane permeabilized in 5% bovine serum albumin (BSA) and 0.1% Triton X 100 (Sigma) in PBS at room temperature for 30min. Then, the slices were incubated with primary antibody in 0.1% TX 100 for 36 to 48h at 4°C followed by secondary antibody for 1 to 2h at room temperature. Slices were counter stained with DAPI when necessary. The slices were mounted using the same method described above. Antibodies used are: Chicken Anti-Glial Fibrillary Acidic Protein Antibody (AB5541, Millipore Sigma), Rabbit Anti-NeuN Antibody (ABN78, Millipore Sigma), Alexa Fluor® 488 AffiniPure Donkey Anti-Rabbit IgG (H+L) (Code: 711-545-152, JAX), and Alexa Fluor® 647 AffiniPure Goat Anti-Chicken IgY (IgG) (H+L) (Code: 103-605-155, JAX). Brain slices were imaged under a confocal microscope (Zeiss LSM710). Neurite tracing and reconstruction was conducted using Fiji/ImageJ.

Results

To demonstrate the effects of *in vivo* direct reprogramming on visual function and local circuit recovery in V1 following cortical ischemic injury, visually evoked responses and local circuit connectivity were measured in mice with induced ischemic injury and treated by reprogramming. Moderate ischemic injury was induced by ET-1 local injection into one or both hemispheres of the visual cortex (details see methods). Robust gliosis develops in around 8 to 10 days, at which point we delivered the cre-dependent reprogramming gene NeuroD1 (FLEX-NeuroD1-mCherry) along with the cre-recombinase gene under the GFAP promotor (GFAP::Cre) targeting astrocytes using adeno-associated virus (AAV). ET-1 dosage (see methods section) was carefully titrated to induce consistent gliosis, but importantly, not to cause significant tissue loss at the point of experimental assessment. This allowed us to identify and measure the connectivity of a group of surviving neurons. Local circuit connectivity was assessed using *ex vivo* CRACM in acute cortical slices (**Fig. 23**). Histological analysis confirmed robust and localized gliosis at 9 days after ET-1 injection, accompanied by decreased expression of the neuronal marker NeuN (**Fig. 24*A***). As expected, the induced glial scar does not resolve if no treatment is applied to the injury site (**Fig. 25**). Newly reprogrammed neurons expressing the neuronal marker NeuN, but importantly not the astrocyte marker Glial Fibrillary Acidic Protein (GFAP), were detected as early as 10 days after the viral injection delivering the reprogramming gene (**Fig. 24*B***). An example of a cell undergoing reprogramming was captured at the transitional stage (**Fig. 24*C***). This mCherry positive cell expressed both neuronal and astrocyte markers. The timeline of astrocyte-to-neuron conversion was consistent with previously reported data from an open-wound cortical stab injury model (Guo et al., 2014) and an ischemic injury model (Y. Chen et al., 2018).

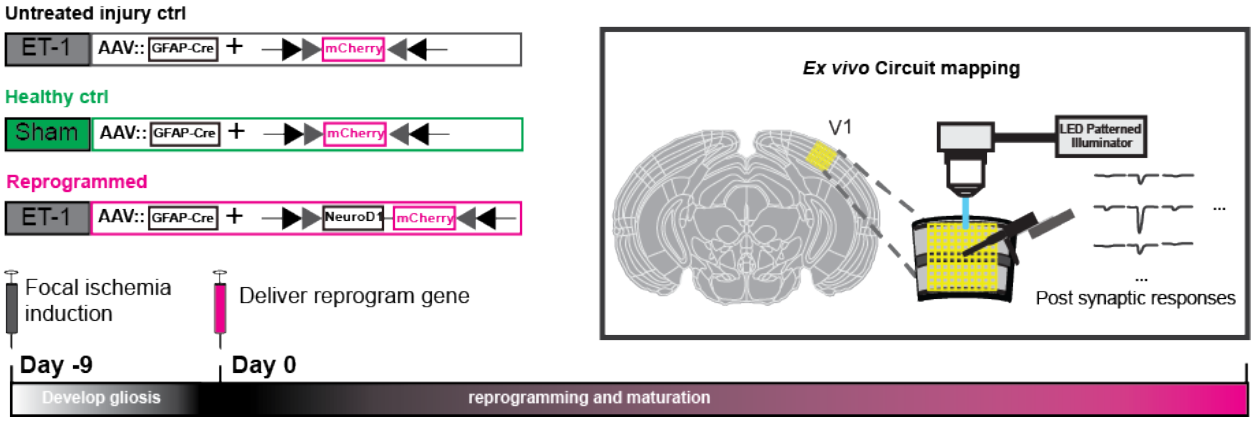

Figure 26. Focal ischemic stroke model and *in vivo* direct reprogramming in the primary visual cortex.

The schedule to induce focal ischemic stroke by injecting endothelin-1 (ET-1) and to reprogram astrocytes into neurons by injecting two viruses carrying the targeting gene and the reprogramming gene or empty control. After desired time of gene expression and reprogramming, V1 local circuit connectivity was assessed by Channelrhodopsin-Assisted Circuit Mapping (CRACM) in *ex vivo* acute brain slices.

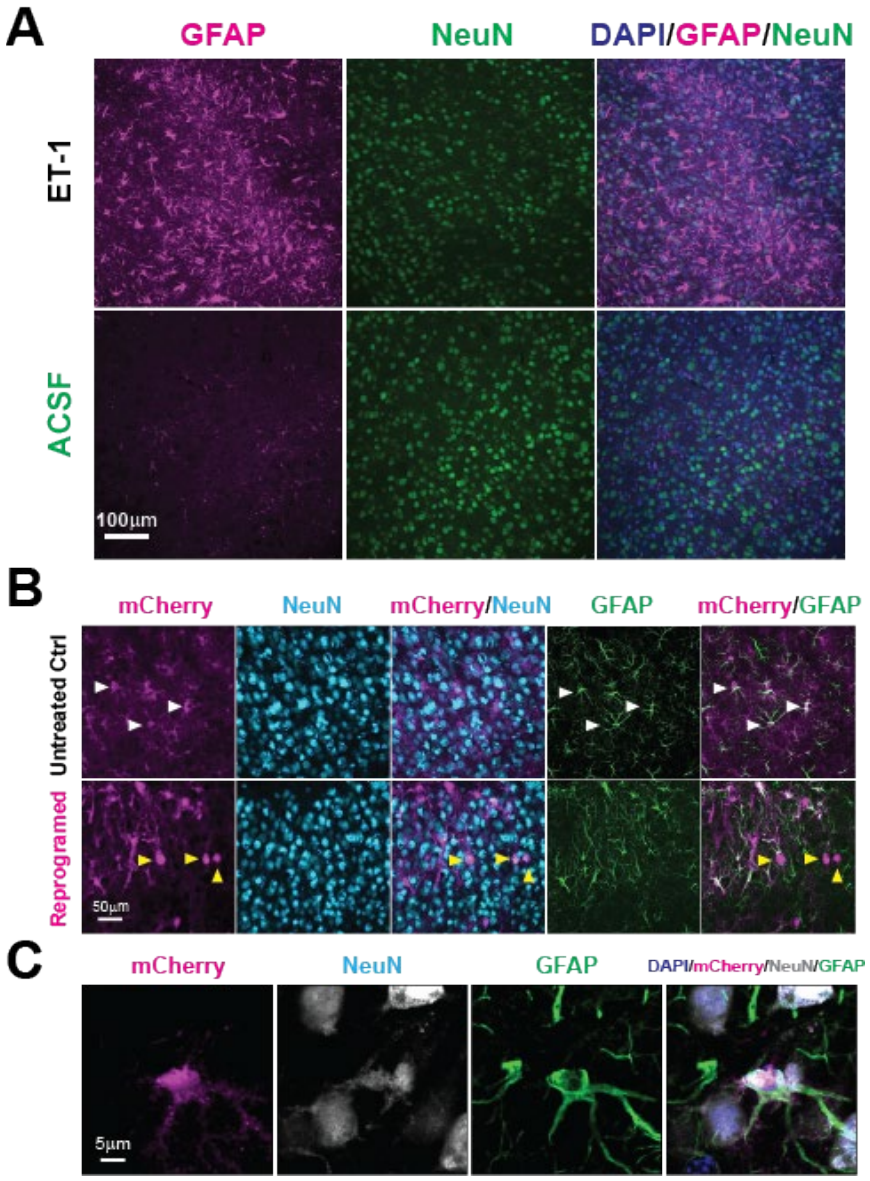

Figure 27. ET-1 induced gliosis and reprogramming.

A) 9 days after ET-1 injection (top) and sham artificial cerebral-spinal fluid (ACSF) injection control (bottom), immunohistochemistry staining astrocyte (magenta) and neuronal (green) markers showed robust gliosis developed. This gliosis persists if left untreated (supplementary figure 1-1). **B)** Newly reprogrammed neurons were detected 10 days after viral infection. In the reprogrammed group (bottom), mCherry positive reprogrammed cells (yellow arrow heads) co-stained with neuronal marker NeuN while in control group (white arrow heads) mCherry positive cells co-stained with astrocyte marker GFAP. **C)** mCherry positive infected cells at the transitional stage expressing both astrocyte and neuronal markers are also observed at this time point.

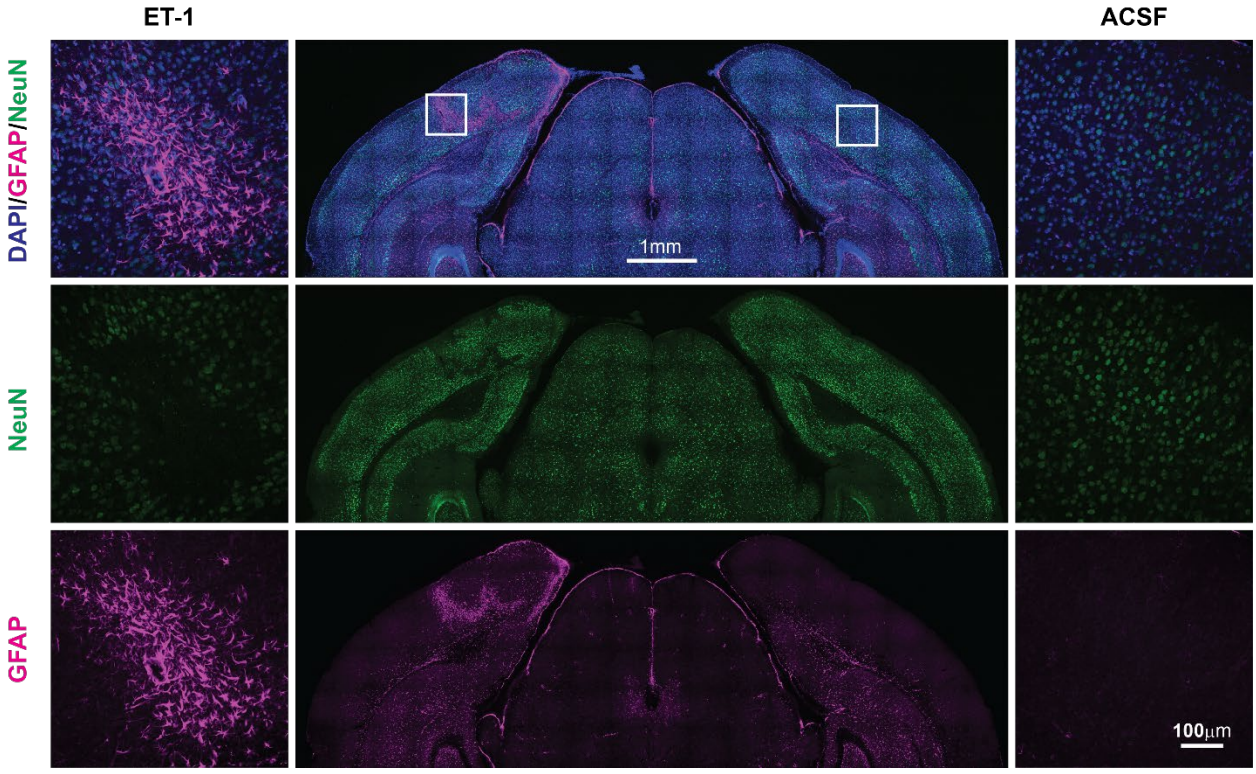

Figure 28. ET-1 injection induced ischemic stroke and glial scaring could not resolve without intervention.

Young mice were injected with ET-1 (left) and sham control (right). They were left undisturbed for 4 to 4.5 weeks. Immunohistochemistry staining of NeuN (green) and GFAP (magenta) showing prominent glial scar and loss of NeuN signal at the scar site, while very low GFAP signal and normal NeuN signal can be seen on the control side.

Reprogrammed neurons receive abundant input from pre-existing neurons

To directly measure the circuit connectivity of newly reprogrammed neurons, we used Channelrhodopsin-assisted circuit mapping (CRACM) in *ex vivo* acute slices. We used male and female (no difference between sex, data combined) heterozygous Thy1-ChR2-YFP mice that has sparse distribution of ChR2-eYFP positive cells in L5 cortical pyramidal cells (Asrican et al., 2013). Focal ischemia induction and reprogramming viral injection procedures were the same as for animals used for *in vivo* recordings (**Fig. 26*A***). Age matched animals were randomly assigned to one of three groups: healthy control (sham injection + empty viral vector injection), untreated ischemia control (ET-1 injection + empty viral vector injection) and reprogram group (ET-1 injection + reprogram viral vector injection). For each animal, both hemispheres received

the same treatment. We further divided neurons in the reprogrammed group into mCherry+ reprogrammed cells and mCherry- surviving neighbors. Both DIC and fluorescent image guided whole-cell patching of target neurons (**Fig. 26*B***). Basic electrophysiological properties were characterized by recording the potential change against a series of step currents for each cell (**Fig. 26*C***). Then, CRACM map was collected with the presence of TTX and 4-AP to isolate mono-synaptic connections (**Fig. 26*D***, details see "Methods"). For some mCherry+ reprogrammed cells, a fluorescent dye (Alexa Fluor™ 568 Hydrazide, ThermoFisher) was included in the patching pipette and extra time was allowed after recording for the dye to diffuse into the cell processes (**Fig. 26*E***). Morphological reconstructions showed that all examined cells had extensive neurites that resembled mature cortical neurons (**Fig. 26*F***).

All mCherry$^+$ cells in the reprogrammed group showed robust light-induced excitatory post-synaptic currents (EPSCs) (**Fig. 26*G***). Surviving neighbors (16 cells from 6 animals) also received considerable excitatory inputs (**Fig. 26*H***) qualitatively similar to that of neurons healthy controls (26 cells from 5 animals, **Fig. 26*J***). On the contrary, there were minimal EPSCs in cells on average in the untreated ischemia group (19 cells from 4 animals, **Fig. 26*I***). The maximal EPSC profile along tangential (**Fig. 26*K***) and vertical (**Fig. 26*L***) directions averaged across cells for each group revealed no shift in the overall shape of the EPSCs spatial distribution. We then compared the distributions of EPSC amplitudes among the four groups of cells. Firstly, the healthy control group significantly differed from the untreated ischemia control (**Fig. 26*M***, 2 sample Kolmogorov–Smirnov test, D = 0.119, p = 5.579e-14). The reprogrammed group had significantly larger responses than all the other groups as shown in the cumulative density curve (2 sample Kolmogorov–Smirnov test, Reprogram vs. Untreated: D = 0.508, p = 7.867e-226; Reprogram vs. Healthy: D 0.420, p = 2.213e-179; Reprogram vs. Surviving: D = 0.336, p = 3.638e-90. Significance level α=0.005). To compare the relative connection strength between groups, we transformed the original EPSC distributions to normal distributions by taking natural log of the absolute value of each EPSC amplitude. It is known that synaptic strengths in the cortex follow a log normal distribution (Buzsaki & Mizuseki, 2014). Our $\log_e$-transformed EPSCs were normally distributed in all four groups (see methods section for normality test details). The reprogrammed group had the largest mean of $\log_e$-EPSC values while the untreated ischemia group had the smallest (**Fig. 26*M*** insert). The CRACM experiment at 3 weeks post-infection directly demonstrated that functional synaptic inputs from the pre-existing local circuits

were formed onto the newly reprogrammed neurons. The relative strength of these projections was stronger than projections onto neurons in the same cortical area without ischemic insult (healthy control). Surviving endogenous neurons in the ischemic injury in the reprogrammed group had stronger synaptic connections with the circuit than surviving neurons in the untreated ischemia condition.

Figure 29. Reprogrammed neurons are integrated into the local circuit and may be hyper-connected at early stage.

A) Thy1-ChR2-YFP mice were used for inducing local ischemic stroke and reprogramming for Channelrhodopsin-Assisted Circuit Mapping (CRACM) experiments. **B)** An example whole cell patch in Differential Interface Contrast (DIC) image (left) and epifluorescence image (right), showing the patched cell was an mCherry positive cell. **C)** Step-current injection with hyperpolarizing and depolarizing current steps showing evoked action potentials. Same cell as shown in B. **D)** CRACM heat map overlaid with Excitatory Post Synaptic Current (EPSC) traces at each point of stimulation. Color gradient represent the amplitude of the EPSC response. Same cell as shown in B. **E)** Maximum intensity projection of a z-stack confocal image of the acute brain slice post-fixed after CRACM recordings. ChR2-YFP expressing layer5 neurons (from the mice genetic background) are shown in green. Reprogrammed cells expressing mCherry are shown in orange. The patched cell was filled with fluorescent dye and shown in magenta. Same cell as shown in B. **F)** Morphological tracing of the cell processes based on z-stack fluorescent images shown in E. **G)** Averaged CRACM heat map of mCherry positive reprogrammed cells (n = 21 cells) and **H)** their surrounding mCherry negative survived neighbors (n = 16 cells). Data from G and H were collected from the same cohort of 6 animals. **I)** Averaged CRACM heat map of untreated ischemia control (n = 19 cells from 4 mice) **J)** Averaged CRACM heat map of sham injected healthy control (n = 26 cells from 5 mice). **K)** Averaged maximal EPSC ± SEM by grid position in tangential direction (parallel to the brain surface) **L)** Averaged maximal EPSC ± SEM by grid position in vertical direction (perpendicular to the brain surface) **M)** Cumulative density curve of EPSCs distribution from each group (same data set as shown in G and H). All groups are significantly different from each other based on Kolmogorov–Smirnov test, significance level $p<0.001$. Insert compares the mean of the natural log-transformed EPSCs amplitude in each group. $p=1.26x10^{-284}$, one-way ANOVA. **** represents $p<0.00001$ from Tukey's post-hoc analysis.

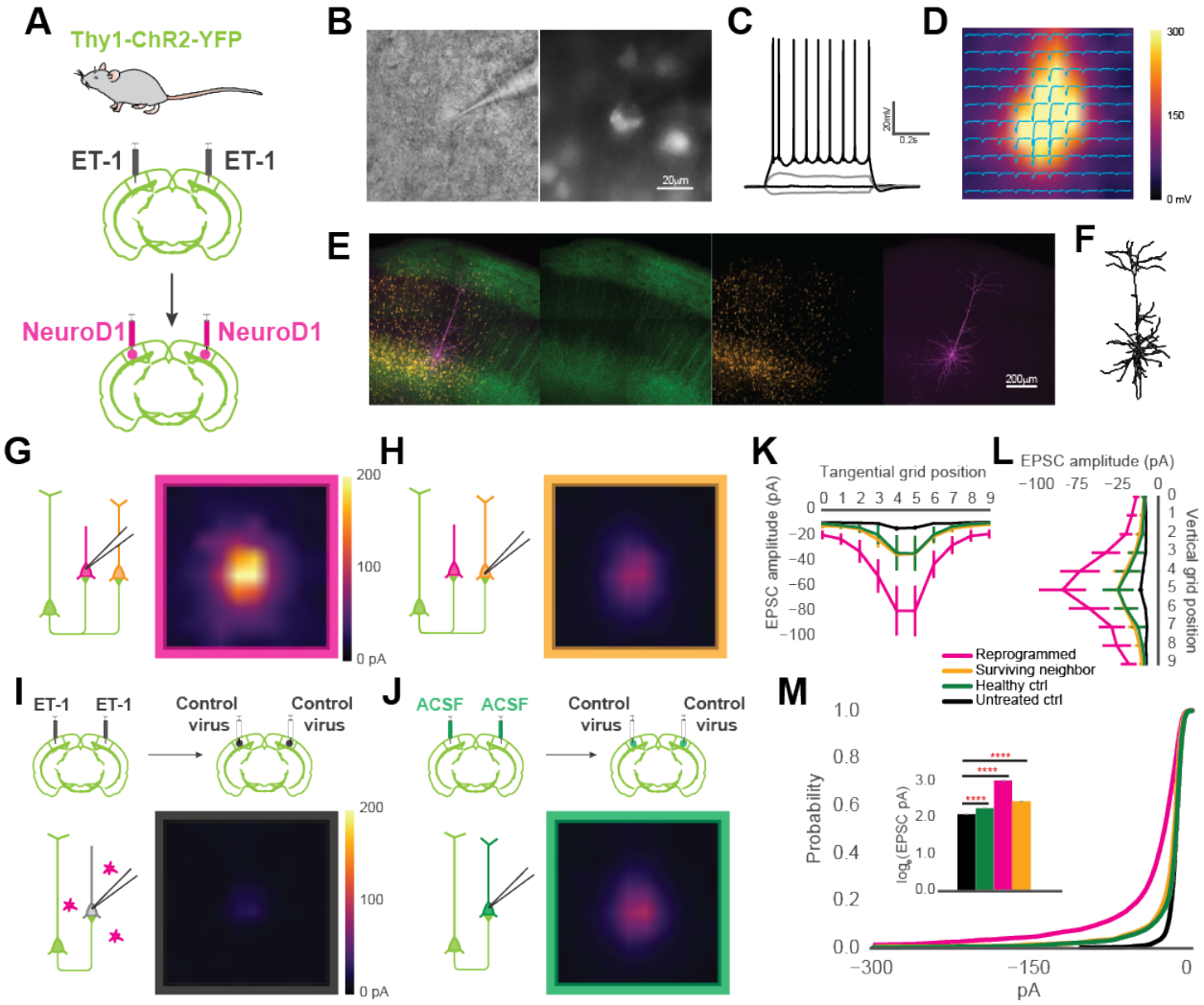
A
Thy1-ChR2-YFP
ET-1
ET-1
NeuroD1
NeuroD1
B
20μm
C
20mV
0.2s
D
300
150
0 mV
E
200μm
F
G
200
100
0 pA
H
K
Tangential grid position
0 1 2 3 4 5 6 7 8 9
EPSC amplitude (pA)
0
−20
−40
−60
−80
−100
L
EPSC amplitude (pA)
−100 −75 −25 0
Vertical grid position
0 1 2 3 4 5 6 7 8 9
Reprogrammed
Surviving neighbor
Healthy ctrl
Untreated ctrl
I
ET-1
ET-1
Control virus
Control virus
200
100
0 pA
J
ACSF
ACSF
Control virus
Control virus
M
Probability
1.0
0.8
0.6
0.4
0.2
0.0
−300
−150
0
pA
log10(EPSC pA)
3.0
2.0
1.0
0.0
****
****
****

Remodeling of connectivity strength after reprogramming

Circuit connectivity improved after delivering the reprogramming gene. However, differences were observed between the reprogrammed and the healthy control groups at 3 weeks after viral infection. To examine long-term effects of *in vivo* direct reprogramming on the functional connectivity of the local circuits, we further measured circuit connectivity at 6 weeks after viral injections.

We conducted CRACM on *ex vivo* brain slices to compare the connectivity profile of the newly reprogrammed cells, their surviving neighbors, surviving cells in the untreated ischemia controls, and cells in the healthy controls. The acute brain slices were prepared using the NMDG recovery method (Ting et al., 2018) due to the age of the animals (2.5 months at the time of CRACM, details see methods section). Reprogrammed cells were well connected to local circuits (**Fig. 27*A***, top left) as well as their surviving neighbors (**Fig. 27*A***, top right). The average connectivity maps of reprogrammed cells and surviving neighbors were comparable to that of the healthy control group (**Fig. 27*A***, bottom right), and were more prominent (qualitatively) than the untreated ischemia control (**Fig. 27*A***, bottom left). When comparing the EPSC amplitude distribution of each group at 6 weeks post-infection (**Fig. 27*B***), the reprogrammed group, surviving neighbors, and the healthy controls all significantly differed from the untreated ischemia control (2 sample Kolmogorov–Smirnov test, Reprogram vs. Untreated: $D = 0.216$, $p = 1.346e\text{-}28$; Surviving vs. Untreated: $D = 0.107$, $p = 8.961e\text{-}8$; Healthy vs. Untreated $D = 0.127$, $p = 1.339e\text{-}13$). Interestingly, the hyper-connectivity to the local circuits in the reprogrammed group was much less prominent compared to at 3 weeks post-infection. The relative connectivity strength indicated that while the reprogrammed group still received significantly stronger projections than the other groups (**Fig. 27*B*** inset, one-way ANOVA $F(3, 5750)=54.69$, $p = 7.514e\text{-}35$; Tukey's HSD test, $p < 0.0001$ between reprogrammed and the other three groups), their surviving neighbors received projections that were not significantly different from the healthy control (Tukey's HSD test, $p = 0.9692$). These results indicated that newly converted neurons survived for at least 6 weeks and received functional connections from the local circuits while allowing surviving neurons to re-integrate. Also, the relative connectivity strength of reprogrammed neurons was modulated over time towards the level of the healthy controls, without additional therapeutic intervention.

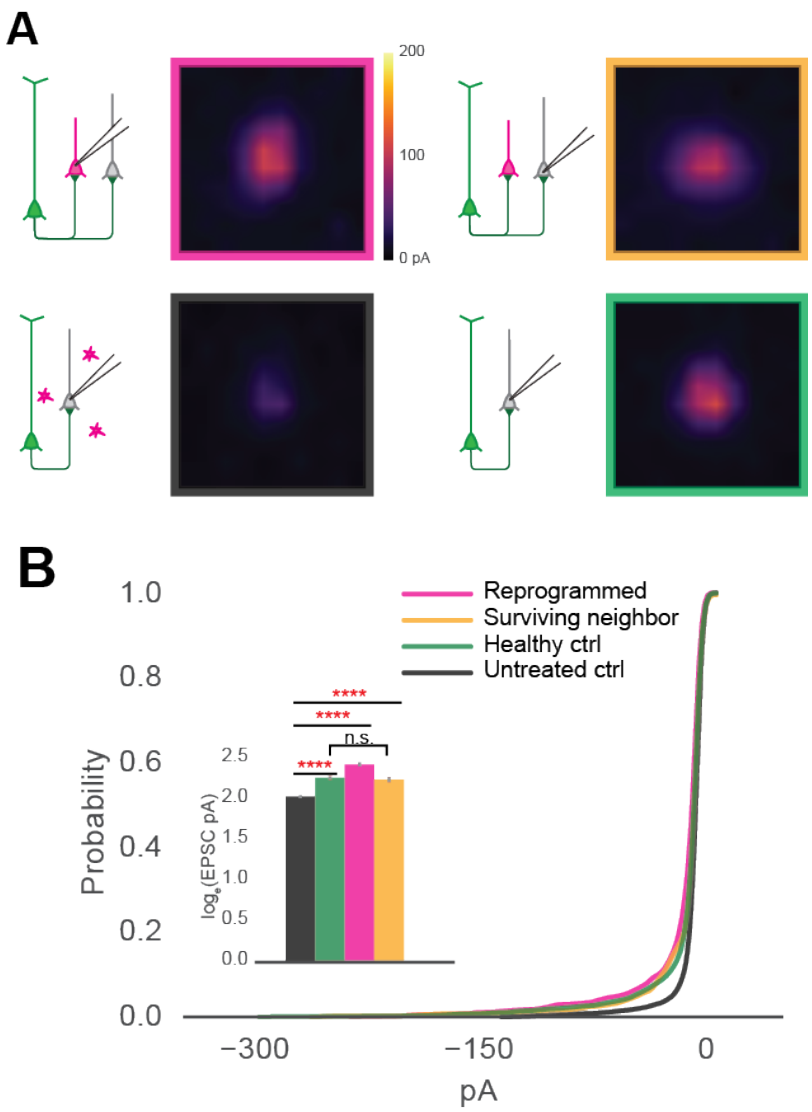

Figure 30. Circuit hypoconnectivity were self-corrected over prolonged recovery time after *in vivo* direct reprogramming following ischemic stroke.

A) Averaged CRACM maps of each group measured at 6 weeks after viral infection. Reprogrammed group (magenta): n = 12 cells from 9 animals; surviving neighbor group (orange): n = 8 cells from 9 animals (same cohort as reprogram); healthy control (green): n = 22 cells from 4 animals; untreated control (grey): n = 16 from 6 animals. **B)** Cummulative density curve showing the distribution of pooled EPSCs amplitude (same data set as shown in C). All groups are significantly different from each other except for between Surviving neighbor and Healthy control (p = 0.002). Two sample Kolmogorov–Smirnov test, significant level p<0.001. Inset compares the mean of the natural log-transformed EPSCs amplitude in each group. $p=7.514x10^{-35}$, one-way ANOVA. **** represents p<0.00001 from Tukey's HSD test, significance level p<0.001.

Circuit restoration through reprogramming is robust across ages

Ischemic injury prevalence increases with age (Johnston et al., 2003; Ovbiagele & Nguyen-Huynh, 2011). Therefore, we conducted similar experiments in older adults to test whether the positive effect of reprogramming in treating ischemic injury also applies to old animals (ischemic injury at over 3 months of age and final assessment at over 5.5 months of age).

Direct local projections were measured with CRACM in older adults and the results were compared to those from young adults. The averaged CRACM maps showed the same trend that newly converted neurons (18 cells from 9 animals) received robust projections, as well as their surviving neighbors (16 cells from the same cohort of 9 animals as above), at a comparable level as in healthy control (34 cells from 8 animals), and the projections were much more prominent than in untreated ischemia control (28 cells from 9 animals, **Fig. 28*A***). The EPSC distribution of the reprogrammed cells was significantly different from all the other groups (2 sample Kolmogorov–Smirnov test, Reprogram vs. Untreated: D = 0.250, p = 1.916e-60; Reprogram vs. Surviving: D = 0.082, p = 2.595e-5; Reprogram vs. Healthy D = 0.077, p = 1.672e-6). The EPSC distribution from surviving neighbors and healthy control were very similar with borderline significance (D = 0.054, p = 0.004), and were both significantly different from the untreated ischemia control (Healthy vs. Untreated: D = 0.183, p = 2.866e-45, Surviving vs. Untreated: D = 0.230, p = 2.601e-46). The same trends were observed for the $\log_e$ transformed EPSC distribution, which is also similar to that of younger adults (**Fig. 28*B*** inset, compared to **Fig. 27*B*** inset). The results here show that *in vivo* reprogramming is equally effective in older adults in creating functionally connected neurons and promoting circuit re-integrations of neighboring neurons after ischemic injury.

We then compared the relative connectivity strengths across the three time points (young adults 3 weeks after reprogramming, young adults 6 weeks after reprogramming, and old adults 6 weeks after reprogramming), as quantified by EPSC magnitude. To account for the overall cortical connectivity change and the concomitant Channelrhodopsin 2 expression level changes over time, we normalized $\log_e$ EPSC values of each group against the healthy control of the same time point (**Fig. 28*C***). The ischemic injury from the same ET-1 injection dosage caused progressively worse damage as time and age increased (Two-way ANOVA, Groups: F(3)=429.34, p = 1.613e-271; Time points: F(2)=187.82, p = 1.209e-81; interaction: F(6)=70.64, p = 1.341e-87. Tukey's HSD test, untreated group: Young 3w vs. Old 6w p<0.0001). 3 weeks

after viral infection, the reprogrammed cells had very prominent hyper-connectivity, the magnitude of which largely decreased at 6 weeks post-infection in both young and old adults (Reprogrammed: Young 3w vs. Young 6w $p<0.0001$; Young 3w vs. Old 6w $p< 0.0001$, Young 6w vs. Old 6w $p = 1.0000$). Interestingly, the surviving neighboring cells in the reprogrammed animals also had slight hyper-connectivity at 3 weeks post-infection, but the connection strength matched the healthy control at 6 weeks post-infection (Surviving: Young 3w vs. Young 6w $p<0.0001$; Young 3w vs. Old 6w $p< 0.0001$, Young 6w vs. Old 6w $p = 0.9999$). In addition to synaptic connections, intrinsic properties such as resistance may also impact circuit activities. We analyzed input resistance based on membrane potential change upon current injections for each patched cell. The newly converted cells at 3 weeks after viral infection had significantly lower input resistance compared to the other groups (**Fig. 28*D***, Two-way ANOVA, Groups: $F(3)=7.79$, $p = 0.0001$; Time points: $F(2)=8.14$, $p = 0.0004$; interaction: $F(6)=0.73$, $p = 0.630$. Tukey's HSD test, among Groups at Young 3 weeks: Reprogram vs. Surviving $p = 0.0067$; Reprogram vs. Untreated $p = 0.033$; Reprogram vs. Healthy $p = 0.030$). This input resistance difference disappeared at 6 weeks post-infection in both young and old adults ($p>0.05$ for all 10 pairs of comparison at Young 6 weeks and Old 6 weeks). We also observed slight increase in input resistance in older mice than in younger mice (Tukey's HSD test between time points: Old 6 weeks vs. Young 6 weeks $p = 0.0004$, Old 6 weeks vs. Young 3 weeks $p = 0.021$) but no difference between the two younger groups (Young 3 weeks vs. Young 6 weeks $p = 0.248$). This finding is consistent with the literature that aging leads to a slight increase in input resistance (Coskren et al., 2015). The result here demonstrated initial hyper-connectivity in newly converted neurons and spontaneous re-modeling of the circuit connectivity towards normalization over longer periods.

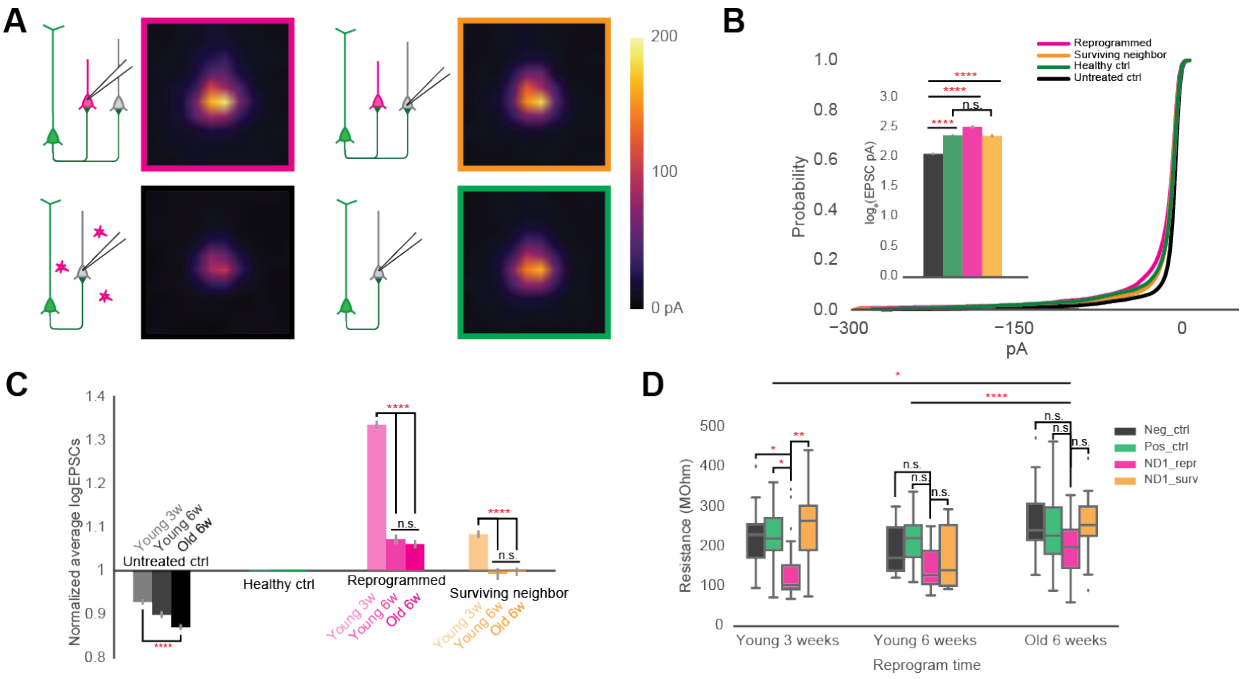

Figure 31. Visual function restoration and circuit repair through *in vivo* direct reprogramming after ischemic stroke was consistent in adult mice.

A) Averaged CRACM maps of each group measured at 6 weeks after viral infection in animals older than 3 months of age. Reprogrammed group (magenta): n = 18 cells from 9 animals; surviving neighbor group (orange): n = 16 cells from 9 animals (same cohort as reprogram); healthy control (green): n = 34 cells from 8 animals; untreated control (grey): n = 28 from 9 animals. **B)** Cummulative density curve showing the distribution of pooled EPSCs amplitude (same data set as shown in C). All groups are significantly different from each other except for between Surviving neighbor and Healthy control (p = 0.004). Two sample Kolmogorov–Smirnov test, significant level p<0.001. Inset compares the mean of the natural log-transformed EPSCs amplitude in each group. $p=9.925\times10^{-72}$, one-way ANOVA. **** represents p<0.00001 from Tukey's HSD test, significance level p<0.001. **C)** $\log_e$EPSC at each time point normalized against the healthy control group. 2-way ANOVA $p_{group}(3)=0.0001$, $p_{time}(2)=0.0004$, $p_{interaction}(6)=0.6294$. **** represents p<0.00001 from Tukey's HSD test. **D)** Box plot comparing input resistance distribution in each group at each time point. 2-way ANOVA $p_{group}(3)=1.613\times10^{-271}$, $p_{time}(2)=1.209\times10^{-81}$, $p_{interaction}(6)=1.341\times10^{-87}$. *-p<0.05, **-p<0.01, ***-p<0.001, ****-p<0.0001 from Tukey's post-hoc analysis. Error bar indicates mean ± SEM.

Discussion

We demonstrated visual functional recovery after V1 ischemic injury by applying NeuroD1-mediated *in vivo* direct reprogramming, which converted astrocytes into mature functionally integrated neurons. The AAV and cre-recombinase cell targeting and gene delivery system effectively converted astrocytes into functional neurons *in situ* in live animals that had focal ischemic injury. Optogenetics-aided *ex vivo* circuit mapping directly revealed that reprogrammed cells received abundant inputs having similar spatial distribution as in healthy controls. More importantly, surviving neurons within the ischemic region also regained local inputs when reprogramming treatment was applied. This population functional recovery and integration of individual cells into the circuit was robust over time in both young and adult mice, indicating potential long-lasting therapeutic effects of *in vivo* direct reprogramming.

Like all brain regions, the visual cortex processes information through highly coordinated activities of the local circuitry (Grossberg, 2003). Insults to the brain may disrupt local circuits and affect normal functions even with little neuronal loss. An example is mild diffuse traumatic brain injury (Greer, Povlishock, & Jacobs, 2012; Lifshitz, Kelley, & Povlishock, 2007). The mild form of focal ischemia that we used in this study consistently induced gliosis but not severe tissue volume loss. Visual responses were significantly attenuated 10 days after the ischemic insult and did not spontaneously recover. Studies on post-stroke circuit plasticity have demonstrated spontaneous circuit rewiring in the penumbra, but the infarct core may lack the ability to remodel (Timothy H. Murphy & Dale Corbett, 2009). It has been recently reported that the Ascl 1 gene can be used to directly reprogram astrocytes into neurons in healthy visual cortices. Similar to our results using NeuroD1-reprogramming, these Ascl 1-reprogrammed neurons were precisely integrated into the local circuitry and adopted retinotopic responses. However, in the focal ischemia condition, the source astrocytes, local environment, and input activities may coordinate differently in determining the fate of the converted cells and circuit wiring. The transcription factor NeuroD1 used in this study was demonstrated to be able to convert astrocytes into neurons in large numbers, up to 40% of total neuronal loss in a severe ischemic injury model (Y. Chen et al., 2018). It is important to study whether *in vivo* direct reprogramming using NeuroD1 could also result in spontaneous circuitry re-organization where newly reprogrammed neurons account for the majority of the neuronal population.

Following reprogramming, we observed initial hyper-connectivity *ex vivo* in newly reprogrammed neurons at 3 weeks after viral injection. This largely diminished after 3 additional weeks, resulting in normal levels of connectivity, while surviving neighbors retained their inputs at levels comparable to the level of the healthy controls. This finding suggested that spontaneous synaptic regulation may be present in the newly reprogrammed neurons, resembling neonatal neuronal development processes (Chechik, Meilijson, & Ruppin, 1999). Two well-studied developmental mechanisms could play a role in this reconfiguration of synaptic strength: microphage-mediated synaptic pruning (Paolicelli et al., 2011) and experience-dependent synaptic plasticity (Holtmaat & Svoboda, 2009), are likely to both play important roles here. During neonatal development, visual input is crucial to the maturation of V1 circuitry, which leads to sparsification of activity. At the early stage of astrocyte-to-neuron conversion, the newly reprogrammed cells receive little input from the environment. As they assume neuronal fate and undergo synaptogenesis, more and more inputs drive the activity of the cell, which in turn could regulate the dynamics of synapses. Surviving neurons also regain connections that are well regulated at the healthy level indicates that glial scar is advantageous to re-opening of the window for circuit plasticity (L. Zhang et al., 2018).

In summary, this study examined the impact of *in vivo* direct reprogramming of astrocytes into neurons on circuit functions after ischemic brain injury. We demonstrated increased connectivity in the local circuit from measurements in *ex vivo* brain slices. Following viral infection, circuit connectivity remodeling occurs spontaneously without any additional therapeutic intervention, and are robust across age groups. Our findings support that *in vivo* direct reprogramming technology has the potential to be a revolutionary treatment, to promote functional recovery after brain injury through replenishing the neuronal population and restoring connectivity of brain circuitry.

References

Asrican, B., Augustine, G. J., Berglund, K., Chen, S., Chow, N., Deisseroth, K., . . . Zhao, S. (2013). Next-generation transgenic mice for optogenetic analysis of neural circuits. *Front Neural Circuits, 7*, 160. doi: 10.3389/fncir.2013.00160

Benjamin, E. J., Virani, S. S., Callaway, C. W., Chamberlain, A. M., Chang, A. R., Cheng, S., . . . Muntner, P. (2018). Heart Disease and Stroke Statistics—2018 Update: A Report From the American Heart Association. *Circulation, 137*(12), e67-e492. doi: doi:10.1161/CIR.0000000000000558

Bernstock, J. D., Peruzzotti-Jametti, L., Ye, D., Gessler, F. A., Maric, D., Vicario, N., . . . Hallenbeck, J. M. (2017). Neural stem cell transplantation in ischemic stroke: A role for preconditioning and cellular engineering. *J Cereb Blood Flow Metab, 37*(7), 2314-2319. doi: 10.1177/0271678X17700432

Blanchard, J. W., Eade, K. T., Szűcs, A., Lo Sardo, V., Tsunemoto, R. K., Williams, D., . . . Baldwin, K. K. (2014). Selective conversion of fibroblasts into peripheral sensory neurons. *Nature Neuroscience, 18*, 25. doi: 10.1038/nn.3887 https://www.nature.com/articles/nn.3887#supplementary-information

Buzsaki, G., & Mizuseki, K. (2014). The log-dynamic brain: how skewed distributions affect network operations. *Nat Rev Neurosci, 15*(4), 264-278. doi: 10.1038/nrn3687

Carmichael, S. T. (2003). Plasticity of Cortical Projections after Stroke. *The Neuroscientist, 9*(1), 64-75. doi: 10.1177/1073858402239592

Chechik, G., Meilijson, I., & Ruppin, E. (1999). Neuronal Regulation: A Mechanism for Synaptic Pruning During Brain Maturation. *Neural Computation, 11*(8), 2061-2080. doi: 10.1162/089976699300016089

Chen, G., Wernig, M., Berninger, B., Nakafuku, M., Parmar, M., & Zhang, C. L. (2015). In Vivo Reprogramming for Brain and Spinal Cord Repair. *eNeuro, 2*(5). doi: 10.1523/ENEURO.0106-15.2015

Chen, Y., Ma, N., Pei, Z., Wu, Z., Do-Monte, F. H., Huang, P., . . . Chen, G. (2018). Functional repair after ischemic injury through high efficiency in situ astrocyte-to-neuron conversion. *bioRxiv*, 294967. doi: 10.1101/294967

Coskren, P. J., Luebke, J. I., Kabaso, D., Wearne, S. L., Yadav, A., Rumbell, T., . . . Weaver, C. M. (2015). Functional consequences of age-related morphologic changes to pyramidal neurons of the rhesus monkey prefrontal cortex. *J Comput Neurosci, 38*(2), 263-283. doi: 10.1007/s10827-014-0541-5

Endres, M., Dirnagl, U., & Moskowitz, M. A. (2008). Chapter 2 The ischemic cascade and mediators of ischemic injury. *92*, 31-41. doi: 10.1016/s0072-9752(08)01902-7

Fitch, M. T., & Silver, J. (2008). CNS injury, glial scars, and inflammation: Inhibitory extracellular matrices and regeneration failure. *Exp Neurol, 209*(2), 294-301. doi: 10.1016/j.expneurol.2007.05.014

Greer, J. E., Povlishock, J. T., & Jacobs, K. M. (2012). Electrophysiological Abnormalities in Both Axotomized and Nonaxotomized Pyramidal Neurons following Mild Traumatic Brain Injury. *The Journal of Neuroscience, 32*(19), 6682. doi: 10.1523/JNEUROSCI.0881-12.2012

Grossberg, S. (2003). How Does the Cerebral Cortex Work? Development, Learning, Attention, and 3-D Vision by Laminar Circuits of Visual Cortex. *Behavioral and Cognitive Neuroscience Reviews, 2*(1), 47-76. doi: 10.1177/1534582303002001003

Guo, Z., Zhang, L., Wu, Z., Chen, Y., Wang, F., & Chen, G. (2014). In vivo direct reprogramming of reactive glial cells into functional neurons after brain injury and in an Alzheimer's disease model. *Cell Stem Cell, 14*(2), 188-202. doi: 10.1016/j.stem.2013.12.001

Hermann, D. M., & Chopp, M. (2012). Promoting brain remodelling and plasticity for stroke recovery: therapeutic promise and potential pitfalls of clinical translation. *The Lancet Neurology, 11*(4), 369-380. doi: https://doi.org/10.1016/S1474-4422(12)70039-X

Holtmaat, A., & Svoboda, K. (2009). Experience-dependent structural synaptic plasticity in the mammalian brain. *Nature Reviews Neuroscience, 10*, 647. doi: 10.1038/nrn2699 https://www.nature.com/articles/nrn2699#supplementary-information

Johnston, S. C., Fayad, P. B., Gorelick, P. B., Hanley, D. F., Shwayder, P., van Husen, D., & Weiskopf, T. (2003). Prevalence and knowledge of transient ischemic attack among US adults. *Neurology, 60*(9), 1429-1434. doi: 10.1212/01.wnl.0000063309.41867.0f

Kawano, H., Kimura-Kuroda, J., Komuta, Y., Yoshioka, N., Li, H. P., Kawamura, K., . . . Raisman, G. (2012). Role of the lesion scar in the response to damage and repair of the central nervous system. *Cell Tissue Res, 349*(1), 169-180. doi: 10.1007/s00441-012-1336-5

Levin, M. F., Kleim, J. A., & Wolf, S. L. (2008). What Do Motor "Recovery" and "Compensation" Mean in Patients Following Stroke? *Neurorehabilitation and Neural Repair, 23*(4), 313-319. doi: 10.1177/1545968308328727

Li, H., & Chen, G. (2016). In Vivo Reprogramming for CNS Repair: Regenerating Neurons from Endogenous Glial Cells. *Neuron, 91*(4), 728-738. doi: 10.1016/j.neuron.2016.08.004

Li, J. Y., Christophersen, N. S., Hall, V., Soulet, D., & Brundin, P. (2008). Critical issues of clinical human embryonic stem cell therapy for brain repair. *Trends Neurosci, 31*(3), 146-153. doi: 10.1016/j.tins.2007.12.001

Lifshitz, J., Kelley, B. J., & Povlishock, J. T. (2007). Perisomatic Thalamic Axotomy After Diffuse Traumatic Brain Injury Is Associated With Atrophy Rather Than Cell Death. *Journal of Neuropathology & Experimental Neurology, 66*(3), 218-229. doi: 10.1097/01.jnen.0000248558.75950.4d

Marro, S., Pang, Z. P., Yang, N., Tsai, M. C., Qu, K., Chang, H. Y., . . . Wernig, M. (2011). Direct lineage conversion of terminally differentiated hepatocytes to functional neurons. *Cell Stem Cell, 9*(4), 374-382. doi: 10.1016/j.stem.2011.09.002

Murphy, T. H., & Corbett, D. (2009). Plasticity during stroke recovery: from synapse to behaviour. *Nature Reviews Neuroscience, 10*, 861. doi: 10.1038/nrn2735 https://www.nature.com/articles/nrn2735#supplementary-information

Murphy, T. H., & Corbett, D. (2009). Plasticity during stroke recovery: from synapse to behaviour. *Nat Rev Neurosci, 10*(12), 861-872. doi: 10.1038/nrn2735

Nakayma, H., Jørgensen, H. S., Raaschou, H. O., & Olsen, T. S. (1994). Compensation in recovery of upper extremity function after stroke: The Copenhagen Stroke Study. *Archives of Physical Medicine and Rehabilitation, 75*(8), 852-857. doi: https://doi.org/10.1016/0003-9993(94)90108-2

Ovbiagele, B., & Nguyen-Huynh, M. N. (2011). Stroke epidemiology: advancing our understanding of disease mechanism and therapy. *Neurotherapeutics : the journal of the American Society for Experimental NeuroTherapeutics, 8*(3), 319-329. doi: 10.1007/s13311-011-0053-1

Paolicelli, R. C., Bolasco, G., Pagani, F., Maggi, L., Scianni, M., Panzanelli, P., . . . Gross, C. T. (2011). Synaptic Pruning by Microglia Is Necessary for Normal Brain Development. *Science, 333*(6048), 1456. doi: 10.1126/science.1202529

Patel, R. A. G., & McMullen, P. W. (2017). Neuroprotection in the Treatment of Acute Ischemic Stroke. *Prog Cardiovasc Dis, 59*(6), 542-548. doi: 10.1016/j.pcad.2017.04.005

Pena, I. D., Borlongan, C., Shen, G., & Davis, W. (2017). Strategies to Extend Thrombolytic Time Window for Ischemic Stroke Treatment: An Unmet Clinical Need. *J Stroke, 19*(1), 50-60. doi: 10.5853/jos.2016.01515

Powers, W. J., Rabinstein, A. A., Ackerson, T., Adeoye, O. M., Bambakidis, N. C., Becker, K., . . . Tirschwell, D. L. (2018). 2018 Guidelines for the Early Management of Patients With Acute Ischemic Stroke: A Guideline for Healthcare Professionals From the American Heart Association/American Stroke Association. *Stroke, 49*(3), e46-e99. doi: doi:10.1161/STR.0000000000000158

Roby-Brami, A., Feydy, A., Combeaud, M., Biryukova, E. V., Bussel, B., & Levin, M. F. (2003). Motor compensation and recovery for reaching in stroke patients. *Acta Neurol Scand, 107*(5), 369-381.

Steinbeck, J. A., & Studer, L. (2015). Moving stem cells to the clinic: potential and limitations for brain repair. *Neuron, 86*(1), 187-206. doi: 10.1016/j.neuron.2015.03.002

Ting, J. T., Lee, B. R., Chong, P., Soler-Llavina, G., Cobbs, C., Koch, C., . . . Lein, E. (2018). Preparation of Acute Brain Slices Using an Optimized N-Methyl-D-glucamine Protective Recovery Method. *Journal of visualized experiments : JoVE*(132), 53825. doi: 10.3791/53825

Tsunemoto, R., Lee, S., Szucs, A., Chubukov, P., Sokolova, I., Blanchard, J. W., . . . Baldwin, K. K. (2018). Diverse reprogramming codes for neuronal identity. *Nature, 557*(7705), 375-380. doi: 10.1038/s41586-018-0103-5

Wu, H., Xu, J., Pang, Z. P., Ge, W., Kim, K. J., Blanchi, B., . . . Sun, Y. E. (2007). Integrative genomic and functional analyses reveal neuronal subtype differentiation bias in human embryonic stem cell lines. *Proc Natl Acad Sci U S A, 104*(34), 13821-13826. doi: 10.1073/pnas.0706199104

Yang, N., Ng, Y. H., Pang, Z. P., Südhof, T. C., & Wernig, M. (2011). Induced neuronal cells: how to make and define a neuron. *Cell Stem Cell, 9*(6), 517-525. doi: 10.1016/j.stem.2011.11.015

Zhang, L., Lei, Z., Guo, Z., Pei, Z., Chen, Y., Zhang, F., . . . Chen, G. (2018). Reversing Glial Scar Back To Neural Tissue Through NeuroD1-Mediated Astrocyte-To-Neuron Conversion. *bioRxiv*, 261438. doi: 10.1101/261438

Zhang, Y., Pak, C., Han, Y., Ahlenius, H., Zhang, Z., Chanda, S., . . . Sudhof, T. C. (2013). Rapid single-step induction of functional neurons from human pluripotent stem cells. *Neuron, 78*(5), 785-798. doi: 10.1016/j.neuron.2013.05.029

CHAPTER 5: DISCUSSION

Neural circuits and circuit dynamics form the foundation of brain function. Mapping circuit connectivity is vital for understanding mechanisms of sensory perception and learning. However, largely due to technical challenges, there is a knowledge gap in functional neural connectivity at the mesoscale local circuit level.

Significance and innovation

To address this issue, we first tackled the technical hurdles. We developed an imaged-guided automated patch-clamp system, "Autopatcher IG", based on the gold-standard classical patch-clamp experiment procedures. This system augmented the manual patch-clamp hardware with computer vision for target cell detection. It enabled fully motorized and automatic control of manipulators and microscope stages. An algorithm based on patching parameters including resistance and pressure achieved robust and consistent giga-sealing and whole-cell access. Autopatcher IG is one of the first systems to achieve image-guided whole-cell patching in acute brain slices (as opposed to dissociated cells or cell culture). It is fully compatible with existing experimental rigs for investigating synaptic connections and brain circuits *ex vivo*. Another advantage of this system is that it is built on conventional manual patching rigs, rather than a completely new hardware system. This means that laboratories can convert existing conventional patch rigs into autopatchers if the rig meets a few basic requirements like motorized microscope stage and manipulators and an available developer's kit for digital control. If these requirements are met, any rig can be automated following the same principle of Autopatcher IG. The same structure can also be applied to automate imaged-guided *in vivo* patch-clamp setups (Long, Li, Knoblich, Zeng, & Peng, 2015).

Equipped with Autopatcher IG and optogenetics technology, we were well positioned to study local circuit connectivity *ex vivo*. The unique advantage of the *ex vivo* acute brain slice preparation is that specific circuits can be characterized in detail at the synaptic and whole cell level. This complements studies in behaving animals, where experimental manipulations can be applied under physiological conditions. We took advantage of optogenetic transgenic mice for consistent and stable Channelrhodopsin expression levels in targeted cell populations. This

approach enabled us to compare the absolute synaptic strength between different groups of age-matched animals. This precise quantitative comparison of absolute synaptic strength would not have been feasible if ChR2 expression was achieved through viral infection, due to the inherent expression variability of that approach. In the case of using viral infection to label presynaptic neurons with ChR2, only internal comparisons can be drawn, usually between two closely located cells in the same brain slice. Because *ex vivo* brain slice preparation is a terminal procedure, studying the effect of experience or disease condition requires direct comparison between different individual animals. To the best of our knowledge, the study of visual experience-dependent circuit plasticity described in Chapter 3 is the first to directly demonstrate the causal relationship of visual experience and local circuit plasticity in V1.

On the other hand, brain function is lost when circuits are disrupted. The search for brain repair technologies, including treatment for neural trauma, stroke, and neurodegenerative diseases, is at the center of attention in neuroscientific research. Unfortunately, very few laboratory studies have thus far translated into effective clinical therapies. Besides the inherent challenges to regenerate neurons, there is also a lack of effective pre-clinical tests to evaluate functional circuit restoration. Although the ultimate standard for a successful treatment of brain damage is behavioral recovery (including sensory, motor, cognitive, etc.), there are significant differences between animal and human behavioral outcomes which make translation between animal and human studies problematic. Animals may compensate behavior in very different ways than do humans. Sensory outcomes can only be indirectly measured in animals. Moreover, high level cognitive function cannot be easily modeled in animals. In Chapter 4, we described using optogenetics-aided circuit mapping *ex vivo* to directly measures functional circuit restoration. The circuit mapping result implicates functional outcomes but could be better generalized beyond the specific animal and disease models described. It also provides a pre-clinical method to quantitatively compare the efficacy between different treatments.

Future directions

To summarize, we approached the need for local circuit mapping with both technical development and innovative methodology, and successfully applied them to demonstrate circuit dynamics during experience and recovery from brain injury. Stemming from discoveries described in Chapters 1 to 4, future studies can be done in the following directions:

Target-cell specific CRACM

In all our circuit mapping experiments, projection targets were non-discriminatively selected. Only the laminar location was considered. Patched post-synaptic neurons could be categorized based on their electrophysiological properties post-hoc. However, this approach is less feasible when the minority cell-type is of research interest. In this case, it would require a very large number of neurons to be mapped so that a useful number of the cell-type of interest is included in the population sample. There is a much easier solution for this problem: use genetics to label the cell-of-interest and only map those cells.

Cell-of-interest can be a distinct cell type marked by specific gene expression, for example parvalbumin-expressing (PV) interneurons. Our findings described in Chapter 3 showed that the excitatory drive onto fast-spiking inhibitory interneurons is where experience-dependent circuit plasticity occurred. Based on this result, we can further explore this projection in different layers as well as interneuron cell-types. We could use reporter transgenic mouse lines such as PV-tdtomato (C57BL/6-Tg(Pvalb-tdTomato)15Gfng/J, JAX) which labels PV+ interneurons and cross it with ChR2 expressing transgenic lines such as Thy1-ChR2-YFP (see Chapter 3 methods). Alternatively, we could cross the PV-cre transgenic line (B6.129P2-Pvalbtm1(cre)Arbr/J, JAX) and ChR2 expressing line, then inject the animals with AAV carrying cre-dependent fluorescent protein gene to the desired brain region. In both cases, we obtain animals that have PV+ neurons labeled with fluorescent protein and have ChR2 expression in pre-synaptic neurons. We have conducted a pilot experiment using the later labeling strategy. We injected AAV carrying the cre-dependent mCherry gene at V1 in neonatal mice with heterozygous PV-cre and heterozygous Thy1-ChR2 background. We mapped mCherry+ (PV+) cells in V1 in L2/3, L4, and L5 receiving L5 excitatory input (**Fig. 29**). We also applied visual training to one group (n=3) of animals while leaving another group (n=4) naïve to the stimulus. This proof-of-principle experiment demonstrated the feasibility to map activities in specific interneuron populations. Similarly, we could target somatostatin-expressing interneurons and indeed this approach is generalizable to allow targeting of any other cell-type with a distinct gene expression marker.

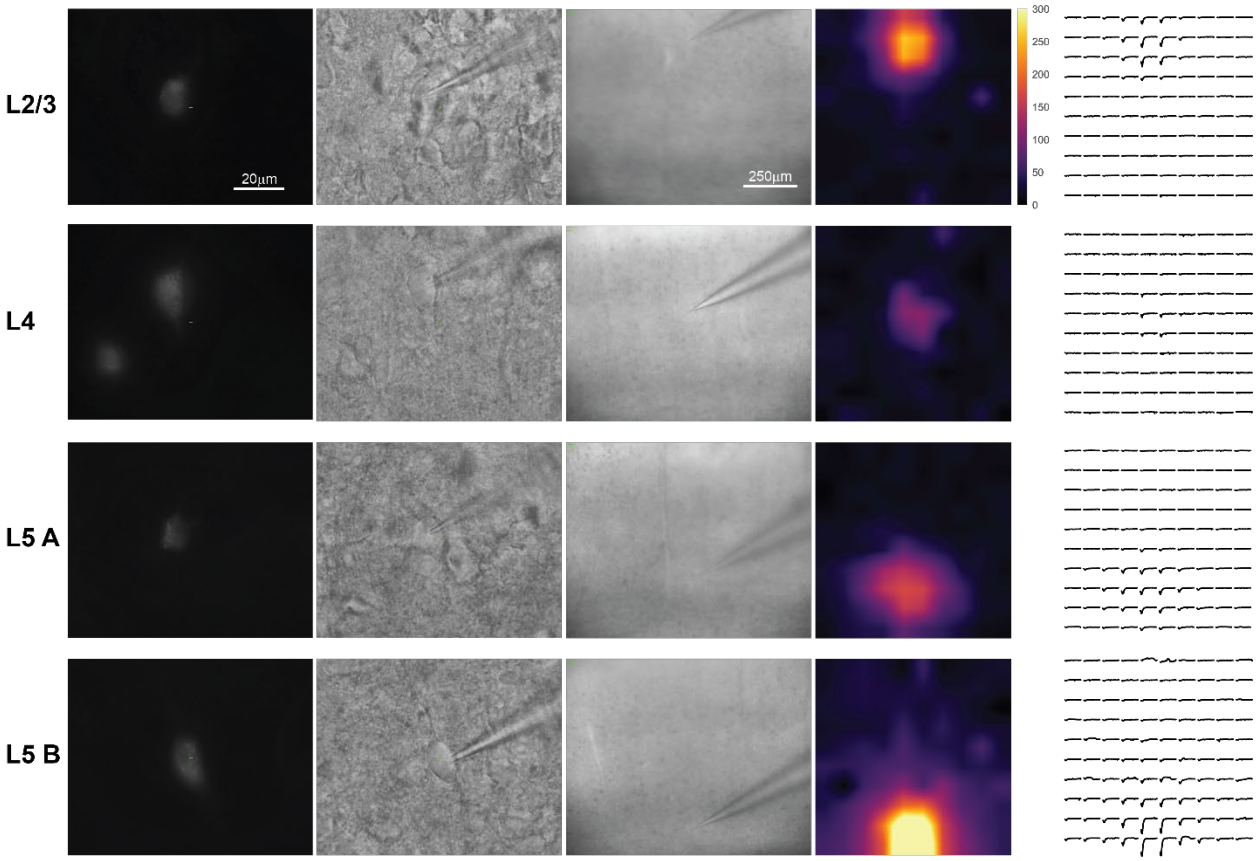

Figure 32. Targeting PV+ cells in different cortical layers for CRACM

For a separate question about how task-specific neuronal ensemble change their connectivity, we could target those neurons using cfos activity-dependent labeling (Kawashima, Okuno, & Bito, 2014). Only neurons that were highly active during the labeling window would express the fluorescent protein that allows us to specifically map their connectivity *ex vivo*. We could apply this approach to identify neurons that were activated during the visual training and compare their connectivity to cells that were not activated. This experiment will provide insight into whether the circuit plasticity observed after visual experience is ubiquitous or specific to the cells associated to the trained visual stimuli.

Inhibitory CRACM

We have only measured excitatory projections using CRACM by optogenetically stimulating glutamatergic excitatory neurons to elicit EPSCs in the patched cell. However, it is also important to measure the strength of inhibitory inputs originating from interneurons. Expressing ChR2 in interneurons will allow us to activate inhibitory cells and record Inhibitory Post-

Synaptic Currents (IPSCs). We conducted a pilot experiment on mice from cross breeding PV-cre and cre-dependent ChR2 (B6.Cg-Gt(ROSA)26Sortm32(CAG-COP4*H134R/EYFP)Hze/J, JAX) transgenic lines (Madisen et al., 2012). We targeted ChR2-YFP negative neurons and recorded inhibitory CRACM maps (**Fig. 33**). IPSCs are slower compared to EPSCs, which needs to be considered during data analysis. One caveat is that the use of Cesium-based pipette internal solution for recording IPSCs prevents some of the cell property characterization because potassium current is abolished. Laminar location, cell morphology, as well as genetic labeling if applicable, can still be used to achieve high specificity in targeting.

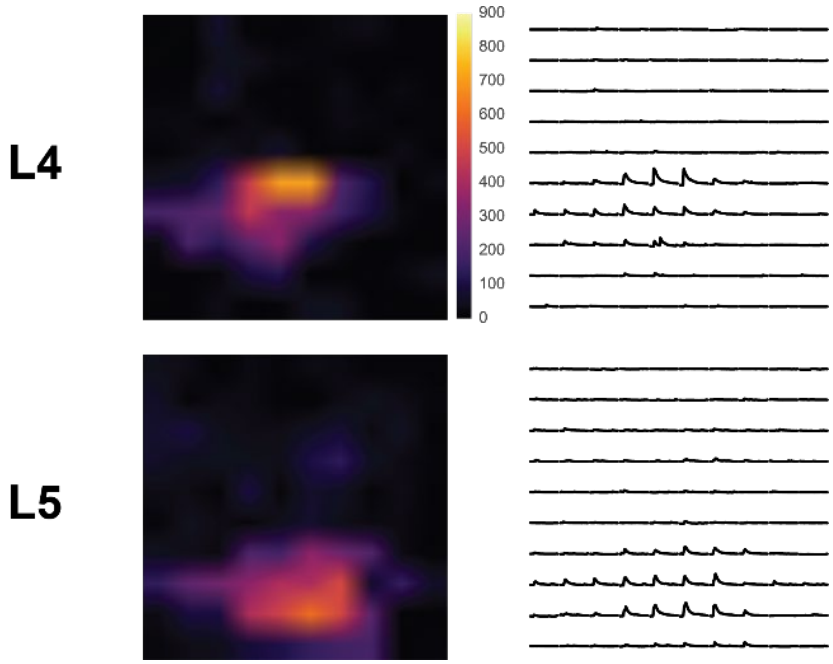

Figure 33. Mapping inhibitory projections from PV+ interneurons using CRACM

Furthermore, CRACM can be used to map the distribution of long-range projections within a small area. For example, we can map the distribution of thalamocortical projections from the LGN to V1 and within V1 using the exact same method described in Chapter 3. Similarly, we can map afferent projections from the V1 newly reprogrammed neurons that synapse in secondary visual areas. We could also incorporate more complex behavioral interventions to study the causal effect on circuits. For instance, whether experience can enhance circuit

restoration by adding training for animals having received reprogramming treatment. Or, whether reward associated to a visual stimulus selectively alters circuit plasticity.

It is the hope that with broader application of CRACM as a functional circuit mapping method, there will be renewed perspective on brain circuitry, function, and repair.

References

Kawashima, T., Okuno, H., & Bito, H. (2014). A new era for functional labeling of neurons: activity-dependent promoters have come of age. *Frontiers in neural circuits, 8*, 37-37. doi: 10.3389/fncir.2014.00037

Long, B., Li, L., Knoblich, U., Zeng, H., & Peng, H. (2015). 3D Image-Guided Automatic Pipette Positioning for Single Cell Experiments in vivo. *Scientific Reports, 5*, 18426. doi: 10.1038/srep18426

https://www.nature.com/articles/srep18426#supplementary-information

Madisen, L., Mao, T., Koch, H., Zhuo, J. M., Berenyi, A., Fujisawa, S., . . . Zeng, H. (2012). A toolbox of Cre-dependent optogenetic transgenic mice for light-induced activation and silencing. *Nat Neurosci, 15*(5), 793-802. doi: 10.1038/nn.3078

APPENDIX

Study the role of Gq signaling in synaptic plasticity using a light-activated Gq coupled receptor melanopsin

This is an incomplete project using optogenetic to study the role of GPCRs signaling in synaptic plasticity. Progress of the project and major problems as well as suggested solutions are described below.

Significance and rationale

There is growing evidence that G_q signaling is involved in different forms of synaptic plasticity, G_q-coupled receptors activation is necessary for the induction of NMDA receptor-dependent LTD in the visual cortex. Furthermore, addition of IP_3 is sufficient to elicit the same effect as receptor activation (Choi et al., 2005). In other cases, such as type I metabotropic glutamate receptor (mGluR)-dependent LTD, plasticity is directly induced by activation of G_q-coupled mGluR with agonist (Huber, Roder, & Bear, 2001). Blocking mGluR results in the failure of a tetanus burst to induce LTP in the hippocampus, indicating that this type of LTP is mGluR-dependent (Wang et al., 2016). Type I mGluRs, including mGluR1 and mGluR5, are expressed selectively in different regions of the brain and induction of mGluR-dependent plasticity varies from low frequency stimulation (LFS), pair pulse LFS, high frequency stimulation (HSF), to stimulating glutamatergic axons and pharmacological activation (Luscher & Huber, 2010). Postsynaptic mechanisms of expression of mGluR-dependent long term plasticity are also protein synthesis-dependent (Huber et al., 2001).

We hypothesize that different G_q -coupled GPCRs in different neurons converge onto the same second messenger signaling pathway to regulate synaptic plasticity. My goal is to map the working range of direct G_q pathway activation to dissect how it can regulate synaptic plasticity in vitro using Melanopsin. Melanopsin is an evolutionally conserved G_q protein-coupled opsin that is expressed in intrinsically photosensitive retinal ganglion cells, and is involved in regulation of the circadian cycle (Freedman et al., 1999). Ectopically expressed melanopsin provides a temporally precise way to control G_q activation, mimicking the activity of neuromodulatory

systems (Bailes & Lucas, 2013). Bypassing different neuromodulator receptors will eliminate the factor of receptor kinetics and downstream signaling differences from different G-protein isoforms, as well as alleviate the difficulties caused by pharmacodynamics of chemical compounds. In contrast, using optogenetics to directly manipulate G_q signaling, and precisely control temporal duration and latency in relation to the synaptic activation will allow me to map the temporal range of G_q activation leading to modulation of synaptic plasticity.

Proposed approach

These experiments will be conducted in acute visual cortical brain slices using whole cell patch clamp. There will be two phases:

I. Probing the role of G_q signaling in the mGluR-dependent LTD

Type I mGluRs are GPCRs that are involved in several kinds of long-term plasticity. mGluR LTD was classically induced by bath application of type I mGluR agonist (Huber, Gallagher, Warren, & Bear, 2002; Palmer, Irving, Seabrook, Jane, & Collingridge, 1997). We will first try to reproduce this phenomenon by prolonged activation (in the scale of minutes) of the Gq pathway using light stimulation of the slices prepared ex vivo following injection of HSV-melanopsin/tdTomato virus into the primary visual cortex (V1) of a mouse. We predict that continuous light activation of melanopsin will lead to LTD. We will determine the optimal light intensity required for the induction of LTD (**AppFig. 1**)

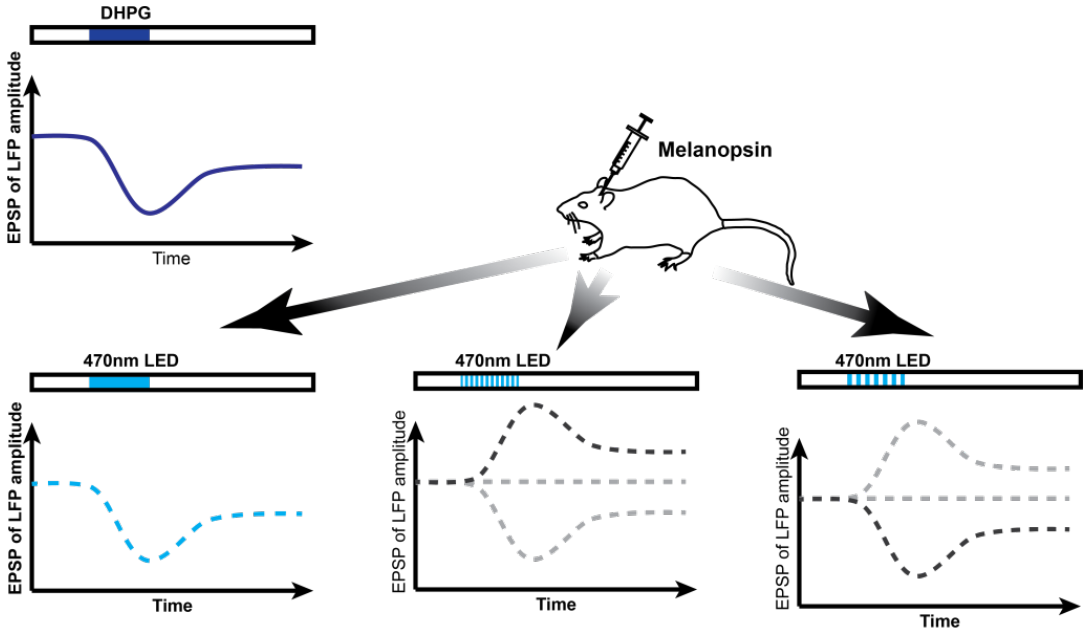

Appendix figure 1. Experimental design for probing Gq signaling in mGluR-dependent long-term plasticity.

Stereotaxic injection of the HSV-Melanopsin/tdTomato virus into the primary visual cortex (V1). Ex vivo brain slices preparation. Modulating frequency, power and duration of light stimulation to recapitulate mGluR-LTD or to trigger mGluR-LTP.

After confirming the above LTD, I will try to use light pulses at different frequencies to activate G_q and measure the outcome. We hypothesize that G_q activation can result in either LTP or LTD depending on the activation pattern.

II. The role of G_q signaling in reward timing

Another question that we want to ask is how G_q signaling affects the direction and the magnitude of long-term plasticity when paired with Hebbian conditioning. Previous findings suggest that cholinergic system acts phasically during the time of reward or punishment, and the cholinergic projections are required for many forms of visual cortical plasticity, including reward timing. Furthermore, cholinergic timing-dependent plasticity has been reported in the hippocampus (Gu & Yakel, 2011). In the hippocampus, activation of the cholinergic projections 10 ms following the glutamatergic Schaffer Collaterals (SCs) activation leads to LTP, while activation of the cholinergic projections 10 ms before SCs leads to depression. Similar to the hippocampus, the visual cortex might also have a similar type of cholinergic-dependent synaptic plasticity. This plasticity is consistent with the previous reports that induction of STDP may require co-activation of various neuromodulators (He et al., 2015). Our first goal is to reproduce a classical STDP protocol. However, it is also possible that similarly to other laboratories, at some synapses we will have difficulties inducing synaptic changes, if both "pre before post" and "pre after post" stimulations do not lead to long term plasticity which can be transformed by G_q activation (**AppFig. 2**).

After we establish a "neutral" STDP protocol (STDP protocol that does not induce any long term plasticity), we will pair light activation of melanopsin with synaptic activation in STDP paradigm at different time intervals and sequences to measure the change of synaptic strength before and after the pairing compared to no G_q activation (classical STDP only).

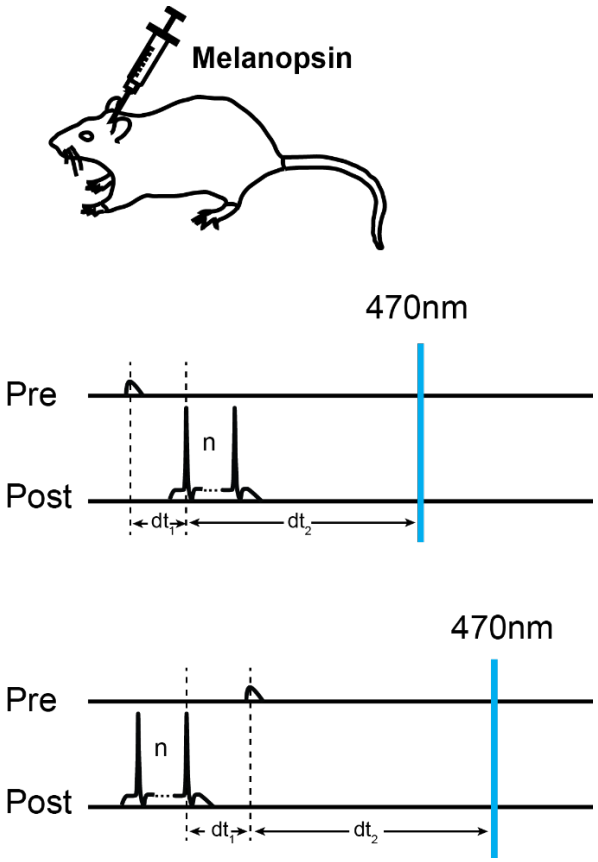

Appendix figure 2. Experimental design for probing Gq signaling in mGluR-dependent STDP.

Preliminary results:

Validating melanopsin expression:

I have injected HSV-melanopsin/tdTomato (human melanopsin construct) into V1 using stereotaxic surgery. The animals were allowed 2 to 3 days to recover and express the protein before acute brain slices preparation. Red fluorescent signal was observed under epifluorescence microscope for slice electrophysiology. Some fluorescence positive cells were patched and stimulated with prolonged LED light at 470nm. Continuous activation of Gq signaling will increase the intracellular calcium level and eventually lead to depolarization and action potential, which was what was observed (**AppFig. 3**). I have validated that the construct is working properly under our experimental conditions.

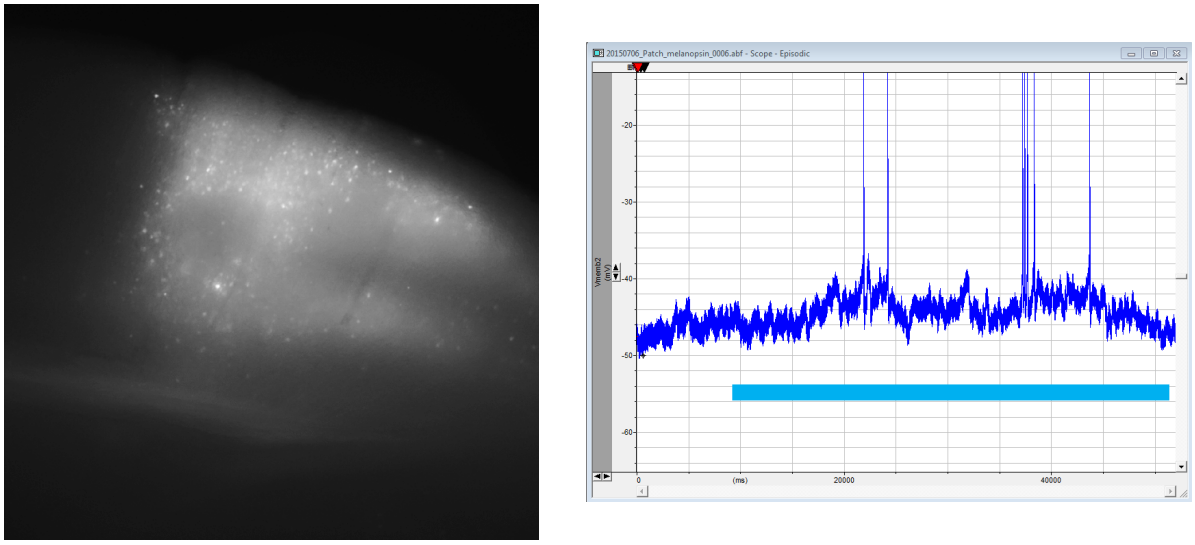

Appendix figure 3. Melanopsin expression in V1.

Exploring long-term plasticity range:

After optimizing melanopsin virus injection parameters and the length of expression, I have conducted the first step of an experiment which is to use prolonged continuous light to induce long-term plasticity. I used layer 5 (L5) to layer 2/3 (L2/3) feedback projection as the target synapse to modulate and I used electrical stimulation from electrode placed on the surface of the brain slice. The recording was first done in the whole-cell patch configuration. Melanopsin-positive cells were patched and low-intensity light (2% LED source power focused by the 40x objective lens) was applied continuously for 5 minutes after a 10min baseline (**AppFig. 4*B***). About 20% LTD was observed at the end of 60min recording (**AppFig. 4*D***). However, it was very difficult to obtain stable baseline in many trials and very difficult to record the full 60min without losing the patch. The quality of the patch and the health of the melanopsin-tdtomato positive cells was the main concern. Following this experiment, I tried to record local field potential (LFP) as a read-out for synaptic strength. The rationale behind using LFP is that if enough cells/synapses express melanopsin, plasticity should be observed on the populational level. We saw broad expression of melanopsin which supports this assumption. However, I was not able to induce LFP at L2/3 by stimulating L5. I stimulated at layer 4 (L4) instead and was able to record LFP comparable to studies in the literature. 100% LED source power was applied to the slice through 4X objective lens continuously for 10min (**AppFig. 2*A***). About 20% LTP was observed at the end of the 60min recording (**AppFig. 2*C***). It was still difficult to obtain stable baseline and the slice dies occasionally during the 60min recording.

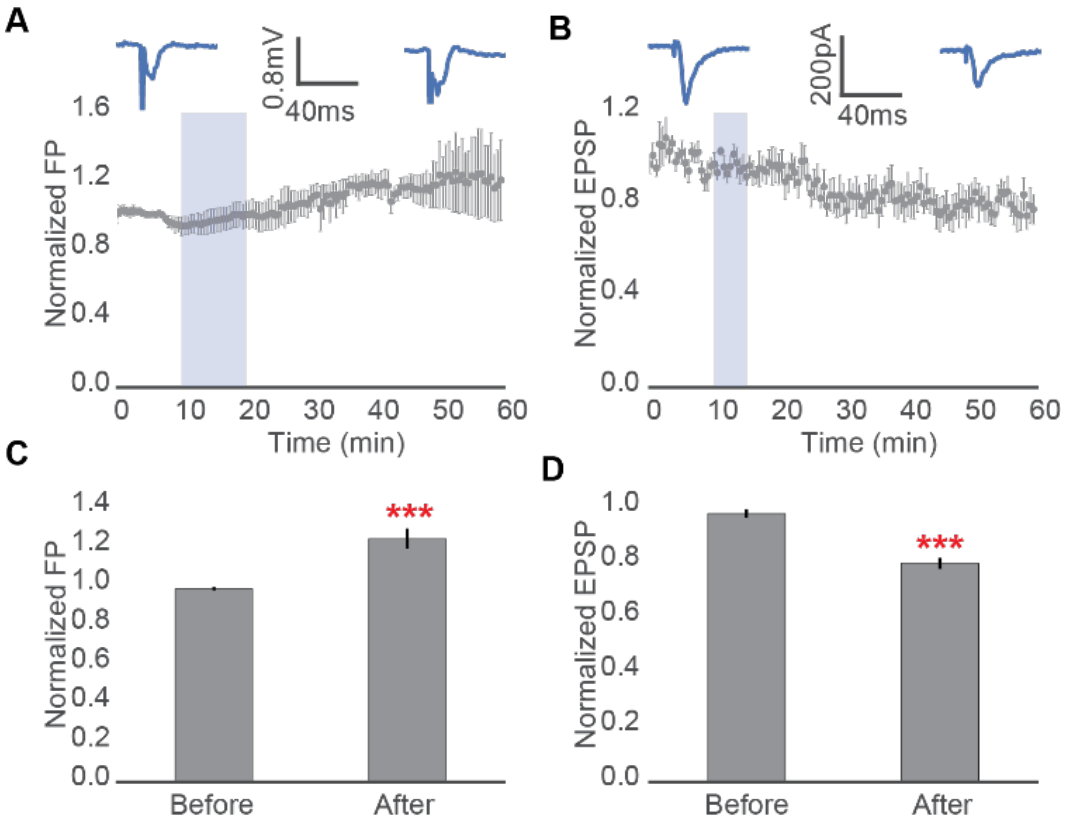

Appendix Figure 4. Melanopsin activation resulted in bi-directional long-term plasticity in the primary visual cortex (V1) layer 2/3 neurons.

A)10min continuous illumination (shaded) at lower intensity induced long term potentiation measured by field potential (n=3, from 2 animals). **B)** 5min continuous illumination (shaded) at higher intensity induced long term depression measured by whole cell patch clamp (n=9, from 5 animals). **C)** Lower light activation of melanopsin (corresponds to A resulted in 20% LTP, p=5.37x10-6. D: Higher light activation of melanopsin (correspond to B resulted in 20% LTD, p=2.05x10-11. Response amplitude was normalized to the average response amplitude of the 10min baseline before stimulation. Statistics of before and after stimulation were taken from 5 to 10min and 55 to 60min.

The actual total light power applied onto the slice measured by a power meter showed that there was about 39mW power for 100% LED source under 4X lens and 0.51mW power for 2% LED source under 40X lens. Assume that the visual field of 4X lens is 100 times of the visual field at 40X, the irradiance intensity (mW/cm^2) ratio 100% LED 4X : 2% LED 40X = 1:1.3. In other words, we observed LTD under higher intensity focused activation of melanopsin close to the target cell and LTP under lower intensity broad activation of melanopsin in the whole slice. Given that the light power is likely to have exceeded saturation of melanopsin excitation, the important factor is the range of excitation.

To address the toxicity of viral injection, we purchased HSV carrying both melanopsin-tdtomato and melanopsin-GFP constructs. The expression of both was high but cells appear similarly unhealthy. This result ruled out the possibility that td-tomato fluorescent protein was causing the toxicity. Attempts to conduct further melanopsin experiments were paused due to the low throughput of at most 1 successful recording per day. The low success rate suggests potential problems with the current experimental design and/or slice preparation. The possible problems are:

- Toxicity from HSV
- Sub-optimal acute brain slice preparation technique
- LED light power too high or too low

Establish STDP protocols:

First, I attempted to reproduce classical STDP experiments in V1 slices. The presynaptic stimulations were administered through electrical stimulation of white matter (thalamocortical synapse) in WT animals or by light activation in Thy1-ChR2 (L5 to L2/3 synapse) or Vglu2-ChR2 (thalamocortical synapse) mouse lines. The post synaptic spiking delay was 10 or 50ms after the presynaptic stimulation, the number of spikes was 1 or 4, and the training frequency varied from 0.03Hz to 0.3Hz. I have tried both current (IC) and voltage clamp (VC), following protocols in the literature. However, I could not get consistent results, and most of the protocols I tried resulted in apparent LTD, which I suspect was actually the result of unhealthy slices.

Additional backgrounds

After the original discovery in 1998(Provencio, Jiang, De Grip, Hayes, & Rollag, 1998), properties of melanopsin has been gradually characterized including its expression profile(Provencio et al., 1998), physiological function to regulate circadian cycle(Hannibal & Fahrenkrug, 2002; Provencio et al., 2000), and downstream G_q-coupled signaling pathway(Panda et al., 2005; Qiu et al., 2005; Terakita et al., 2008). Later it was discovered that melanopsin signals through both G_q and $G_{i/o}$ pathway(Bailes & Lucas, 2013; Cao et al., 2012) although it is likely that the downstream signaling depends on the membrane domain localization and G-protein availability. However, the fact that melanopsin can signal through two different GPCR pathways raises the concern that we cannot pinpoint the effect of melanopsin activation to a specific pathway without further investigation.

More importantly, melanopsin activation/inactivation is bi-stable, meaning that it stays activated upon illumination near 480nm and is inactivated upon illumination near 570nm(Spoida et al., 2016). We were not aware of this property of melanopsin when we designed the experiment. It is most likely that melanopsin was "turned on" and never inactivated during our experiment, and possibly "turned on" before baseline during exploration period in experiments using melanopsin-GFP construct. In the same study, they also reported that mouse melanopsin variant is superior to human melanopsin variant because the activation magnitude does not diminish upon repeated or prolonged activation.

Adjusted approach

With the available human melanopsin construct, I am planning to repeat the plasticity experiment but activate with one 10s 488nm light pulse and inactivate with 10s 570nm light pulse (wavelength limited to LED light source fixed wavelength). Also, taking into account that melanopsin is extremely light sensitive (much more sensitive than Channelrhodopsin), I suggest taking special precaution to light contamination during slice recovery and exploration. I suggest using melanopsin-tdtomato construct and use 570nm light to locate melanopsin-expressing cells. I suggest using both synaptic events recorded through whole-cell patch and LFP as the read-outs of synaptic strength until one method is proven to be better than the other.

References

Bailes, H. J., & Lucas, R. J. (2013). Human melanopsin forms a pigment maximally sensitive to blue light (lambdamax approximately 479 nm) supporting activation of G(q/11) and G(i/o) signalling cascades. *Proc Biol Sci, 280*(1759), 20122987. doi: 10.1098/rspb.2012.2987

Cao, P., Sun, W., Kramp, K., Zheng, M., Salom, D., Jastrzebska, B., . . . Feng, Z. (2012). Light-sensitive coupling of rhodopsin and melanopsin to G(i/o) and G(q) signal transduction in Caenorhabditis elegans. *Faseb j, 26*(2), 480-491. doi: 10.1096/fj.11-197798

Choi, S. Y., Chang, J., Jiang, B., Seol, G. H., Min, S. S., Han, J. S., . . . Kirkwood, A. (2005). Multiple receptors coupled to phospholipase C gate long-term depression in visual cortex. *J Neurosci, 25*(49), 11433-11443. doi: 10.1523/jneurosci.4084-05.2005

Freedman, M. S., Lucas, R. J., Soni, B., von Schantz, M., Munoz, M., David-Gray, Z., & Foster, R. (1999). Regulation of mammalian circadian behavior by non-rod, non-cone, ocular photoreceptors. *Science, 284*(5413), 502-504.

Gu, Z., & Yakel, J. L. (2011). Timing-dependent septal cholinergic induction of dynamic hippocampal synaptic plasticity. *Neuron, 71*(1), 155-165. doi: 10.1016/j.neuron.2011.04.026

Hannibal, J., & Fahrenkrug, J. (2002). Melanopsin: a novel photopigment involved in the photoentrainment of the brain's biological clock? *Ann Med, 34*(5), 401-407.

He, K., Huertas, M., Hong, Su Z., Tie, X., Hell, Johannes W., Shouval, H., & Kirkwood, A. (2015). Distinct Eligibility Traces for LTP and LTD in Cortical Synapses. *Neuron, 88*(3), 528-538. doi: 10.1016/j.neuron.2015.09.037

Huber, K. M., Gallagher, S. M., Warren, S. T., & Bear, M. F. (2002). Altered synaptic plasticity in a mouse model of fragile X mental retardation. *Proc Natl Acad Sci U S A, 99*(11), 7746-7750. doi: 10.1073/pnas.122205699

Huber, K. M., Roder, J. C., & Bear, M. F. (2001). Chemical induction of mGluR5- and protein synthesis--dependent long-term depression in hippocampal area CA1. *J Neurophysiol, 86*(1), 321-325.

Luscher, C., & Huber, K. M. (2010). Group 1 mGluR-dependent synaptic long-term depression: mechanisms and implications for circuitry and disease. *Neuron, 65*(4), 445-459. doi: 10.1016/j.neuron.2010.01.016

Palmer, M. J., Irving, A. J., Seabrook, G. R., Jane, D. E., & Collingridge, G. L. (1997). The group I mGlu receptor agonist DHPG induces a novel form of LTD in the CA1 region of the hippocampus. *Neuropharmacology, 36*(11-12), 1517-1532.

Panda, S., Nayak, S. K., Campo, B., Walker, J. R., Hogenesch, J. B., & Jegla, T. (2005). Illumination of the melanopsin signaling pathway. *Science, 307*(5709), 600-604. doi: 10.1126/science.1105121

Provencio, I., Jiang, G., De Grip, W. J., Hayes, W. P., & Rollag, M. D. (1998). Melanopsin: An opsin in melanophores, brain, and eye. *Proc Natl Acad Sci U S A, 95*(1), 340-345.

Provencio, I., Rodriguez, I. R., Jiang, G., Hayes, W. P., Moreira, E. F., & Rollag, M. D. (2000). A novel human opsin in the inner retina. *J Neurosci, 20*(2), 600-605.

Qiu, X., Kumbalasiri, T., Carlson, S. M., Wong, K. Y., Krishna, V., Provencio, I., & Berson, D. M. (2005). Induction of photosensitivity by heterologous expression of melanopsin. *Nature, 433*(7027), 745-749. doi: 10.1038/nature03345

Spoida, K., Eickelbeck, D., Karapinar, R., Eckhardt, T., Mark, M. D., Jancke, D., . . . Masseck, O. A. (2016). Melanopsin Variants as Intrinsic Optogenetic On and Off Switches for Transient versus Sustained Activation of G Protein Pathways. *Curr Biol, 26*(9), 1206-1212. doi: 10.1016/j.cub.2016.03.007

Terakita, A., Tsukamoto, H., Koyanagi, M., Sugahara, M., Yamashita, T., & Shichida, Y. (2008). Expression and comparative characterization of Gq-coupled invertebrate visual pigments and melanopsin. *J Neurochem, 105*(3), 883-890. doi: 10.1111/j.1471-4159.2007.05184.x

Wang, H., Ardiles, A. O., Yang, S., Tran, T., Posada-Duque, R., Valdivia, G., . . . Kirkwood, A. (2016). Metabotropic Glutamate Receptors Induce a Form of LTP Controlled by Translation and Arc Signaling in the Hippocampus. *J Neurosci, 36*(5), 1723-1729. doi: 10.1523/JNEUROSCI.0878-15.2016

VITA

Qiuyu Wu (Rachel), PhD candidate in Biology, Purdue University (May 2019 completion)

• Translational neurobiology expert • Cross-functional project leader • Technology innovator • Mentor

Scientific expertise

Neurophysiology

Neurological diseases

Gene therapy

Programming

Training and mentorship

Technology transfer

Communication skills

Communicating science to broad audience

Scientific illustration and graphic design

Cross-functional team collaboration

Languages

English

Chinese Mandarin

Chinese Cantonese

Fellowships and Awards

- Purdue University Lynn fellowship (2014~2015)
- Hong Kong Baptist University undergraduate summer research fellowship (awarded twice in 2010 & 2011)
- West Virginia University Organic Chemistry Award (2012)

Laboratory skills

Ex vivo acute brain and spinal cord slices

In vitro patch clamp

Stereotaxic surgery in rodents

Immunohistochemistry

Confocal imaging Primary cell culture

Gene cloning and expression *in vitro* and *in vivo*

Routine molecular and cellular biology techniques

Education

Ph.D. Neuroscience: Purdue University 2014~May 2019

BSc. Applied Biology: Hong Kong Baptist University 2009~2013
First class (highest) honor BSc. in Applied Biology, minor in German.

Work experience

Graduate teaching assistant (Jan. 2019~present) at Purdue University for the class "Data Analysis in Neuroscience". Design course material and assist in an interactive class setting where students learn how to analyze large life science dataset using Python.

Graduate research assistant (Aug. 2014~Jan. 2019) at Purdue University in Dr. Alexander Chubykin's lab studying neural circuit mapping. Also initiated and lead an external collaborative project with Pennsylvania State University.

Staff research assistant (Aug. 2013~2014) at Hong Kong Baptist University School of Chinese Medicine Clinical division, supervised by Prof. Zhaoxiang Bian (MD, PhD), leading the project "the effect of neonatal maternal separation on adult hippocampus neurogenesis."

Leadership positions

President
Purdue University Interdisciplinary Life Science Program (PULSe) Graduate Student Organization (GSO)

Board Member
Science Philanthropy Student Board (SPSB), Purdue Research Foundation

Seminar Chair (PULSe GSO)

Diversity and inclusion Chair (PULSe GSO)

Research and Project Management

Project I: Functional neural-circuit mapping technology development.

- Teamed with software engineers to **develop an automated image-guided patch clamp electrophysiology system** "Autopatcher IG" (two publications, one ***patent application***).
- Combined state-of-the-art optogenetic technology and Autopatcher IG for direct measurement of neural functional connectivity.

Project II: Evaluating circuit functional restoration of a novel brain repair therapy

- **Pre-clinical efficacy evaluation** of a new brain repair therapy: *in-vivo* direct reprogramming of reactive astrocytes into functional neurons. This therapy has the potential to be used for all gliosis-inducing **traumatic brain injury, stroke,** and **neurodegenerative diseases.**
- Initiated **inter-institutional collaboration** between Purdue University and Pennsylvania State University. Assisted **legal** and **administrative** processes.
- Drafted project plan and formed a team, **influenced without having authority**.
- **Managed project progress** and **facilitated communications** among team members and collaborators from both institutions.
- Conducted experiments and drafted manuscript. Publication is in preparation.

Project III: Experience-dependent circuit plasticity and the impairment in Fragile X syndrome

- Dissected the circuit mechanism of learning disability in an **Autism Spectrum Disorder** mouse model by directly measuring circuit connectivity.

Collaborations: instrumentation, Nano-technology, neural stimulation, etc.

- Collaborated with material engineers to develop novel quantum semi-conductor material for biological sensing and machine-neural interface. **Designed and implemented biological testing protocol.**
- Collaborated with electrical engineers to develop next-generation micro wireless implantable Multi-Electrode Array (MEA) for chronic *in vivo* recording of neural activities. **Effectively communicated to multiple parties** with varying neuroscience background and **achieved the team goal** of prototyping and testing.
- Collaborated with chemical engineers to evaluate a Nano-structure in aiding neurite regeneration and guidance. **Upheld rigorous research ethics** when facing pressure from multiple entities, some were highly influential personnel.

Patent

US patent "Automated image-guided patch-clamp electrophysiology in vitro", pending approval.

Application publication number: US20170138926 A1 **Qiuyu Wu is the second inventor**

Invited presentations

1. Hong Kong Baptist University (Dec. 2018) "In vivo direct reprogramming restores local circuit connectivity after focal stroke" (**Invited as international speaker**)
2. Beijing Normal University (Jan. 2018) "Automated functional local circuit mapping" (**Invited as international speaker**)
3. Biological Sciences Cellular molecular biology seminar (Dec. 2016) "Autopatcher IG--Image assisted automatic whole cell patch clamp system in vitro" (**Invited as external speaker**)
4. 2016 BioCrossroads Indiana Life Sciences Summit (**Invited poster presentation**)
5. Eli Lilly & Co. Grand Rounds Seminar Series poster session (**Invited poster presentation**)

Publications

1. Zhang, H.-T., Zuo, F., Li, F., Chan, H., **Wu, Q.**, Zhang, Z., . . . Ramanathan, S. (2019). Perovskite nickelates as bio-electronic interfaces. Nature Communications, 10(1), 1651. doi: 10.1038/s41467-019-09660-6
2. Huang, Y., Jiang, Y., **Wu, Q.**, Wu, X., An, X., Chubykin, A. A., . . . Yang, C. (2018). Nanoladders Facilitate Directional Axonal Outgrowth and Regeneration. ACS Biomaterials Science & Engineering, 4(3), 1037-1045. doi: 10.1021/acsbiomaterials.7b00981
3. **Wu, Q.**, & Chubykin, A. A. (2017). Application of Automated Image-guided Patch Clamp for the Study of Neurons in Brain Slices. J Vis Exp(125). doi: 10.3791/56010
4. **Wu, Q.**, Kolb, I., Callahan, B. M., Su, Z., Stoy, W., Kodandaramaiah, S. B., . . . Chubykin, A. A. (2016). Integration of autopatching with automated pipette and cell detection in vitro. J Neurophysiol, 116(4), 1564-1578. doi: 10.1152/jn.00386.2016
5. Jou, A. Y., Shan, H., Pajouhi, H., Tsai, M., Ghotbi, S., **Wu, Q.**, . . . Mohammadi, S. (2017, 4-9 June 2017). A single-chip wireless microelectrode array for neural recording and stimulation. Paper presented at the 2017 IEEE MTT-S International Microwave Symposium (IMS).
6. Jia, L., **Wu, Q.**, Ye, N., Liu, R., Shi, L., Xu, W., . . . Zhang, J. (2012). Proanthocyanidins inhibit seed germination by maintaining a high level of abscisic acid in Arabidopsis thaliana. J Integr Plant Biol, 54(9), 663-673. doi: 10.1111/j.1744-7909.2012.01142.x

Services

Student organization: Purdue University Interdisciplinary Life Sciences Program (PULSe) Graduate Student Organization (GSO) (2015~present)

Philanthropy: Purdue University College of Science Student Philanthropy Board (2016~present)

Mentoring: Mentored 4 graduate students and 5 undergraduate students in research. Mentored in Summer Undergraduate Research Fellowship (SURF) program for multiple years. Frequent speaker at student panels about career development.

Community outreach:

- Volunteer teaching in rural China (Summer of 2013)
- Purdue University Spring Fest (Spring of 2015, 2016, and 2017)
- PULSe Science in Schools (SIS) program
- The Lafayette Regional Science and Engineering Fair
- Big Ten Plus Graduate Exposition (GradExpo)

Grant application success

- The Graduate Student Organization Grant Allocation (GSOGA) award (October 2017)

  Awarded the maximum amount of $1500 to the PULSe GSO for its service to the graduate student community. Authored and applied as the president of the organization.

- National Institute of Mental Health R01 research grant (1R01MH116500-01A1): Neural Mechanisms of Predictive Impairments in Autism (September 2017). PI: Alexander Chubykin.

  Provided essential preliminary data figures and text, and created illustrations of the central concept for the grant application.

PUBLICATIONS

1. Zhang, H.-T., Zuo, F., Li, F., Chan, H., **Wu, Q**., Zhang, Z., . . . Ramanathan, S. (2019). Perovskite nickelates as bio-electronic interfaces. *Nature Communications, 10*(1), 1651. doi: 10.1038/s41467-019-09660-6

2. Huang, Y., Jiang, Y., **Wu, Q**., Wu, X., An, X., Chubykin, A. A., . . . Yang, C. (2018). Nanoladders Facilitate Directional Axonal Outgrowth and Regeneration. *ACS Biomaterials Science & Engineering, 4*(3), 1037-1045. doi: 10.1021/acsbiomaterials.7b00981

3. **Wu, Q**., & Chubykin, A. A. (2017). Application of Automated Image-guided Patch Clamp for the Study of Neurons in Brain Slices. *J Vis Exp*(125). doi: 10.3791/56010

4. **Wu, Q**., Kolb, I., Callahan, B. M., Su, Z., Stoy, W., Kodandaramaiah, S. B., . . . Chubykin, A. A. (2016). Integration of autopatching with automated pipette and cell detection in vitro. *J Neurophysiol, 116*(4), 1564-1578. doi: 10.1152/jn.00386.2016

5. Jou, A. Y., Shan, H., Pajouhi, H., Tsai, M., Ghotbi, S., **Wu, Q**., . . . Mohammadi, S. (2017, 4-9 June 2017). *A single-chip wireless microelectrode array for neural recording and stimulation.* Paper presented at the 2017 IEEE MTT-S International Microwave Symposium (IMS).